TARGETED COLLAGEN PHOTOCROSSLINKING FOR TREATMENT OF GLAUCOMA

A Dissertation
Presented to
The Academic Faculty

by

Brandon Grant Gerberich

In Partial Fulfillment
of the Requirements for the Degree
Doctor of Philosophy in the
Wallace H. Coulter Department of Biomedical Engineering at Georgia Institute of Technology and Emory University

Georgia Institute of Technology & Emory University
May 2020

TARGETED COLLAGEN PHOTOCROSSLINKING FOR TREATMENT OF GLAUCOMA

Approved by:

Dr. Mark R. Prausntiz, Advisor
School of Chemical and Biomolecular Engineering
Georgia Institute of Technology

Dr. M.G. Finn
School of Chemistry and Biochemistry
Georgia Institute of Technology

Dr. C. Ross Ethier
Wallace H. Coulter Department of Biomedical Engineering
Georgia Institute of Technology

Dr. Anastasios Costarides
Emory Eye Center
Emory University

Dr. Machelle T. Pardue
Wallace H. Coulter Department of Biomedical Engineering
Georgia Institute of Technology

Date Approved: March 27, 2020

To Mom, Dad, Lauren, and Diana

ACKNOWLEDGEMENTS

I wish to acknowledge my family, whose guidance has been unfailing for as long as can be remembered. Dad, your example, and Mom, your encouragement, especially led me to pursue my doctoral studies in biomedical engineering. Thank you, Lauren and Diana, likewise, for your support!

Thank you, Dr. Prausnitz, for your guidance and mentorship. I am especially thankful for your keen senses of technical reasoning and communication which sharpened my maturity as a researcher. Without your encouragement to pursue complementary studies, I also would not have discovered my newfound passions for computational modeling and statistics. Though I owe many varieties of thanks, the last I will mention here is my gratitude for allowing me to pursue my MBA (and TI:GER Fellowship) concurrently with my PhD research.

Thank you as well to my collaborating advisors, Dr. Ethier and Dr. Pardue - your expertise in ocular mechanics and eye biology greatly enhanced the breadth and depth of my research foundation. I am especially appreciative of your encouragement throughout the *in vivo* studies in chapter 4 and thank you for making possible the whole globe inflation testing and rat microbead experiments critical to chapters 3 and 4.

Thank you to my thesis committee members for your time and expertise which guided my research path and thesis writing. In addition to Dr. Ethier and Dr. Pardue acknowledged above, I would like to acknowledge Dr. Costarides for his clinical expertise related to the mechanisms of glaucoma and his view to clinical translation. I would also like to

acknowledge Dr. Finn for his expertise on the subject of chemical mechanisms involved in crosslinking.

I wish to acknowledge my colleague, Bailey Hannon, without whom much of the 3rd and 4th chapters would not have been possible. She is responsible for developing the glaucoma rat model used in these studies and for collecting the functional outcomes data including ERG, OMR, and OCT measurements as well as IOP data. Thank you, Bailey, for all your hard work – it's been a pleasure working together these past four years!

Thank you to Dr. Thomas Read and Dr. Stephen Schwaner for your assistance and expertise in axon sectioning and inflation testing data analysis, respectively. Thank you to Dr. Andrew Feola for your guidance and assistance with rat microbead studies. Thank you to Amir Hejri and Dr. Hans Grossniklaus for histological tissue sections and their interpretation.

I would also like to acknowledge those in the Prausnitz Lab who have especially impacted my studies at Georgia Tech: Amir Hejri, Bryce Chiang, Jeremy Chae, Jaehwan Jung, and Yoo Chun Kim (eye research team), Juan Mena Lapaix, Youngeun Kim, Matthew Mistilis, (cubicle neighbors), and all Prausnitz Lab Members, past and present.

A special note of thanks goes to Dr. Richard Schaefer who generously taught me the inner workings of a microscope, lending both his expertise and optics hardware. His assistance was foundational for my development of the customized microscope described in chapter 3 and used in chapter 4.

Thank you to Drs. Laura O'Farrell and Richard Noel and all PRL staff, from whose time/talent I benefitted in learning veterinary techniques and whose dedication to excellence in biomedical research made possible the studies in chapters 3-5.

To all the undergraduate and master students who worked with me on my research, your dedication and ambition for learning furthered the progress of these studies far beyond that achieved by my own capacity. Thank you to: Matthew Dalton (BS), Hannah Gersch (BS), Srishti Gupta (BS), Niyati MacLeod (BS), Lauren Nichols (BS), Afsane Radmand (BS), Sahana Ravishankar (MS), Elisa Schrader (BS), and Erin Winger (BS). Your combined efforts amounted to approximately 27 person-semesters (9 academic years).

Finally, and most especially, I wish to thank Donna Bondy, whose cheerful assistance with all matters of logistics has been a tremendous asset to the Prausnitz Lab. Thank you for your patience and unfailing support, both in the "uh-oh" moments and the "aha" moments.

TABLE OF CONTENTS

LIST OF TABLES

LIST OF FIGURES

LIST OF SYMBOLS AND ABBREVIATIONS

AA	Amino Acid
ANCOVA	Analysis of Covariance
ANOVA	Analysis of Variance
CXL	Collagen Crosslinking
DIC	Digital Image Correlation
His	Histidine
FMN	Flavin Mononucleotide
HBSS	Hank’s Balanced Salt Solution
IOP	Intraocular Pressure
LC	Lamina Cribrosa
Mel	Melanin
Met	Methionine
MB	Methylene Blue
ON	Optic Nerve
ONH	Optic Nerve Head
PP	Peripapillary
PS	Photosensitizer
RB	Rose Bengal
RF	Riboflavin
RPE	Retinal Pigmented Epithelium
Trp	Tryptophan
Tyr	Tyrosine

SUMMARY

Glaucoma is the leading cause of irreversible blindness worldwide and has a complex etiology associated with elevated intraocular pressure. Biomechanical forces induce vision loss through strain-induced damage to the retinal ganglion cells conducting visual information from the retina to the brain. This work tests the hypothesis that stiffening the peripapillary scleral (collagenous tissue adjacent to the optic nerve) protects against glaucomatous vision loss. A photocrosslinking approach was 1) developed to selectively stiffen the peripapillary sclera *in vivo,* 2) tested for efficacy in a rat animal model of glaucoma, and 3) simulated using a computational model to predict optimal photocrosslinking parameters.

Scleral photocrosslinking was successfully targeted to the peripapillary sclera *in vivo* and found to have moderate treatment toxicity. *In vivo* studies in glaucomatous rats revealed that our treatment did not worsen glaucomatous damage contrary to a previous study. Computational modeling predicted key treatment parameter values and showed that crosslinking is most sensitive to tissue rather than sensitizer properties. Together, this body of work demonstrates the feasibility of using targeted scleral photocrosslinking as a potential future treatment of glaucoma.

CHAPTER 1. INTRODUCTION

Glaucoma is a leading cause of blindness worldwide and has been the subject of pharmacological and biomechanical research[1–3]. This work consists of a novel method for treatment for glaucoma described in three parts: 1) *in vivo* proof of concept in healthy rats, 2) *in vivo* safety and efficacy studies in glaucomatous rats, and 3) a theoretical computational model for treatment optimization.

1.1 Scleral Stiffening as a Therapeutic Strategy in Glaucoma

It has been hypothesized that reducing the pressure-induced strain on the optic nerve head will reduce glaucomatous vision loss. Previously, Coudrillier et al. showed that mechanically stiffening the peripapillary sclera (sclera adjacent to the optic nerve head) will reduce the pressure-induced strain experienced by the optic nerve head[4]. This finding suggested that scleral stiffening is a promising therapeutic strategy for preventing pressure-induced glaucomatous damage. However, it was recently shown that whole globe scleral stiffening increased glaucomatous axon loss in mice contrary to the anticipated effect of preserving axon health[5]. We believe whole globe stiffening may exacerbate glaucomatous damage due to the inability for the sclera to attenuate cyclical fluctuations in intraocular pressure. Therefore, we propose to selectively stiffen the peripapillary sclera as a method for preventing pressure-induced damage in glaucoma.

1.2 Targeted Peripapillary Stiffening Approach

In the investigated approach, targeted peripapillary scleral stiffening is enabled by directing a transpupillary light beam at the peripapillary region to excite a photosensitive

crosslinking agent. In comparison to non-photoactivated crosslinking agents, photosensitive crosslinking agents allow for selective stiffening with millimeter resolution only where both light and crosslinking agents are present. We designed a microscope which allows for controlled illumination of the peripapillary sclera by means of a transpupillary approach. The transpupillary approach is advantageous because it is non-invasive (unlike catheterized delivery) and provides a clear optical path for targeting the peripapillary region. A photosensitive crosslinking agent was administered using a retrobulbar injection whereby the agent is injected into the retrobulbar muscle cone adjacent to the posterior scleral surface. This injection approach, while already in common clinical practice, also delivers the crosslinker near the target peripapillary scleral tissue achieving local concentration sufficient for crosslinking.

1.3 Theoretical Computational Modeling

In addition to experimental evidence for targeted photocrosslinking at the peripapillary sclera, a theoretical model for predicting degree of crosslinking was created to optimize treatment parameters. The model incorporates elements of molecular photodynamics, diffusion, and chemical kinetics to predict the final distribution of crosslinks in the sclera over time and 1-dimensional space. A combination of temporal and spatial information is useful for analyzing trends in the distribution of crosslinking and for assessing optimal treatment time scales, especially if reaction mechanisms change over time. Key treatment parameters of interest (inputs) include crosslinker concentration, light intensity, and irradiation duration. Additionally, the model may be used to simulate the efficiencies of various crosslinking agents, thus informing research decisions to pursue future crosslinking experiments.

CHAPTER 2. BACKGROUND

2.1 Glaucoma

Glaucoma is the second leading cause of blindness in the world affecting an estimated 70 million individuals globally[1]. It is a pressure-sensitive optic neuropathy which damages retinal ganglion cells responsible for transmitting visual information from the retina to the brain[6,7]. The only known effective therapy is IOP pressure management. Glaucoma is closely associated with aging and is the leading cause of blindness in African Americans[8–10]. Retinal ganglion cell death may remain undetected until there is significant visual loss, leading to late diagnoses at which point loss is permanent[11]. When diagnosed early, treatment strategies aiming to reduce elevated IOP are employed[12]. Unfortunately, certain patients experiencing little or no IOP elevation may still progress towards glaucomatous vision loss[13]. Therefore, a preventative treatment which can reduce or entirely inhibit loss of vision from glaucomatous RGC damage is of vital interest and would change the treatment paradigm for glaucoma management.

2.2 Intraocular Pressure Elevation

Elevated intraocular pressure associated with hypertension glaucoma is caused by impaired outflow of aqueous humor from the anterior chamber of the eye combined with unimpaired production. In healthy eyes, aqueous humor is generated by the ciliary body and is cleared through the trabecular meshwork, a network of extracellular lamellae and cells located at the iridocorneal angle[14]. In addition to clearance through the trabecular meshwork to episcleral veins (conventional outflow), there exists a second, less prevalent route of

clearance, the uveoscleral pathway, whereby aqueous humor ultimately exits through a number of structures including the sclera, suprachoroidal space, or uveal blood vessels[15]. Increased resistance for aqueous outflow in the trabecular meshwork has been associated with changes in tissue mechanical properties, gene expression, and induced decellularization[16–18].

2.3 Retinal Ganglion Cell Loss

Hypertensive IOPs result in biomechanical insult to posterior ocular tissues, leading to RGC death. Specifically, RGC death is caused by increased IOP-induced mechanical strains at the lamina cribrosa which trigger cellular apoptosis[19]. This apoptotic pathway is believed to be mediated by mechanical strain-induced dysfunction of axonal transport mechanisms leading to deficits in neurotrophic factors[20]. While the biological pathway of strain-mediated apoptosis is not well defined, effects of elevated IOP on RGC loss have been well characterized. For example, it is known that retinal ganglion cell death occurs in a spatially inhomogeneous manner with superior/inferior quadrant axon loss preceding that of the nasal/temporal quadrants[21].

2.3.1 Current Treatment Strategies

Glaucoma treatment research focuses on two main strategies for protecting against vision loss: 1) reduction of IOP, and 2) neuroprotection[22][23]. Pressure reduction strategies aim to lower IOP in order to prevent pressure-induced damage to RGCs. Neuroprotection aims to confer resistance to apoptosis to retinal ganglion cells by modulating cellular biochemistry[24].

2.3.2 Pressure Reduction

Pressure reduction strategies are the only clinically-utilized glaucoma treatments[25]. These include 1) pressure-lowering pharmaceutical eye drops, 2) trabeculoplasty (laser treatment), 3) shunts (surgery), 4) trabeculectomy (surgery), and 5) cyclophotocoagulation (laser ablation)[26][27]. Medication is preferred for ease of use and generally positive outcomes. In cases where pressure management is difficult with medication, trabeculoplasties, shunting procedures, and trabeculectomies (incisional pressure relief) are used[28].

2.3.3 Neuroprotectants

Neuroprotectants are a relatively new class of drug recently entering clinical trials which aims to protect retinal ganglion cells against oxidative stress, immune dysregulation, and apoptotic pathway initiation[24]. Memantine, a glutamate receptor antagonist shown to be promising in Alzheimer's clinical trials, was recently tested for neuroprotection in glaucoma but failed to show benefit compared to placebo[29]. Despite great research interest in the area of neuroprotection for treatment of glaucoma, few agents have succeeded in early clinical trials[30].

2.4 Eye Structure

2.4.1 Optic Nerve

Elevated IOP is directly associated with optic nerve deformation and retinal ganglion cell loss[31]. Retinal ganglion cells form the retina nerve fiber layer. RGC axons travel from the retina nerve fiber layer through the optic nerve head to the optic nerve. The optic nerve

head in humans is supported structurally by a thin connective tissue, the lamina cribrosa, through which retinal ganglion cell axons pass[32]. It is hypothesized that glaucomatous damage will be more severe in individuals with weaker material structure of the lamina cribrosa[33]. The lamina cribrosa itself is structurally weaker than the surrounding collagenous scleral tissue and is observed to become "cupped" in glaucomatous individuals[34]. Cupping is the indentation of the lamina cribrosa posteriorly and is identified by the loss of axons of the retinal nerve fiber layer from the space normally occupied by healthy axons flush with the surrounding sclera. In glaucomatous individuals, cupping depth increases with disease severity ranging from approximately 344 μm in healthy individuals to 448 μm in moderate/late stage glaucoma[35]. For visual representation of these changes in optic nerve head morphology, see Wollstein et al. [36].

2.4.2 Sclera & Peripapillary Collagen

The sclera is the collagen-rich outer layer of the eye which provides the primary structural support for the retina and other ocular tissues and has a distinctive white color in human eyes[37]. It separates the choroid, a vascularized layer of tissue posterior to the retina, from the tenon capsule, a fibrous fascia posterior to the sclera. The sclera begins anteriorly at the limbal interface with the cornea and contiguously encompasses the posterior globe with the exception of the scleral canal, a small circular opening through which the optic nerve passes[38]. The peripapillary sclera is defined as the scleral region immediately proximate to the scleral canal and is suspected to play a role in the biomechanics of the optic nerve head[4]. Type I collagen constitutes the major structural protein of the sclera which has a collagen composition of approximately 22.5% - 50% in humans [39,40].

2.4.3 Collagen Structure

Type I collagen is one of the most abundant proteins in animals and is organized into a triple helix comprised of three separate fibrils[41]. The primary structure of collagen is rich with glycine and proline residues, comprising approximately 34% and 25% respectively of the helical chain[42]. Natural crosslinks formed between lysine and arginine residues provide structural connectivity between fibers[43].

2.5 Glaucoma Biomechanics and Scleral Stiffening

2.5.1 Peripapillary Scleral Stiffening

Optic nerve head biomechanical properties have long been hypothesized to play a key role in glaucoma progression[44]. Furthermore, properties of the surrounding sclera including stiffness and thickness are predicted to strongly impact optic nerve head biomechanics[45][46]. Peripapillary scleral stiffening has been shown by Coudrillier et al. to reduce strain applied to the optic nerve in porcine whole globe inflation tests with a 47% reduction in lamina cribrosa strain corresponding with a 34% increase in peripapillary scleral stiffening [4]. This finding reveals the potential for a glaucoma treatment utilizing peripapillary scleral stiffening for reduction of lamina cribrosa strains and therefore for preservation of RGC health in glaucoma.

2.5.2 Whole Scleral Stiffening

It has been shown by Kimball et al. that mice treated with the scleral stiffening agent glyceraldehyde throughout the posterior segment experience greater axonal loss than those without treatment[5]. These findings were unexpected in light of the Coudrillier study as

they contradict the expectation that axon loss would be mitigated due to reduction of peripapillary scleral strain, and thus lamina cribrosa strain. However, we believe the findings of Kimball et al. could not be used to rule out the possibility for axon protection by peripapillary scleral stiffening for a few reasons. First, the injection osmolarity used in the Kimball study (900 mOsm) was higher than physiological conditions (285-295 mOsm)[47]. Second, we believe whole sclera stiffening may worsen glaucomatous damage by reducing the eye's natural compliance capable of attenuating fluctuations in the intraocular pulse. Targeted peripapillary stiffening, on the other hand, may preserve the eye's natural compliance while mitigating damaging strain at the optic nerve head. It has been shown that increasing IOP in hypertension glaucoma increases amplitude of the ocular pulse, leading to our suspicion that the ocular pulse is a potential driver of biomechanical insult[48,49].

2.6 Chemical Crosslinking

2.6.1 Chemical Crosslinkers

Chemical collagen crosslinkers include glutaraldehyde, glyceraldehyde, and genipin. Glutaraldehyde is perhaps the strongest of these, but it suffers from high toxicity[50]. Chemical crosslinkers readily react with collagen without the need for additional reactants and have been shown to induce stiffening in both *ex vivo* and *in vivo* rat sclera[51][52]. However, chemical crosslinkers currently have yet to find clinical use in vivo.

2.6.2 Mechanisms of Chemical Crosslinking

Both glyceraldehyde and glutaraldehyde contain reactive aldehyde groups. Glutaraldehyde reacts with free amine groups, particularly with those of the side chains of lysine[53]. Likewise, glyceraldehyde reacts with amines of lysine or arginine[54]. Though not containing aldehydes in its chemical structure, genipin reacts with primary amines through an aldehyde intermediate[55].

2.7 Photosensitizers & Photocrosslinking

Photosensitizers have been used both to kill unwanted cells and to strengthen collagenous tissues throughout the body, though they have only recently found use in the eye. Previous non-ophthalmic experimental studies have used photosensitizers for oncological treatment, pericardial tissue stabilization, tendon repair and dentin crosslinking[56][57][58–60].

2.7.1 Photodynamic Therapy (PDT)

Photodynamic therapy is the use of a photosensitizer and incident photons to target and destroy select tissues *in vivo.* As a cancer treatment, PDT has been in use clinically since the 1970s with an established body of accompanying research from which numerous photosensitizers (Table 1) have emerged[61–64]. The primary disadvantage of PDT is the limited depth of light penetration through biological tissues resulting in use for superficial rather than deep tissue applications. Therefore, PDT treatments have been developed for tissues (such as skin) where light may be easily delivered as in the example of actinic keratosis[65].

2.7.2 Desirable Photosensitizer Properties

Desirable properties for photodynamic therapeutic agents include efficient localization to cancer sites, low off-target localization, efficient absorbance of incident photons, absorbance in the phototherapeutic window, efficient triplet state energy transfer to triplet oxygen, and low dark toxicity[66]. Generally, strong absorbance at longer wavelengths is desirable since biological absorber efficiency declines in the 650-800 nm regime encompassing most current sensitizers[67]. Novel photosensitizer development has evolved continuously to meet these standards with an emphasis on improving energy transfer efficiency by preventing aggregation of molecules as well as improved absorbance at longer wavelengths[68,69].

2.7.3 *Photosensitization Mechanism*

Photosensitization reactions begin with the absorbance of a photon by a photosensitizer in the ground state, the condition in which all electrons are in the lowest energy state[70]. Upon absorption of the photon, an electron enters an elevated singlet excited state (excited electron has opposite spin state compared to paired ground state electron), from which it may lose its energy through three processes: 1) vibrational relaxation (heat dissipation), 2) fluorescence emission of a lower energy photon, or 3) intersystem crossing where the excited singlet state electron converts to a triplet excited state thus resulting in two unpaired electrons with identical spin state[70]. Triplet states are long-lived in most sensitizers, for example, on the order of 29 μs for riboflavin in water and 77μs for methylene blue in water[71,72]. The efficiency at which an absorbed photon will result in a triplet excited state sensitizer molecule is the triplet quantum yield ($\boldsymbol{\phi}_T$). Photosensitizers with high triplet

quantum yield and long triplet lifetimes are the most efficient since the triplet excited state subsequently reacts with ground-state oxygen to produce reactive oxygen species.

2.7.4 *Photophysical Properties of Photosensitizers*

Two important quantifiable properties of photosensitizers are 1) molar absorptivity (ε), and 2) singlet oxygen quantum yield ($\boldsymbol{\phi}_{\Delta}$.) Molar absorptivity describes the absorbance of a photoactive molecule and is useful as a component of the Beer-Lambert Law, with higher molar absorptivity values indicating more proficient absorbance. Singlet oxygen quantum yield is defined as the fraction of absorbed photons which result in the generation of a molecule of singlet oxygen. Mathematically, this value is represented as the product of the triplet quantum yield, fraction of triplets quenched by oxygen, and the fraction of oxygen molecules which have quenched the triplet state and convert to singlet oxygen[73]. High singlet oxygen quantum yields indicate greater photophysical efficiency of sensitization, with a value of 1 indicating highly efficient conversion and 0 indicating no conversion. Singlet oxygen quantum yields greater than 1 are theoretically possible, though small molecule sensitizers generally have yields in the range of 0.3-0.8. The photophysical properties of some common sensitizers are listed below:

Table 1: Photosensitizers and their properties.

Photosensitizer	Peak Absorbance	Molar Absorptivity	Singlet Oxygen Quantum Yield	Reference
Porfimer Sodium	632 nm	3,000 $M^{-1}cm^{-1}$	0.89	[62,67]
Temoporfin	652 nm	30,000 $M^{-1}cm^{-1}$	0.87	[62,67]
Mono Aspartyl Chlorin e6	654 nm	40,000 $M^{-1}cm^{-1}$	0.56-0.77	[74,75]
Methylene Blue	664 nm	79,800 $M^{-1}cm^{-1}$	0.52	[76,77]
Zinc Phthalocyanine Tetrasulfonate	670 nm	100,000 $M^{-1}cm^{-1}$	0.46-0.49	[78–80]
Aluminum Phthalocyanine Tetrasulfonate	675 nm	105,000 $M^{-1}cm^{-1}$	0.38	[81,82]
Verteporfin	689 nm	33,000 $M^{-1}cm^{-1}$	0.78	[83]
Motexafin Lutetium	732 nm	40,000 $M^{-1}cm^{-1}$	0.38	[84]
Redaporfin	743 nm	140,000 $M^{-1}cm^{-1}$	0.17	[67]
Padeliporfin	762 nm	110,000 $M^{-1}cm^{-1}$	0.15-0.21†	[67,85]
Indocyanine Green	800 nm	115,000 $M^{-1}cm^{-1}$	0.012-0.12	[86,87]

† Oxygen consumption quantum yield – padeliporfin does not generate singlet oxygen

2.7.5 Molecular Classifications of Photosensitizers

Photosensitizers are a class of light-absorbing molecules which mediate cell death by direct interaction of the excited dye molecule with cellular constituents or by energy transfer to form toxic reactive oxygen species[63]. They can be classified into groupings based on chemical structure with those absorbing in the phototherapeutic window including porphyrins, chlorins, pheophorbides, bacteriopheophorbides, texaphyrins, phthalocyanines, naphthalocyanines, and phenothiazines[62]. Photosensitizers in FDA-approved products include Levulan (5-amniolevulinic acid) indicated for actinic keratosis,

Visudyne (verteporfin) indicated for AMD, and Photofrin (porfimer sodium) indicated for endobronchial cancer[62].

2.7.6 Methylene Blue

Methylene blue (Figure 1) is a small molecule phenothiazinium dye photosensitizer with marked blue color due to its strong absorbance at approximately 665nm[88]. It is primarily a type II sensitizer[89]. Historically used as a cyanide antidote, methylene blue is presently FDA-approved for intravenous injection as a treatment for the blood disorder, methemoglobinemia[90,91]. Methylene blue has been shown to be well-tolerated by the rat retina after intravitreal injection, indicating reasonable biocompatibility in the eye[92]. Interestingly, it has also recently shown promise as a neuroprotectant for Alzheimer's[93].

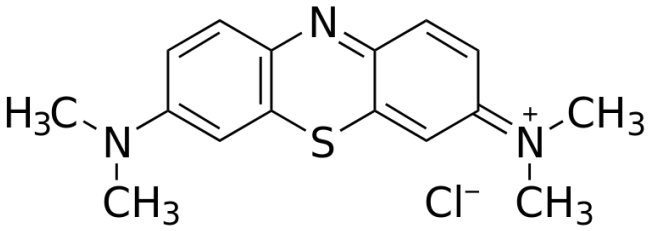

Figure 1: Molecular structure of methylene blue. Methylene blue is a synthetic cationic dye with molecular weight of 318.95 g/mole containing a centralized sulfur atom. Source: https://commons.wikimedia.org/wiki/File:Methylene_blue.svg

Methylene blue is an attractive photosensitizer because it is relatively inexpensive, absorbs light in the phototherapeutic window, has high solubility in water (approximately 16 mM in water), has a high molar absorptivity (79,800 $M^{-1}cm^{-1}$) and has a strong singlet oxygen quantum yield (0.52)[76,77,94]. With an octanol-water partition coefficient of -0.1, methylene blue's partitioning into hydrophilic environments makes it suitable for delivery

to the relatively acellular sclera, though Prausnitz and Noonan found no evidence for a relationship between partition coefficient and scleral permeability[95,96]. Furthermore, its cationic nature should slightly decrease its permeability in the sclera compared to neutral or negatively charged species, though this may be advantageous for slowing clearance from the sclera[97].

2.7.7 Collagen Photocrosslinking Mechanism

The mechanisms of collagen crosslinking by photocrosslinkers are categorized into two types: type I reactions and type II reactions[62]. Type I reactions require the direct reaction of an excited state sensitizer with substrate. Type II reactions require that the excited state energy of a sensitizer be transferred to oxygen, thus generating singlet oxygen, which then reacts with collagen to form crosslinks[70]. Amino acids selectively participate in crosslinking reactions depending upon type I or type II mechanism. Histidine has been found to be a strong target for singlet oxygen and has been shown to readily dimerize in the presence of rose bengal, an exclusively type II sensitizer[98][99]. Histidine crosslinking is believed to occur through initial reaction of singlet oxygen with the histidine imidazole ring to form a hydroperoxide, the decomposition of which is amenable to nucleophilic attack by another histidine side chain[100]. Tryptophan, tyrosine, and cysteine are known to be involved in sensitized crosslinking reactions as well[101]. However, the reaction of these residues with methylene blue-generated singlet oxygen was shown to be less significant than that with histidine[102].

2.7.8 Clinical Applications of Photosensitizers in Ophthalmology

2.7.8.1 Age-Related Macular Degeneration (AMD) Treatment (Verteporfin)

Verteporfin is a notable FDA-approved photosensitizer (formulated as Visudyne) for its use in the eye to treat AMD by facilitating laser ablation of aberrant retinal vasculature[103]. It is injected intravenously and facilitates selective ablation of vessels targeted with a transpupillary laser beam due to its localization in the vascular lumen[103]. Structurally, verteporfin belongs to the class of sensitizers derived from the chlorophyll ring (chlorins) and is an efficient absorber at 689nm[66].

2.7.8.2 Keratoconus Treatment (Riboflavin 5'-Phosphate)

Riboflavin 5'-phosphate (FMN), a derivative of riboflavin (vitamin B2), is another notable FDA-approved photosensitizer indicated for use in the eye. Unlike verteporfin treatment for AMD, riboflavin collagen crosslinking (CXL) was developed to treat keratoconus, a disease of the cornea characterized by weakened corneal collagen, by introducing collagen crosslinks[104]. Riboflavin crosslinking utilizes a topical application of riboflavin to the corneal stroma after removal of the corneal epithelium followed by irradiation with 365nm UV light for 30 minutes and prevents further corneal deformation due to the mechanical stiffening conferred on the stroma from crosslinking[105].

2.8 Scleral Photocrosslinking Challenges

Studies to date on scleral photocrosslinking have focused on the equatorial/anterior regions where topical application of photosensitizer and direct external illumination are most feasible[106,107]. Drug delivery to the posterior globe is difficult due to limited access but

important for treating diseases of the retina/optic nerve[108]. While drug delivery to the posterior hemisphere of the eye is difficult, injection techniques exist both for localization to the suprachoroidal space and to the retrobulbar space[109].

2.8.1 Drug Delivery Considerations

The first challenge of scleral photocrosslinking is physical delivery of a photosensitizer to the sclera. Delivery of photosensitizers to the sclera may be achieved in one of three primary routes: 1) through the posterior scleral surface, 2) through the anterior scleral surface, and 3) intrasclerally. The epithelialized conjunctiva and Tenon capsule layers present barriers to posterior surface scleral sensitizer delivery. However, these barriers may be overcome using targeted injections such as sub-conjunctival and sub-Tenon injections which place the injected volume directly against the posterior scleral surface[110]. Anterior scleral surface delivery is made difficult by the anterior structures of the eye, namely the retina. Recent advances in targeted suprachoroidal injections capable of reaching the posterior pole have made a suprachoroidal route feasible[111]. The disadvantage of a suprachoroidal delivery route is perhaps the rapid clearance of the adjacent choroid combined with limited potential space[112,113]. Finally, an intrastromal delivery, while most direct, is currently not feasible due to the difficulty of precisely positioning a needle within the sclera at the posterior globe.

2.8.2 Light Delivery Considerations

Light absorbance in biological tissues is well characterized with melanin, hemoglobin, and water being the primary absorbing species in the visible/NIR spectrum[67]. The phototherapeutic window is a region of the visible spectrum where absorbance of these

species in biological tissues is minimal. This region ranges from approximately 650nm to 850nm and is bounded by the decreasing absorbance of melanin on the higher frequency wavelengths and by the increasing absorbance of water on the lower frequency wavelengths[67]. Photosensitizer research has focused heavily on photosensitizers with strong peak absorbance in the phototherapeutic window[78,114,115].

2.8.3 Light Absorbance in the Eye

The eye's structure presents a unique opportunity for use of photodynamic agents due to the highly transparent cornea, lens, and vitreous. Furthermore, the opaque sclera and choroid are thin tissues (<1mm in humans) amenable to light penetration despite their propensity for absorbing visible light[116]. Notably, the retinal pigmented epithelium presents a formidable barrier to light penetration due its highly pigmented (melanin) nature[117][118][119]. With melanin and hemoglobin ranked as leading absorbing biological species in the visible spectrum, the choroid represents a unique challenge for light delivery. The sclera, on the other hand, is only moderately absorbing compared to the choroid[120,121]. Light absorbance by a bulk medium (rather than concentration-varying species) is described using the linear attenuation coefficient (μ). The linear attenuation coefficient is defined for a given wavelength and is useful for mathematically modeling light attenuation in a medium such as the sclera or cornea using the Beer-Lambert Law, especially when modeling sensitizer activity in that tissue. For the choroid/RPE, it is perhaps more practical to consider percent light transmission at a given wavelength since these tissues merely represent a barrier to light penetration before light can reach the posterior sclera. For example, 660nm light used for excitation of methylene blue has an

approximate transmission of 20% in the human retina/choroid, while 808nm light used to excite indocyanine green has an approximate transmission of 50%[118].

2.8.4 Light Toxicity in the Eye

The wavelengths of the phototherapeutic window, visible to near infrared, require different toxicity considerations as far as transpupillary illumination approaches are concerned. The visible spectrum has a stricter range of maximum permissible exposure limits compared to near infrared due to the potential not only for photothermal impacts but also photochemical damage[122]. The maximum permissible retinal exposure limit for 660nm light with exposure duration of 30 minutes and beam size proportional to the size of the (rat) peripapillary sclera is approximately 160 mW/cm^2 based on calculations from Delori et al [123]. Wollensak et al found that transscleral illumination of riboflavin with blue light results in retinal toxicity[124]. In addition to phototoxicity of light, photosensitizer-mediated singlet oxygen generation is expected to have toxicity as is the case for cancer treatment and antibacterial applications[125,126].

2.9 Theoretical Photocrosslinking Computational Modeling

A predictive model of scleral photocrosslinking should account for 1) diffusion, 2) light propagation/absorbance, and 3) chemical reaction kinetics. An abundance of modeling has been performed for riboflavin crosslinking simulation including both analytical and numerical methods with variation in the physical phenomena considered[127][128][129].

2.9.1.1 Retrobulbar Injection Distribution & Diffusion

While the film thickness of riboflavin on the corneal surface during riboflavin crosslinking is small, it is deemed significant enough to include in mathematical models (though also neglected in others)[130][131]. However, in these models it is considered constant rather than dynamic as would need to be the case for a retrobulbar injection where replenishment of the reservoir does not occur. Furthermore, clearance of photosensitizer through retrobulbar vasculature complicates transport dynamics and requires experimental justification for modeling. Diffusion can be modeled using Fick's Second Law:

$$\frac{\partial C}{\partial t} = D\frac{\partial^2 C}{\partial x^2} \tag{1}$$

where C represents concentration of the diffusing species, D represents the diffusion constant, and x and t represent position and time, respectively. While Fick's Second Law may be solved analytically easily using a steady state assumption, a model accounting for dynamic changes in boundary conditions and accounting for reaction conditions will make solving an analytical solution impractical.

2.9.1.2 Oxygen Supply and Consumption

Considering the role of reactive oxygen species in collagen photocrosslinking, the concentration and interaction of oxygen with sensitizer are both important for accurate modeling[132][133]. Oxygen diffusion dynamics were previously measured and modeled for riboflavin crosslinking representing an important milestone providing an experimental reference against which computational models may be tested[129]. Unlike riboflavin

crosslinking models, a posterior scleral photocrosslinking model would need to account for oxygen supply from the choroid rather than atmospheric oxygen.

2.9.1.3 Light Absorbance

Light attenuation by molecular and bulk absorbers is popularly modeled using the Beer-Lambert Law (Beer's Law) [134]. According to Beer's Law, the change of light intensity as it travels through a medium is proportional to the intensity times the absorbance of the medium on an infinitesimal length:

$$\frac{dI}{dx} = -IC\varepsilon \tag{2}$$

where I is light intensity, x is the distance in the direction of photon travel, and C and ε are the concentration and molar absorptivity of light-absorbing species, respectively. The analytical solution to the Beer-Lambert Law yields a light intensity function with exponential decay over distance. Unlike riboflavin crosslinking models where light attenuation in the cornea is the only tissue-dependent photophysical property, modeling transpupillary penetration of light through the fundus requires that light attenuation by the choroid/RPE be accounted for as well as attenuation of light by the sclera. Furthermore, pigmentation of the choroid/RPE may vary by species or individual, and thus a melanin concentration-dependent parameter for light attenuation would be advantageous[118].

2.9.1.4 Sensitizer Degradation and Aggregation

Sensitizer degradation and aggregation are significant detractors from photocrosslinking efficiency which are often well-characterized[135,136]. Riboflavin suffers from facile

degradation under UV light[137]. Methylene blue on the other hand is less photolabile, but aggregates far more readily than does riboflavin, leading to quenching of the triplet state[138][76,139]. It is also notable that methylene blue is believed to form higher order aggregates beyond simple dimerization[140,141]. Simple dimerization is described according to binding kinetics with a dissociation coefficient, K_d, defined as:

$$K_d = \frac{[D]}{[M]^2} \tag{3}$$

where M is the concentration of monomeric photosensitizer and D is the concentration of aggregated (dimeric) photosensitizer[76]. Thus, concentration of aggregated species changes nonlinearly with total concentration, complicating the estimation of photosensitizer efficiency in an environment with dynamic concentration changes.

2.9.1.5 Chemical Kinetics

Kinetic rate laws have been applied in many riboflavin crosslinking models and provide important temporal information dependent upon dynamic reactant concentrations[129,130]. Fortunately, photochemical studies of photosensitizers and reactions involving target amino acid residues are abundant for riboflavin and for methylene blue and involve first order assumptions for reaction kinetics[142–144]. For a simple bimolecular reaction as would be the case for singlet oxygen generation from triplet oxygen and triplet state photosensitizer, the reaction can be modeled as:

$$\frac{d[C]}{dt} = k[A][B] \tag{4}$$

where A and B are the concentrations of reactants, C is the concentration of product, t is time, and k is the reaction rate constant. Solving the differential equation results in an analytical solution with product concentration increasing exponentially over time.

2.9.2 Experimental Studies as Test Cases for Computational Model

Riboflavin crosslinking experiments provide a wealth of test cases against which computational models may be validated. Particularly, studies have investigated oxygen concentration over time, crosslinking magnitude as a function of illumination intensity and duration, riboflavin concentration as a function of stromal depth, and fluorescent crosslink concentration as a function of stromal depth[129,145–147]. Since these studies track a single parameter over space or time (usually not both), they may be used in combination to provide multiple points of reference against which a model can be tested.

2.9.3 Quantification of Crosslinking and Stiffening

Crosslinking has been estimated variously by either assuming singlet oxygen reacts with histidine or by using broad polymer reaction rate kinetics simplifications[130][128,148]. One notable limitation to these methods is the inability to relate crosslinking to tissue stiffening. While studies exist which attempt to relate the two, it is difficult to find studies with material properties matching those of the cornea/sclera[149,150]. Therefore, comparison of theoretical crosslink densities achieved during transpupillary illumination of scleral photosensitizers with those of riboflavin crosslinking would provide a useful benchmark for stiffening as stiffness increase has been quantified experimentally for riboflavin crosslinking[104,107,124,151,152].

2.10 Scleral Stiffening as a Therapeutic Strategy in Glaucoma

It has been hypothesized that reducing the pressure-induced strain on the optic nerve head will reduce glaucomatous vision loss. Previously, Coudrillier et al. showed that mechanically stiffening the peripapillary sclera (sclera adjacent to the optic nerve head) will reduce the pressure-induced strain experienced by the optic nerve head[4]. This finding suggested that scleral stiffening is a promising therapeutic strategy for preventing pressure-induced glaucomatous damage. However, it was recently shown that whole globe scleral stiffening increased glaucomatous axon loss in mice contrary to the anticipated effect of preserving axon health[5]. We believe whole globe stiffening may exacerbate glaucomatous damage due to the inability for the sclera to attenuate cyclical fluctuations in intraocular pressure. Therefore, we propose to selectively stiffen the peripapillary sclera as a method for preventing pressure-induced damage in glaucoma.

2.11 Targeted Peripapillary Stiffening Approach

In the investigated approach, targeted peripapillary scleral stiffening is enabled by directing a transpupillary light beam at the peripapillary region to excite a photosensitive crosslinking agent. In comparison to non-photoactivated crosslinking agents, photosensitive crosslinking agents allow for selective stiffening with millimeter resolution only where both light and crosslinking agents are present. We designed a microscope which allows for controlled illumination of the peripapillary sclera by means of a transpupillary approach. The transpupillary approach is advantageous because it is non-invasive (unlike catheterized delivery) and provides a clear optical path for targeting the peripapillary region. A photosensitive crosslinking agent was administered using a retrobulbar injection

whereby the agent is injected into the retrobulbar muscle cone adjacent to the posterior scleral surface. This injection approach, while already in common clinical practice, also delivers the crosslinker near the target peripapillary scleral tissue achieving local concentration sufficient for crosslinking.

2.12 Theoretical Computational Modeling

In addition to experimental evidence for targeted photocrosslinking at the peripapillary sclera, a theoretical model for predicting degree of crosslinking was created to optimize treatment parameters. The model incorporates elements of molecular photodynamics, diffusion, and chemical kinetics to predict the final distribution of crosslinks in the sclera over time and 1-dimensional space. A combination of temporal and spatial information is useful for analyzing trends in the distribution of crosslinking and for assessing optimal treatment time scales, especially if reaction mechanisms change over time. Key treatment parameters of interest (inputs) include crosslinker concentration, light intensity, and irradiation duration. Additionally, the model may be used to simulate the efficiencies of various crosslinking agents, thus informing research decisions to pursue future crosslinking experiments.

CHAPTER 3. SPATIALLY TARGETED SCLERAL PHOTOCROSSLINKING WITH METHYLENE BLUE

Note on Contribution: Data presented in this chapter are the product of contributions from a number of individuals I wish to acknowledge. Bailey Hannon contributed the data pertaining to ERG studies and axon counts and to analysis of data pertaining to ERG studies. Dr. Thomas Read contributed axon sections used in axon count data. Amir Hejri contributed histological sectioning/staining of ocular tissues. Dr. Hans Grossniklaus contributed to histological sectioning/staining of ocular tissues as well as expertise in analysis of these tissues. Elisa Schrader, Lauren Nichols, and Erin Winger contributed to DIC data analysis. Hannah Gersch, Erin Winger, Niyati MacLeod, and Elisa Schrader contributed to collection of confocal microscopy data for determination of methylene blue retrobulbar distribution. Lauren Nichols contributed to data analyses of methylene blue confocal microscopy data.

3.1 Abstract

To prevent optic nerve head cupping associated with glaucomatous retinal ganglion cell damage, this study sought to selectively stiffen the peripapillary sclera, and thereby reduce tissue deformation near the optic nerve head. Previously, scleral crosslinking has been used to stiffen tissue for treatments of glaucoma or myopia but has either been regionally non-selective or regionally selective but with limited access to the posterior globe. We present a method for selectively stiffening the peripapillary sclera using a transpupillary annular light beam to activate methylene blue administered by retrobulbar injection. Unlike prior

approaches to photocrosslinking in the eye, this approach avoided the damaging effects of ultraviolet light by employing a red visible light crosslinking method. Targeted photocrosslinking in this way reduced average strain of the peripapillary region in treated eyes by 54% compared to untreated eyes and by 46% compared to the untreated peripheral sclera of the treated eye for at least 6 weeks post injection. Post-treatment characterization with optic nerve axon counts, electroretinography, and retinal histology revealed evidence of moderate toxicity of the procedure. In conclusion, this study shows that a transpupillary photocrosslinking approach enables selective scleral stiffening targeted to the peripapillary region that may be useful in future treatments of glaucoma and myopia.

3.2 Introduction

Glaucoma is the second leading cause of blindness in the industrialized world and affects approximately 70 million individuals worldwide [153,154]. Disease progression is strongly linked to elevated intraocular pressure (IOP) which has been shown to correlate with cupping of the lamina cribrosa and damage to retinal ganglion cell axons in the optic nerve head[6]. While IOP management is the primary modality of treatment, direct prevention of optic nerve head deformation through modulation of tissue mechanical properties may confer protective advantages to retinal ganglion cells[12,155].

Stiffening of the peripapillary sclera was previously shown to reduce strain on the lamina cribrosa of *ex vivo* porcine eyes[4]. However, an *in vivo* study in glaucomatous mice found that whole-globe scleral stiffening worsened axon loss in glaucomatous mice[5]. This result was unexpected considering the prior evidence of peripapillary scleral stiffening leading to reduction in lamina cribrosa strain. An explanation for this result may be that

whole-globe scleral stiffening reduces the overall compliance of the eye to an extent that IOP fluctuations become larger in amplitude may no longer be safely accommodated[156]. We believe such an effect may be overcome by targeted crosslinking of the peripapillary sclera, rather than whole globe stiffening.

Collagen crosslinking (CXL) has been employed as a means of scleral stiffening through either photomediated ("light") or non-photomediated ("dark") crosslinking. Riboflavin crosslinking is a well-established procedure in the cornea for treatment of the refractive disorder, keratoconus, in which the photosensitizer riboflavin is applied topically to de-epithelialized corneas and exposed to ultraviolet A (UVA) light for 30 minutes[105,157]. The success of this method in keratoconus treatment has led to additional studies testing riboflavin's effects on scleral stiffening for myopia management[106,152]. However, riboflavin crosslinking has largely been limited to the anterior sclera due to the toxicity of UVA light at high doses and difficulty of reaching posterior ocular tissues[124,151]. Recently, UVA light was delivered by optic waveguide/optical fiber to equatorial rabbit sclera *in vivo* for targeted photocrosslinking, illustrating the recent interest for regionally selective scleral stiffening[158].

In addition to light-activated photocrosslinking strategies, dark crosslinkers have been used for corneal and scleral stiffening[159,160]. Recently, we have shown the feasibility of *in vivo* scleral crosslinking with a single injection of the dark crosslinker, genipin, which was motivated by the need for scleral stiffening with less cytotoxicity compared to dark crosslinkers used in the past[52]. Previously-used dark crosslinkers such as glutaraldehyde and glyceraldehyde are known to have toxicity profiles which may limit the effective scleral dose due to proximity to the retina[161]. However, small molecule dark crosslinkers

typically stiffen the entire globe non-selectively, as they diffuse quickly through tissues and react with collagen on contact.

Despite advances in both dark- and light-mediated crosslinking approaches in the eye, none have achieved *in vivo* spatial selectivity on the millimeter scale, which is fine enough to selectively crosslink the peripapillary sclera to test the hypothesis that targeted crosslinking of the peripapillary sclera confers protection on retinal ganglion cells in glaucomatous eyes, a stiffening approach is needed which selectively crosslinks the peripapillary sclera while leaving the remainder of the globe unaffected. The goal of this study was to develop a targeted stiffening method capable of selectively stiffening the peripapillary sclera, resulting in a >38% reduction in strain (comparable to the strains used in Coudrillier et al.) [4]. A photocrosslinking approach was chosen to achieve millimeter-scale targeted stiffening, and therefore considerations were made for using a light-activated crosslinking agent, delivery of that agent to the peripapillary sclera, and illumination of that agent with a transpupillary light beam.

We have developed a targeted scleral crosslinking approach capable of selectively stiffening the peripapillary sclera. With our targeted approach, an annular light beam of 660nm light with dimensions measuring 2 mm outer diameter and 1 mm inner diameter was projected onto the peripapillary sclera through a transpupillary approach.

Methylene blue is a known type II (singlet oxygen-generating) photosensitizer and has found many medical uses since its discovery over a century ago including as an anti-malarial, antidote for cyanide poisoning, and currently as a treatment for methemoglobinemia[90,91,96,126,162]. We chose MB for its efficient absorbance of red

light (molar absorptivity, ε = 73,300 $M^{-1}cm^{-1}$), high triplet quantum yield (Φ_T = 0.52) , solubility, and availability [76,163]. Selection of a sensitizer absorbing in the phototherapeutic window (650-850 nm), where melanin and hemoglobin absorbances are relatively low, was an important criterion[67]. Furthermore, MB has been shown to increase collagen stability in rat tail tendon and to induce crosslinking of porcine pericardial tissue, suggesting it would perform well as a crosslinker in a collage-rich tissue such as the sclera[102,164,165].

While current glaucoma treatments primarily aim to lower intraocular pressure associated with mechanical insult at the optic nerve head, an alternative future strategy may be to mechanically reinforce the peripapillary sclera. Therefore, an alternative treatment which confers protection on retinal ganglion cells independently of pressure would be advantageous. This study aims to establish the method for targeted peripapillary photocrosslinking as a step towards testing the viability of such treatment in a future glaucomatous animal model.

3.3 Materials and Methods

3.3.1 Rats

Brown Norway retired male breeder rats (age 6-12 months) were obtained from Charles River Laboratories (Wilmington, MA). All procedures involving animals were approved by the Georgia Institute of Technology Institutional Animal Care and Use Committee (IACUC) and complied with the ARVO statement for the Use of Animals in Ophthalmic and Vision Research. Rats were housed and maintained by veterinary staff at the institute animal facility and were fed standard rodent diet (LabDiet 5001, Lab Supply, Fort Worth,

Texas). Prior to any procedure, rats were allowed at least three days to become acclimated to the animal facility.

3.3.2 Anaesthesia and Eye Dilation

Rats were placed under anesthesia using a mixture of isoflurane gas (5%) and oxygen gas (95%) supplied through a stereotaxic head positioner (Kopf Instruments, Tujunga, CA). A heating pad was placed under the rats to maintain body temperature throughout the procedure. After induction of anesthesia, 0.5% tetracaine eye drops (Tetracaine Hydrochloride Ophthalmic Solution, Amici Pharmaceuticals, Melville, New York) were applied topically to the eyes bilaterally. Excess fluid was gently wicked away from the surface of the eyes, and 1% tropicamide dilating drops (Tropicamide Ophthalmic Solution, Henry Schein, Melville, New York) were applied bilaterally and allowed to take effect for approximately 10 min. Pupil dilation was confirmed visually prior to each experiment to ensure sufficient visual access to the fundus. Anesthesia was maintained throughout the remaining duration of the procedure with an isoflurane/oxygen flow rate of approximately 800 mL/min. At the conclusion of survival procedures, rats were allowed to recover from anesthesia, returned to their housing, and were monitored for any adverse effects of the procedure. For non-survival procedures, rats were euthanized by exposure to 100% CO^2.

3.3.3 Ocular Imaging and Photocrosslinking by Microscopy

We constructed an ophthalmic microscope (Figure 2) to enable simultaneous transpupillary fundus visualization and annular beam projection from an incoherent diode light source (Thorlabs, Newton, NJ). The microscope was constructed from readily available optical components and was mounted on a three-axis manual micro-positioner, allowing for fine

corrections in beam alignment. The microscope was mounted with the objective and projected beam facing downwards toward a platform mounted on laboratory jacks on which anesthetized rats were supported. Light intensity was adjusted using a variable power source/controller. An annular beam was formed from the diode source using an aperture, axicon lens, and microscope objective. A microscope camera connected to a computer was used to visualize the projected annular beam as it was projected through a beam splitter and the microscope objective. See Supplemental Materials for additional information on microscope design.

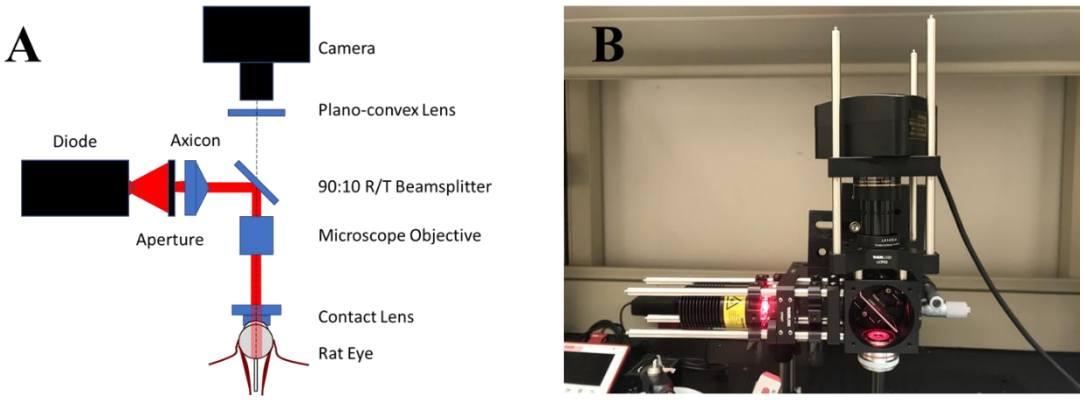

Figure 2: Ophthalmic microscope designed to enable simultaneous transpupillary fundus visualization and annular beam projection in the rat eye *in vivo*. A) Component diagram, and B) photographic image of the microscope set-up. The microscope allows a user to simultaneously project an annular beam onto a rat fundus, observe the location of the beam on the fundus, and precisely position the beam using a three-axis manual micro-positioner stage (behind the microscope).

3.3.4 Photocrosslinking Materials

Methylene blue (Apollo Scientific, Stockport, UK) in powder form was solubilized in Hank's balanced salt solution (HBSS) (Mediatech, Manassas, Virginia) resulting in a

buffered solution with final MB concentration of 3 mM. HBSS buffer vehicle solution was chosen to neutralize the otherwise acidic nature of dissolved MB. The solution was heated to 100°C for 15 min to facilitate MB solubilization and subsequently allowed to cool prior to injection. Sterile, disposable syringes (300 µL) with 31 G needles (BD Insulin Syringes with BD Ultra-Fine™ needle, Becton, Dickinson and Company, Franklin Lakes, New Jersey) were filled with 100 µL of either HBSS or 3 mM MB in HBSS.

3.3.5 Retrobulbar Injection

After anesthesia induction and pupil dilation, a single 100 µL retrobulbar injection was administered to each eye using forceps to gently proptose the eye. Our stereotaxic head mount equipped with a tooth bar (but no ear bars) allowed for rotation and elevation of the head as well as unobstructed access to the eyes. Injections were administered at the inferior quadrant using tactile feedback to determine position of the needle tip in the muscle cone. Syringes/needles were held in place for 10 s after injection to avoid reflux of fluid from the retrobulbar space. After injection was complete, hydrating eye lubricant (Puralube Vet Ointment, Dechra, Northwich, United Kingdom) was applied topically to the eye not receiving light to prevent dehydration during the photocrosslinking procedure.

3.3.6 Photocrosslinking Procedure

Following retrobulbar injection, the rat was positioned with the eye receiving light treatment facing upward in the optical path of the microscope. A contact lens designed for fundus imaging in rat eyes (OFA5.4, Ocular Instruments, Bellevue, Washington) was placed on the cornea and optically coupled to the surface with HBSS, allowing clear visualization of the fundus (Figure 3A). A low intensity (<0.1 mW) “guide” beam was used

to locate the optic nerve head through the microscope's camera. The beam projection was then aligned so that the optic nerve was positioned at the dark center of the annular beam using three manual micropositioners to translate the entire microscope in the vertical and two horizontal planes. After alignment, light intensity was adjusted to a power of 10 mW measured using an optical power meter (ThorLabs) and maintained for 30 min (Figure 3B). The diode's output centered at a frequency of 660 nm (i.e., visible red light). Annular beam dimensions were 1 mm inner diameter and 2 mm outer diameter, resulting in an intensity of approximately 425 mW/cm^2. Right and left eyes received alternating treatments from rat to rat to control for any variation due to orientation of the eyes.

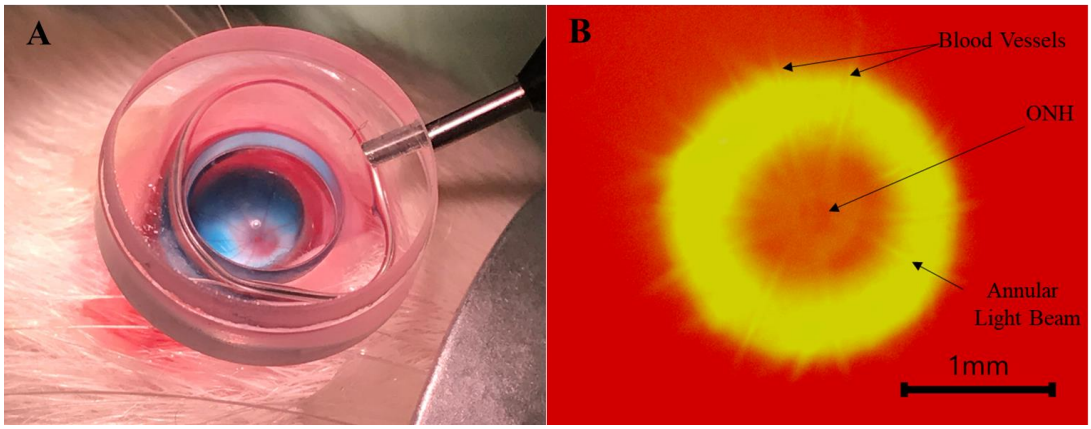

Figure 3: Selective illumination of the peripapillary region of the rat eye. A) A contact lens placed on the corneal surface creates a clear visual path for viewing the fundus. The optic nerve can be seen (red dot) from which blood vessels emanate. The blue color is due to the retrobulbar injection of MB, visible in this case, in a non-pigmented Wistar rat. B) Image from microscope camera during illumination procedure showing annular beam spot relative to the optic nerve head (center). The beam appears yellow due to false color imaging used to help visualize the optic nerve head (ONH) and blood vessels during the procedure. The surrounding red region is the non-irradiated peripheral retina.

3.3.7 Whole Globe Inflation Testing

Scleral stiffness was measured post mortem using a digital image correlation (DIC) system (Dantec Dynamics, Skovlunde, Denmark) as previously described in Hannon et al. and others[4,52,166]. Eyes were enucleated immediately after CO^2-induced euthanasia and excess orbital tissue was carefully removed with dissection microscissors to expose the sclera. After tissue removal, each eye was mounted with the optic nerve positioned upward under the downward-facing cameras on a custom pressurization apparatus by applying cyanoacrylate-based adhesive (Henkel, Düsseldorf, Germany) to the circumferential contact point with the limbus. The cornea was excised, and the lens was removed to prevent any hinderance to subsequent pressurization, leaving only the mounted scleral shell, which was filled with phosphate-buffered saline (PBS). The optic nerve was trimmed to leave approximately 1 mm protruding from the scleral surface.

Graphite powder was applied to the posterior scleral surface to create a speckled pattern used by the digital image correlation system cameras to track displacement of the surface. The mount with attached scleral shell was then secured with the anterior scleral surface in fluidic communication with a PBS pressure reservoir and in-line flow sensor (SLG64-0075, Sensirion, Staefa, Switzerland) used to monitor flow of PBS into the eye upon pressurization. A walled, open-top chamber surrounding the eye was filled with PBS to prevent drying of the eye, and a layer of mineral oil was floated on top of the PBS to prevent evaporation of the PBS while maintaining a clear optical path between the sclera and cameras.

Eyes were mechanically preconditioned prior to testing by cycling the height of the pressure reservoir to create IOPs from 3 mmHg to 15 mmHg (10 cycles), thus improving consistency of mechanical measurements across tests. Immediately following preconditioning, eyes were pressurized at 3, 10, 20, and 30 mmHg in sequential steps. Pressure was only increased when the measured PBS flow rate stabilized to a near-constant value, ensuring that a steady state had been reached. Digital microscopic images were collected throughout the experiment.

Two-dimensional displacement maps were generated by the DIC system's software (Dantec Dynamics), from which regional strain averages were calculated. For analysis, we defined the peripapillary region as the scleral region within a 2 mm diameter circle centered at the optic nerve. Care was taken to avoid excess light exposure during inflation testing to reduce the possibility of post mortem photocrosslinking. Right and left eyes as well as control and experimental eyes were alternated in order of testing to reduce the possibility of systematic error due to testing order.

3.3.8 Confocal Microscopy/Distribution Study

Injection solutions were prepared using 3 mM MB diluted in HBSS. Rats were randomly selected for each experiment and assigned to a diffusion time group (30, 20, or 10 min from injection to death). To begin the procedure, rats were anesthetized using isoflurane gas. Topical tropicamide (0.5%) followed by topical tetracaine (0.5%) were applied bilaterally. Topical administration was used to match the experimental procedure used for photocrosslinking (though in this study, light was not applied). A retrobulbar injection of 50 μl of methylene blue solution was performed using a 3 mL insulin syringe in the OD

eye. Immediately after, a retrobulbar injection of 50 μl of HBSS was administered in the contralateral OS eye.

Five minutes prior to the total diffusion time assigned to each rat (10, 20, or 30 min), rats were exposed to CO^2 for euthanasia. This was done to ensure an accurate diffusion time since prior studies have shown that time from first breath of CO^2 to cessation of pulsatile blood flow (with the endpoint being death) is 5 min[167,168]. Following euthanasia, the OD (experimental) eye was immediately enucleated and fat and excess tissue from the posterior eye were removed. The eye was then flash frozen in optimal cutting temperature compound using liquid nitrogen for sectioning and imaging. While the OD eye was freezing, the same enucleation, cleaning, and freezing procedure was started for the OS eye. The time from death to complete freeze for both eyes was typically no more than 5 min. Once frozen, eyes were cryosectioned within 20 min and immediately imaged by confocal microscopy, with each OD eye being sectioned and imaged before each OS eye. Multiple sagittal sections were taken for each eye, and sections were then evaluated by two different researchers to ensure that the section chosen to be imaged was in the center of the eye in the sagittal plane. Care was taken to ensure the post-death diffusion time for each eye (death to imaging) was less than 30 min. The same pre-determined set of optimal settings for MB fluorescence was used to image each eye. All images were taken on a Zeiss LSM 780 Confocal microscope (Oberkochen, Germany) using optimal settings for MB fluorescence.

Data acquisition was performed using the “Profile” tool in the Zeiss imaging software. This tool allows distance and intensity data to be collected across a user-defined region drawn on the image. Data sampling was performed with average profiles defined across

the thickness of the sclera (normal to the scleral surface) at a number of measured distances from the optic nerve. Average fluorescence intensity at each point in the sclera was tabulated for each eye and values were normalized to the brightest intensity value within each respective eye. The normalized intensities were then averaged across rats with similar treatment to mitigate the effects of variability caused by injection technique.

3.3.9 DIC Data Analysis

Raw displacement values were converted to strain values using a custom script coded in MATLAB Software (MathWorks, Natick, Massachusetts). Strain values for the peripapillary region and peripheral region were averaged separately and recorded for each pressure step. A pressure-strain relationship was established by fitting the measured strain average at each inflation pressure step to a Fung-type model, from which strain at any pressure within our tested range was calculated using the following relationship:

$$Pressure = \frac{A}{B}\left(e^{B\varepsilon} - 1\right) \tag{5}$$

where ε is the calculated strain, and A and B are parameters fitted with MATLAB's least squares non-linear regression function[169]. The non-linear regression was calculated with pressure as the independent variable and strain as the dependent variable. As done previously, percent strain reduction was calculated using means of the strain in two compared regions according to:

$$\% \, Strain \, Reduction = \frac{\varepsilon_{exp} - \varepsilon_{ctrl}}{\varepsilon_{ctrl}} \times 100\% \quad (6)$$

where ε_{exp} and ε_{ctrl} are the strain values of the experimental and control regions of the eye being compared, respectively[52].

3.3.10 Six-Week Crosslinking Study

To test the safety and duration of photocrosslinking, rats (n=8) were treated unilaterally with MB photocrosslinking and monitored for 6 weeks. Electroretinograms were conducted prior to euthanizing the rats to assess safety. Digital image correlation was performed on the eyes after euthanasia to investigate scleral stiffness. Optic nerves were collected immediately after euthanasia, fixed, and sectioned for axon counting.

3.3.11 Electroretinograms

Electroretinograms were measured using a full-field ERG in a Ganzfeld dome (UTAS Big Shot, LKC Technologies, Gaithersburg, MD). Rats were dark-adapted for 30 min prior to testing for measurement of scotopic photoreceptor response. After dark adaptation, rats were anesthetized with a subcutaneous injection of ketamine/xylazine. Tetracaine (1%) and tropicamide (1%) were applied topically to locally anesthetize and dilate the eyes, respectively. Electrodes were placed subcutaneously in the cheek (reference) and tail (ground), and a gold loop electrode was placed in contact with the cornea. Scotopic measurements were taken at -3.0 to 2.1 log cd s m^{-2} and photopic measurements were taken at 0.4 to 1.4 log cd s m^{-2}. Representative voltage traces were reported for scotopic and photopic responses at the brightest flash intensities (2.1 and 1.4 log cd s m^{-2}, respectively).

3.3.12 Optic Nerve Axon Counts

Axon counts were performed on the histological cross sections of optic nerves fixed in Sorensen's buffer containing glutaraldehyde (2.5%) and PFA (2%, EMS, Hatfield, PA) after enucleation. The nerves were subsequently embedded in araldite-epon plastic (Araldite 502/Embed 812, EMS, Hatfield, PA). Cross sections (0.5 µm thickness) were stained with toluidine blue and imaged. Whole images of the optic nerve cross sections were then analyzed using a custom designed computer algorithm coded in AxoNet for automatic counting of axons deemed healthy using the code's image recognition features[170].

3.3.13 Retinal Histology

Two groups of rats (n=3 each) were treated with either methylene blue and light or with light alone, allowed to recover, and euthanized 10 days later. Upon euthanasia, eyes were enucleated and placed in 2.5% glutaraldehyde solution for embedding, sectioning, and hematoxylin and eosin staining. Paraffin embedding was used for the group receiving methylene blue and light. Cryosectioning was used for the group receiving light only.

3.3.14 Optical Coherence Tomography

Optical coherence tomography images (Bioptigen 4300, Leica Microsystems, Buffalo Grove, IL) were taken at 10 days post-injection. Anaesthesia was administered using ketamine/xylazine, and topical tetracaine (1%) and tropicamide (1%) were applied for local anaesthesia and dilation, respectively. A 3 mm radial scan (1,000 A-scans per B-scan) was

collected for each eye centered at the optic nerve head. B-scans were assessed from the superior-inferior and nasal-temporal axes for evidence of treatment toxicity.

3.3.15 Statistical Analysis

Data are reported as mean ± standard deviation. Statistical analyses were performed using GraphPad Prism version 8.0.0 for Windows (GraphPad Software, San Diego, California). In cases where a t-test or ANOVA was used, the t-statistic and F-statistc are reported, respectively as well as degrees of freedom (df). For the study of whole globe scleral mechanical properties, strain values were compared using a two-way ANOVA (on the factors of experiment duration and scleral region) with matched pairs and adjusted for multiple comparisons using a Sidak correction. Axon counts were analyzed with a paired t-test. Electroretinograms were analyzed using a two-way ANOVA with Sidak correction. All data were considered statistically significant at $p<0.05$. For electroretinograms, where multiple flash intensities were employed, a two-way repeated measures ANOVA was used to compare effects across flash intensity and treatment and *post hoc* tests with Sidak correction were conducted where the effect of treatment was significant.

3.4 Results

3.4.1 In Vivo Targeted Peripapillary Scleral Stiffening

We used a whole globe inflation test to determine tissue strain under a range of different applied stresses as a function of position on the posterior, external scleral surface (Figure 4). This approach enabled us to measure local strain values across the ocular surface, and thereby determine average strain in the peripapillary and non-papillary regions of eyes that

were either exposed to the selective photocrosslinking procedure or naïve to treatment. This was accomplished by distributing graphite microparticles across the external ocular surface (Figure 4A) and imaging to measure the movement of theses particle as a function of whole globe inflation pressure. Digital image correlation analysis of these data produced strain maps showing the spatial distribution of strain values on the scleral surface (Figure 4B).

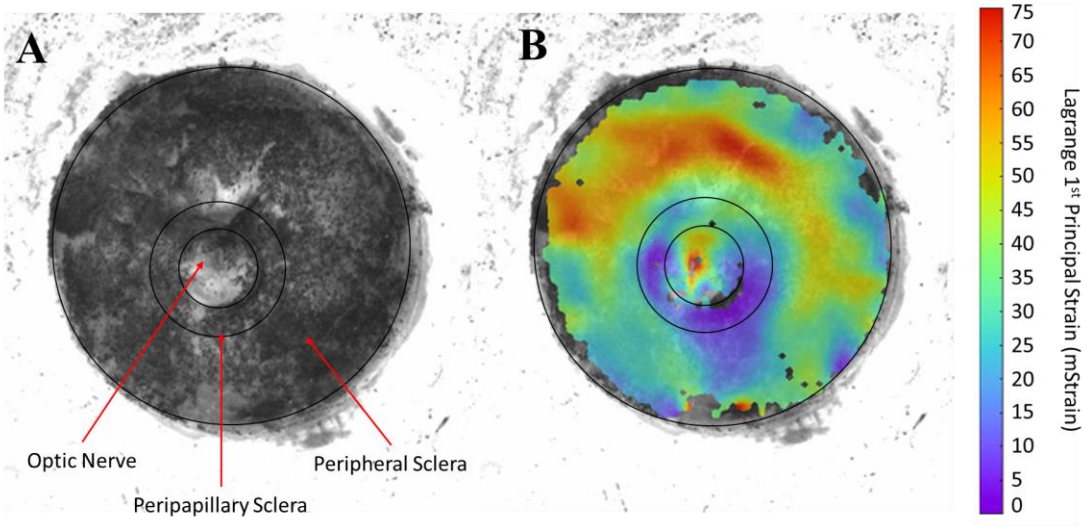

Figure 4: Whole globe inflation testing to determine the spatial distribution of strain values on the posterior, external scleral surface. (A) The position of graphite microparticles was tracked on the scleral surface as a function of applied intraocular pressure. (B) Digital image correlation analysis generated spatial strain maps, from which average strain was calculated. Strain values were determined across the peripapillary scleral region and the peripheral scleral region (labeled in A) separately and reported for both untreated eyes and photocrosslinking-treated eyes, resulting in four values per animal.

3.4.2 Scleral Stiffening at Day 0

Immediately after selective photocrosslinking, there was a statistically significant decrease in strain (i.e., indicating an increase in stiffening) in the peripapillary region compared to the peripheral region (12.0 ± 4.7 mStrain vs 22.2 ± 7.3 mStrain, $p<0.05$, respectively), corresponding to a 46% strain reduction (Figure 5). Strain in the peripapillary sclera in the photocrosslinked eye also decreased compared to the peripapillary region of the untreated eye (12.0 ± 4.7 mStrain vs 33.6 ± 8.9 mStrain, $p<0.0001$), corresponding to a 64% strain reduction. Together, these findings show that selective photocrosslinking significantly stiffened the peripapillary sclera compared to both the peripheral region of the same eye and the peripapillary region of the untreated contralateral eye.

Additional analysis showed that there was a statistically significant decrease in the peripheral region of the treated eye compared to that of the control eye (26.7 ± 7.1 mStrain vs 33.2 ± 13.2 mStrain, $p<0.05$, respectively, Figure 5). This may be due to off-target stiffening resulting from methylene blue diffusion beyond the peripapillary region and non-zero light illumination in the peripheral region due to light scattering along the light beam path.

3.4.3 Scleral Stiffening at 6 Weeks

To determine if the scleral stiffening observed immediately after photocrosslinking persisted, we euthanized and enucleated eyes from rats 6 weeks after treatment. This analysis showed that there was again a statistically significant decrease in strain in the peripapillary region compared to the peripheral region of photocrosslinked eyes (14.2 ± 2.9 mStrain vs 26.7 ± 7.1 mStrain, $p<0.05$, respectively), corresponding to a 47% strain

reduction (Figure 5). Peripapillary sclera strain in treated eyes were also still reduced compared to the peripapillary region of the untreated contralateral eye (14.2 ± 2.9 mStrain vs 32.0 ± 9.5 mStrain, $p<0.0001$, respectively), corresponding to a 56% strain reduction. Moreover, comparison of strain in the peripapillary region of treated eyes at Day 0 and Week 6 revealed no significant difference (12.0 ± 4.7 mStrain vs 14.2 ± 2.9 mStrain, $p>0.05$). These data show that selective stiffening of the peripapillary sclera persisted for at least 6 weeks after treatment.

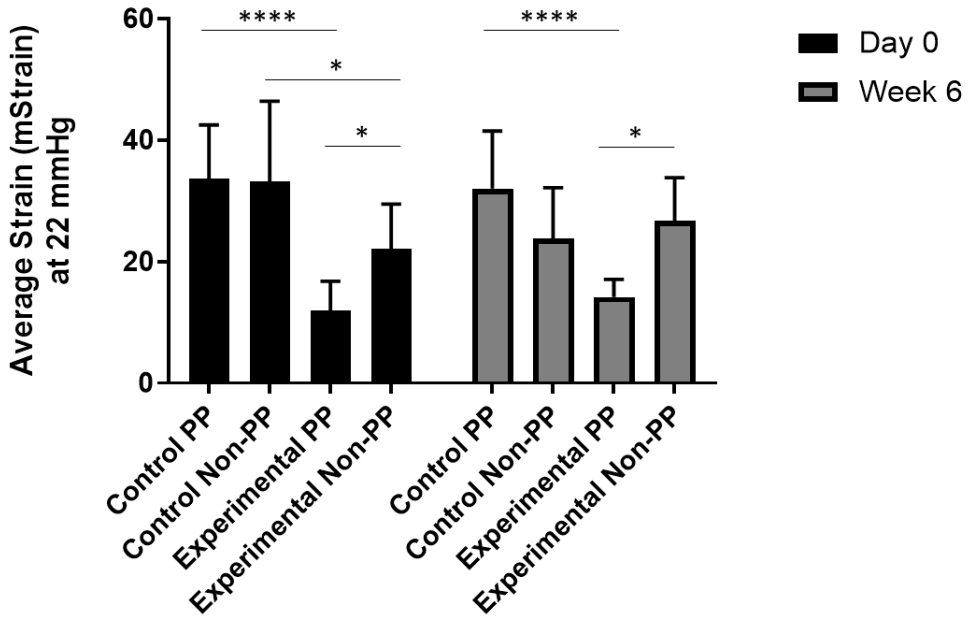

Figure 5: Effect of selective photocrosslinking treatment and time on scleral strain. Whole globe inflation testing at 22 mmHg with digital image correlation analysis compared strain in peripapillary regions (PP) to non-peripapillary (i.e., peripheral) regions of the sclera in the posterior rat eye. Experimental eyes received selective photocrosslinking of the peripapillary region, whereas control eyes were HBSS-injected contralateral eyes. Eyes were enucleated from rats either immediately (Day 0) or six weeks after (Week 6) photocrosslinking treatment. Data points show mean + standard deviation from n = 7 replicates per data point. * $p<0.05$. **** $p<0.0001$.

3.4.4 Changes in Strain Ratios

To better understand the comparative changes in strain by region and thereby assess extent and selectivity of scleral stiffening, strain data were analyzed as ratios of the crosslinked region strain divided by the strain in the non-crosslinked region strain of interest (Figure 6). These were subsequently compared with the corresponding ratio for the control region or eye using two-way ANOVAs followed by *post hoc* comparisons with Sidak correction (Figure 6). Strain ratio between identical regions of different eyes differed significantly on the main effects of regions compared ($F_{1,12}$ = 30.81, p = 0.0010) and by study duration ($F_{1,12}$ = 9.832, p = 0.0086), though there was not a significant interaction ($F_{1,12}$ = 3.808, p = 0.0747). *Post hoc* analysis showed a significant difference between the peripapillary (0.48 +/- 0.20 mStrain) and peripheral (1.18 +/- 0.37 mStrain) regional strain ratios across eyes at week 6 (p = 0.0004). Strain ratio between different regions within the same eye differed significantly by contralateral regions compared ($F_{1,12}$ = 30.81, p = 0.0010) and study duration ($F_{1,12}$ = 9.832, p = 0.0086), though there was not a significant interaction ($F_{1,12}$ = 0.9878, p = 0.3399). *Post hoc* analysis showed a significant difference between the strain ratios of the peripapillary to peripheral region in the experimental (0.57 +/- 0.22 mStrain) and control (1.10 +/- 0.37 mStrain) eyes at day 0 (p = 0.0180). A significant difference existed as well at week 6 between the peripapillary to peripheral region strain ratios for experimental (0.61 +/- 0.39 mStrain) and control (1.38 +/- 0.25 mStrain) eyes (p = 0.0014).

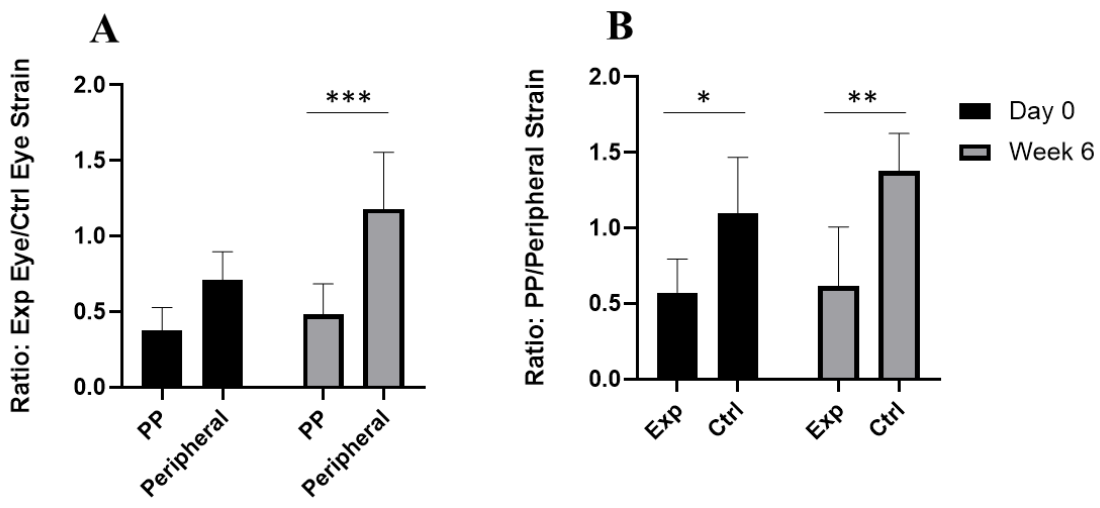

Figure 6:Strain values expressed as ratios between scleral regions on Day 0 and Week 6. A) Ratio of strain in experimental eye to control eye, and B) ratio of strain in peripapillary region to peripheral region. Ratios were determined from data in Figure 4. Data points show mean + standard deviation from n = 7 replicates per data point. * $p<0.05$. ** $p<0.01$. *** $p<0.001$.

3.4.5 Confocal Imaging Study

Photocrosslinking of the peripapillary region requires that methylene blue photosensitizer injected into the retrobulbar space reaches that region on the time scale of laser illumination (i.e., 30 min). Moreover, localization of the methylene blue just to the peripapillary space can facilitate targeted crosslinking, in addition to the targeting enabled by controlling the shape and location of the annular light beam.

Methylene blue fluorescence was observed in the scleras of rats sacrificed at 10, 20, and 30 minutes after retrobulbar injection. Mean normalized fluorescent intensity shows a qualitative trend in MB localization near the optic nerve head (Figure 7). The average normalized intensity was greatest at 1-2 mm from the optic nerve head and relatively

decreased in the +/- 0.5 mm distance region. Furthermore, the intensity gradually decreased at a distance greater than 2 mm distance from the optic nerve head. Little difference was seen between 10, 20, and 30 min diffusion times.

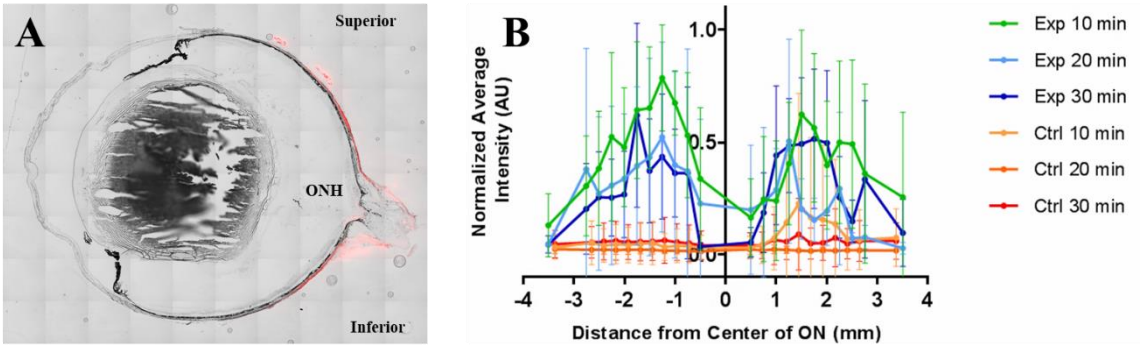

Figure 7: Fluorescence intensity of methylene blue in sclera of rats. A) Representative red fluorescence distribution of methylene blue can be seen at the posterior globe near the optic nerve head (ONH). B) Relative fluorescence intensity of methylene blue in rats euthanized 10 (*n*=5), 20 (*n*=3), or 30 (*n*=5) min after injection. Experimental (Exp) animals received methylene blue injection. Control (Ctrl) animals receives sham injection of HBSS. Average intensity was first calculated at each distance from the optic nerve. The average intensity at each distance was then normalized to the greatest average intensity value in each animal. Negative and positive values indicate distance in the inferior and superior direction from the ONH, respectively. Data points show mean + standard deviation.

Toxicity of Scleral PhotocrosslinkingGiven the known toxicity of other sensitizers, we sought to characterize the possible toxicity of methylene blue photocrosslinking in the peripapillary sclera using optic nerve axon counts, electroretinograms, histology and OCT imaging. Retinal OCT imaging of rats treated with light only showed no evidence of retinal toxicity (Appendix A, Figure 36). Optic nerves collected from rats 6 weeks post-treatment indicated a deficit in retinal ganglion cell count in photocrosslinked rats compared to the HBSS injected contralateral control eyes (Figure 8). Control optic nerves had an average

axon count of 74,500 ± 6,600 axons while nerves of the crosslinked eyes had an average of 56,300 ± 15,200 axons (*p = 0.0205*, paired t-test).

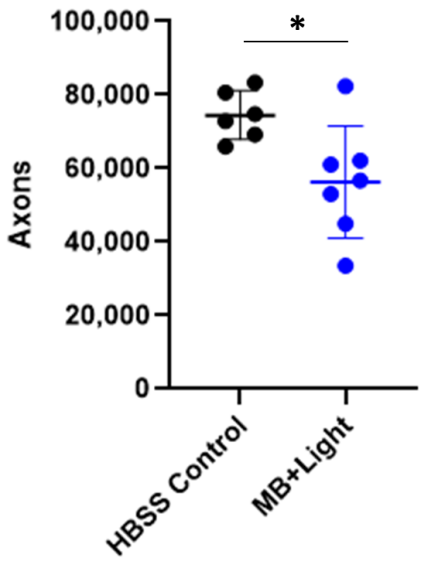

Figure 8: Axon counts obtained from the optic nerve of rats 6 weeks after treatment with MB photocrosslinking (MB+Light). Control eyes were injected with HBSS and did not receive MB or light. Data points show mean + standard deviation from n = 6 replicates for HBSS Control and n= 7 replicates for MB + Light. * p<0.05.

3.4.6 Electroretinograms

Full flash electroretinograms provide a measure of retinal function, and identified a moderate deficit across various cell types when assessed 6 weeks after the photocrosslinking procedure (Figure 9).

Positive scotopic threshold response (pSTR) amplitude, which is a measure of dark-adapted retinal ganglion cell function, was significantly decreased in photocrosslinked eyes compared to the HBSS contralateral eyes (paired t-test, $t = 2.728$, $df = 7$, $p = 0.0294$).

Scotopic A-wave amplitude, which is a measure of dark-adapted photoreceptor function, was found to have a significant interaction between flash intensity and treatment ($F_{3,21}$ = 7.787, p = 0.0011). A-wave amplitudes were significantly decreased in photocrosslinked eyes compared to HBSS contralateral eyes at the 0.7 and 2.1 log(cd s/m^2) intensities (p = *0.0003*, $p < 0.0001$, respectively).

Scotopic b-wave amplitude, which is a measure of dark-adapted amacrine cell function, increased was found to have a significant interaction between flash intensity and treatment ($F_{1.353,9.469}$ = 7.311, p = 0.0177). However, no significant differences were found between the photocrosslinked and HBSS groups in *post hoc* tests (p = *0.2108*, p = *0.1314*, p = *0.1434*, p = *0.1049*, p = *0.0972* at -3.0, -1.9, -0.6, 0.7, and 2.1 log cd s m^{-2}, respectively).

Photopic b-wave amplitude, which is a measure of light-adapted amacrine cell function, was found to have a significant interaction between flash intensity and treatment ($F_{1.166,8.161}$ = 5.154, p = 0.0239). Photocrosslinked eyes had significantly lower photopic b-wave amplitudes in *post hoc* tests at all three flash intensities (p = *0.0161*, p = *0.0153*, p = *0.0139* at 0.4, 1.0, and 1.4 log cd s m^{-2}, respectively).

Finally, photopic negative response (PhNR) amplitude, which is a measure of light-adapted inner retinal activity, was found to have a significant interaction between flash intensity and treatment ($F_{1.291,9.038}$ = 18.05, p = 0.0025). Photocrosslinked eyes had significantly decreased PhNR amplitudes in *post hoc* testing at the 1.0 and 1.4 log(cd s/m^2) intensity levels (p = *0.0540*, p = *0.0012*, p = *0.0011* at 0.4, 1.0, and 1.4 log cd s m^{-2}, respectively). Overall, we conclude that the photocrosslinking procedure used here caused moderate deficits in retinal function in the treated rats.

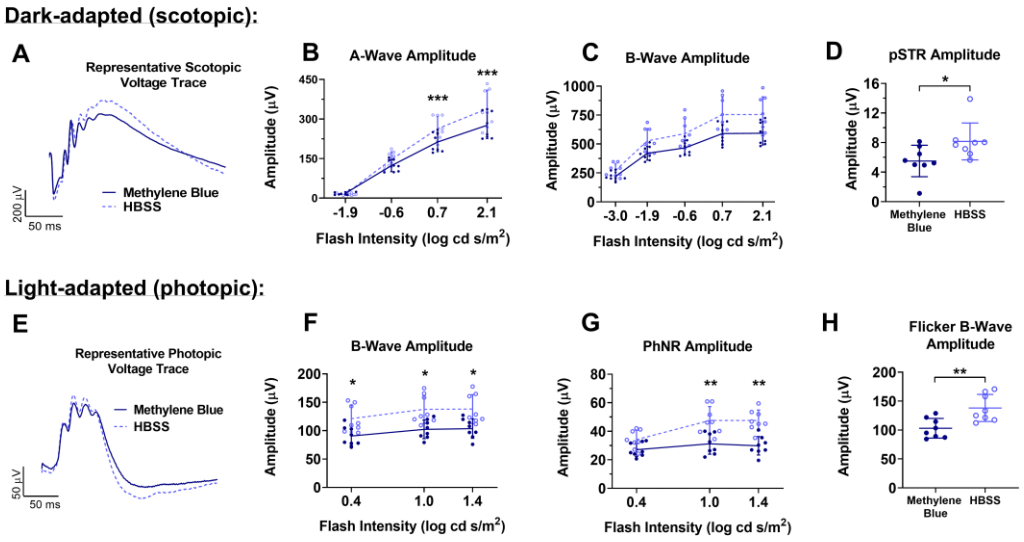

Figure 9: Electroretinogram (ERG) measurements in rats 6 weeks after photocrosslinking. In all animals, one eye received methylene blue injection followed by photocrosslinking, and the contralateral eye received HBSS injection. Retinal function was assessed in both eyes under scotopic (dark-adapted) conditions by measuring A) positive scotopic threshold response (pSTR) amplitude, B) scotopic A-wave amplitude and C) scotopic B-wave amplitude and under photopic (light-adapted) conditions by measuring F) flicker B-wave amplitude, G) photopic B-wave amplitude and H) photopic negative response (PhNR) amplitude. Representative ERG voltage traces showing A) scotopic (at 2.1 cd s m^{-2} flash intensity) and (E) photopic response (at 1.4 log cd s m^{-2} intensity). Data points show mean ± standard deviation from n = 8 replicates per data point. * $p<0.05$. ** $p<0.01$. *** $p<0.001$ for comparisons between photocrosslinked and non-photocrosslinked eyes.

3.4.7 Histology

Safety of photocrosslinking was further assessed by examination of histological sections from rats euthanized 10 days after unilateral photocrosslinking treatment with methylene blue and light to identify possible optic nerve and retinal damage. Sections were imaged at the optic nerve head and peripheral retina (>2 mm from the optic nerve head) to assess localization of damage. The contralateral control eye was untreated. Among the three rats in this study, one did not have any obvious damage to the optic nerve or retina, one had

evidence of a foreign body reaction in the optic nerve sheath and retinal degradation adjacent to the optic nerve head (Figure 10), and the third rat appeared to have gliosis localized near the optic nerve head. Notably, all three rats had no damage in the peripheral retinas of the treated eyes, indicating focal damage likely caused by the presence of both methylene blue and light near the peripapillary sclera.

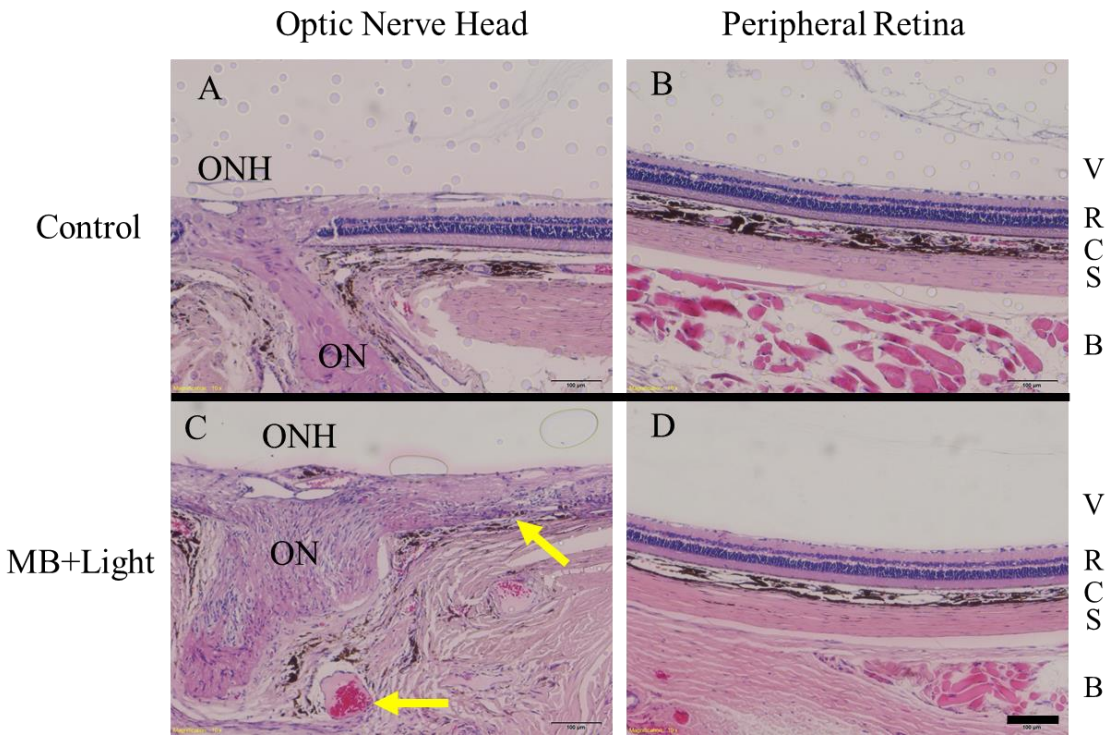

Figure 10: Histological sections of optic nerve head and peripheral retina to assess safety after photocrosslinking. Paraffin embedded sections with hematoxylin and eosin staining of optic nerve head and peripheral retina (< 2 mm from optic nerve head) of rats euthanized 10 days after unilateral treatment with targeted methylene blue photocrosslinking. Scale bars = 100 μm. Tissues are labeled including the optic nerve head (ONH), optic nerve (ON), vitreous (V), retina (R), choroid (C), sclera (S), and retrobulbar tissue (B). While local tissue responses varied in eyes after photocrosslinking, the most severe damage seen among the three rat eyes examined is exhibited. A) Control eye injected with HBSS showing healthy optic nerve and healthy retina both adjacent to the optic nerve head, and B)in the periphery. C) Immune foreign body response (lower arrow) and retinal damage (upper arrow) near the optic nerve. This damage was localized to the region adjacent to the optic nerve as D) retina in the periphery appeared normal. Data are representative of histological sections examined in 6 eyes from 3 rats.

To assess possible damage from light alone (without methylene blue), another cohort of rats was treated according to the photocrosslinking procedure previously described with light but HBSS was injected instead of methylene blue. Histological analysis did not reveal significant evidence of retinal damage in either the optic nerve region or the peripheral retina (Figure 11).

We also assessed possible effects of light exposure without methylene blue by OCT (Figure 36, Appendix A). There were no apparent morphological differences between eyes exposed to targeted illumination compared to contralateral eyes receiving no treatment, further supporting finding from retinal histology indicating that light alone does not damage the retina.

The light intensity used in this study (i.e., 424 mW/cm^2) exceeded the maximum permissible intensity for human eyes (211 mW/cm^2, calculated using ANSI 2000) exposed to 660 nm light for the given exposure conditions (see Appendix A)[123]. Considering the intensity used in this study exceeded the calculated maximum permissible intensity, it was unexpected that treatment with light alone caused no apparent changes in retinal morphology. We conclude that damage seen near the optic nerve due to the photocrosslinking procedure was not due to light alone and was probably a result of methylene blue-mediated photochemistry.

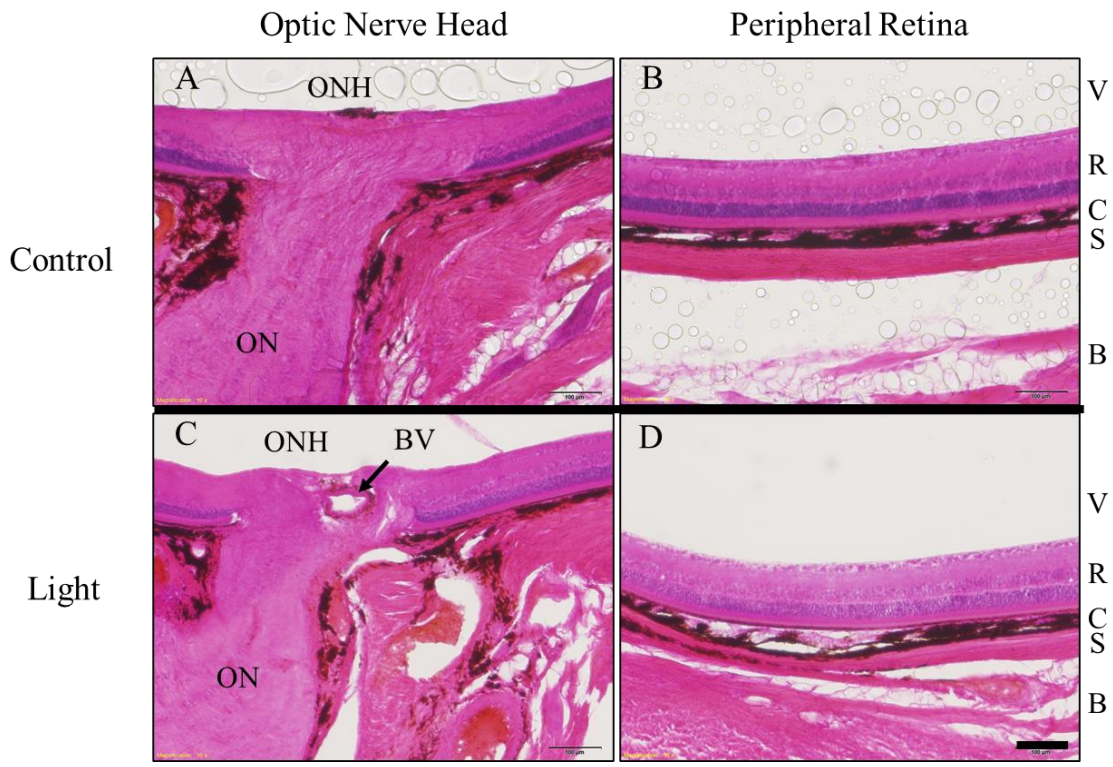

Figure 11: Cryosections with hematoxylin and eosin staining of rat optic nerves/retinas treated unilaterally with targeted light exposure (no MB). Scale bar = 100 μm. Tissues are labeled including the optic nerve head (ONH), optic nerve (ON), blood vessel (BV), vitreous (V), retina (R), choroid (C), sclera (S), and retrobulbar tissue (B). A) Control eye injected with HBSS showing healthy tissue in both the optic nerve head region and B) peripheral retina. C) Treated eye showing healthy optic nerve region and D) healthy periphery. Note, the vacant circular region in the center left of the optic nerve head is likely a retinal blood vessel.

3.5 Discussion

We have shown for that selective peripapillary scleral crosslinking at the millimeter scale *in vivo* is possible and reported a new procedure for its implementation. Our approach used a photosensitizer, MB, administered by retrobulbar injection followed by transpupillary illumination of the peripapillary region with 660nm red light. Importantly, this demonstration shows that the drug and light delivery challenges presented by crosslinking

the posterior sclera may be overcome *in vivo*. This method is unique from existing photocrosslinking protocols in the eye for its spatially targeted nature at the peripapillary sclera. While it appears that laser light illumination itself did not harm the eye, the photocrosslinking resulting from light exposure in the presence of methylene blue had moderate adverse effects. This finding is consistent with the literature on other singlet-oxygen generating photosensitizers are known to have toxic effects when irradiated *in vivo*[171–173]. Consistent with our targeted delivery approach, damage was isolated to the peripapillary region, as shown by histological analysis. Deficits seen in the electroretinography data may be related to damage in the retina and in the optic nerve, since unabsorbed light passing through the fundus may excite MB within the optic nerve/sheath. Likewise, axon loss may have been caused by damage directly to the optic nerve or indirectly by collateral damage to axons in the retina that extend into the optic nerve.

Electroretinography revealed greater functional deficits at higher flash intensities than at lower flash intensities. This observation may indicate selective damage of cone photoreceptors compared to rod photoreceptors since cone function corresponds with brighter flash intensities[174]. A possible explanation for selective cone damage is presence of a cone subpopulation with preferential absorbance for red light (red cones) compared to rods which have preferential absorbance in the blue-green wavelength range. However, rats generally lack sensitivity in the red wavelengths[175].The damage to retinal function may also be non-specific photothermal damage in the in the strongly absorbing retinal pigment epithelium.

Methylene blue alone may play a role in the damage observed to the retina and optic nerve, as shown in prior studies that reported retinal ganglion cell toxicity in rats injected

intravitreally with 2 μL at 2% (6.25 mM) concentration[92]. Comparatively, our 100 μL retrobulbar injection at 3 mM represents a significantly higher dose, but our injection is separated from the retina by the choroid which serves as a formidable clearance route and barrier to retinal entry, so local methylene blue concentrations in the retina were certainly lower. The proximity of the optic nerve to the retrobulbar injection may have caused the optic nerve to experience a high concentration of methylene blue.

Observed off-target stiffening may be caused by light scattering within the posterior fundus tissues. Narrowing the beam size and reducing light intensity may help to further localize stiffening. For practical reasons in this study, we chose not to reduce the beam size since doing so would approach the lower bounds of spatial resolution on our globe inflation testing platform. Future studies may make use of atomic force microscopy to overcome this limitation. Additional *ex vivo* testing or tissue mechanics computational modeling is warranted to understand the lower limits of beam size which would result in sufficient stiffening.

Toxicity of the photocrosslinking procedure could be reduced by lowering light intensity. While reducing light intensity may result in lower crosslink density, strain reductions in this study (54%, 64%) exceeded those reported by Coudrillier et al. (38%) to reduce strain on the lamina cribrosa. Therefore, it may be possible to reduce light intensity and still induce sufficient crosslinking, but at less toxic levels. It has been reported by Wernli et al. and that for identical fluences of UVA irradiation during riboflavin collagen crosslinking, higher light intensities result in less efficient crosslinking than lower light intensities[176,177]. The intensity of light reaching the sclera in our study would in fact be at the high end of the intensities used in the Wernli et al. study (~90mW/cm^2), though direct

comparison is difficult considering the different diffusion direction, sensitizer molecule, and tissue studied.

Slowing methylene blue diffusion to the optic nerve and retina could also reduce photocrosslinking toxicity. Formulation strategies may include methylene blue conjugation to macromolecules or encapsulation in liposomes/carriers. Diffusion across the Tenon capsule at the posterior scleral surface may present a challenge. Its epithelialized surface is likely similar to that of the optic nerve sheath, making it difficult to design a delivery formulation capable of discriminating between the two. Alternatively, methylene blue could be delivered by suprachoroidal injection placing it at the interface of the sclera and choroid. This approach is minimally invasive and overcomes any physical barriers to diffusion. However, only small volumes may be injected, and the choroid's adjacency would lead to rapid clearance.

A strategy to improve photocrosslinking efficiency may be to use an alternative sensitizer instead of methylene blue. Methylene blue was chosen for its known low dark toxicity *in vivo*, efficient triplet yield, absorbance of red light in the phototherapeutic window, and its low cost/high availability. However, there exist many other sensitizers which may overcome limitations in this study due to their mechanisms of action, wavelengths of absorbance, and transport properties[103,178].

Besides potential application as a future glaucoma treatment, another interesting application for our targeted crosslinking approach is for treatment of myopia. Recently, the possibility of preventing myopic progression through scleral stiffening has attracted interest[179,180]. Targeted stiffening may be especially useful for correction of refractive

error by differentially modulating scleral stiffness, resulting in controlled shaping of the eye. This technique would work similarly to the LASIK procedure or refractive keratotomy in the cornea by artificially producing regions of relative weakness in the sclera which mechanically deform to produce the desired eye shapes.

3.6 Conclusion

In conclusion, this study introduces a method for implementing regionally targeted scleral photocrosslinking in the posterior globe using a novel microscope apparatus. We have shown methylene blue and 660 nm red light to be efficacious at reducing scleral strain by as much as 64% compared to untreated contralateral eyes and peripheral sclera in the same eye. In its current form, this treatment generated moderate toxicity localized near the optic nerve head that affected retinal function; effects of visual acuity remain to be assessed. Future studies should further optimization the procedure to reduce these adverse effects. Importantly, this study provides the means for future work to assess the impact of targeted peripapillary stiffening on functional and morphological glaucoma disease outcomes in a glaucomatous animal model. Such a targeted approach to mechanical stabilization of the peripapillary region of the eye could provide a powerful new approach to glaucoma therapy that is mechanistically different from other approaches in use or under development today.

CHAPTER 4. EFFECTS OF SCLERAL PHOTOCROSSLINKING IN GLAUCOMATOUS RATS

Note on Contribution: My colleague, Bailey Hannon, contributed significantly to the following chapter in execution of experiments, data analysis, and in its writing/composition. She induced ocular hypertension in glaucomatous rats and collected IOP, OMR, ERG, OCT, and axon count data. Dr. Thomas Read contributed axon sections for axon count data. Matthew Ritch contributed to axon counting software to produce axon count data. Elisa Schrader and Lauren Nichols contributed data analysis for DIC and other experimental studies.

4.1 Introduction

Glaucoma is the leading cause of irreversible blindness and affects an estimated 80 million people worldwide[1]. This optic neuropathy is characterized by the loss of retinal ganglion cell axons in the optic nerve head, which is the main and early site of damage in the disease[32]. Since a major risk factor for glaucoma is elevated intraocular pressure (IOP), current treatments aim to lower IOP by increasing aqueous outflow or by decreasing aqueous humor production [181,182]. Although these treatments can be successful in slowing or preventing progression of glaucomatous damage, they are not always effective; further, medication-based treatments have poor patient compliance [183,184]. Therefore, treatments that overcome the limitations of current therapies are desirable.

It is known that elevated IOP leads to increased biomechanical strain in the ONH tissues which is thought to promote RGC loss in glaucoma, and thus a promising alternative

treatment approach for glaucomatous optic neuropathy is to protect against mechanical insult at the ONH due to ocular hypertension. Finite element modeling studies have analyzed the main factors that influence ONH mechanical insult, finding that scleral stiffness is the main such factor [45,46]. Experimentally, Coudrillier et al. found that localized stiffening of the peripapillary sclera reduced strain in the lamina cribrosa in ex vivo porcine eyes[4]. Therefore, it is hypothesized that scleral stiffening may confer protection against IOP-induced glaucomatous damage [185].

A previous study (Kimball et al. 2014) assessed the effects of scleral stiffening on glaucomatous damage in mice[5]. Specifically, Kimball et al. induced scleral stiffening in ocular hypertensive mice using the collagen crosslinking agent glyceraldehyde. Contrary to the expected outcome, they found that scleral stiffening increased rather than decreased glaucomatous damage. There are several possible explanations for this observed outcome. For example, whole globe scleral stiffening is known to increase the magnitude of IOP fluctuations [156], which may in turn damage RGC axons [186]. Alternatively, glyceraldehyde toxicity may have outweighed the neuroprotection due to scleral stiffening.

To further investigate the neuroprotective potential of scleral stiffening, we considered two different stiffening approaches (Table 13). In the first, we specifically stiffened only the peripapillary sclera, hypothesizing that such a localized stiffening would prevent glaucomatous damage by reducing ONH strain while maintaining the native compliance of the globe and thus minimizing IOP fluctuations. Our second approach was to stiffen the entire posterior sclera using a well-tolerated collagen crosslinking agent. For this purpose we used genipin, which has recently been shown to provide prolonged scleral stiffening at a much lower concentration than glyceraldehyde [52,166] and which has a promising safety

profile [187–190]. We here assess the protective effects of these two stiffening paradigms in a rodent model of ocular hypertension.

4.2 Methods

4.2.1 Rationale for Using the Rat Model of Glaucoma

We chose to use the widely used rat model of glaucoma because of its many parallels to glaucoma in humans. Specifically, rat models of OHT demonstrate several of the clinical hallmarks of glaucoma, including: the ONH being a main and early site of damage, RGC apoptosis, remodeling of extracellular matrix components in the ONH, and ONH 'cupping' [191–193]. Rodents are also more cost-effective and ethically defensible than non-human primates. Considering only rodents, rat eyes are twice the size of mouse eyes and are therefore easier to work with than mice, e.g. for surgical techniques related to our targeted crosslinking procedure and for mechanical testing [194]. Additionally, IOP measurements in mice are typically performed under anesthesia, which has been shown to underestimate the IOP by as much as 50% in OHT mice[195]. Our chosen strain of rat, the Brown Norway rat, is notably more docile than other strains and therefore IOP can be measured without anesthesia. Further, we can confidently assess visual function in Brown Norway rats because they are a pigmented strain, and thus have a strong optomotor response (OMR), whereas albino rodents have little to no OMR [196]. Together, these reasons make the Brown Norway rat model of glaucoma suitable for evaluating our two stiffening paradigms.

4.2.2 Decision to Implement an Unpaired Treatment Paradigm

Our study design (Figure 12) was guided by the desire to prioritize statistical power for comparing axon counts between crosslinking treatment groups in microbead-treated eyes. In other words, we wished to minimize variance for axon counts in crosslinked microbead-treated eyes. Thus, an unpaired experimental design ("Design A") was used in this study in which, for each rat, one eye was received both a scleral stiffening treatment and microbeads to induce OHT (hypertensive experimental), while the contralateral eye was untreated (naïve normotensive control). In addition, three alternative study designs were considered (Table 2) involving the hypertensive experimental eye treatment above but with different normotensive control eye treatments, including: (1) a paired design in which the control eye received a crosslinking treatment only ("Design B"), (2) a paired design in which the control eye received an HBSS (vehicle) injection only ("Design C"), and (3) a paired design in which the contralateral eye received a microbead injection only ("Design D"). Design C was eliminated because preliminary data suggested that HBSS injections do not cause significant axon loss and would only risk adding potential damage due to bilateral injection. Design D was eliminated due to ethical concerns for animal wellbeing.

Table 2: Experimental designs considered in this study. Ultimately, an unpaired design was chosen with rats receiving a unilateral crosslinking and microbead treatment to reduce potential variability of measured outcomes expected to arise from bilateral injections.

Design	**Axon Comparison**	**Variance**	**Strengths/Weaknesses**
A (Unpaired)	I (Unpaired)	Lowest variance	Does not account for parity between eyes or for treatment toxicity in individual rats
A (Unpaired)	II (Paired)	Moderate variance due to computed difference	Accounts for parity between eyes of individual rats
B (Paired)	I (Unpaired)	Moderate variance due to injection variability	Accounts for treatment toxicity in individual rats
B (Paired)	II (Paired)	High variance due to both computed difference and injection variability	Accounts for both parity between eyes and for treatment toxicity in individual rats

In addition to the two remaining options (Designs A and B) for control eye conditions discussed above, we considered two ways to assess RGC axon count differences between crosslinking treatment groups, including: (1) using raw values of axon counts in crosslinked hypertensive eyes ("Comparison I"), or (2) computing the difference in axon counts between the crosslinked hypertensive eye and control eye for each rat ("Comparison II"). The four possible combinations of two study designs and two comparisons are listed in Table 2 with our assessment of advantages and disadvantages of each.

The key advantage of a paired design is the ability to account for (or explain) animal-specific variance in axon count comparisons between crosslinking groups. However, a paired design only increases statistical power if the required control eye treatment does not introduce greater variability. Therefore, merits of various design and comparison combinations rely on (1) the expected degree of parity between eyes of the same rat and the expected variance between rats, and (2) the expected variance in axon counts attributed

to the control eye treatments. While axon count parity between eyes of healthy rats has been demonstrated previously, we believe that injection variability and measurement variability offset the potential statistical advantage gained by using a paired design[197].

In further support of an unpaired design, we have previously observed that crosslinking treatments increase variance in axon counts. Additionally, preliminary data in our lab suggested that bilateral crosslinking treatment leads to greater axon loss than a unilateral treatment, possibly due to increased systemic inflammation from two injections instead of one. In conclusion, we considered consequences of control eye injections and statistical comparisons involving parity between eyes. We concluded an unpaired design would maximize statistical power while sacrificing the ability to account for within-rat toxicity effects of each treatment.

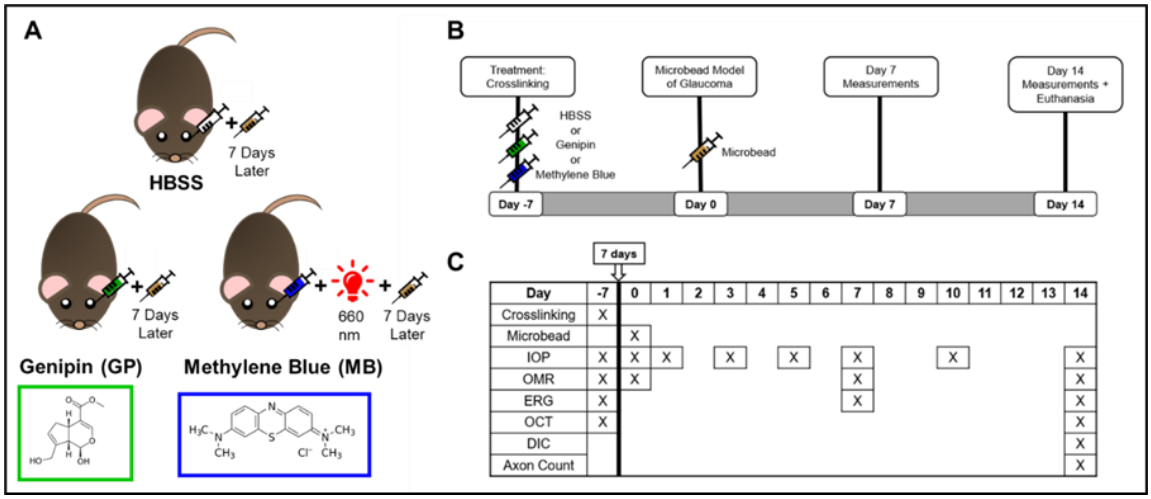

Figure 12: A) Scleral crosslinked eyes received one of three treatments by retrobulbar injection: HBSS (vehicle), Genipin (GP), or Methylene blue (MB). Those in the MB group also received 30 minutes of localized red light (660nm) to selectively stiffen the peripapillary (but not peripheral) sclera. B) Timeline of experiments. Seven days after scleral stiffening treatment. the treated ("experimental") eye received a microbead injection to induce ocular hypertension. Ocular hypertension was induced at Day 0. Rats were sacrificed at Day 14. C) Timing of experiments. IOP measurements were taken at Days -7, 0, 1, 3, 4, 7, 10 , and 14. OMR measurements were taken at Days 0, 7, and 14. ERG measurements were taken at Days -7, 7, and 14, and OCT measurements were taken at Days -7 and 14. DIC and axon count measurements were necessarily taken post mortem after collecting the sclerae and optic nerves on Day 14 immediately after euthanasia.

4.2.3 Animals and Study Design

86 male, retired breeder Brown Norway rats (8 - 10 months old) were purchased from Charles River Laboratories (Wilmington, MA). All procedures involving animals were approved by the Georgia Institute of Technology Institutional Animal Care and Use Committee and the Atlanta VA Medical Center Institutional Animal Care and Use Committee (IACUC). All procedures complied with the ARVO statement for the Use of Animals in Ophthalmic and Vision Research.

Our study design followed a “crosslink then OHT” approach. In other words, animals received a scleral stiffening treatment (or sham) unilaterally, were allowed to recover for one week, and then received a treatment to induce ocular hypertension in the same crosslinked eye. We chose to stiffen the sclera prior to inducing OHT to facilitate comparison of our results with those of Kimball et al.[5]. We used the well-established magnetic microbead model to induce OHT, which was applied to all eyes that received scleral crosslinking treatment (or sham). As noted above, all contralateral eyes were naïve, i.e. received no scleral crosslinking treatments (or sham) and no microbead injections. Animals were followed for 2 weeks after induction of OHT and then sacrificed.

In more detail, rats were randomly divided into three “treatment groups” (Figure 12A and Figure). Hanks balanced salt solution (HBSS) was used as the vehicle for treatments and as the sham injectate. One group (HBSS rats, n = 32) received this sham injection. The second group (GP Rats, n = 27) received genipin chemical crosslinking. The third group (MB Rats, n = 27) received methylene blue photocrosslinking. Treatments were applied unilaterally seven days prior to microbead injections using retrobulbar injections for the HBSS Rats (“HBSS hypertensive experimental” eyes), GP Rats (“GP hypertensive experimental” eyes), and MB Rats (“MB hypertensive experimental” eyes). Contralateral eyes received no injections and therefore served as normotensive controls for each animal (“HBSS normotensive control” eyes, “GP normotensive control” eyes, and “MB normotensive control” eyes). Within each animal, the eye (left (OS) or right (OD)) receiving treatment was randomly assigned.

4.2.4 Intraocular Pressure Measurements

IOP measurements for each rat were taken between 7:00am and 10:00am using a Tonolab rebound tonometer (Icare Finland Oy, Vantaa, Finland) at baseline and at Day 0, 1, 3, 5, 7, 10, and 14 after microbead injection. Awake rats were gently restrained by hand while eight tonometer readings were acquired from each eye. The lowest and highest IOP values were excluded from each set of daily measurements and the remaining six IOP values were averaged to obtain a representative IOP measurement. Prior to this study, the rebound tonometer was calibrated using a cannulated intact rat eye in which IOP was externally imposed using a hydrostatic pressure reservoir set to heights ranging from 5 to 50 mmHg (data not shown). Calibration results showed good agreement between set IOP values and measured IOP values, and thus no IOP correction was necessary. We then calculated the IOP burden, also referred to as cumulative IOP difference, IOP exposure, or positive integral IOP, which provides an estimate of the total IOP "insult" to the hypertensive eye[198–200]. We defined IOP burden as the area between the OHT and normotensive eyes on the IOP versus time plot. If the measured IOP in the OHT eye was transiently lower than IOP in the contralateral (normotensive) eye, the IOP difference was set to zero at that time point, i.e. we did not allow negative contributions to the IOP burden.

4.2.5 Crosslinking Injection Preparation

Genipin and methylene blue solutions were both freshly prepared the morning of the retrobulbar injection. Genipin (Wako Pure Chemical Industries, Ltd., Richmond, VA) and methylene blue of USP grade (Apollo Scientific, Stockport, UK) were obtained in powder form and dissolved in Hank's balanced salt solution (HBSS). Genipin was solubilized at a

concentration of 15 mM by vortexing the solution for 15 minutes. Methylene blue was solubilized at a concentration of 3 mM by vortexing the solution in a microcentrifuge tube and heating to a temperature not greater than 100 degrees Celsius for 5 minutes. Care was taken to minimize light exposure of the methylene blue solution to prevent possible photodegradation.

4.2.6 HBSS and Genipin Crosslinking Injection Procedures

For HBSS and genipin retrobulbar injections, rats were anesthetized with a ketamine (60 mg/kg) and xylazine (7.5 mg/kg) cocktail. Once anesthetized, rats were placed on a heating pad and received a drop of topical tetracaine (0.5 %, Tetracaine Steri-Units, Alcon, Geneva, Switzerland) as a local anesthetic. Retrobulbar injections were performed on the eye designated as hypertensive experimental by gently proptosing the eye with curved forceps and inserting a disposable insulin syringe with a 31 G needle (BD 300 µl Insulin Syringe Ultra-Fine™ needle, Becton, Dickinson and Company, Franklin Lakes, New Jersey) into the muscle cone through the inferior quadrant of the conjunctiva. 150µl of either HBSS or genipin (15 mM) was then injected into the muscle cone. After injections, rats were given topical antibiotic (Vetropolycin, Dechra Pharmaceuticals, Northwich, United Kingdom) to prevent infection and antisedan (1 mg/kg) to reverse anesthesia [201].

4.2.7 Methylene Blue Photocrosslinking Procedure

Rats were anesthetized with isoflurane/oxygen (5%/700 mL/min) and placed in a stereotaxic head mount (Kopf Instruments, Tujunga, CA) equipped with tooth bar over a heating pad, allowing facile manipulation of head position. 0.5% tetracaine (Tetracaine Hydrochloride Ophthalmic Solution, Amici Pharmaceuticals, Melville, New York) was

applied topically as a local anesthetic to the eye designated as MB hypertensive experimental, followed by topical application of a 1% tropicamide eye drop (Tropicamide Ophthalmic Solution, Henry Schein, Melville, New York). An additional eye drop of 1% tropicamide was applied after 5 minutes and allowed to take effect for another 10 minutes to ensure maximal dilation of the iris. A hydrating eye lubricant (Puralube Vet Ointment, Dechra Pharmaceuticals, Northwich, United Kingdom) was applied to the contralateral eye designated as normotensive control, to prevent dehydration during the procedure. After dilation of the eye designated as MB hypertensive experimental, a 100 µL retrobulbar injection of 3 mM methylene blue was administered using a sterile 31 G insulin needle and syringe.

Immediately after injection, a contact lens was placed on the corneal surface to eliminate refraction from the cornea/lens, allowing for visualization of the fundus (Figure 38). The rat's head was positioned with the eye designated as hypertensive experimental aligned on the optical axis of a custom-designed microscope capable of simultaneously imaging the fundus and projecting an annular beam of light tuned to excite methylene blue at 660 nm wavelength. Upon alignment of a low intensity guide beam (<0.1 mW) with the optic nerve, the light intensity was increased to a dose of 10mW for 30 minutes to facilitate scleral crosslinking. During this time, beam position relative to the optic nerve head was monitored with the microscope and adjusted if necessary, using micropositioners to move the microscope position relative to the eye. At the conclusion of the 30-minute illumination period, the light source was turned off, the contact lens was removed, and once ambulatory on the heating pad, the rat was returned to its cage.

4.2.8 Microbead Injection Preparation and Procedure

The magnetic microbead model of glaucoma was used to induce unilateral ocular hypertension in the eyes designated as hypertensive experimental. All microbead injections occurred at Day 0, which was seven days after crosslinking procedures. A mixture (1:1) of 2 µm and 6 µm magnetic polystyrene microbeads (micromer®-M, Micromod, Rostock, Germany) with PEG-COOH surface chemistry (to promote biocompatibility) was used for microbead injections. Beads were autoclaved according to manufacturer's specifications (20 minutes at 121 °C and 3500 mbar pressure) and then rinsed five times with sterile HBSS using cell culture sterility practices. Rats were anesthetized with a single dose of ketamine (60mg/kg) mixed with xylazine (7.5 mg/kg) and placed on a heating pad. Tetracaine (0.5%, Tetracaine Steri-Units, Alcon, Geneva, Switzerland) was then applied to the eye. The bead suspension was vortexed for 15 seconds to suspend the beads, and a volume of 25µl was pipetted onto a sheet of wax parafilm. Deposited solutions were then drawn into sterile, disposable syringes with 31 G needles.

The eye designated as hypertensive experimental was proptosed with a small section of a latex glove so that an annular magnet could be placed within the same plane as the iridocorneal angle. A neodymium, grade N40, nickel plated annular magnet (H125D, Amazing Magnets, Anaheim, CA) with dimensions of 7.14 mm inner dimeter, 12.70 mm outer diameter, and thickness of 3.18 mm was placed around the limbus after proptosing, and the eye received a intracameral injection of magnetic microbeads (2.25 x 106 to 4.5 x 106 beads total per 25 µl injection) into the anterior chamber. The needle was held in the anterior chamber for 60 seconds following injection and then slowly removed to minimize fluid reflux. After injection, the section of latex glove was removed, and the magnet was

placed back on the eye for 10 minutes to ensure that beads had settled into the iridocorneal angle. Both eyes (hypertensive experimental and normotensive control) of each rat received topical antibiotic (Vetropolycin, Dechra Pharmaceuticals, Northwich, United Kingdom) to prevent infection and hydrate the eye. Rats were placed on heating pads until ambulatory.

IOP was measured 1, 3, 5, and 7 days following induction of ocular hypertension via microbead injection. If the experimental (injected) eye did not demonstrate at least one day of OHT, defined as an IOP elevation of >5 mmHg compared to contralateral control eye within 7 days of injection, the eye was considered to be a non-responder and was then reinjected with 15 µl of microbead solution on Day 7 (n = 12 of 74 total rats). Rats for which IOP elevation failed 7 days after reinjection were removed from the study (n = 3) and therefore no rat was reinjected with microbeads more than once. Additionally, 7 rats were removed from the study upon reaching IACUC endpoint criteria for health/safety and 2 rats died during anesthesia recovery, leaving a total of 74 rats analyzed in the study.

4.2.9 Assessment of Retinal Function: Electroretinography

Dark-adapted electroretinograms (ERGs) were used to assess inner and outer retinal neuronal function. ERG measurements were taken at baseline, before both the crosslinking procedure and microbead injection, and at 7 and 14 days after microbead injection. At each timepoint, rats were dark-adapted for 30 minutes under dim red light and anesthetized using a cocktail of ketamine (60 mg/kg) and xylazine (7.5 mg/kg). Once asleep, both eyes received drops of tetracaine (0.5%) and tropicamide (1%) topically to anesthetize corneas and dilate pupils, respectively. A ground electrode was inserted into the tail of the rat and

reference needle electrodes were inserted subcutaneously into the cheek by each eye. Custom gold-loop electrodes were placed on the cornea of each eye and a layer of carboxymethylcellulose (Celluvisc, Allergan, Dublin, Ireland) was applied over the corneal electrode to ensure electrical conductivity and prevent drying. Under dark-adapted conditions, a 6-step series of increasing flash intensities (-6.0 to 2.1 log cd s/m2) was used. Electrical responses to various full-field flash stimuli in a Ganzfeld dome were recorded using a signal-averaging ERG system (UTAS BigShot; LKC Technologies, Gaithersburg, MD). Oscillatory potentials (OPs) were filtered with a 65-275 Hz bandpass fifth order Butterworth filter. Amplitudes and implicit times were measured in the following way: baseline to peak (positive scotopic threshold (pSTR)), baseline to trough (negative scotopic threshold (nSTR) and a-wave), trough to peak (b-waves and OPs). We elected to analyze ERG amplitudes of the positive scotopic threshold (pSTR) and negative scotopic threshold (nSTR) at -6.0 log cd s/m2, the b-wave at -3.0 log cd s/m2 (b-wave), and the third OP (OP3) at 2.1 log cd s/m2 because these amplitudes have been shown to be associated with retinal ganglion cell damage in rodent models of glaucoma [202–205].

4.2.10 Ischemic Damage Exclusion Criteria

Rats with likely ischemic damage to the retina were excluded from analysis. Exclusion was based on the b-wave amplitude from the brightest flash (2.1 log cd s/m2) at Day 14, since bipolar cell function (which drives b-wave amplitude) is known to be sensitive to ischemic damage at bright scotopic flashes [206,207]. The 99.5% confidence interval of the b-wave amplitude was computed for all normotensive control eyes (n = 74). If the b-wave amplitude of the hypertensive experimental eye lay below this 99.5% confidence interval, that rat was excluded from analysis. Of the 74 rats analyzed, 14 rats were excluded by this

criterion. The final total number of animals was thus 60, divided into HBSS rats (n = 21), GP rats (n = 20), and MB rats (n = 19).

4.2.11 Assessment of Visual Function: Optomotor Response

Visual function was assessed via quantitative analysis of optomotor response (OMR) thresholds of spatial frequency and contrast sensitivity (OptoMotry®; Cerebral-Mechanics, Lethbridge, AB, Canada). OMR was measured at baseline (prior to crosslinking treatment), Day 0 (7 days after crosslinking procedure, but prior to microbead injection that day), Day 7, and Day 14, following a protocol similar to that of Prusky and Douglas [196,208]. In brief, rats were placed on a raised platform in the middle of a box consisting of four flat screen monitors which displayed black and white vertical gratings that rotated at a speed of 12 degrees/second (d/s) to create a virtual drum. A trained observer then monitored the rat for a positive or negative reflexive head movement in response to the rotating gratings moving in a clockwise or counterclockwise direction, assessing the responses of the OS and OD eyes, respectively [196]. To determine an animal's spatial frequency threshold, the vertical bands were held at 100% contrast and spatial frequency was adjusted in a staircase paradigm starting at 0.042 cycles/degree (c/d) until the threshold where the rat could no longer see the gratings was established. Contrast sensitivity threshold was determined using a similar staircase paradigm, but the spatial frequency was held at 0.064 (c/d) while the contrast was decreased from 100% until the threshold was determined. Contrast sensitivity is reported as the reciprocal of the Michelson contrast from the screen's luminance, as previously described [208]. Prior to OMR measurements, each rat eye was carefully inspected for any opacity or speckling of microbeads in the anterior chamber that might occlude the rat's visual axis. If this was the case, that eye's OMR was not recorded,

making the final number of data used in OMR analysis 48, with 16 rats in each treatment group.

4.2.12 Assessment of Retinal Morphology: Optical Coherence Tomography

A Spectral-Domain Optical coherence tomography (SD-OCT) system (Bioptigen 4300, Leica Microsystems, Buffalo Grove, IL) was used to measure total retinal thickness and qualitative retinal morphology in the posterior eye at baseline and Day 14. Total retinal thickness was measured at locations 0.5 mm and 1.2 mm from the center of the ONH. Rats were anesthetized using ketamine/xylazine, and eyes received drops of tetracaine and tropicamide as described above. A 3-mm radial scan (1,000 A-scans per B-scan) centered at the optic nerve head was acquired in both normotensive control and hypertensive experimental eyes. B-scans from the superior-inferior and nasal-temporal axes of all eyes were assessed manually by a trained technician blinded to treatment group using a customized MATLAB program (MATLAB R2019a, Mathworks, Natick, MA). If fewer than two scans were of sufficient quality to measure retinal thickness accurately, the rat was eliminated from the OCT retinal thickness dataset. Measurements were taken at locations avoiding local vasculature, and these individual values from each quadrant were averaged together.

4.2.13 Optic Nerve Sectioning and Imaging

Immediately after euthanasia via CO2 overdose, rat optic nerves were dissected from enucleated eyes and fixed in isotonic Sorensen's buffer containing glutaraldehyde (2.5%) and PFA (2%, EMS, Hatfield, PA). Tissue was post-fixed in osmium tetroxide, dehydrated in an ethanol series, infiltrated and embedded in araldite-epon plastic (Araldite 502/Embed

812, EMS, Hatfield, PA). Semi-thin sections of (0.5 µm thick) were cut on a Leica UC7 Ultramicrotome (Leica Microsystems, Buffalo Grove, IL) approximately 1.5mm posterior to the sclera. Sections were stained with 1% toluidine blue and imaged with a Leica DM6 B microscope (Leica Microsystems, Buffalo Grove, IL) using a 63x lens and 1.6x multiplier for a total magnification of 100x. The entire nerve was imaged with a series of z-stack tile scans from which, the optimally focused image within each z-stack tile was selected using the "find best focus" feature in the LAS-X software (Leica Microsystems, Buffalo Grove, IL). Contrast was then adjusted for each tile by maximizing grey-value variance. Finally, normal axons were automatically counted using AxoNet, a fully convolutional neural-network previously developed in our lab [170].

4.2.14 Whole Globe Inflation Testing

After euthanasia, eyes underwent inflation testing as previously described [52]. A few modifications to the previously published method were made to adapt to the altered mechanical properties of microbead-injected eyes. In brief, when eyes were pressurized during whole globe inflation testing, we observed leakage of PBS through the scleral shell via vasculature and the scleral canal. Such leakage was not previously observed in untreated eyes. Therefore, to reduce leaking, we substituted previously used PBS or mineral oil with a more viscous silicone oil as the pressurization medium.

After enucleation, eyes were refrigerated on ice in PBS until preparation for inflation testing. Orbital muscle, fat, and connective tissues were removed to expose the posterior sclera. Eyes were blotted dry and adhered to a custom-designed thin aluminum plate incorporating a machined cup in the surface perforated with a hole, as follows. The cornea

was positioned in this cup so the posterior sclera faced upward (away from the plate), and cyanoacrylate-based adhesive was cured with PBS to adhere the eye to the plate, taking care to remove any air bubbles that might have been trapped in the adhesive with the tip of a 30-gauge needle. The cornea was then carefully excised through the hole in the bottom side of the mounting plate, allowing for removal of the aqueous humor, lens, and vitreous humor. Silicone oil was used to replace the contents of the eye to reduce leakage of fluid through the sclera upon pressurization as noted above. The eye and aluminum plate were then mounted onto a threaded acrylic base with screws such that the interior of the eye was in fluidic communication with channels in the acrylic plate. PBS was perfused through tubing connecting an adjustable pressure reservoir to the acrylic base. The eye was then pressurized to maintain its natural shape and blotted dry atop the aluminum plate. Black graphite powder (#970 PG, General Pencil Company, Inc., Redwood City, CA) was applied to the scleral surface with a cotton Q-tip to form a speckled pattern on the surface. Residual powder was flushed away with water and the eye was covered with PBS solution facilitated by placement of a removable reservoir atop the aluminum plate. Silicone oil was added to cover the surface of PBS in the reservoir, thus reducing loss of water through evaporation during testing as visualized in [52].

Mounted scleral shells were subsequently prepared for inflation testing. Sensors were used to monitor pressure (142PC01G; Honeywell, Charlotte, NC) and flow rate (SLG64-0075; Sensirion, Stafa, Switzerland) of PBS into the eye. After confirming absence of major leaks at 15 mmHg, pressure was maintained at 15 mmHg for 5 minutes. Shells were then preconditioned for 10 cycles at a rate of 1 cycle per minute with pressure linearly varied from 3 mmHg to 15 mmHg and back to 3 mmHg as previously described [52]. At the

conclusion of preconditioning, pressure was set to 1 mmHg and allowed to stabilize for 10 seconds. Pressure was then increased sequentially to 3, 10, 20, and 30 mmHg at time intervals dictated by a flow rate stabilization criterion. Specifically, we required the magnitude of the measured rate of change in flow rate to be less 2 (nl/min)/s over a 10 minute window, thus allowing the shells to reach steady state at each pressure level. During inflation, images of the scleral surface were captured using a digital image correlation system (Dantec Dynamics, Skovlunde, Denmark).

At the conclusion of testing, Lagrange first principal strain over the scleral shell was computed from images using Dantec's Istra 4D software (v4.4.1, Dantec Dynamics, Holtsville, NY). Data were exported to MATLAB for analysis with a customized script which identified/removed outliers as previously specified [52]. Steady state strain values at each pressure step were averaged over the peripapillary and over the non-peripapillary regions, and a Fung model was fit to the data. For each region an average strain value at 22 mmHg (physiological condition) was calculated and reported.

4.2.15 Data Analysis

Data were analyzed using SPSS (IBM Corp. IBM SPSS Statistics for Windows, Version 25.0. Armonk, NY: IBM Corp) and GraphPad software (GraphPad Software, San Diego, California) and graphed using GraphPad. For each outcome measure, a linear regression was calculated for each treatment group, and outliers were removed by controlling the false discovery rate at 1% in GraphPad. Subsequently, the remaining data were analyzed using a two-way ANCOVA in SPSS with cumulative IOP burden at Day 14 as the covariate. IOP burden was chosen as the covariate since it is a measurable indicator of the degree of

biomechanical insult. All data are reported as mean ± standard deviation, unless otherwise stated.

A two-way ANCOVA was used to analyze mean differences for each measured experimental parameter. Simple comparisons were made between hypertensive and normotensive eyes in each of the three crosslinking treatment groups (3 comparisons). Additionally, simple comparisons were made between mean values of the hypertensive eyes of each crosslinking group (3 comparisons). Bonferroni correction was applied for each parameter analyzed. For DIC strain analysis, a two-way ANCOVA was used with factors of: (1) "Region" having levels of (a) peripapillary sclera and (b) peripheral sclera; and (2) "Crosslinking Treatment" with levels of (a) HBSS, (b) GP, and (c) MB. Unless otherwise specified, all other outcome measures were analyzed with two-way ANCOVAs having two factors defined as: (1) "Microbead Treatment" having levels of (a) normotensive and (b) hypertensive; and (2) "Crosslinking Treatment" with levels of (a) HBSS, (b) GP, and (c) MB. Levene's test was used to assess inequality of variance. Homogeneity of regression slopes was assessed using interaction terms of the factors and IOP burden covariate. In cases where statistically significant interactions existed for either factor and the IOP burden covariate, significance was interpreted only at the mean value of IOP burden for comparisons involving that factor.

We created correlation matrices for ease of visualizing all outcome parameters at once. Parameters were grouped into the categories of "biomechanical", "morphological", or "functional". Specifically, biomechanical parameters were those related to elevated IOP insult, including IOP burden, peripapillary scleral strain, peripheral scleral strain, equatorial diameter, axial length, and anterior chamber depth. Morphological parameters

were those related to ON and retinal structure, including ON cross-sectional area, ON axon count, ON axon density, and retinal thicknesses 0.5 mm and 1.2 mm from the ON. Functional parameters were those related to visual acuity and retinal function, including contrast sensitivity, spatial frequency, pSTR amplitude, nSTR amplitude, b-wave amplitude, and oscillatory potential 3 amplitude.

4.3 Results

4.3.1 Microbead Injection Successfully Increased IOP

Induction of ocular hypertension after microbead treatment at Day 0 produced an IOP elevation with an initial rapid rise peaking at Day 3, followed by a gradual decrease until Day 14 (Figure 13D). Though not statistically significant, we observed that HBSS-treated eyes tended to have higher mean IOP burden compared to both GP- and MB-treated eyes. We accounted for any possible differences in IOP burden between individual rats or groups of rats by incorporating IOP burden as a covariate in our statistical analyses. Furthermore, to eliminate those rats which may have experienced IOP levels corresponding to ischemic damage, we introduced an ERG-based exclusion criterion. This functional ERG criterion eliminated rats with non-glaucomatous retinal damage.

At all time points after microbead injection, mean IOP in microbead eyes was significantly elevated compared to normotensive controls (two-way RM ANOVA, time x treatment: $F(30, 684) = 8.716$, $p < 0.0001$, Tukey post-hoc) except for the GP cohort at Day 14. No significant differences in IOP were found between experimental treatment groups at any time point. Mean IOP burden values did not differ statistically significantly between treatment groups (Figure 13C one-way ANOVA, $F(2, 57) = 1.629$, $p = 0.21$).

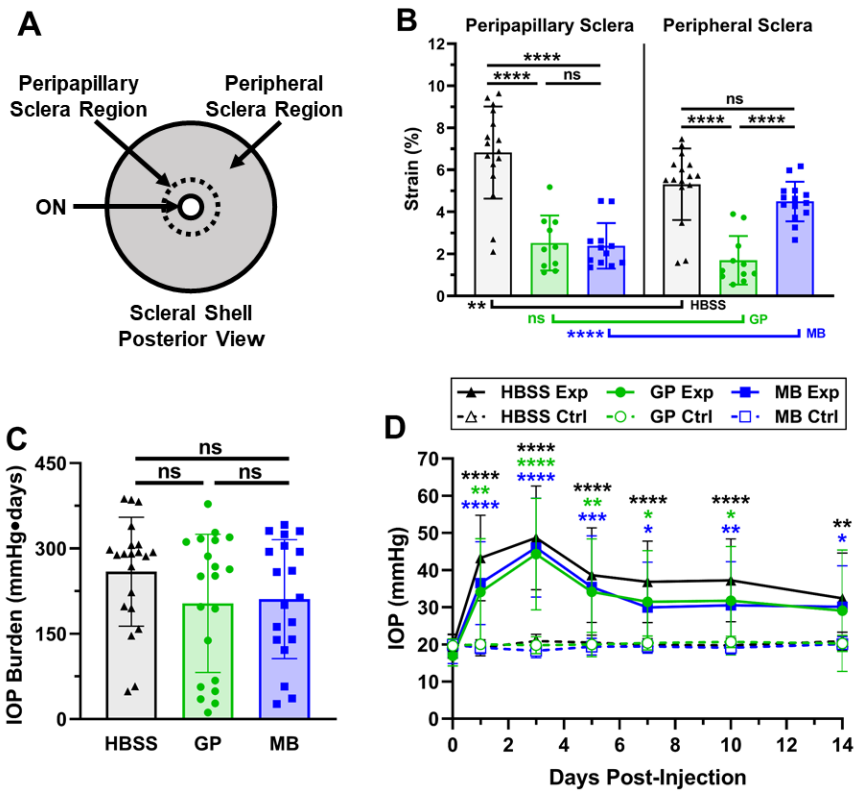

Figure 13: A) Representation of the posterior eye showing the peripapillary sclera, here defined as the region enclosed by a 2 mm diameter circle centered at the ON. The peripheral sclera was defined as the sclera outside this region. B) Whole globe inflation tests indicated whole sclera stiffening with GP and targeted peripapillary sclera stiffening with MB. Mean values are plotted. Statistical comparisons were performed using an ANCOVA and therefore are comparisons of adjusted means. C) Mean IOP burden (pressure x time) did not differ significantly between crosslinking treatment groups. D) IOP levels increased after induction of ocular hypertension at Day 0 in microbead-injected eyes compared to normotensive control eyes. Statistical significance is indicated using the following convention: "*" for $p < 0.05$, "**" for $p < 0.01$, "***" for $p < 0.001$, and "****" for $p < 0.0001$.

4.3.2 Mechanical Testing Confirmed that Crosslinking Effectively Increased Scleral Stiffness

It was important to verify that Genipin and MB stiffened the sclera in treated eyes. For this purpose, we conducted inflation testing of post-mortem eyes and quantified their deformation using DIC analysis. We report adjusted mean strains from the ANCOVA analysis over the peripapillary and peripheral scleral regions (Figure 13A), a quantity that is inversely proportional to scleral stiffness. Peripapillary strain was greater than peripheral strain ($p < 0.01$, Figure 13B) in HBSS-injected (control) eyes, likely due to presence of the scleral canal in the peripapillary region. We found that mean scleral strain was 2- to 3-fold lower in both scleral regions in GP eyes compared to the corresponding regions in HBSS eyes ($p < 0.0001$, Table 3), indicating successful whole-scleral crosslinking by GP. There was no significant difference in scleral strains between regions within GP eyes. In MB eyes, peripapillary scleral strain was approximately 3-fold lower than in HBSS-treated eyes ($p < 0.001$,Table 3), but strains in the peripheral sclera did not differ significantly between HBSS and MB eyes, indicating that targeted peripapillary MB stiffening was successful. MB eyes had significantly reduced strain in the PP region compared to the peripheral region within the same MB eye ($p < 0.0001$). Mean scleral strain values in hypertensive experimental eyes were analyzed using a two-way ANCOVA with IOP burden as the covariate (Figure 13; see Methods: Data Analysis). Strains were significantly correlated with IOP burden ($p < 0.01$, Figure 13 and Figure 44).

Table 3: Adjusted means and simple comparisons for each parameter measured from rat microbead study. Two-way ANCOVAs were used to analyze each parameter with IOP burden as the covariate.

Outcome Parameter	Normotensive Eye Adjusted Means			Hypertensive Eye Adjusted Means			Hypertensive Eye Comparisons			Normotensive-Hypertensive Comparisons		
	HBSS	GP	MB	HBSS	GP	MB	HBSS-GP	HBSS-MB	GP-MB	HBSS	GP	MB
Peripapillary Strain (%)	3.43	2.68	3.04	6.24	2.77	2.68	**<0.0001**	**<0.0001**	n.s.	**<0.0001**	n.s.	n.s.
Peripheral Strain (%)	2.41	1.92	2.20	4.86	1.92	4.58	**<0.0001**	n.s.	**<0.0001**	**<0.0001**	n.s.	**<0.0001**
Equatorial Diameter (mm)	7.29	7.31	7.24	8.01	7.81	8.04	n.s.	n.s.	n.s.	**<0.0001**	**<0.0001**	**<0.0001**
Axial Length (mm)	7.18	7.17	7.08	8.20	8.03	8.10	n.s.	n.s.	n.s.	**<0.0001**	**<0.0001**	**<0.0001**
Anterior Chamber Depth (mm)	2.34	2.31	2.13	2.77	2.74	2.63	n.s.	n.s.	n.s.	<0.001	<0.01	**<0.0001**
Nerve Cross-sectional Area (mm^2)	0.259	0.267	0.277	0.247	0.276	0.275	n.s.	n.s.	n.s.	n.s.	n.s.	n.s.
Axon Count (Axons)	78,900	82,400	83,700	39,400	46200	45500	n.s.	n.s.	n.s.	**<0.0001**	**<0.0001**	**<0.0001**
Axon Density (Axons/mm^2)	306,000	317,000	300,000	152,000	163,000	165,000	n.s.	n.s.	n.s.	**<0.0001**	**<0.0001**	**<0.0001**
Retinal Thickness at 0.5 mm (mm)	0.214	0.209	0.213	0.185	0.198	0.163	n.s.	<0.05	**<0.0001**	<0.001	n.s.	**<0.0001**
Retinal Thickness at 1.2 mm (mm)	0.194	0.193	0.193	0.18	0.194	0.187	**<0.0001**	n.s.	n.s.	**<0.0001**	n.s.	n.s.
Contrast Sensitivity (AU)	5.356	5.574	5.586	2.132	1.774	2.107	n.s.	n.s.	n.s.	**<0.0001**	**<0.0001**	**<0.0001**
Spatial Frequency (c/d)	0.573	0.568	0.579	0.329	0.293	0.302	n.s.	n.s.	n.s.	**<0.0001**	**<0.0001**	**<0.0001**
pSTR Amplitude (µV)	6.77	7.28	8.91	2.27	1.96	1.56	n.s.	n.s.	n.s.	**<0.0001**	**<0.0001**	**<0.0001**
nSTR Amplitude (µV)	6.75	7.84	8.07	4.43	3.75	4.01	n.s.	n.s.	n.s.	<0.05	**<0.0001**	**<0.0001**
B-wave Amplitude (µV)	219.99	242.69	268.20	82.37	100.12	83.68	n.s.	n.s.	n.s.	**<0.0001**	**<0.0001**	**<0.0001**
OP3 Amplitude (µV)	80.86	81.33	91.10	44.64	42.83	45.71	n.s.	n.s.	n.s.	**<0.0001**	**<0.0001**	**<0.0001**

4.3.3 Retinal Thickness Measurements Suggest Protective Effects of Scleral Stiffening

We used OCT imaging to measure total retinal thickness, expected to be decreased in eyes experiencing RGC axonal loss. Total retinal thickness at 0.5 mm from the ONH was not significantly different between hypertensive GP and HBSS eyes (Figure 14A, Table 3), and was less in hypertensive MB eyes compared to HBSS eyes ($p < 0.05$,Table 3) and GP eyes ($p < 0.0001$,Table 3). Total retinal thickness at 0.5 mm from the ONH was significantly decreased in hypertensive experimental eyes for both HBSS and MB cohorts compared to respective normotensive controls ($p < 0.0001$, Figure 14A) but not for GP eyes. Total retinal thickness at 0.5 mm from the ONH significantly correlated with IOP burden ($p < 0.05$,Figure 44). Thus, there was a trend (not reaching statistical significance) suggesting that scleral stiffening using GP (but not MB) preserved retinal thickness at 0.5 mm from the ONH in hypertensive eyes.

In contrast to the situation at 0.5 mm from the ONH, hypertensive GP eyes showed significantly larger mean total retinal thickness at 1.2 mm from the ONH compared to HBSS eyes ($p < 0.0001$,Table 3), potentially indicating a protective effect of GP against retinal changes (Figure 14B). No significant differences were observed in this measure of retinal thickness between hypertensive GP eyes and MB eyes, or between MB eyes and HBSS eyes. Total retinal thickness was significantly less in hypertensive experimental eyes compared to normotensive control eyes for HBSS eyes ($p < 0.0001$,Table 3: Adjusted means and simple comparisons for each parameter measured from rat microbead study. Two-way ANCOVAs were used to analyze each parameter with IOP burden as the covariate.) but not for GP or MB eyes. Representative OCT images shown in Figure 43 reveal minor qualitative differences as well as indications of 'cupping' at higher IOP burdens. We conclude that GP, but not MB, treatment offers some protection against retinal thinning induced by OHT but that this thinning is spatially heterogeneous.

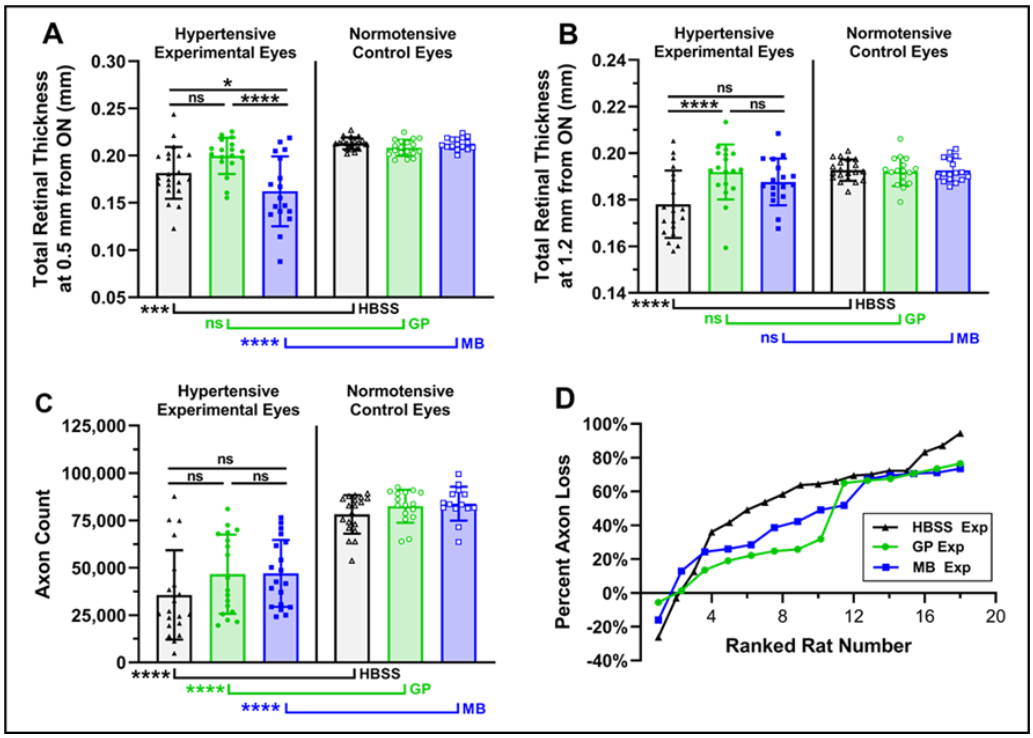

Figure 14: A) Total retinal thickness measured 0.5 mm from the ONH. Retinal thickness in hypertensive GP eyes was not different than in GP normotensive controls, while thickness in hypertensive HBSS eyes was significantly less than in HBSS normotensive controls. Thickness in hypertensive MB eyes was less than in hypertensive GP and HBSS eyes. B) Total retinal thickness measured 1.2 mm from the ONH. Thicknesses in both GP- and MB-treated hypertensive eyes were not significantly different from their respective contralateral eye (normotensive) thicknesses, while thickness in hypertensive HBSS-treated eyes was significantly less than in HBSS normotensive control eyes. Thickness in hypertensive GP eyes was significantly greater than in hypertensive HBSS-treated eyes, suggesting a protective effect of GP against retinal thinning. C) Axon counts derived from ON cross-sections showed no significant protective effects of crosslinking. D) Percent axon loss in hypertensive experimental eyes (compared to normotensive control) ranked by rat number from least to greatest axon loss suggests that axon loss is decreased in GP and MB treated eyes.

4.3.4 Axon Counts are not Preserved by Scleral Stiffening

We quantified optic nerve axons using a machine learning-based software package [170]. No significant differences were found between any hypertensive eye treatment groups (Figure 14C and Table 3), with adjusted mean axon counts of 78,900 and 39,400 axons in

HBSS normotensive and hypertensive eyes, respectively; 82,400 and 46,200 axons in GP normotensive and hypertensive eyes, respectively; and 83,700 and 45,500 axons in MB normotensive and hypertensive eyes, respectively. Axon count and axon density were both lower in hypertensive experimental eyes compared to their respective normotensive controls (all $p < 0.0001$,Table 3). Axon counts and axon density were also significantly correlated with IOP burden ($p < 0.001$, Table 14 and Figure 40). Representative optic nerve images in Figure 42 qualitatively show an increase in axonal damage with increased IOP burden. As alternative measures of RGC axon count, we calculated axon density (axon count divided by ON cross-sectional area). We observed no significant differences between any hypertensive eye treatment groups (Table 3) when considering axon density and ON cross-sectional area, nor a significant correlation with IOP burden (Table 14).

4.3.5 Eye Size Increased with IOP Burden

Eye size was measured to understand possible sources of glaucomatous damage and physiological differences compared to clinical glaucoma. Hypertensive experimental eyes were significantly larger than normotensive control eyes for all three crosslinking treatment groups, as measured by axial length, equatorial width, and anterior chamber depth (all $p < 0.05$,Table 3). Further, all eye size measurements were correlated with IOP burden ($p < 0.0001$, Table 15 and Figure 47). No significant differences in any eye size measurements were found between any hypertensive eye treatment groups. This increase of eye size differs from the situation in human adult glaucoma, where elevated IOP is not known to lead to ocular enlargement. However, other rodent models of OHT have observed similar findings of OHT-induced globe enlargement[5,198].

4.3.6 Visual Function is not Preserved by Scleral Stiffening

Spatial frequency and contrast sensitivity thresholds were measured to assess possible preservation of visual function due to crosslinking treatment. No significant differences were found between mean resolved spatial frequencies of any hypertensive eye treatment groups. Spatial frequency and contrast sensitivity thresholds were significantly decreased in hypertensive experimental eyes compared to normotensive control eyes for all three crosslinking treatment groups ($p < 0.0001$,Figure 3). Both spatial frequency and contrast sensitivity were significantly correlated with IOP burden ($p < 0.0001$, Table 14). Hypertensive eye spatial frequency and contrast sensitivity were not significantly different for comparisons between crosslinking treatment groups

4.3.7 RGC Function is not Preserved by Scleral Stiffening

No significant differences in mean pSTR, nSTR, b-wave, nor oscillatory potential 3 (Figure 15Figure 15C-F) amplitudes were found between any hypertensive eye treatment groups (Table 3). Significant decreases in mean pSTR, nSTR, b-wave, and oscillatory potential 3 amplitudes were observed in hypertensive experimental eyes compared to normotensive control eyes for all three crosslinking treatment groups (all $p < 0.05$,Table 3). pSTR and Oscillatory potential 3 amplitudes were significantly correlated with IOP burden ($p < 0.05$, Table 14 and Figure 46). Hypertensive eye ERG outcomes were not significantly different for comparisons between crosslinking treatment groups, indicating that our treatments did not protect against RGC functional loss.

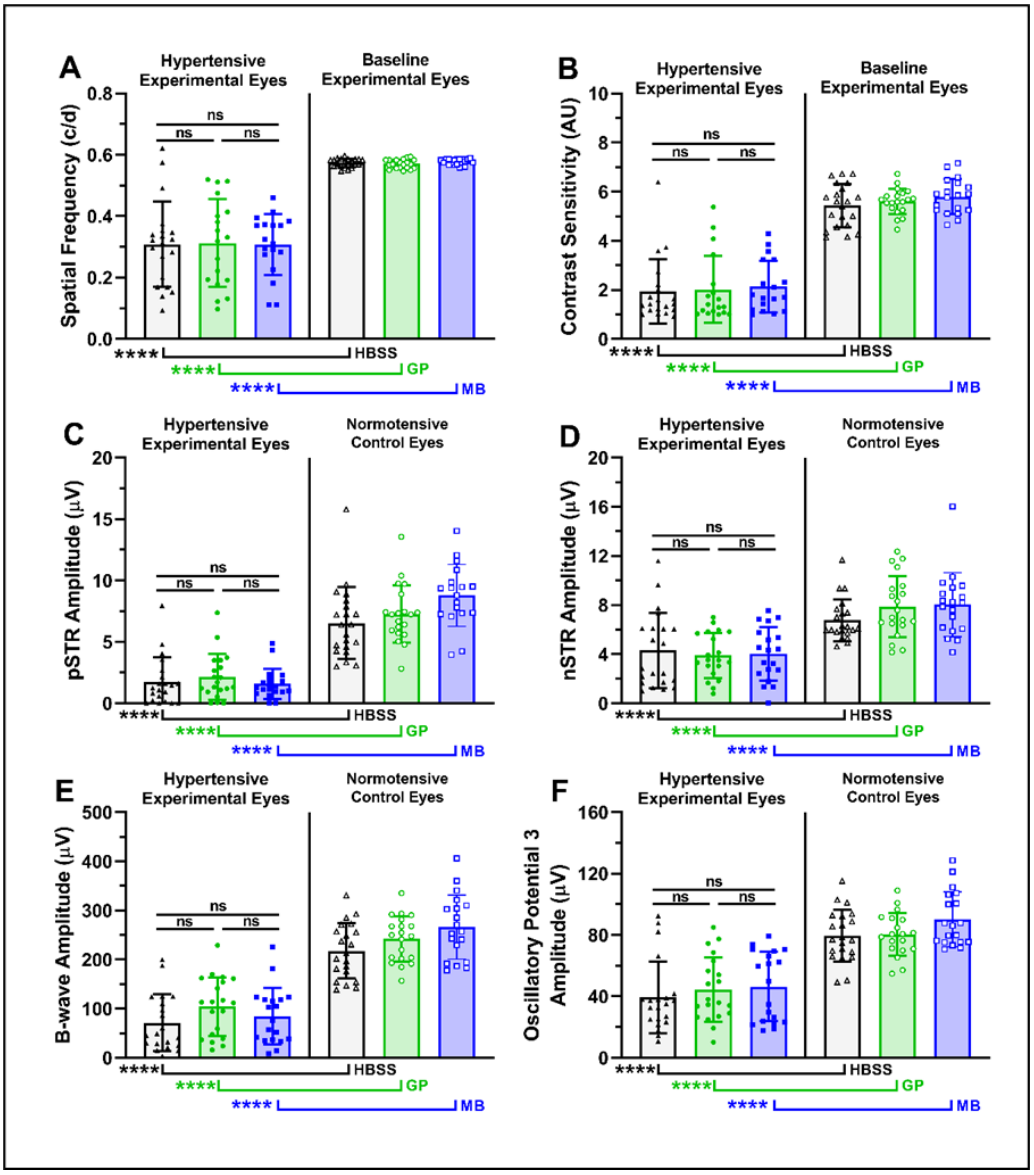

Figure 15: Functional outcome measurements across crosslinking treatment groups. We show OMR measurement outcomes, namely A) spatial frequency and B) contrast sensitivity; and ERG outcomes, namely C) pSTR amplitude, D) nSTR amplitude, E) b-wave amplitude, and F) oscillatory potential 3 amplitude. In all cases, a significant deficit was observed for hypertensive experimental eyes compared to normotensive control eyes. No significant differences were found between hypertensive eye treatment groups. These data indicate crosslinking did not preserve visual acuity or retinal function as measured by OMR and ERG.

4.3.8 Outcome Parameter Correlation Trends Differ by Treatment

Parameters measured in the study were cross correlated to detect associations between biomechanical, morphological, and functional outcomes within treatment groups, and differences in these associations across treatment groups (Figure 16). We found that the strength of associations (either positive or negative) were different between groups, with ranking HBSS > GP > MB (ranked stronger to weaker). This was particularly evident for the comparison of morphological and functional outcomes with biomechanical insult. We believe this indicates that either: (1) MB treatment generally reduced the impact of biomechanical insult on morphological and functional outcomes, or (2) that MB-treated eyes experienced greater variability in the relationship between functional/morphological outcomes and mechanical insult, leading to the observed weaker correlation.

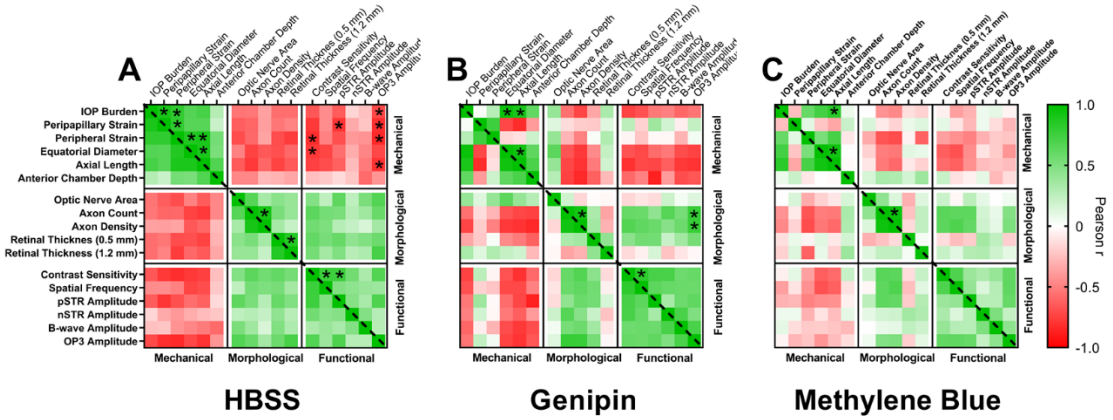

Figure 16: Parameters measured in hypertensive rat eyes were cross correlated and organized by mechanical, morphological, and functional categories for each crosslinking treatment. Stronger correlations were found for HBSS than for GP-treated rats, and for GP-treated rats compared to MB-treated rats, particularly in the relationship between morphological/functional with biomechanical parameters. Mechanical parameters included IOP burden, scleral strain, and eye dimensions. Morphological parameters include optic nerve size, axon count/density, and retinal thickness. Functional parameters include OMR and ERG data. A) HBSS hypertensive experimental eye matrix. B) GP hypertensive experimental eye matrix. C) MB hypertensive experimental eye matrix. Statistical significance was calculated for null hypothesis of zero correlation (significance indicated with "*" for the Bonferroni-corrected $p<0.05$ level).

4.4 Discussion

We assessed the effects of peripapillary (targeted) scleral stiffening and whole-globe scleral stiffening on glaucomatous outcomes in a microbead model of ocular hypertension in rats. We successfully stiffened the sclera, as confirmed by inflation testing of whole globes, and, as expected, we observed significant changes in morphological and functional outcomes in hypertensive eyes compared to normotensive eyes.

In general, we did not observe significant protective effects of scleral stiffening on retinal ganglion cell function as measured by ERG, nor on visual function as measured by spatial

frequency or contrast sensitivity. Further, we did not observe a significant preservation of retinal ganglion cell axons by scleral stiffening. However, we did observe preservation of retinal thickness at 1.2 mm from the ONH in GP-treated eyes compared to HBSS treated eyes (although not in MB-treated eyes), suggesting that stiffening may confer some protective effects against hypertension-induced morphological changes in the retina. We conclude that scleral crosslinking did not preserve retinal or visual function but might slow the progression of morphological glaucomatous damage. Importantly, we saw no evidence to conclude that scleral stiffening worsens glaucomatous damage, in contrast to a previous report[5].

4.4.1 Toxicity of Crosslinking Treatments May Have Contributed to RGC Loss

We have previously evaluated the toxicity of HBSS, GP, and MB treatments in healthy rats at 4 weeks, 4 weeks, and 6 weeks (respectively) following injections. The average axon losses in these cohorts, compared to untreated controls, were 0%, 8%, and 24% for HBSS, GP, and MB respectively. Additionally, deficits in retinal function as measured by ERG were observed in MB-treated rats. In the current study, we observed deficits in visual function measured by OMR seven days following crosslinking treatments, but prior to microbead injections (Figure 39). Thus, GP and MB-treatments have inherent toxicity in the absence of ocular hypertension, which likely accounts for some of the damage observed in this study. With this understanding, one could interpret a finding of no difference in axon counts between stiffened eyes and sham-treated eyes as indicating protection by scleral stiffening against IOP-induced axon loss, which was offset by inherent toxicity of the stiffening agent. Indeed, there was a trend (that did not reach statistical significance) of axon preservation in GP- and MB-treated eyes, suggesting some inherent benefit of

stiffening due to IOP-induced axon loss. Unfortunately, it is difficult to statistically separate the contributions of treatment toxicity and hypertension-induced damage, and thus we cannot make definitive conclusions in this regard.

4.4.2 Limitations of the Microbead Model Complicate Interpretation of Results

Intracameral delivery of microbeads may be associated with some inflammation which could lead to retinal/RGC axon injury. It was thus of interest to estimate microbead procedure "toxicity", which we did by extrapolating axon counts in low-IOP burden rats. More specifically, the y-intercept of the linear axon loss regression versus IOP burden can be considered to yield an estimated value of axon loss due to the microbead procedure alone without IOP elevation. These y-intercepts for the hypertensive HBSS, GP, and MB groups were 69,400 ± 14,000, 68,000 ± 9,000, and 62,300 ± 9,100 axons, respectively, which can be compared to average axon count values for normotensive controls in our study of 78,100 ± 7,200, 82,400 ± 4,700, and 83,800 ± 7,400 axons, respectively. Comparing the axon counts in low IOP burden rats to those of the normotensive controls, we estimate axon losses of 11% for HBSS, 17% for GP, and 26% for MB rats due to the crosslinking and microbead injections alone. These values are higher than the losses due to crosslinking treatment alone which were 0%, 8%, and 24% for HBSS, GP, and MB, respectively. Subtracting axon losses due to crosslinking toxicity alone from axon losses calculated in this study at low IOP burden, we find losses due to microbead treatment to be 11%, 9%, and 2% for HBSS, GP, and MB treatments. These data support the hypothesis that the microbead procedure itself in Brown Norway rats leads to some axon loss, in an IOP-independent manner.

In interpreting our results, it is important to recall that the model of ocular hypertension that we used caused rapid and large pressure elevations after microbead delivery, representing a severe challenge compared to a typical IOP history seen in open-angle glaucoma. In other words, the biomechanical insult seen in our study was perhaps more severe than would be observed clinically. Furthermore, our 14-day study duration was far shorter than time scales in open-angle glaucoma with OHT, so that adaptive responses such as collagen remodeling in the sclera would have had less chance to take effect in our study. Therefore, we interpret the results of our study to conservatively support the conclusion that scleral stiffening does not worsen glaucomatous damage and may confer some protection against aggressive mechanical insult.

4.4.3 Scleral Stiffening May Protect Against Morphological, but not Functional RGC Damage

Interestingly, we did not observe functional protection due to crosslinking, yet did observe some evidence of structural protection (retinal thickness preservation, a trend towards RGC axon preservation). Previously it has been shown that axon loss precedes retinal thinning, which may explain the relatively large deficit in axon count observed compared to the more minor retinal thinning in our study [209]. We attribute the loss of retinal thickness in MB eyes at 0.5 mm distance from the ONH to localized toxicity of the photocrosslinking procedure. Recall that the region 0.5 – 1.0 mm from the ONH was selectively targeted for treatment in these eyes, likely inducing more damage at 0.5 mm than at 1.2mm. Another interpretation of this result is the potential of retinal edema which would balance out the loss of RGCs. However, histological analysis of the retina after GP and MB treatment alone did not show any signs of retinal edema (data not shown).

It should be noted that our OCT measurements are of total retinal thickness because we could not confidently resolve the retinal nerve fiber layer in our imaging. However, we suspect our measurement of total retinal thinning at both locations (0.5 mm and 1.2 mm from the ONH) was caused in part by retinal nerve fiber layer thinning since we also observed significant loss of RGC axons (Figure 14C) and RGC function (Figure 15C-F) in HBSS hypertensive experimental eyes compared to normotensive controls.

Although we did not observe any significant differences in RGC axon counts among hypertensive experimental eyes treated with GP or MB compared to HBSS eyes, we did see a trend towards preservation of axons with both treatments (Figure 14C). We hypothesize that over the short timescale of our experiment (14 days) RGC bodies were still present in the retina despite RGC axonal death, which explains why we saw preservation of the retinal thickness, but not RGC axon counts.

Although our ERG results suggest a loss of RGC function across all treatment groups, differences were not seen between HBSS and GP or MB groups, suggesting that variability in the ERG and OMR data was large compared to effect size, thus yielding statistically insignificant differences. Functional outcomes are perhaps most relevant to clinical translation irrespective of morphological changes. Although we observed some protection against retinal thinning, we hypothesize that remaining RGCs had impaired function which may indicate scleral stiffening can slow the progression of glaucomatous damage.

4.4.4 We Were Able to Successfully Stiffen the Posterior Sclera with Both Targeted and Non-targeted Treatments

Scleral strain measured post mortem by whole globe inflation testing confirmed successful targeted peripapillary stiffening with MB and whole sclera stiffening with GP. We observed increasing strain values (decreased stiffness) with increasing IOP burden in HBSS eyes, indicating weakening of the sclera under hypertensive conditions in this study. These effects have been observed on short time scales previously [210].

An unexpected observation in this study was the apparent similarity in measured strain values of HBSS eyes with those of GP and MB treated eyes at low IOP burdens. We have previously shown that MB and GP treatments reduce scleral strain significantly compared to HBSS in healthy rats. Since microbead-treated rats experiencing low IOP burdens should have scleral mechanical properties comparable to those of healthy rats, the observed similarity is difficult to explain. This observed effect could be an artifact of low sample (n = 2) size when only considering low IOP burden values, or due to inflammatory processes associated with the microbead model as discussed above.

4.4.5 Key Differences Exist Between This Study and a Similar Previous Study

It is of interest to compare our results with those of the related study of Kimball et al. To stiffen the sclera, Kimball et al. used glyceraldehyde in 100 mM sodium phosphate (Na3PO4), the latter having an osmolarity of 400 mOsm[5]. After addition of 500 mM glyceraldehyde, the solution's final osmolarity would have been 900 mOsm, well in excess of the physiological osmolarity of 285-295 mOsm [47]. Therefore, some of the axon loss observed may be attributed to hyperosmolarity of the injection solution.

Additionally, Kimball et. al did not assess any functional or morphological outcomes in glaucomatous eyes. We have expanded upon this previous research by including assessments of visual function (OMR), retinal function (ERG), and retinal thickness (OCT), helping to paint a more complete picture of the effects of scleral stiffening on clinically relevant outcomes.

4.5 Conclusion

Neither targeted peripapillary nor non-targeted posterior scleral stiffening worsened morphological and functional outcomes in a glaucomatous rat model. We found a modest potential preservation of total retinal thickness by genipin-induced scleral stiffening. Interpretation of these results is hindered by drawbacks of the microbead model of ocular hypertension (high variability, some inherent retinal toxicity). Further research is needed to investigate the impact of scleral stiffening on glaucomatous damage.

CHAPTER 5. THEORETICAL COMPUTATIONAL MODEL FOR COLLAGEN PHOTOCROSSLINKING IN THE EYE

Note on Contribution: Data presented in this chapter were made possible by contributions from colleagues including Afsane Radmand who contributed to model development. Lauren Nichols collected data and calculated the diffusion constant of methylene blue in rat sclerae. Additionally, she assisted in collecting data pertaining to the study of methylene blue distribution in retrobulbar tissues. Amir Hejri assisted with experiments involved in calculating the diffusion constant of methylene blue in rat sclerae.

5.1 Abstract

Scleral photocrosslinking is increasingly investigated for treatment of myopia and glaucoma. In this study a computational model was developed to predict crosslinking efficiency of visible/NIR photosensitizers in the sclera. Photocrosslinking was validated against riboflavin corneal crosslinking experimental studies and subsequently modeled for the sensitizer, methylene blue, administered by retrobulbar injection to the posterior sclera and irradiated with a transpupillary light beam. Optimal ranges were determined for treatment parameters including light intensity, methylene blue concentration, injection volume, and inspired oxygen concentration. Additionally, sensitivity of crosslinking to various parameters was quantified. The most sensitive parameters (in order of greatest to least sensitive) were tissue parameters (including scleral thickness and choroidal melanin concentration), treatment parameters (including treatment duration and inspired oxygen concentration), and sensitizer parameters (including triplet quantum yield).

5.2 Introduction

Glaucoma is the leading cause of irreversible blindness in the industrialized world affecting approximately 80 million individuals[1]. It is an optic neuropathy sensitive to elevated intraocular pressure resulting in retinal ganglion cell death leading to vision loss[32]. Specifically, pressure-induced strain at the optic nerve head mediated by tissue biomechanical properties causes retinal ganglion cell apoptosis[44–46]. Therefore, it is desirable to develop strategies to reduce optic nerve head strain. Recently, it has been shown that peripapillary scleral stiffening resulted in strain reduction at the optic nerve head in *ex vivo* porcine eyes, suggesting that peripapillary scleral stiffening may be a strategy to prevent retinal ganglion cell loss in glaucoma[4]. We have developed a photocrosslinking technique to selectively stiffen the peripapillary sclera *in vivo* using methylene blue excited by red light at 660 nm. In this study, we present a computational model to identify conditions which enable safe and effective scleral photocrosslinking with methylene blue and red light.

To develop this model, we identified prior experimental ocular collagen crosslinking studies and found that there are multiple scenarios where changes in ocular tissue mechanical properties are implicated in disease. In addition to glaucoma, these include keratoconus and myopia[211,212]. Keratoconus prevalence is estimated to range between 0.0003% and 2.3% of the population depending on geographic region studied. The condition is characterized by weakening of the cornea leading to refractive errors[213–215]. Myopia affects 1.4 billion people worldwide and is characterized by elongation of the globe, resulting in refractive errors, and in severe cases, retinal detachment, choroidal neovascularization, and glaucoma[216–221]. Glaucoma is the second leading cause of

blindness in the world, and disease progression is believed to be linked to mechanical deformation of the lamina cribrosa and peripapillary sclera[154,222].

Photoinduced crosslinking has been increasingly studied since the early 2000s as a method for modulating tissue mechanical properties by strengthening collagenous tissues *in vivo*[223,224]. We have recently shown that transpupillary activation of methylene blue (MB) stiffens rat sclerae *in vivo* and therefore may be a viable future stiffening strategy for treatment of glaucoma and myopia. Clinically, riboflavin corneal crosslinking is an FDA-approved procedure for treatment of keratoconus[225].riboflavin's absorbance of UV light results in crosslinking through either direct interaction of riboflavin excited state triplets with collagen amino acids or through generation of singlet oxygen which reacts with amino acids to form crosslinks[226,227]. On the other hand, photocrosslinking treatments for myopia are still in the research phase while only dark crosslinking has been investigated for glaucoma treatment[52,228]. To increase crosslinks, reduce treatment time, and improve safety profiles for riboflavin corneal crosslinking, experimental studies have aimed to optimize treatment parameters such as light intensity, crosslinker concentration, and irradiation duration[229–231].

Riboflavin crosslinking is known to follow complex reaction dynamics involving the sensitizer molecule, oxygen, and collagen substrate[129,227]. Riboflavin may react with collagen through two different pathways (type I and type II) distinguished by the absence or presence of singlet oxygen[62,70]. The type I mechanism involves direct interaction of excited state sensitizer triplets with collagen amino acids, resulting in radical-mediated crosslinking. The type II mechanism is characterized by energy transfer from the excited riboflavin triplet to oxygen, producing singlet oxygen which reacts with collagen amino

acids. Exact mechanisms for each pathway have been a subject of great interest, and the relative importance of each pathway has been the subject of much debate.

Computational models can be used to predict optimal crosslinking parameters used for clinical or research photocrosslinking applications. These models incorporate elements of light transmission/absorbance, chemical reactions, and diffusion of molecular species[129,130,148,232]. To date, extensive modeling has been performed for riboflavin corneal crosslinking, aided by the abundance of experimental data against which models may be validated. Experimental studies provide valuable test cases for validation of experimental models. Such studies are available primarily from riboflavin crosslinking literature and have investigated riboflavin and oxygen concentrations *in situ* during treatment and mechanical stiffness of the cornea after treatment[129,146,176,177].

Towards development of efficient posterior scleral photocrosslinking strategies, we modeled transpupillary illumination of visible/NIR sensitizers delivered to the posterior sclera by retrobulbar injection. In this approach, sensitizers may be delivered to the posterior sclera by retrobulbar, sub-Tenon, or suprachoroidal injection. From any of these injection spaces, sensitizer molecules passively diffuse to the sclera in similar fashion to the diffusion of riboflavin into the corneal stroma during riboflavin crosslinking procedures. Subsequently, a light beam may be directed through the cornea/intraocular media to the sclera after passing through the retina, retinal pigmented epithelium, and choroid. We believe this transpupillary illumination approach holds promise for posterior photocrosslinking especially in light of recent advances in efficiency of posterior ocular drug delivery strategies[233,234].

While riboflavin is a valuable sensitizer for corneal crosslinking, its use in the posterior sclera is limited due to the need to deliver light externally through more invasive surgical techniques and waveguides[158,228,235]. A transpupillary approach, on the other hand, would be inefficient for riboflavin excitation both due to toxicity concerns at the retina and energy absorbance in the cornea. However, for red to near infrared wavelengths, an optical phenomenon exists whereby biological tissues have reduced absorbance at 650-800nm wavelengths compared to surrounding wavelengths[67]. This optical window, we believe, makes possible transpupillary illumination of photosensitizers delivered to the sclera. A critical uncertainty exists as to whether light may pass sufficiently through the highly melanized retinal pigmented epithelium and choroid to satisfy crosslinking requirements in the sclera. While intensity may be increased, photothermal damage to the retina and retinal pigment epithelium (RPE) is a concern. Another constraint is the presumably rapid clearance of sensitizer from the extraocular tissues upon injection. The proper combination of light intensity, sensitizer concentration, oxygen concentration, excitation wavelength, and sensitizer molecule may enable scleral photocrosslinking with a transpupillary excitation beam despite these constraints.

In this study, we developed a computational model to predict the efficiency of visible/NIR sensitizers for posterior scleral photocrosslinking. Specifically, we investigated the sensitizer MB delivered to the sclera by means of a retrobulbar injection. We first tested our model against existing riboflavin crosslinking literature data to confirm validity of the underlying model dynamics. Subsequently, we exchanged cornea/riboflavin-specific parameters for parameters of MB which efficiently absorbs red photons. Mass transport parameters for sensitizer diffusion after injection in the retrobulbar space were validated

experimentally in rats, as they can be expected to differ from those of topical delivery as in the case of riboflavin crosslinking.

5.3 Materials and Methods

5.3.1 Experimental Quantification of MB Distribution in Rat Eye Tissues after Retrobulbar Injection

Brown Norway male retired breeder rats aged 6-12 months (Charles River Laboratories, Wilmington, MA) were placed under anesthesia with 5% isoflurane gas and 800mL/min oxygen flow rate. Topical anesthetic eye drops (Tetracaine Hydrochloride Ophthalmic Solution, Amici Pharmaceuticals, Melville, NY) were administered bilaterally followed by 1% tropicamide eye drops (Tropicamide Ophthalmic Solution, Henry Schein, Melville, New York) administered bilaterally to induce pupillary dilation, thus replicating the conditions for scleral photocrosslinking procedures using a transpupillary light administration approach.

A 30 mM solution of MB (Apollo Scientific, Stockport, UK) dissolved in Hank's balanced salt solution was prepared by warming the solution to 100 °C and allowing the solution to cool to room temperature (20 – 25 °C). After inducing anesthesia, a 100 μL volume of 30 mM MB was administered by means of retrobulbar injection unilaterally with 100 μL of Hank's balanced salt solution (HBSS) administered similarly as a control in the contralateral eye using 0.3 mL volume, 31G insulin syringes/needles (BD Insulin Syringes with BD Ultra-Fine™ needle, Becton, Dickinson and Company, Franklin Lakes, NJ). Anesthesia was maintained for 30 minutes after which the rat was euthanized by inhalation of 100% CO_2. All procedures involving animals were approved by the Georgia Institute of

Technology Institutional Animal Care and Use Committee (IACUC) and complied with the ARVO statement for the Use of Animals in Ophthalmic and Vision Research.

Immediately after euthanasia, eyes were enucleated and dissected with tissues individually distributed into centrifuge tubes containing 2 mL radioimmunoprecipitation assay (RIPA) lysis buffer. The tissues collected included 1) a 1 mm diameter scleral disk centered at the scleral canal, 2) a 2mm diameter scleral annulus centered at the scleral anal (less the 1 mm scleral disk), and 3) a 3 mm diameter scleral annulus centered at the scleral canal (less the 2 mm scleral annulus, all collected using biopsy punches, as well as 4) all remaining sclera not contained within 3 mm diameter of the scleral canal, and 5) the cornea, lens, vitreous, and retina (collectively termed "anterior globe" in this study).

The mass of each sample was determined gravimetrically and used to calculate the approximate volume of the collected tissue based on an assumed density of 1 g/cm^3. Each sample was then ultrasonicated for 1 min to disrupt tissue structures and thus facilitate MB release from the tissues into the lysis buffer. All samples were then allowed to rest, protected from light exposure, overnight (12-18 hours) before being centrifuged at 2400 RPM for 10 minutes. The supernatant was then collected, serially diluted on a 96-well plate, and MB fluorescence intensity was analyzed using a Synergy H4 plate reader (BioTek, Winooski, VT). Fluorescence intensity was converted to sample concentration based on a reference standard calibration curve included for each plate. Average concentration of MB in each tissue was derived from the mass of MB calculated for each sample divided by the volume.

5.3.2 Experimental Determination of MB Diffusion Constant in Rat Sclera

Brown Norway retired male breeder rats age 10-20 months (Charles River Laboratories, Wilmington, MA) were euthanized by exposure to 100% CO^2. The cornea, vitreous, and retina were removed from each eye immediately after enucleation. From each eye, four scleral samples of approximately equal size were taken, one each from the superior, inferior, temporal, and nasal quadrants. Scleral thickness was measured with calipers.

Glass Franz cells with an exposed circular tissue area of 3.14 mm^2 were modified to accommodate the scleral samples (3-5 mm diameter) by sandwiching the tissues between two glass microscope slides customized with a 2mm drilled hole in the center (Figure 17). Scleral samples were centered on the 2mm holes between two slides. A rubber O-ring was placed on the flat flange joint of the receiving and donor components of the Franz cell, and the drilled cover slips holding the tissue were centered between the O-rings in order to prevent leakage. The Franz cell was clamped together, and the receiving chamber was filled with phosphate-buffered saline (PBS). A 1 mL volume of 3 mM MB solution prepared in PBS was placed in the donor chamber of the Franz Cell.

The Franz cells were incubated at room temperature with a stir bar in the receiving chamber. For each scleral sample, 6 samples were taken from the receiving chamber at 1 h intervals, and the volume sampled was replenished with an equal volume of PBS. Collected samples were tested for MB concentration by spectrophotometry using a Synergy H4 plate reader (BioTek) with excitation set to 665nm and emission to 690nm. Diffusivity was calculated using Fick's First Law of Diffusion:

$$J = -D\frac{dC}{dx} \quad (7)$$

where J is the flux of MB across the sclera, C is the concentration of the diffusing MB, D is the diffusion constant of MB, and x is the distance over which diffusion occurs.

Upon testing, lag time was calculated and used to confirm that steady state diffusion had been achieved. Any sample that had not reached steady state during the procedure was excluded from analysis, as it would not have satisfied the conditions required to accurately measure the diffusion constant. A total of N = 9 samples were analyzed and mean diffusion constant and lag time were calculated.

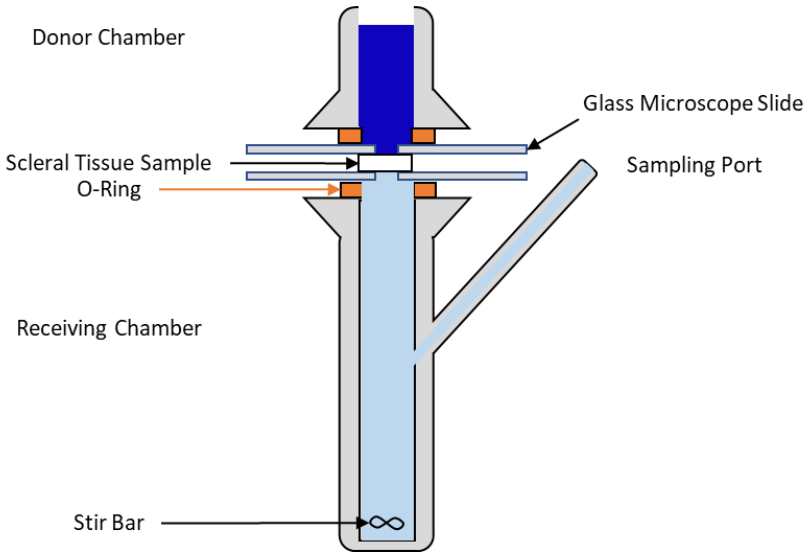

Figure 17 Schematic representation of Franz Cell apparatus used to determine MB diffusion constant through 3.14 mm surface area of Brown Norway rat sclerae. A 3 mM solution of MB was placed in the donor chamber for diffusion across the sclera and into the receiving chamber. The scleral samples were mounted between two glass microscope slides sealed with O-rings.

5.3.3 Model Validation Against Past Riboflavin Crosslinking Studies

We validated our model predictions by comparing with data from three different studies of riboflavin crosslinking found in the literature. In the first study, Kamaev et al. measured oxygen concentration during riboflavin crosslinking treatment in *ex vivo* porcine eyes[236]. Experimental conditions described in that study were inserted into our model, and oxygen concentration predicted by the model was compared against that measured by Kamaev et al. as a validation of transport kinetics and reaction dynamics predicted by the model. Because oxygen concentration changes are derived from the intertwined photochemical reactions, diffusion, and light absorbance phenomena, the ability of the model to predict the complex oxygen concentration profile in Kamaev et al. provides a holistic measure of model validity.

In the second study, Hammer et al. measured the change in stiffness in *ex vivo* porcine eyes treated with riboflavin crosslinking in accelerated and normal irradiation procedures[177]. In this study, light fluence was maintained at the traditional 5.4 J/cm^2 dose (i.e. that is commonly used in clinical corneal crosslinking). Intensity was varied over a range of three different intensities of 3, 9, and 18 mW/cm^2. Irradiation duration was adjusted(30, 10, and 5 min, respectively), to maintain identical fluence across experiments. Using these data, we calculated the percent increase in stiffness compared to untreated control from the reported raw stiffness values in the Hammer study and compared these values to our computational model predictions at the same experimental parameters. We represented crosslinking predicted by our model as a fraction of total possible crosslinking sites utilized and took this as a surrogate and proportional measure of scleral stiffness. Experimental conditions described in the Hammer study were inserted in our model, and percentage of

available sites crosslinked was generated and compared to the percentage increase in stiffness reported by Hammer et al.

In the third study, Aldahlawi et al. investigated riboflavin crosslinking using similar experimental conditions to those of Hammer et al., but evaluated crosslinking using enzymatic degradation by measuring the dry weight remaining after 12 days[237]. We compared our model to the raw values of corneal dry weight that they reported.

5.3.4 Theoretical Computational Model Structure

We developed a theoretical model employing the method of lines using the ordinary differential equation solver function ode15s in MATLAB software (MathWorks, Natick, MA). The model considered a one-dimensional thickness of tissue discretized into n finite segments (Figure 18) of width Δx with index i that was bounded on the left side by a reservoir of injected sensitizer solution in the retrobulbar space (or on the corneal surface) and bounded on the right side by the choroid (or the aqueous humor). Molecular diffusion, light propagation, and chemical reactions provided the physical bases for tracking crosslink formation over time and one-dimensional space.

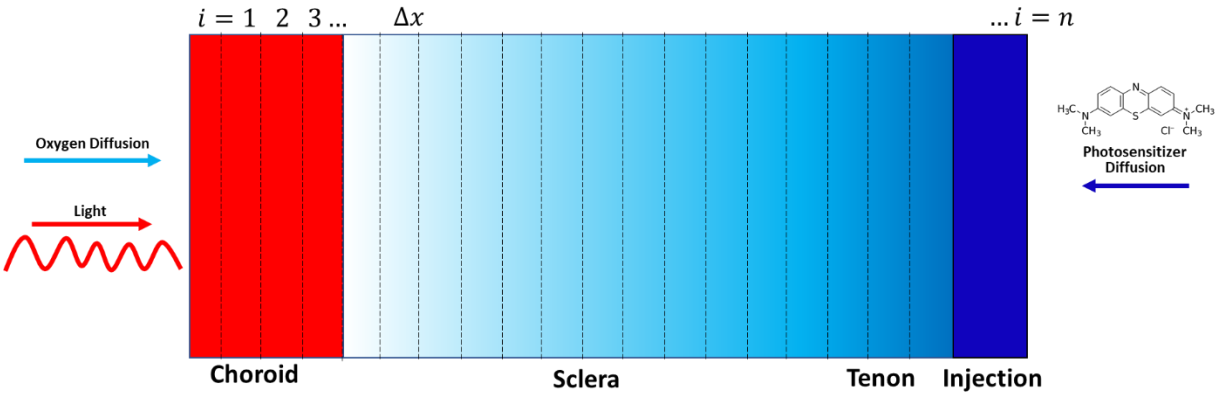

Figure 18: Schematic representation of the model spatial domain including (left to right): choroid, sclera, Tenon capsule, injection reservoir. Light enters through the anterior surface of the choroid from a transpupillary illuminating source. Oxygen diffuses from the choroid (and to a lesser extent, from the retrobulbar tissue). The photosensitizer diffuses from the injection reservoir to the Tenon capsule, sclera and choroid (where vascular clearance can occur) as well as to the retrobulbar tissue (not shown) which is assumed to be a sink due to systemic clearance. The model uses the method of lines to discretize a system of partial differential equations in space, thus creating a system of ordinary differential equations in time. Node thickness (Δx) was uniform in the choroid and in the sclera, and non-uniform in the injection reservoir.

5.3.5 Modeling Diffusion

5.3.5.1 Fick's Second Law and its Discretization

Diffusion was modeled according to Fick's Second Law:

$$\frac{\partial C}{\partial t} = \frac{\partial}{\partial x}\left(D\frac{\partial C}{\partial x}\right) \tag{8}$$

where C represents concentration of the diffusing species, D represents its diffusion constant, and x and t represent position and time, respectively. A finite difference approximation was used to reduce the diffusion equation to a set of ordinary differential equations by [238]:

$$\frac{dC_i}{dt} = D\,\frac{C_{i-1} - 2C_i + C_{i+1}}{\Delta x^2} \tag{9}$$

where C_i represents the concentration of the diffusing species (photosensitizer, oxygen) at the i^{th} node of the spatial domain.

5.3.5.2 Derivation of Discretized Fick's Second Law for Unequal Node Spacing

To accommodate constraints modeling various tissue thicknesses on finite intervals as well as different diffusion constants between adjacent nodes, a modified form of equation (2) was employed which does not assume equal node distances or diffusivities. Unequal node spacing was accommodated using a rectangle approximation (adapted from the trapezoid approximation)[239]. Unequal diffusion constants were handled by calculating the harmonic mean of diffusion constants between adjacent nodes[240]. . To implement the rectangle approximation, we defined the distance between the i^{th} node and adjacent nodes as h_1 and h_2 where h_1 is the distance between the i^{th} and$(i+1)^{th}$ nodes and h_2 is the distance between the i^{th} and $(i-1)^{th}$ nodes (Figure 19).

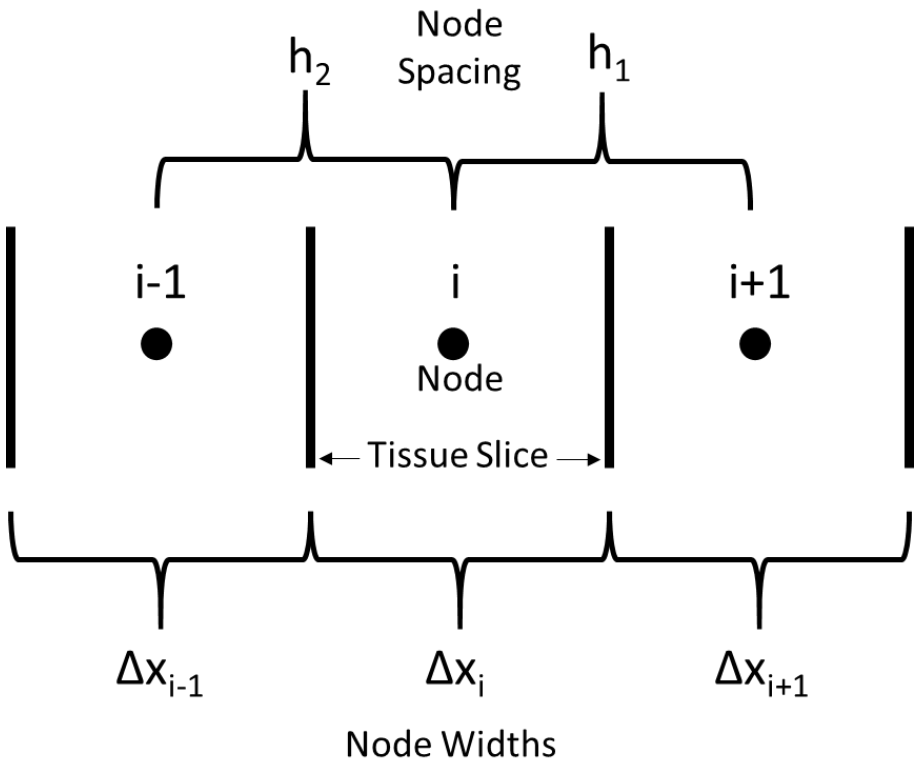

Figure 19: Schematic representation of the 1-dimensional tissue discretization scheme showing three adjacent tissue slices of finite thickness, Δx. The i^{th} node with $(i-1)^{th}$ and $(i+1)^{th}$ nodes are shown at left and right, respectively. Nodes were defined at the center of each tissue slice. Node spacings represented by h_1 and h_2 were allowed to vary as a function of tissue slice thickness in the model. Unequal node spacing was used to reduce computation time and provide increased spatial resolution in tissues of interest (sclera, choroid).

The values of h_1 and h_2 may be expressed in terms of the node widths:

$$h_1 = \frac{\Delta x_i + \Delta x_{i+1}}{2} \tag{10}$$

$$h_2 = \frac{\Delta x_i + \Delta x_{i-1}}{2} \tag{11}$$

where Δx_{i-1}, Δx_i, and Δx_{i+1} are the widths of the $(i-1)^{th}$, i^{th}, and $(i+1)^{th}$ nodes, respectively. In order to additionally account for unequal diffusion constants between nodes, we elected to use the harmonic mean for the values of D such that:

$$D_1 = \frac{2D_i D_{i-1}}{D_i + D_{i-1}} \tag{12}$$

$$D_2 = \frac{2D_i D_{i+1}}{D_i + D_{i+1}} \tag{13}$$

such that D_1 and D_2 represent the diffusivities between the i^{th} and $(i+1)^{th}$ or $(i-1)^{th}$ tissue slices, respectively. The resulting discretized first order derivative accounting for unequal node spacing and unequal diffusion constants is:

$$D\frac{\partial C}{\partial x} at\ x + h_2 = D_2 \frac{(C_{i+1} - C_i)}{h_2} \tag{14}$$

$$D\frac{\partial C}{\partial x} at\ x - h_1 = D_1 \frac{(C_i - C_{i-1})}{h_1} \tag{15}$$

where h and D are defined as previously stated above. The second order derivative is therefore:

$$D\frac{\partial^2 C}{\partial x^2} = \frac{1}{\frac{h_1 + h_2}{2}}\left(D_2 \frac{\partial C}{\partial x} at\ x + h_2 - D_1 \frac{\partial C}{\partial x} at\ x - h_1\right) \tag{16}$$

$$D\frac{\partial^2 C}{\partial x^2} = \frac{2}{h_1 + h_2}\left(D_2\frac{(C_{i+1} - C_i)}{h_2} - D_1\frac{(C_i - C_{i-1})}{h_1}\right) \quad (17)$$

where the left and right sides of Eq (17) represents the continuous and discretized forms of the second order derivative, respectively. Substitution of Eqs (10, 11, 12, 13) into Eq (17) results in the final discretized form of Fick's Second Law used in this study. Table 4 shows the Dirichlet boundary conditions chosen for each diffusing species used to satisfy Eq (17).

5.3.6 Modeling Sensitizer Dimerization

Photosensitizers are known to readily dimerize or form higher order aggregates[140,241–243]. We assumed bimolecular dimerization with dimerization constant, K_d:

$$K_d = \frac{[M][M]}{[D]} \quad (18)$$

where $[M]$ and $[D]$ are the monomer and dimer concentrations of the sensitizer, respectively. The concentration of monomer or dimer can be calculated as a function of the total sensitizer concentration that would occur if all molecules were in the monomer form, $[S]$, by substituting Eq (18) with the following equation for total concentration (based on stoichiometry):

$$[S] = [M] + 2[D] \quad (19)$$

Combining Eqs. (18) and (19) yields a quadratic equation with roots:

$$[M] = \frac{-1 + \sqrt{1 + 8K_d[S]}}{4K_d} \tag{20}$$

$$[D] = [S] - \frac{-1 + \sqrt{1 + 8K_d[S]}}{8K_d} \tag{21}$$

5.3.7 Boundary Conditions and Initial Conditions

Boundary conditions were defined at the leftmost and rightmost nodes which represented the anterior surface of the choroid and the posterior surface of the retrobulbar tissue, respectively (Table 4). The choroid and retrobulbar tissues were assumed to act as sinks for MB and singlet oxygen. Note, singlet oxygen was modelled as a diffusing species and therefore was modelled with boundary conditions identical to MB. Triplet oxygen was modelled with constant concentration source boundary conditions defined according to literature derived values (Table 16)[244]. Finally, light intensity was assumed to be constant entering the leftmost node to simulate a transpupillary beam of light used for photoexcitation of MB.

Initial conditions were defined at the moment of retrobulbar injection of MB at which point photons from the light source were also first introduced (Table 5). MB concentration therefore was 0 M in the tissues and equal to the injection concentration in the reservoir. Light intensity was 0 mW/cm2. As a result of having no MB or light in the tissue at the initial state, initial concentrations of excited state species (singlet oxygen and triplet MB) were set to 0 M. The initial concentration of triplet oxygen was assumed to have a linear profile over the choroid, sclera, and tenon capsule with the values at each boundary equal

to those defined in Table 4. Concentration of triplet oxygen in the reservoir was assumed to be that of atmospheric oxygen. Initial concentrations of amino acids and melanin were derived from literature (see Table 12 for values used in this study and Table 19 and Table 20 for values pertaining to other species).

Table 4: Boundary conditions for MB scleral photocrosslinking. C is the concentration of a given species. C_R and C_L represent the specific literature derived values for triplet oxygen concentration at the right and left boundaries, respectively. I represents light intensity, and I_0 represents the specific value of light source intensity incident on the retinal surface.

Species	**Right BC**	**Left BC**	**Justification**
Sensitizer*	$C = 0$	$C = 0$	Right BC: The retrobulbar tissue is assumed to act as a perfect sink, clearing MB systemically**. Left BC: The anterior (left) boundary of the choroid is assumed to act as a perfect sink, clearing MB systemically.
Triplet Oxygen†	$C = C_L$	$C = C_R$	Right BC: The choroid provides continuous replenishment of oxygen due to its heavy vascularization Left BC: Heavily vascularized retrobulbar tissues supply oxygen to the posterior sclera
Light	–	$I = I_0$	Left BC: Light source intensity is constant

* The boundary conditions for sensitizer applied to both ground state and triplet excited state species as well as for singlet oxygen.
** We assumed the retrobulbar tissue is a perfect sink, though the extent of clearance is uncertain. Our experimental studies (Figure 25) support this assumption.
† Triplet oxygen represents the form of oxygen most commonly found in the atmosphere (as opposed to singlet oxygen produced by photochemical reaction, which is accounted for separately).

Table 5: Initial conditions for MB scleral photocrosslinking. C is concentration of the respective species, $C_{0\ MB}$ is the initial total concentration of MB molecules if each molecule were in the monomeric state, and C_R and C_L are the concentrations of triplet oxygen at the right and left boundaries, respectively, and $C_{0\ (AA)}$ represents the specific value of a particular amino acid (denoted by AA). K_D is the dimerization equilibrium constant of MB. $X_{Choroid,}$ X_{Sclera} and X_{Tenon} are the thicknesses of the choroid, sclera, and Tenon tissues, respectively. Finally, x is the distance through the tissue with x = 0 defined at the left boundary and x equal to the sum of the tissue and reservoir layer thicknesses at the right boundary.

Species	**Domain**	**Value**	**Justification**
Sensitizer (Monomer)	Reservoir	$C = \frac{-1 + \sqrt{1 + 8K_d(C_{0\,MB})}}{4K_d}$	Initial concentration in reservoir is that of the injected MB
Sensitizer (Dimer)	Reservoir	$C = C_{0\,MB} - \frac{-1 + \sqrt{1 + 8K_d(C_{0\,MB})}}{8K_d}$	Initial concentration in reservoir is that of the injected MB
Triplet Oxygen	Choroid, Sclera, Tenon capsule	$C = \frac{C_R - C_L}{X_{choroid} + X_{sclera} + X_{Tenon}} \times x$	The choroid and retrobulbar tissues supply oxygen to the sclera
Amino Acids	Choroid, Sclera, Tenon capsule	$C = C_{0\,(AA)}$	AA concentration is constant throughout Tenon capsule, sclera, and choroid.

5.3.8 Modeling Light Absorbance by Sensitizer

Absorption of photons was modeled according to the Beer-Lambert Law:

$$\frac{dI}{dx} = -IC\varepsilon \tag{22}$$

where I is light intensity and C and ε are the concentration and molar absorptivity of light-absorbing species, respectively. Eq. (23) is applicable for species having known

concentration and molar absorptivity. Our model specifically accounts for light absorbance by monomeric MB, dimeric MB, melanin, and absorbance by the tissue. The Beer-Lambert Law accounting for these absorbers becomes:

$$\frac{dI}{dx} = -IC_M\varepsilon_M - IC_D\varepsilon_D - IC_{Mel}\varepsilon_{Mel} - I\mu \tag{23}$$

where C_M and ε_M are the concentration and molar absorptivity of monomeric MB, respectively, C_D and ε_D are the concentration and molar absorptivity of dimeric MB, respectively, C_{Mel} and ε_{Mel} are the concentration and molar absorptivity of melanin, respectively, and μ is the linear attenuation coefficient of the tissue. To calculate the generation rate of excited tripletMB, light intensity was converted to photon flux by:

$$\frac{dp}{dt} = \frac{I}{E} \tag{24}$$

where p is the number of photons, E is the energy of a single photon which may be expressed as a function of Planck's constant, h, the speed of light, c, and photon wavelength, λ:

$$E = \frac{hc}{\lambda} \tag{25}$$

Thus, after substitution, photon flux is represented in units of moles per second as:

$$\frac{dp}{dt} = \frac{I\lambda}{Ahc} \tag{26}$$

where A is Avogadro's number. The fraction of photons absorbed by MB at any finite segment was assumed to be equal to MB's absorbance as a fraction of total absorbance of all species in that segment:

$$f_{abs} = \frac{\varepsilon_M C_i \Delta x}{\varepsilon_M C_i \Delta x + \varepsilon_D C_i \Delta x + \varepsilon_{Mel} C_i \Delta x + \mu \Delta x} \tag{27}$$

$$f_{abs} = \frac{\varepsilon_M C_i}{\varepsilon_M C_i + \varepsilon_D C_i + \varepsilon_{Mel} C_i + \mu} \tag{28}$$

Therefore, by combining Eqs. (26) and (27), the rate of formation of triplet MB is:

$$\frac{d[^3MB]}{dt} = \phi_T f_{abs} \frac{dp}{dt} = \phi_T \frac{\varepsilon C_i}{\varepsilon C_i + \varepsilon C_i + \varepsilon_{Mel} C_i + \mu} \left(\frac{\Delta I_i \lambda}{Ahc}\right) \tag{29}$$

where ϕ_T is the triplet quantum yield. We assumed that absorbance of a photon by monomeric MB exclusively would result in a triplet state MB molecule. Absorbance of photons by dimeric MB was assumed to result in quenching without generation of a triplet excited state capable of generating singlet oxygen.

The reduction in intensity of light passing through at a spatial segment, ΔI_i, depends upon absorbance in each upstream segment in the beam path, which is transient due to diffusion of absorbing species. Therefore, the light intensity entering the i^{th} segment, α_i, is given

by the product of the source light intensity, I_{source}, and the fraction of light absorbed in each upstream segment. We derive the value of ΔI_i by integrating the Beer-Lambert Law (Eq. (23)) over a discrete spatial segment with thickness Δx, yielding:

$$\int_{I_0}^{I} \frac{dI}{I} = \int_{0}^{\Delta x} (-C_M \varepsilon_M - C_D \varepsilon_D - \varepsilon_{Mel} C_{Mel} - \mu) dx \tag{30}$$

$$I = \alpha_i 10^{-(C_M \varepsilon_M + C_D \varepsilon_D + C_{Mel} \varepsilon_{Mel} + \mu)\Delta x} \tag{31}$$

The fraction of light absorbed in a discrete spatial step, f_i, is given by rearrangement:

$$f_i = \frac{I}{\alpha_i} = 10^{-(C_M \varepsilon_M + C_D \varepsilon_D + C_{Mel} \varepsilon_{Mel} + \mu)\Delta x} \tag{32}$$

Finally, the light intensity loss in a discrete spatial step (ΔI_i) is the product of all the upstream fractional absorbances and the intensity of light reaching the sclera, I_{Scl}. We define the direction of light propagation to be from the $i = 1^{st}$ segment to the $i = n^{th}$segment.

$$\Delta I_i = I_{Scl} \prod_{1}^{n} f_i \tag{33}$$

$$\Delta I_i = I_{Scl} \prod_{1}^{n} 10^{-(C_M \varepsilon_M + C_D \varepsilon_D + C_{Mel} \varepsilon_{Mel} + \mu)\Delta x} \tag{34}$$

The light intensity reaching the sclera may be expressed as a product of the source intensity, I_{Source} and the fraction of light intensity attenuated by the choroid and RPE, ϕ_{RPE}:

$$I_{Scl} = \phi_{RPE} I_{Source} \tag{35}$$

Substituting Eq. (35) into Eq. (34) gives:

$$\Delta I_i = \phi_{RPE} I_{Source} \prod_i^n 10^{-(C_M \varepsilon_M + C_D \varepsilon_D + \mu)\Delta x} \tag{36}$$

Finally, substitution of Eq. (36) into Eq. (29) gives:

$$\frac{d[^3MB]}{dt} = \phi_T \frac{\varepsilon C_i}{\varepsilon_M C_i + \varepsilon_D C_i + \varepsilon_{Mel} C_i + \mu} \left(\frac{\lambda}{Ahc}\right) \phi_{RPE} I_{Source} \prod_i^n 10^{-(C_M \varepsilon_M + C_D \varepsilon_D + C_{Mel} \varepsilon_{Mel} + \mu)\Delta x} \tag{37}$$

5.3.9 Modeling Chemical Reaction Network

MB is known to act as a type II photosensitizer[245]. Previous studies have indicated that histidine, tryptophan, tyrosine, and lysine are likely involved in crosslinks resulting from a type II sensitization process[98–100,246–248]. Therefore, the type II reaction scheme shown in begins with excitation of MB monomers and results in crosslinking of histidine, tryptophan, and tyrosine residues. Lysine was omitted since it is not known to significantly partake in photocrosslinking chemistry other than the crosslink formation[101]. Furthermore, since it exists in excess concentration of the other amino

acids, lysine is assumed to react stoichiometrically in the crosslink formation step (Table 18 and Table 19). See Table 6 for nomenclature pertaining to chemical processes and reactions. Chemical processes and reactions are tabulated in Table 7, Table 8, Table 9, Table 10, and Table 11. Parameters used in the model are tabulated in Table 12.

Table 6: Nomenclature for chemical processes/reactions.

Species	**Nomenclature**
Sensitizer Monomer	S
Sensitizer Dimer	S_D
Sensitizer Singlet	^1S
Sensitizer Triplet	^3S
Sensitizer Semiquinone	$SH^{\cdot}$
Reduced Sensitizer	SH_2
Absorbed Photon	λ
Triplet Oxygen	$^3O_2$
Singlet Oxygen	$^1O_2$
Hydrogen Peroxide	H_2O_2
Amino Acid	AA
Amino Acid Radical	$AA^{\cdot}$
Oxidized Amino Acid	AA_{Ox} (without crosslink)
Crosslink	Xlink
Melanin Monomer	Mel
Oxidized Melanin Monomer	Mel_{Ox}

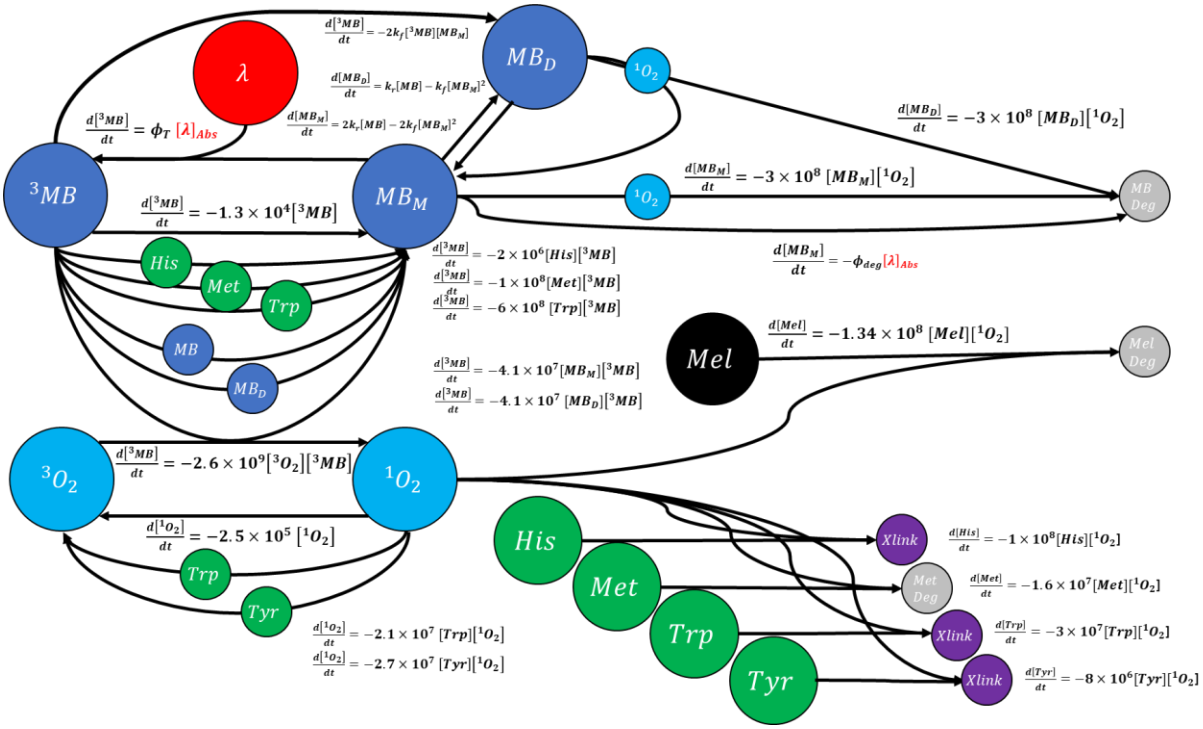

Figure 20: Reaction network for MB photocrosslinking computational model showing modeled species and reaction rates. MB monomer absorbs a photon of red light at 660 nm, resulting in an excited molecule of MB (triplet state). The MB triplet may be quenched physically and returned to the ground state, or it may excite triplet oxygen to the singlet state. Singlet oxygen may be quenched physically, or it may react with amino acids including histidine (His), methionine (Met), tryptophan (Trp), or tyrosine (Tyr). Reactions with His, Trp, and Tyr result in crosslink formation. Singlet oxygen may also react with MB causing it to become degraded, or it may react with melanin, resulting in oxidized melanin.

Table 7: Photoexcitation of sensitizer monomer to singlet and triplet states.

Process	Rate Constant	Reaction Number
$S + \lambda \rightarrow {}^1S \rightarrow S^3$	Φ_T	(1)

Table 8: Type I reaction scheme.

Reactions/Processes	Rate Constant	Reaction Number
${}^3S + AA \rightarrow SH^{\cdot} + AA^{\cdot}$	k_1	(2)
$AA^{\cdot} + {}^3O_2 \rightarrow AA_{peroxide}$	k_2	(3)
$AA_{peroxide} + AA \rightarrow Xlink$	k_3	(4)
$SH^{\cdot} + SH^{\cdot} \rightarrow S + SH_2$	k_4	(5)
$SH_2 + O_2 \rightarrow S + H_2O_2$	k_5	(6)

Table 9 Type II chemical reaction scheme.

Reactions/Processes	Rate Constant	Reaction Number
${}^3S + {}^3O_2 \rightarrow S + {}^1O_2$	k_6	(7)
${}^1O_2 + AA \rightarrow Xlink$	k_7	(8)

Table 10: Non-productive pathways.

Reactions/Processes	Rate Constant	Reaction Number
$^3S \rightarrow S$	k_8	(9)
$^3S + S \rightarrow 2S$	k_9	(10)
$^3S + S_D \rightarrow S + S_D$	k_{10}	(11)
$^3S + AA \rightarrow S + AA$	k_{11}	(12)
$AA^{\cdot} \rightarrow AA$	k_{12}	(13)
$^1O_2 \rightarrow {}^3O_2$	k_{13}	(14)
$^1O_2 + AA \rightarrow {}^3O_2 + AA$	k_{14}	(15)
$S + {}^1O_2 \rightarrow S + {}^3O_2$	k_{15}	(16)
$S_D + {}^1O_2 \rightarrow S_D + {}^3O_2$	k_{16}	(17)
$^1O_2 + AA \rightarrow AA_{ox}$	k_{17}	(18)
$Mel + {}^1O_2 \rightarrow Mel_{Ox}$	k_{18}	(19)

Table 11: Sensitizer dimerization scheme.

Reaction	Rate Constant	Reaction Number
$2S \rightarrow S_D$	k_{19}	(20)
$S_D \rightarrow 2S$	k_{20}	(21)

Table 12 Model parameters.

Symbol	Description	Riboflavin	Methylene Blue
t	Treatment duration	1800 s	1800 s
I_{source}	Light intensity	3 mW cm^{-2}	424 mW cm^{-2}
$C_{0\ S}$	Injection concentration	2.2 mM (0.1%)	3 mM (0.094%)
λ	Light wavelength	365 nm	660 nm
$X_{(Tissue)}$	Thickness of cornea	See Table 17	See Table 17
X_{Inj}	Thickness of injection reservoir	0 mm	1.3 mm*
X_{Retro}	Distance to bulbar vasculature	N/A	0.
C_L	Left boundary $^3O_2$ concentration	See Table 16	See Table 16
C_R	Right boundary $^3O_2$	See Table 16	See Table 16
$C_{0\ (AA)}$	Initial AA concentration	See Table 18	See Table 19
$C_{0\ Mel}$	Initial melanin concentration	See Table 20	See Table 12
Φ_{Lumen}	Luminal fraction of choroid	N/A	0.4[249]
D_{Res}	Diffusion constant, S in injection	4.20 x 10^{-6} cm^2 s^{-1} [250]	4.60 x 10^{-6} cm^2 s^{-1} [251]
D_{Scl}	Diffusion constant, S in sclera	4.60 x 10^{-7} cm^2 s^{-1} [252]	3.16 x 10^{-7} cm^2 s^{-1}**
D_{Ox}	Diffusion constant, O_2 in sclera	4.00 x 10^{-6} cm^2 s^{-1}[236]	4.00 x 10^{-6} cm^2 s^{-1}[236] †
K_d	S dimerization constant	125 M^{-1} [139]	10665 M^{-1} [253]
Φ_{Fundus}	Fraction light reflected by RPE	N/A	0.096 [254]
μ	Attenuation coefficient of tissue	17 cm^{-1} [232]	N/A
ε_M	Molar absorptivity of S	10800 M^{-1} cm^{-1} [139]	79800 M^{-1} cm^{-1} [76]
ε_D	Molar absorptivity of S_D	6500 M^{-1} cm^{-1} [139]	35300 M^{-1} cm^{-1} [76]

ε_{Mel}	Molar absorptivity of melanin	N/A	646 M^{-1} cm^{-1} [255] ††
Φ_T	Sensitizer triplet quantum yield	0.61 [256]	0.52 [163]
k_1	Chemical quenching of ^3S by AA	His: 5.22 x 10^7 M^{-1} s^{-1}[257] Met: 6.36 x 10^7 M^{-1} s^1[257] Trp: 1.75 x 10^9 M^{-1} s^{-1}[257] Tyr: 1.40 x 10^9 M^{-1} s^{-1}[257]	N/A
k_2	Peroxide formation	4 x 10^6 M^{-1} s^{-1}[258]	N/A
k_3	Type I crosslink formation	Assumed very rapid	N/A
k_4	Semiquinone disproportionation	Neglected	N/A
k_5	Oxidation of SH_2 by O_2	Neglected	N/A
k_6	$^1O_2$ generation by ^3S	1.62 x 10^9 M^{-1} s^{-1}[259]	2.6 x 10^9 M^{-1} s^{-1} [260]
k_7	Chemical quenching of $^1O_2$ by AA resulting in crosslinking	His: 1 x 10^8 M^{-1} s^{-1}[143] Met: 0 Trp: 3 x 10^7 M^{-1} s^{-1}[143] Tyr: 8 x 10^6 M^{-1} s^{-1}[143]	His: 1 x 10^8 M^{-1} s^{-1}[143] Met: 0 Trp: 3 x 10^7 M^{-1} s^{-1}[143] Tyr: 8 x 10^6 M^{-1} s^{-1}[143]
k_8	Physical quenching of ^3S by solvent	4.9 x 10^3 s^{-1}[261]	1.3 x 10^4 s^{-1} [72] ‡
k_9	Physical quenching of ^3S by S	1.2 x 10^8 M^{-1} s^{-1}[261]	4.1 x 10^7 M^{-1} s^{-1} [262]
k_{10}	Physical quenching of ^3S by S_D	k_9	k_9
k_{11}	Physical quenching of ^3S by AA	N/A	His: 2 x 10^6 M^{-1} s^{-1}[142] Met: 1 x 10^8 M^{-1} s^{-1}[142] Trp: 6 x 10^8 M^{-1} s^{-1}[142] Tyr: 0 M^{-1} s^{-1}
k_{12}	AA radical termination	100 M^{-1} s^{-1}[258]	N/A
k_{13}	$^1O_2$ solvent quenching	2.56 x 10^5 s^{-1} [263] ‡	2.56 x 10^5 s^{-1} [263] ‡
k_{14}	Physical quenching of $^1O_2$ by AA	His: 0 M^{-1} s^{-1} Met: 0 M^{-1} s^{-1} Trp: 2.1 x 10^7 M^{-1} s^{-1}[143] Tyr: 2.7 x 10^7 M^{-1} s^{-1} [264,265]‡‡	His: 0 M^{-1} s^{-1} Met: 0 M^{-1} s^{-1} Trp: 2.1 x 10^7 M^{-1} s^{-1}[143] Tyr: 2.7 x 10^7 M^{-1} s^{-1} [264,265]‡‡
k_{15}	Physical quenching of $^1O_2$ by S	0 §	3 x 10^8 M^{-1} s^{-1}[266]
k_{16}	Physical quenching of $^1O_2$ by S_D	k_{15}	k_{15}
k_{17}	Chemical quenching of AA by $^1O_2$ resulting in oxidized AA	His: 0 Met: 1.6 x 10^7 M^{-1} s^{-1}[143] Trp: 0 Tyr: 0	His: 1 x 10^8 M^{-1} s^{-1}[143] Met: 1.6 x 10^7 M^{-1} s^{-1}[143] Trp: 3 x 10^7 M^{-1} s^{-1}[143] Tyr: 8 x 10^6 M^{-1} s^{-1}[143]

k_{18}	Chemical quenching of $^1O_2$ by Mel	1.34 x 10^8 M^{-1} s^{-1}[267]	1.34 x 10^8 M^{-1} s^{-1}[267]
k_{19}	Dimer formation	1.09 x 10^9 M^{-1} s^{-1}[241] §§	1.09 x 10^9 M^{-1} s^{-1}[241]
k_{20}	Dimer dissociation	k_{19} x K_d^{-1}	k_{19} x K_d^{-1}

* See reservoir volume calculation in supplemental materials
** Measured in this study
† Assumed identical to oxygen diffusivity in cornea
†† Assumes melanin monomer molecular weight of 200 Da as in [267].
‡ Calculated as inverse of lifetime
‡‡ Bertolotti[264] cites Garcia[265] for Tyr
§ Assumed insignificant compared to chemical quenching
§§ Assumed to be identical to that of MB

5.4 Results

We developed a computational model with the primary objective of using it to describe photocrosslinking in the sclera. Because experimental data on scleral photocrosslinking are lacking in the literature, we are validating the model by comparing model predictions of photocrosslinking in the cornea, where a number of studies report experimental results. Model predictions in the sclera and cornea were performed using not fitted parameters. All parameters were independently obtained from the literature or calculated (see Table 12).

5.4.1 Prediction of Oxygen Concentration during Riboflavin Crosslinking Procedure in Porcine Eye

As a first validation for model predictions, we assess the model's ability to replicate the oxygen depletion and recovery measured under a 130-μm flap of deepithelialized corneal stroma in *ex vivo* porcine eyes undergoing riboflavin crosslinking (Figure 21) as reported

in Kamaev et al.[129]. In the experimental study, an oxygen probe was used to measure oxygen concentration under the corneal flap after the eye had been incubated in riboflavin and irradiated with UV light.

In the experimental data, oxygen concentration decreased rapidly within the first 20 s to <1% of the initial concentration, maintained a steady low-level state until approximately 5 min into the procedure, and increased to approximately 10% of the initial oxygen concentration at 30 min(Figure 21). This unusual triphasic behavior results from the complex interaction between penetration of light, diffusion of chemical species and kinetics of chemical reactions. This complex behavior seen experimentally provides a stringent test of our model's ability to accurately capture the many interdependent processes taking place during photocrosslinking under these conditions.

Model predictions matched the experimental data well, capturing all three phases of the process, and quantitatively matching the experimentally measured oxygen concentrations despite having no fitted parameters in the model (Figure 21). To explain the reasons for the three phases of the process, the model predicted that the initial depletion of oxygen was caused by reaction of triplet riboflavin (created by absorption of photons from the light source) to produce singlet oxygen, which in turn reacts with amino acids of collagen in the corneal stroma to create crosslinks. In the intermediate phase from 20 s to 5 min, uncrosslinked amino acids were being depleted due to reaction with singlet oxygen (type II reaction processes) or through type I reaction processes. The rise in oxygen concentration after 5 minutes was, in our model, due to the depletion of amino acids which, in the intermediate phase, had been consuming oxygen. We found that oxygen consumption per

type I reaction dynamics were necessary to reproduce the experimental data from Kamaev et al.

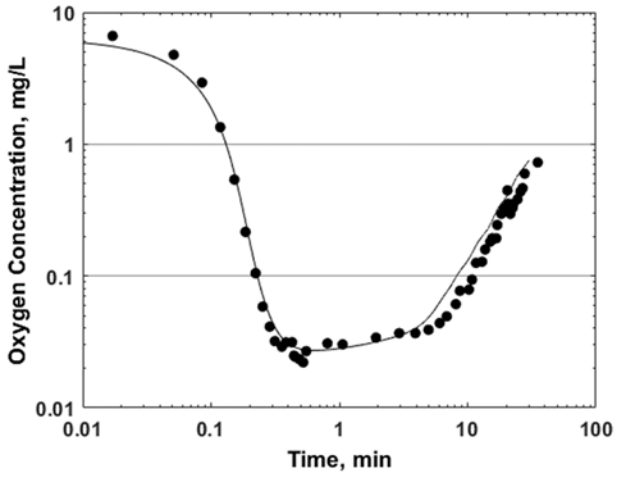

Figure 21: Experimental data from Kamaev et al. 2012 (filled circles) showing oxygen concentration under a 130 μm corneal flap in *ex vivo* porcine eyes during riboflavin crosslinking procedure. Computational model prediction for oxygen concentration (solid line) showing good agreement with the experimental data. No parameters were fitted in the model to produce this result.

5.4.2 Prediction of Riboflavin Crosslinking Data in the Literature

As a further test of our computational model, we predicted crosslinking in *ex vivo* porcine eyes according to the procedure in Hammer et al.[177]. We found reasonable agreement between our model's crosslink utilization prediction and stiffening in the Hammer study using linear regression (Figure 22D). The regression slope of 0.46 percent increase in elastic modulus per percent crosslinks utilized differed statistically significantly from 0 ($p < 0.05$) with goodness of fit of $R^2 = 0.9976$.

In a similar manner, we compared our model predictions for crosslinking against experimental evidence for riboflavin crosslinking violation of the Bunsen-Roscoe Law demonstrated by enzymatic degradation as studied by Aldahlawi et al.[237]. In this study, Aldahlawi et al. used similar experimental conditions as in the Hammer study, maintaining a constant fluence of 5.4 J/cm^2 for riboflavin crosslinking experiments in porcine eyes using irradiation intensities of 3, 9, and 18 mW/cm^2 for 30, 10, and 5 minutes, respectively. Our model agrees with the Aldahlawi study (Figure 22E) generally, though the regression slope is not statistically significant for rejecting the null hypothesis that the slope is different from 0 ($p = 0.0875$). The slope of the regression line is 0.0001895 grams dry weight collagen per percent crosslinks utilized.

The Hammer and Aldahlawi studies were designed to determine whether riboflavin crosslinking in the cornea follows the Bunsen Roscoe Law, which states that the extent of crosslinking should directly correlate with the light fluence[268]. These experimental studies showed that this was not the case, since each study examined three different conditions with the same fluence, but different light intensity and duration, and found that the extent of crosslinking decreased as light intensity increased and exposure duration decreased at constant fluence. These data demonstrate that photocrosslinking depended more strongly on exposure duration and less strongly on light intensity. The trend of this complex interplay among these parameters was captured by model predictions, which helps validate is predictive power.

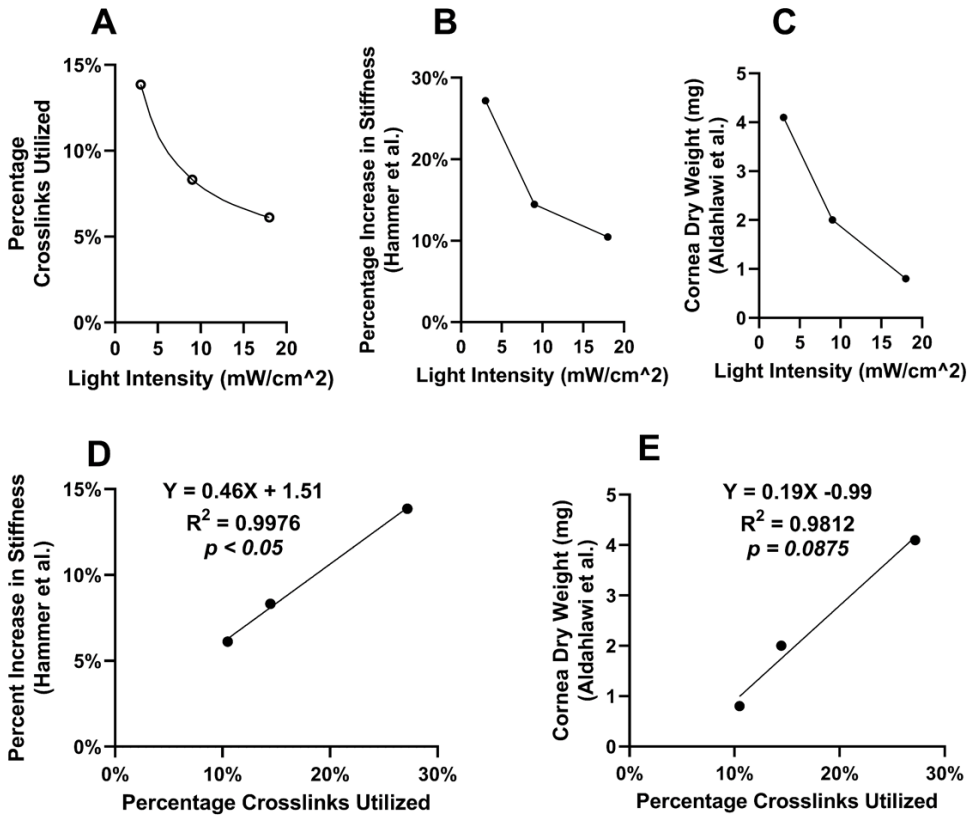

Figure 22: Correspondence of computational model predicted crosslinking with experimental crosslinking. A) Computational model prediction for riboflavin crosslinking with constant fluence (5.4 J/cm^2) at different intensities. Open circles represent the computational model output at light intensities corresponding with those experimentally tested in Hammer et al. and Aldahlawi et al. B) Percentage stiffness increase in porcine corneas treated with riboflavin crosslinking procedure calculated from Hammer et al. 2014. C) Porcine cornea dry weight at 12 days after riboflavin crosslinking and enzymatic digestion reproduced from Aldahlawi et al. 2015. D) Computational model data plotted against Hammer et al. data with linear regression showing reasonable agreement. E) Computational model predicted fraction of crosslinks utilized as a function of cornea dry weight after enzymatic degradation showing reasonable correspondence.

5.4.3 Experimental Determination of MB Diffusion Constant in Rat Sclera

A critical parameter for model predictions is the diffusion constant of MB in the rat sclera. We determined this value by measuring MB diffusion across rat scleral samples ex

vivo (Figure 23A) and calculated a diffusivity of (3.16 ± 1.11) x 10^{-7} cm^2/s from the steady-state region of these data (Figure 23B). The average lag time (time from onset of diffusion to formation of steady state concentration profile and flux) was 45 ± 29 min.

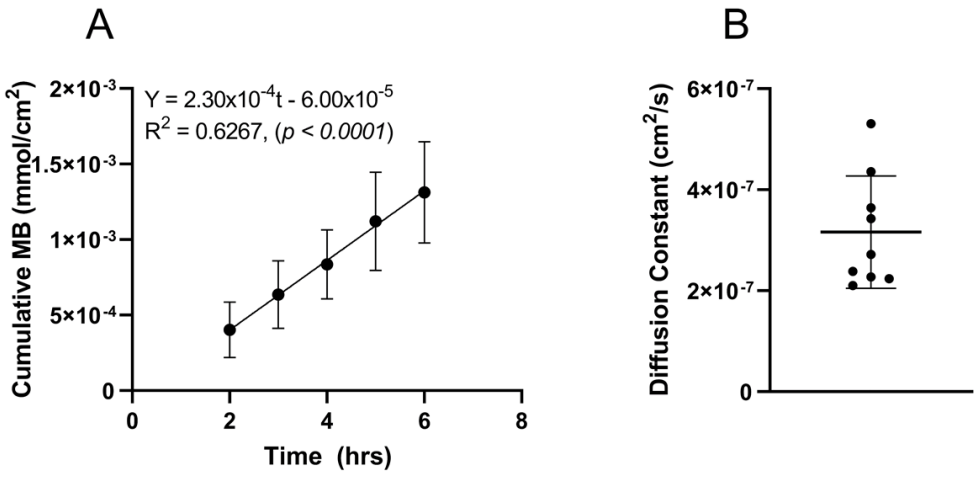

Figure 23: Determination of MB diffusion constant in Brown Norway rat sclerae *ex vivo.* Diffusion constant was determined by A) measuring cumulative mass of MB transported across a fixed surface area of tissue over time. The slope was set equal to MB flux. B) The value of the MB diffusion constant was computed from flux in the steady-state region of transport. Data points represent A) mean ± standard deviation (n=9 replicates) or B) independently calculated values, with mean and standard deviations shown.

5.4.4 Experimental Determination of MB Concentration in Sclera 30 Minutes Post-injection

MB concentration measured 30 minutes after retrobulbar injection in anesthetized Brown Norway rats was significantly different than in the same tissue of the control HBSS-injected eyes in all cases except for the scleral region >1.5 mm from the center of the ON (Figure 24) as measured by two-way ANOVA. Sample size was $N = 5$ in all cases except for the ON fat which was $N = 3$ due to error in sample collection for two rats. MB

concentrations represented as a fraction of the injected concentration were 6.8 ± 2.2% for 0-0.5 mm ($p < 0.001$), 14.4 ± 2.0% for 0.5-1 mm ($p < 0.0001$), 13.7 ± 2.8% for 1-1.5 mm ($p < 0.0001$), and 1.1 ± 0.7% for >1.5 mm ($p = 0.97$) distance from the ON center. Additionally, there were significant differences from control eyes in the MB concentrations in the ON and ON fat. MB concentration in the ON was 6.8 ± 2.7% ($p < 0.0001$) and in the ON fat was 26.2 ± 7.5% ($p < 0.0001$). Mean concentration for the control eyes was calculated based on the threshold for fluorescence detection.

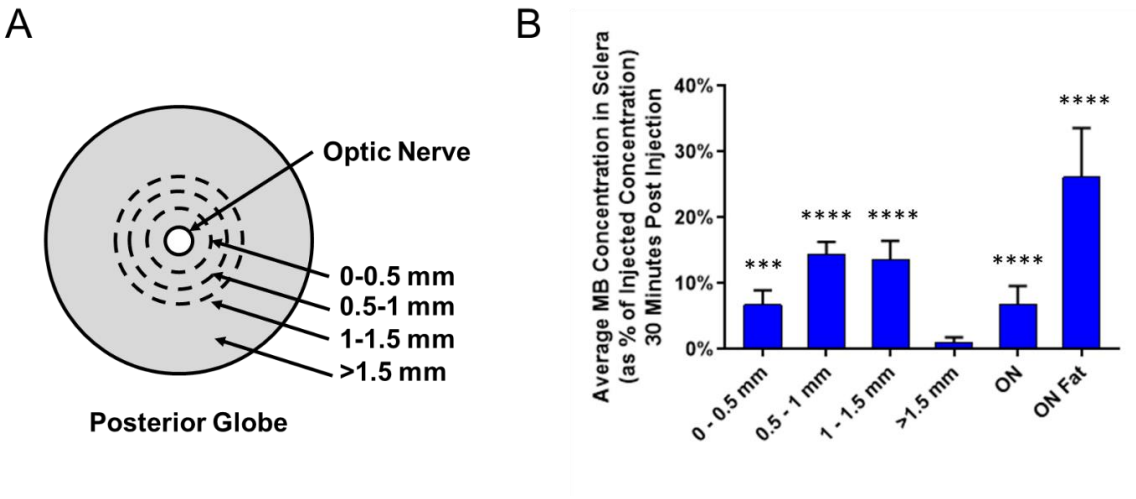

Figure 24: MB concentration in ocular tissues measured 30 min after retrobulbar injection in vivo. A) Diagram of scleral sections dissected from rat eyes. Injections were performed under anesthesia with Brown Norway rats euthanized 30 min after injection to replicate the experimental conditions used in scleral crosslinking. B) Average MB concentration measured in ocular tissues 30 min post injection. Mean concentration for the control eyes was calculated based on the threshold for fluorescence detection in cases where fluorescence was below this threshold. Data represent mean + standard deviation from 5 replicates in all cases except for the ON fat which had only 3 replicates due to error in sample collection for two rats. *** $p < 0.001$, **** $p < 0.0001$ by two-way ANOVA.

5.4.5 Prediction of the Effects of Sensitizer Diffusivity and Injection Volume on Sensitizer Concentration in Sclera

Because sensitizers other than MB might be of interest, we predicted the concentration of sensitizer in the sclera 30 min post retrobulbar injection over a range of diffusion constant (1.00×10^{-8} – 9.5×10^{-6} cm^2/s, Figure 25). Light intensity was entered as 0 mW/cm^2 to capture sensitizer behavior in the absence of MB photodegradation. Interestingly, the model predicts that MB concentration goes through a maximum value. Intuitively, as diffusion coefficient increases, sensitizer concentration in the sclera increases as the sensitizer is able to diffuse into the sclera more quickly. After reaching a peak concentration at a sensitizer diffusivity of approximately 4.80×10^{-8} cm^2/s, sensitizer concentration decreases with increasing diffusivity because by the 30 min time point, a significant amount of sensitizer will have diffused across the sclera and been cleared by the choroidal vasculature. Thus, optimization of scleral concentration of sensitizer depends on both sensitizer diffusivity and time.

We also investigated the model's predicted effects of injection volume on the concentration of MB in the sclera at the 30 min time point (Figure 27A). Over the range 3.2 to 320 μl, injection volume was represented as injection reservoir thickness, the 1D distance from the posterior Tenon capsule surface to the retrobulbar muscle cone tissues. Normalized MB concentration remaining in the sclera after 30 min ranged from 6.0×10^{-6}% to 38.9% of the injection concentration. A notable inflection point in the logarithmically scaled curve at around 40 μl, below which point normalized MB concentration in the sclera is comparatively small. This is likely caused by MB dose reaching a quantity sufficient to attenuate the impact of MB clearance on injection reservoir concentration over the 30 min

time scale studied. At low injection volumes, the clearance rate has a stronger impact on reservoir concentration and therefore on the total MB remaining in the sclera after 30 min.

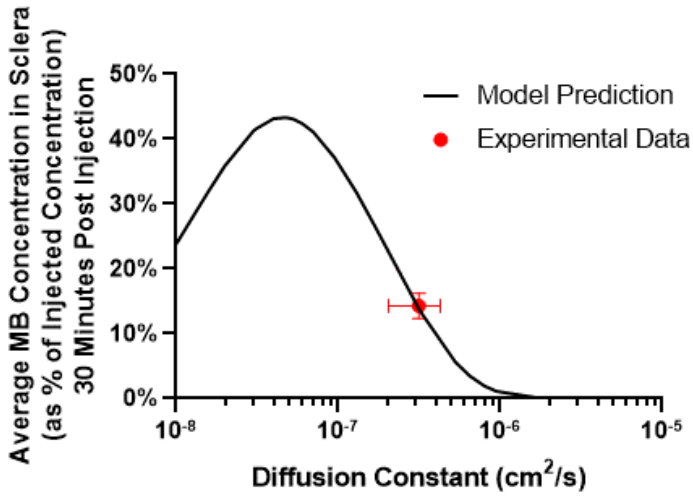

Figure 25: Computational model prediction of average sensitizer concentration in sclera 30 minutes after retrobulbar injection represented as a percentage of the injected concentration. The experimental value for MB concentration (Figure 24) and the corresponding experimental value for MB diffusion constant (Figure 23B) are shown (red datapoint). Error bars represent ± standard deviation. Simulations were performed with light source intensity at 0 mW/cm^2 to isolate the diffusion/clearance kinetics from possible effects of photodegradation.

5.4.6 Prediction of the Effects of MB Concentration, Light Intensity, and Inspired Oxygen on Crosslinking

We next used the model to predict the desired outcome of scleral photocrosslinking as a function of three parameters over which we have experimental control: MB concentration, light intensity, and inspired oxygen concentration (Figure 26). Inspired oxygen at 100% produced approximately 6-fold more tissue crosslinking than did 21% inspired oxygen at

our standard conditions of 3 mM MB and 424 mW/cm^2 light intensity (Figure 26A,B). Increasing light intensity corresponded with an increase in crosslinking in all cases, where crosslinking depended roughly on light intensity.

For MB concentration, effects on crosslinking were more complicated. For example, we found that crosslinking was similar for 3 mM and 30 mM MB, independent of light intensity over the range studied at 100% inspired oxygen (Figure 26A). In contrast, for the 21% inspired oxygen case, the 30 mM MB concentration underperforms the 3 mM MB concentration (Figure 26B). To better isolate the effects of MB concentration, we varied MB concentration, holding light source intensity constant at our standard value of 424 mW/cm^2 (Figure 26C,D). In this case, MB crosslinking efficiency is characterized by local maxima at approximately 8 mM (32% predicted crosslink utilization) with 100% inspired oxygen and at approximately 4.5 mM (6% predicted crosslink utilization) with 21% inspired oxygen. For reference, our standard experimental condition of 3 mM MB with 100% inspired oxygen corresponds to a 30% predicted crosslink utilization, which is close to the maximum value. Competing effects of insufficient sensitizer at low concentrations and sensitizer self-quenching at higher concentrations likely explains the local maxima.

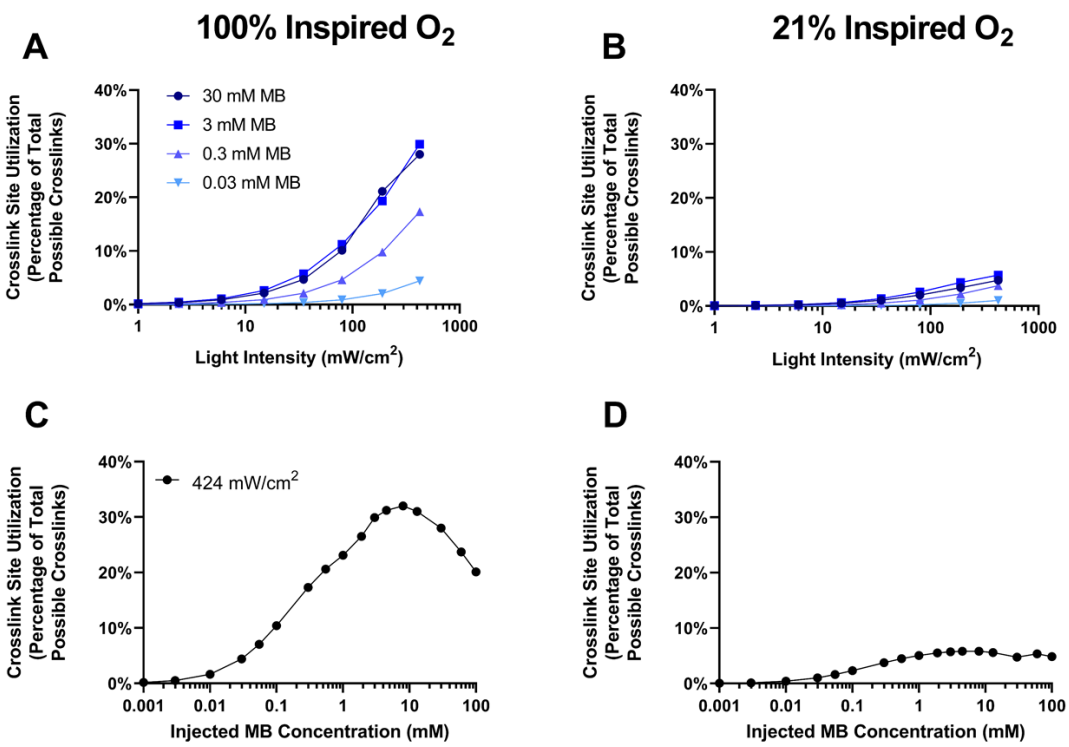

Figure 26: Computational model prediction of MB photocrosslinking efficiency as a function of MB concentration, light intensity, and inspired oxygen. Crosslinking as a function of light intensity and MB concentration was modeled at A) 100% and B) 21% inspired oxygen concentrations corresponding to isoflurane anesthesia with 100% oxygen and anesthesia with subject breathing atmospheric oxygen, respectively. Crosslinking is also shown as a function of MB concentration when light intensity was held constant (424 mW/cm^2) for both C) 100% and D) 21% inspired oxygen. Data points represent the results of simulations performed at the indicated conditions.

5.4.7 Prediction of Effects of Injection Reservoir Volume on Crosslinking Efficiency

Injection volume and MB injection concentration were investigated together for their effects on crosslinking efficiency as they are two important experimenter-selected determinants of MB transport during a photocrosslinking procedure (Figure 27). A trade-off was found where similar crosslinking efficiency occurs for 3 mM MB injections with larger reservoir volumes (>100 µl) and for 30 mM MB injections at lower reservoir

volumes (20-60 µl). Lower MB concentrations did not achieve the same levels of maximum crosslinking on the investigated reservoir volume range. Interestingly, 30 mM MB crosslinking became less efficient at large reservoir volumes, supporting the previous finding that efficiency as a function of concentration experiences a local maximum. The local maximum in Figure 27C for 30 mM MB suggests that crosslinking efficiency increases when the injection volume is sufficiently low to allow significant crosslinker clearance over the course of the procedure, thus decreasing the MB concentration to levels more amenable to crosslinking.

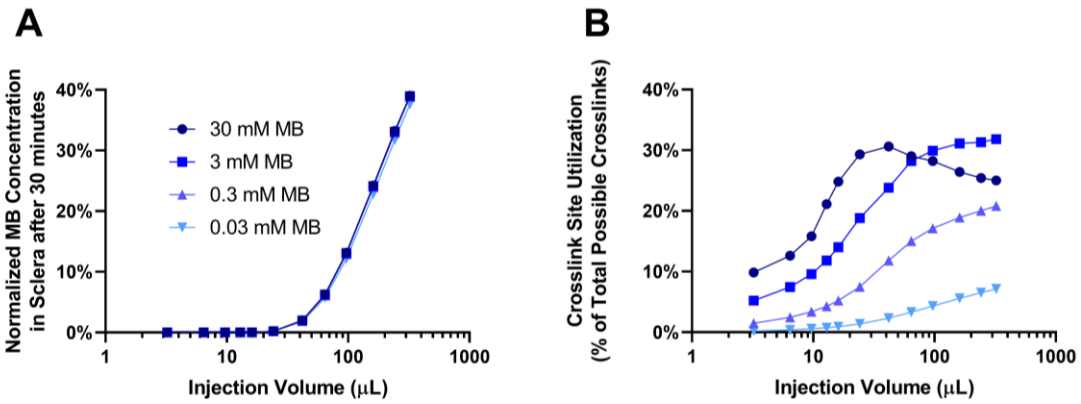

Figure 27: Injection volume and concentration affect MB distribution and crosslinking. A) Normalized MB concentration in the sclera at 30 minutes post injection increases with injection volume but is not affected by concentration. B) At all concentrations studied except for 30 mM MB, increasing injection reservoir volume improved crosslinking efficiency. At 30 mM MB concentration, crosslinking efficiency had a local maximum at approximately 1 mm reservoir volume. Injection volume was represented in the model by assuming a constant scleral surface area and calculating the injection reservoir volume defined as the distance from the posterior Tenon capsule surface to the retrobulbar muscle cone tissues which bounded the MB injection reservoir created by the injection. Data points represent the results of simulations performed at the indicated conditions.

5.4.8 Prediction of MB Concentration during Photocrosslinking

A quasi-steady state profile was reached for MB monomers and dimers after approximately the first 3 minutes of diffusion in the sclera/choroid (Figure 28). Over time, MB concentration decreased due to clearance through the choroid and retrobulbar tissues. Our standard MB photocrosslinking procedure used a 3 mM MB injection at which concentration most MB exists as dimers. MB dimers in (Figure 28B) generally outnumber the monomers (Figure 28A) due to the large dimerization equilibrium constant. However, this effect is less pronounced near the anterior surface of the choroid where MB concentration is lower, thus favoring the monomer species. The negative concavity of the MB monomer concentration profile over tissue distance can be attributed to the disaggregation of dimers as total MB concentration deceases nearer the anterior choroid surface.

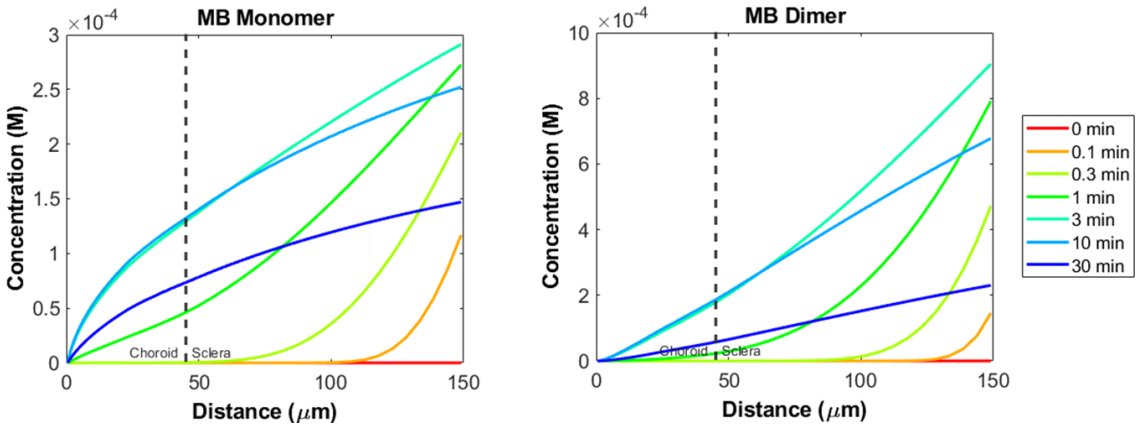

Figure 28: A) Monomeric and B) dimeric MB concentrations over time and distance through the choroid and sclera reach a quasi-steady state equilibrium after approximately 3 minutes from which time they decline due to choroidal and retrobulbar clearance. Note concentration is plotted with a family of curves describing logarithmically spaced time points.

5.4.9 Prediction of Light Intensity across Choroid and Sclera

Light penetration through the tissue maintained a relatively steady state profile with the greatest intensity at the anterior choroid and diminishing quickly towards the posterior due absorbance both by melanin and MB (Figure 29). The MB photocrosslinking procedure used a source light intensity of 424 mW/cm^2, though only approximately 82 mW/cm^2 penetrated the RPE to reach the choroid. Light absorbance was strongest in the heavily pigmented choroid with lesser contribution from the lightly pigmented sclera. MB diffusion was responsible for increased light absorbance in the sclera over time in a manner proportional to MB concentration. However, MB diffusion to the choroid had little effect on the choroidal light intensity profile, as absorbance by melanin greatly exceeded that of MB. The model suggests that only a small percentage of light entering the choroid participates in photocrosslinking reactions with the majority being absorbed by tissue.

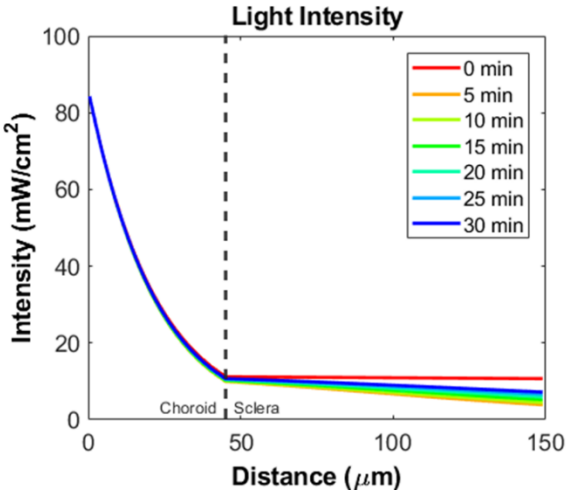

Figure 29: Light intensity profile over space/time in the choroid and sclera during MB photocrosslinking.

5.4.10 Prediction of Triplet Oxygen Concentration

Oxygen concentration depleted rapidly in the first minute of crosslinking in the sclera and posterior choroid, reaching a quasi-steady state equilibrium in the anterior choroid between choroidal oxygen diffusion and consumption reactions (Figure 30). There was a slight recovery in the penetration depth of oxygen at later time points due to depletion of amino acids and melanin which participate in oxygen-consuming reactions. Rapid consumption in the choroid where light intensity was strongest resulted in a steep concentration gradient from anterior to posterior choroid. This steep concentration gradient drove oxygen flux to the site of crosslinking despite there being decreased concentrations of oxygen compared to the pre-irradiation state.

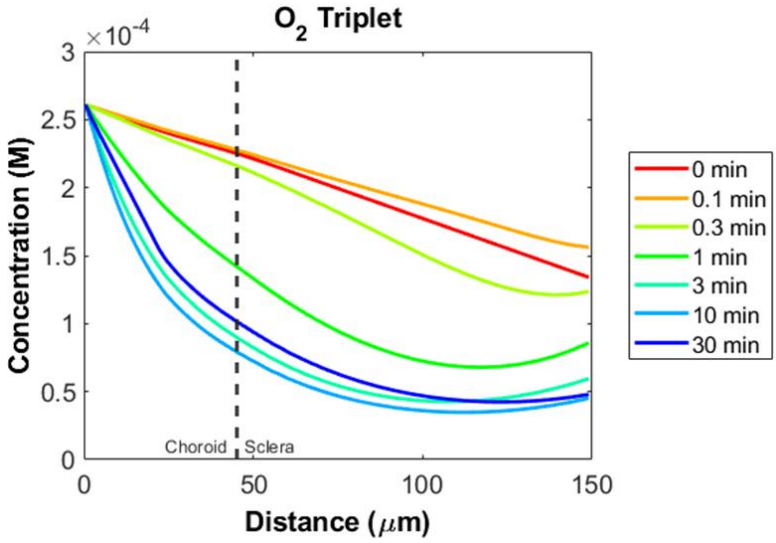

Figure 30: Triplet oxygen concentration over space and time during MB photocrosslinking. Note, concentration is plotted with logarithmically spaced time from 0 to 30 minutes.

5.4.11 Prediction of Amino Acid Concentration

The amino acids His, Trp, Met, and Tyr were all partially depleted in the choroid/sclera during the simulation (Figure 31). All were assumed to have lower initial concentrations in the choroid due to the vascular lumen where collagen is absent. Amino acid concentrations depleted over time due to crosslinking (assumed in the underlying model reactions for His, Trp, and Tyr) and non-productive oxidation (Met). Depletion was most prevalent at later time points near the anterior choroidal surface for all residues. His and Trp showed depletion in the anterior sclera to a lesser extent than in the choroid, while scleral depletion was minimal for Met and Tyr. We attribute this difference to the higher reaction rates of His and Trp (but especially His) with singlet oxygen as well as their relatively lower concentrations compared to Met and Tyr. Similar attribution might be given for the observation that His depleted more gradually over time than did the other amino acids with relatively sharp depletions in the choroid.

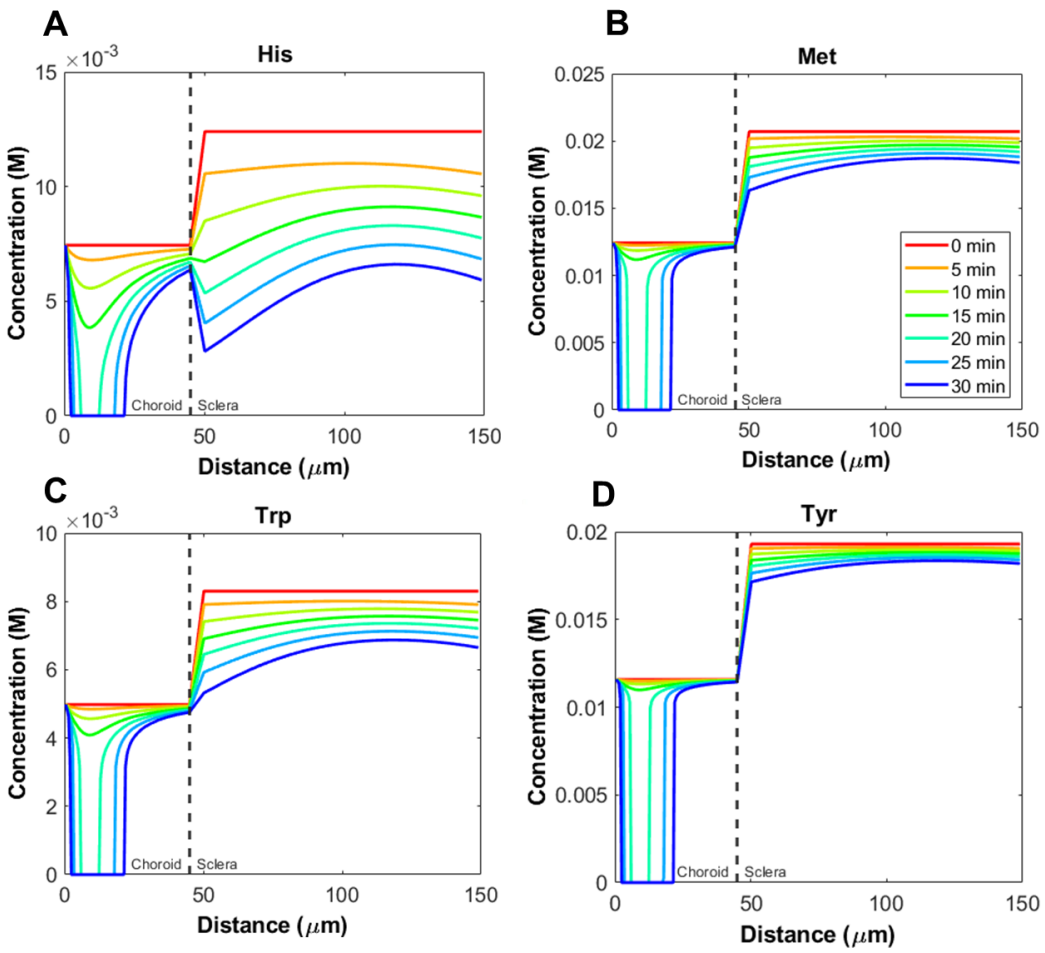

Figure 31: Amino acid concentrations during MB photocrosslinking procedure for A) histidine, B) methionine, C) tryptophan, and D) tyrosine.

5.4.12 Prediction of Melanin Concentration

Melanin, the most concentrated of the singlet-oxygen quenching species, was depleted in a manner most similarly resembling His. It showed a gradual decline after approximately 10 minutes which accelerated towards complete depletion after 20 minutes in the anterior choroid (Figure 32). Melanin has a similar singlet oxygen chemical quenching rate constant to His (1.34 x 10^{-8} $M^{-1}s^{-1}$ vs 1x 10^{-8} $M^{-1}s^{-1}$,

Table 12), perhaps explaining the earlier onset and more gradual decline compared to Met, Trp and Tyr which have significantly slower reaction rates.

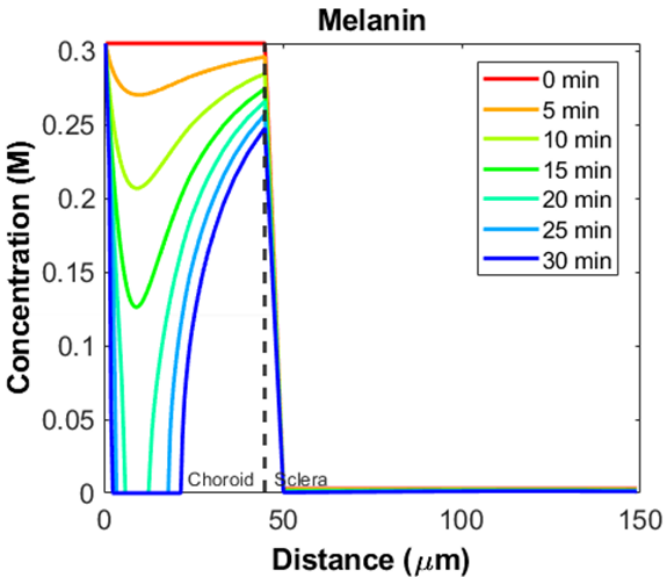

Figure 32: Melanin concentration as a function of space and time during MB photocrosslinking.

5.4.13 Prediction of Singlet Oxygen, MB Triplets, and Cumulative Degraded MB

Changes in singlet oxygen, MB triplet, and degraded MB concentrations reflect the degree of photochemical reaction quenching by amino acids and melanin. Increased concentrations of all three species were seen late in the simulated treatment after 25 minutes in the anterior choroid (Figure 33). The timing and location of their increase paralleled the depletion of amino acids and melanin (Figure 31 and Figure 32). Absence of significant quencher concentrations supported longer-lived singlet and triplet species. Comparing the concentration of singlet oxygen with that of cumulative degraded MB in the anterior choroid, we see that despite having a concentration less than 3×10^{-7} M, singlet oxygen

was responsible for production of approximately 2 x 10^{-4} M concentration of degraded MB molecules in the last 5 minutes of treatment. This comparison illustrates that oxygen concentration alone is not a satisfactory indicator of reaction mechanism or magnitude in photocrosslinking procedures. Rather, the rates of consumption and formation are of equal importance. One might therefore erroneously assume that the low concentrations of triplet or singlet oxygen in the tissues after the first 3 minutes of irradiation would signal an anaerobic crosslinking mechanism.

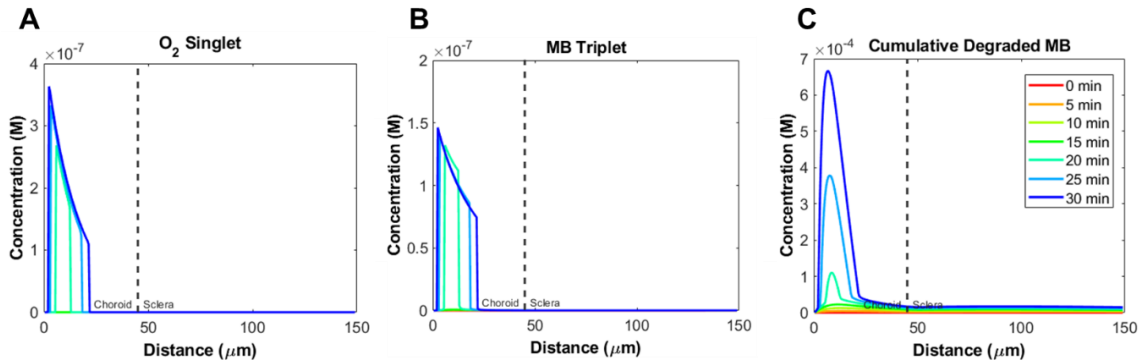

Figure 33: A) Singlet oxygen, B) MB triplet, and C) cumulative degraded MB concentrations modeled as a function of space and time.

5.4.14 Prediction of Scleral and Choroidal Crosslinking

Cumulative average crosslink concentration in the choroid and sclera increased approximately linearly over the 30-minute procedure duration (Figure 34A), reaching a total average concentration of 10.5 mM. Crosslink distribution over tissue thickness showed a discontinuity at the sclera-choroid interface. This discontinuity was caused by the large relative difference in melanin concentration between the two tissues. Higher melanin concentrations in the choroid quench photocrosslinking reactions more strongly

than in the sclera. This quenching effect is offset by the relatively higher light intensity and oxygen concentration in the choroid, resulting in similar crosslink concentrations in both tissues. However, the crosslink distribution in the sclera is more uniform than in the choroid where crosslinks are predominately found at the anterior surface.

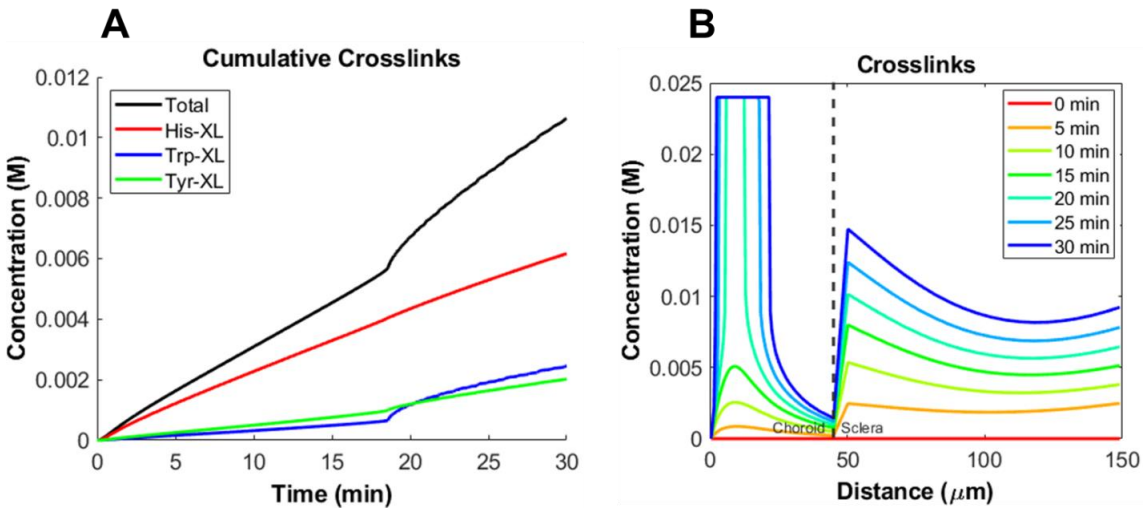

Figure 34: A) Cumulative average crosslink concentration over time in the choroid and sclera with individual contributions from His, Trp, and Tyr, and B) crosslink concentration over time and space during MB photocrosslinking procedure.

5.4.15 Sensitivity Analysis of MB Photocrosslinking Predictions

Model parameters were each individually increased by 1% of their default value, and the resulting increase in crosslinking was quantified from the model output. Parameter sensitivity was ranked and parameters were identified according to their common characteristics as experimental properties, sensitizer properties, or tissue properties (Figure 35). Experimental properties were those under the control of the experimenter and not related to the sensitizer or tissue such as irradiation duration. Sensitizer properties were

physical/chemical characteristics such as absorbance wavelength and triplet quantum yield. Tissue properties were those inherently linked to tissue such as amino acid concentrations.

Sensitivity values are reported as a percentage change in crosslinking for the given 1% change in parameter value. Only choroid thickness sensitivity (-1.02%) was of greater magnitude than 1%, indicating that no single parameter had an inordinate impact on the model for the case in question. Tissue properties such as choroid thickness (-1.02%), scleral thickness (-0.64%), and melanin concentration (-0.52%) comprised all the parameters inversely related to crosslinking. The two leading parameters with which crosslinking was directly related were experimental properties – irradiation duration (0.79%) and choroid oxygen concentration (0.60%). Sensitizer properties of note included the reaction rate of MB with singlet oxygen (0.15%), absorbance wavelength (0.14%), triplet quantum yield (0.14%), and monomer molar absorptivity (0.11%), none of which were in the top 10 most sensitive parameters by magnitude.

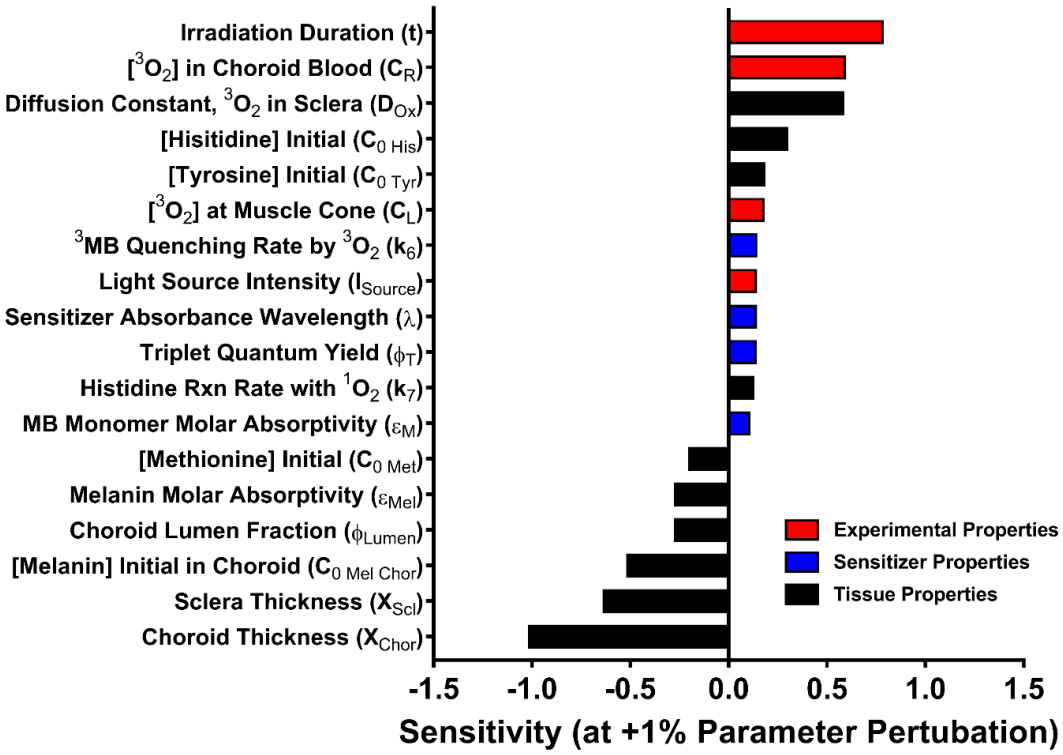

Figure 35: Ranked sensitivities of model parameters categorized by property type for the default MB photocrosslinking procedure considered in this study. Only parameters having a 0.1% or greater magnitude sensitivity were included in this figure. Choroid thickness, irradiation duration, and scleral thickness are among the properties most sensitive to a 1% increase in parameter values.

5.5 Discussion

5.5.1 Model Agreement with Riboflavin Studies

The model's prediction of data from experimental riboflavin studies in the literature provides evidence for satisfactory correspondence of its mathematical assumptions with reality. Good agreement was found for experimental oxygen concentration measurements in porcine corneas, which is notable because the complex triphasic behavior observed experimentally was reproduced by the model[129]. Additionally, the model also predicted relative crosslinking efficiencies observed in experimental studies in the pig eye *ex vivo*. It is interesting to note that these studies were designed to test non-conformity of riboflavin crosslinking with the Bunsen-Roscoe Law[177,237]. Parameters were chosen in the Hammer study to test the applicability of the Bunsen-Roscoe Law, which implies that the extent of crosslinking should be proportional to fluence rather than intensity or irradiation duration. It was found that the Bunsen-Roscoe Law is violated in riboflavin crosslinking in agreement with others[145]. Correspondence of our model with these studies captures an unexpected and well-characterized nonlinear dynamic characteristic of riboflavin crosslinking, the replication of which, was important for model validation.

5.5.2 Effects of MB Concentration, Light Intensity, Inspired Oxygen Concentration, and MB Injection Volume on Crosslinking

Our model results suggest that crosslinking is increased by increases in light intensity over the studied range of 0-424 mW/cm^2 with a nonlinear relationship. However, the effect on crosslinking increase for increasing light intensities is also dependent on MB concentration, with 3 mM and 30 mM concentrations performing best of the four

concentrations modeled (0.03, 0.3 3, and 30 mM). Additionally, the model predicts that inspired oxygen concentration is important, as an increase from 21% to 100% inspired oxygen produced an approximately 6-fold increase in crosslinking. This finding agrees with the model sensitivity analysis which, though only investigating local sensitivities on the range of +1%, found choroidal oxygen concentration to be among the most sensitive parameters correlating positively with crosslinking. This finding suggests that procedures should be performed on subjects breathing elevated levels of oxygen (as safely permitted) rather than atmospheric oxygen.

To elucidate effects of MB diffusion/clearance kinetics on crosslinking, we found nonlinear effects on crosslinking efficiency modeled as a function of MB concentration and injection volume. Similar crosslinking efficiencies found for 30 mM MB at 20-60 μl injection volumes and 3 mM MB at >100 μl injection volume suggest that an optimal MB dose exists as a balance between injection concentration and volume.

5.5.3 Key Model Findings for MB Photocrosslinking as a Function of Space and Time

Light intensity was found to be relatively unchanging in the choroid/sclera throughout the procedure. This corresponds with the findings that 1) most light attenuation occurs in the anterior choroid, and 2) MB (which absorbs photons) diffusion reaches a quasi-steady state linear profile between the injection reservoir and choroid, where the concentration near the choroid is relatively stable. MB concentration decreases over time due to clearance through the choroid and retrobulbar muscle cone. Crosslinking occurs at the anterior choroid and sclera, which is especially pronounced at later time points (after 20 min) and corresponds with a depletion of amino acids and melanin at that location. We believe crosslinking was

favored at the anterior choroid since at that location: 1) oxygen was supplied by the choroid (modeled as a constant-concentration Dirichlet boundary condition), 2) light intensity was highest, and 3) MB dimerization would be lower than at any other location since total MB concentration was lowest near the choroidal sink boundary condition. Increases in concentrations of reactive species (triplet MB and singlet oxygen) corresponded directly with amino acids and melanin depletion near the anterior choroid surface.

Since MB was assumed not to partake in type I reactions, singlet oxygen generation was the only pathway for crosslinking. Despite experiencing lowered oxygen concentrations after the first 3 min of photocrosslinking, the sclera and choroid still sustained significant crosslinking. We believe this can be explained by formation of an equilibrium state whereby oxygen diffuses to the choroid/sclera over a steep concentration gradient. Over the steep gradient, oxygen is rapidly consumed by photochemical processes. While oxygen concentration is decreased due to its rapid depletion by photocrosslinking reactions, we propose that concentration is not indicative of crosslink mechanism or magnitude. Rather, we propose that oxygen flux is most important for crosslinking as it is ultimately responsible for the total mass of oxygen reaching the tissue over time. This hypothesis differs from that of Kamaev et al. who concluded that the low oxygen concentration observed in *ex vivo* porcine eyes during riboflavin crosslinking indicated dominance of oxygen-independent type I reactions. In contrast, our model predicts that the observed decrease in oxygen near the anterior surface of a photocrosslinking procedure may in fact be explained by the activity of oxygen-dependent photocrosslinking mechanisms.

To our knowledge, our model is the first to incorporate individual concentrations of His, Trp, Met, and Tyr, which are the amino acids mainly responsible for crosslinking and

quenching reactions. Additionally, we included melanin in our model, as it has significant presence in the choroid/sclera, unlike in the cornea, during photocrosslinking. Modeling each of these species provided a level of detail into the relative importance of each and deviation in behavior. For example, we found that depletion of His and melanin occurs at a more gradual rate than for other species. We speculate that 1) this is due to their higher chemical quenching rate constants with singlet oxygen relative to the other species, and 2) His and melanin are the dominant quenchers of singlet oxygen in early stages of the procedure, and thus deplete slowly at first when singlet oxygen chemical quenching is lowest. Trp and Tyr on the other hand have the highest rates of physical quenching of singlet oxygen and Trp and Met have the highest rates of physical quenching of triplet MB. When singlet oxygen generation increases due to depletion of His and melanin, subsequent onset of Trp, Tyr, and Met depletion would have an accelerative effect on singlet oxygen generation as they constitute a negative feedback on singlet oxygen generation through physical quenching of reactive species.

Relative contribution of each amino acid to crosslinking was found to occur in the ordering of His > Trp = Tyr where concentration of His crosslinks occurs at 3-fold higher concentration than either Trp or Tyr, which have approximately equal crosslink concentrations. The overall rate of crosslink formation was approximately linear over time for MB photocrosslinking, though a nonlinearity was found in the concentration of Trp-related crosslinks at approximately 18 min where rapid depletion in the choroid corresponded with a temporary jump in crosslinking.

5.5.4 Sensitivity Analysis for MB Photocrosslinking

Current scleral photocrosslinking treatments for glaucoma and myopia are still in early stages of pre-clinical research. Our model provides insights to the key parameters that should receive attention in designing future experiments to optimize crosslinking. Based on our sensitivity analysis, these include parameters linked closely to oxygen penetration (such as oxygen concentration in the choroid and oxygen diffusion constant in tissue) and light propagation (including melanin concentration in the choroid and melanin molar absorptivity). Of the top ten most sensitive parameters, eight were tissue properties and two were properties which can be controlled by the experimenter (irradiation duration and choroid oxygen concentration). However, since 100% inspired oxygen concentration was used in this calculation, it is unlikely that increasing the latter would be a feasible option. The strong representation of tissue properties in our sensitivity analysis suggests that much of the photocrosslinking success would depend on species studied or even individual-to-individual variation. Future studies may attempt even to use this information to develop more creative crosslinking procedure designs.

An unexpected finding of the MB photocrosslinking procedure sensitivity analysis was the relatively low sensitivity of sensitizer parameters. A 1% increase in sensitizer triplet quantum yield, for example, only produced a 0.14% increase in crosslinking. An uninformed assumption would reasonably have been that triplet quantum yield should be directly proportional to crosslinking on a one-to-one basis given it is a necessary step in crosslink formation. However, in light of studies for riboflavin crosslinking indicating violation of the Bunsen-Roscoe Law in that case, such non-linearities should not, perhaps, be surprising. We concluded that over the range of MB photocrosslinking parameters

studied, local optimization of sensitizer properties would likely not be an efficient path towards crosslinking optimization, contrary to our expectations. In this case, efforts would be better spent increasing treatment duration and possibly investigating new avenues of modifying intrinsic tissue properties and reactive sites.

5.5.5 Oxygen Supply Influences Photocrosslinking

Oxygen supply strongly affects scleral photocrosslinking in our model. Corneal crosslinking with riboflavin has been shown to be dependent upon oxygen availability[177]. Furthermore, it is known that the Bunsen-Roscoe Law is violated in riboflavin corneal crosslinking, suggesting that light dose is not solely responsible for crosslinking efficiency[145,177,237]. Instead, it points to the involvement of oxygen in the photochemical processes leading to crosslink generation. We proposed in our model that type I crosslink formation is predominately mediated by a two-step process described in literature: 1) radical formation on aromatic amino acids (we included histidine, tryptophan, and tyrosine), and 2) oxygen reaction with amino acid radicals to form a peroxide intermediate through which subsequent crosslink reactions may occur[258,269]. Since both type I and type II pathways are dependent on oxygen in our fundamental assumptions, our model agrees with Richoz et al. who found that under anaerobic conditions, corneas do not stiffen compared to controls[270].

Recognizing that the pathway for type I-mediated crosslink formation is well under investigation, we anticipate future revision may be needed for the model's type I reaction scheme. Nonetheless, we found good agreement for this scheme with the Kamaev et al. study elucidating oxygen concentration dynamics in *ex vivo* porcine eyes[236]. That study,

however, concluded that oxygen would not contribute to crosslinking after a rapid initial depletion. Our model shows the possibility that in fact, oxygen may be involved at all stages of the irradiation process, despite the observed changes in concentration. Previously it was suggested that low oxygen concentrations in the cornea during photocrosslinking indicated that an oxygen-independent mechanism was responsible for much of the crosslink formation. However, it is possible that concentration may be low, but flux may be high where oxygen participates in crosslinks in equilibrium with the rate of mass transfer, resulting in a steady and significant flux of oxygen to the reaction site, but low concentration.

5.5.6 Data Representation Continuously over Space and Time

In addition to the figures presented in this chapter showing the evolution of each modelled species over space and time, Appendix C contains corresponding heatmap figures for alternative visualization of these data (see Figure 49, Figure 50, Figure 51, Figure 52, and Figure 53). The MATLAB code used to generate the data in this chapter is included in Appendix D.

5.5.7 Model Limitations

While the model is intended to be comprehensive in its scope of physiological and physical factors considered, it not without limitations. First, the model is limited by the experimental accuracy of underlying parameters. For example, it is not uncommon to find large variation in reported literature values for reaction rate constants which could result in inaccurate model results, especially if compounded over many parameters. Interestingly, despite the presence of many reaction rate constants in the model, only two were among the most

sensitive parameters in our MB photocrosslinking sensitivity analysis (quenching of triplet MB by triplet oxygen and chemical quenching of His by singlet oxygen). Additionally, natural variation in tissue properties such as melanin concentration, tissue thicknesses, etc. may result in different experimental crosslinking outcomes in different people. Finally, certain assumptions were required due to the complexities of the posterior scleral environment and availability of known values. For example, we assumed the absence of sensitizer-melanin and sensitizer-collagen binding interactions which are, nonetheless, known to occur in the sclera/collagen[271,272]. Additionally, we assumed a 1-dimensional injection reservoir which can be explained as having thickness equal to the "average" thickness. In reality, the reservoir would likely take the shape of the muscle cone which is difficult to predict or model.

In the case of sensitizer binding to substrate, multiple uncertainties exist. Binding would slow diffusion in the early stage of the treatment when the binding sites have not been fully saturated. Furthermore, binding would both directly quench excited state sensitizer molecules and promote aggregation which would magnify the quenching effect further. On the other hand, triplet state sensitizer interaction with collagen might enhance type I interactions if present. Interestingly, high melanin content of the choroid/RPE may serve as a natural barrier to sensitizer diffusion to the retina, thus reducing the risk of light-activated sensitizer phototoxicity in the retina.

Perhaps the most important limitation of the computational model is its inability to directly calculate changes in tissue mechanical stiffness but instead rely on crosslink utilization or density as a surrogate. Previous studies have characterized the crosslink density-stiffness relationship in collagen fibers and in low-modulus gels, but not in collagenous materials

similar to the cornea/sclera[149,150]. While they likely correlate positively, the nature of the relationship has not been, to our knowledge, characterized for collagen hydrogels of similar density and structure to those of the sclera or cornea. A highly non-linear relationship between crosslinking and elastic modulus would have a significant impact on the conclusions drawn for crosslinker performance. Though the magnitude of stiffening corresponding to changes in crosslinking procedure may not be exactly determined, the model yet provides useful information in the binary sense of increasing or decreasing crosslinking for comparison to a reference procedure.

5.5.8 Future Applications

Our model is useful for simulating photocrosslinking in a variety of potential scenarios. It makes use of common sensitizer parameters such as triplet quantum yield and molar absorptivity, as well as common reaction schemes such as the type I/II pathways, allowing different sensitizers to be compared to one another. Furthermore, it can be applied to multiple animal species with replacement of appropriate tissue properties. Finally, the model can be extended to retrobulbar, sub-Tenon, suprachoroidal, and topical sensitizer delivery methods, all of which may be useful for future scleral photocrosslinking applications.

This study, in addition to providing a mathematical scheme consistent with experimental data, presents a consolidated list of literature parameters for sensitizer and tissue properties relevant for photocrosslinker modeling. Therefore, it is intended to serve as an aggregation of literature references for others seeking to model photocrosslinking in biological tissues.

While many parameters were collected directly from literature, others such as amino acid concentrations were derived from primary sources and may be useful in future studies.

While many model input parameters are available for MB and riboflavin, less studied photosensitizers will require further fundamental research to elucidate these values[273]. Until then, reasonable estimates can be made using sensitivity analyses to assess the effect of such estimates. Future experimental studies elucidating the relationship between crosslinking and stiffness in the sclera and cornea will be of interest for improved predictive computational modeling for guiding expansion of research to new features such as emerging sensitizer molecules. Furthermore, future photocrosslinking studies paralleling those of the corneal crosslinking literature will be needed to validate the model in the case of significant effects from uncertainties such as melanin concentration and drug-melanin interactions.

5.6 Conclusion

In this study, we developed a posterior scleral photocrosslinking model for sensitizer excitation using a transpupillary light beam. The computational model was first validated against existing experimental data for riboflavin corneal crosslinking and subsequently for posterior photocrosslinking using MB sensitizer and tissue parameters from literature. Notably, all model predictions were made using no fitted parameters; all parameters were determined experimentally or from the literature. Light intensity and sensitizer, oxygen, melanin, and amino acid concentrations were modeled over space and time.

A sensitivity analysis of all model parameters revealed that MB scleral photocrosslinking was most sensitive to choroid thickness, irradiation duration, scleral thickness, choroid

oxygen concentration, diffusion constant of oxygen in the sclera, and choroid melanin content, which are parameters closely related to oxygen supply and light penetration, as these appear to be the rate-limiting components of photocrosslinking under the conditions used. Among these parameters, irradiation duration (limited by safety concerns) and choroid oxygen concentration (which cannot exceed that of 100% oxygen saturation in the blood) are to some extent controlled by experimental conditions, whereas the other parameters represent tissue properties that cannot be easily changed.

CHAPTER 6. DISCUSSION

6.1 Targeted Scleral Photocrosslinking using MB

Glaucoma is a leading cause of blindness and is thought to be associated with biomechanical properties of the sclera. We have demonstrated for the first time that transpupillary targeted photocrosslinking is feasible on the millimeter scale to stiffen posterior ocular tissues. While toxicity was found for MB photocrosslinking, considering the proximity of the target peripapillary sclera to both the sensitive optic nerve and retinal tissues and known toxicity of photosensitizers in general, we consider the results to be a promising starting point for future treatment optimization. Desirable criteria selected for development of a transpupillary targeted photocrosslinking approach were:

1. Delivery strategy for introducing sensitizer to posterior sclera
2. Photosensitizer absorbing in the phototherapeutic window (~650-800 nm)
3. Efficient sensitizer production of crosslinks
4. Light intensities which are non-toxic to the retina
5. Sensitizer dark toxicity not damaging to optic nerve and retina

6.1.1 Selection of Retrobulbar Injection as Drug Delivery Strategy

After considering possible sensitizer delivery strategies including retrobulbar injection, sub-Tenon injection, suprachoroidal injection, and subconjunctival injection, we elected to use retrobulbar injections. Compared to sub-Tenon and suprachoroidal injections, retrobulbar and sub-conjunctival injections are far easier to execute without specialized equipment. Retrobulbar injection was chosen over sub-conjunctival injection as we believe

it more efficiently localizes the injection to the posterior sclera, though we have not performed a comparison study. A retrobulbar injection was chosen for these reasons, with an added reason that retrobulbar injection is routinely used in the clinic, thus aiding future clinical translation of the treatment.

6.1.2 Selection of MB as Photocrosslinker

Our selection of methylene blue as the photocrosslinker for our studies was made with consideration of its ease of handling (solubility), a substantial body of existing research on its photophysical properties and other clinical applications, its low cost, its absorbance in the phototherapeutic window (at 665nm), and its reasonable triplet quantum yield efficiency (0.54). Other sensitizers considered were rose bengal, chlorins, porphyrins, and phthalocyanines. However, those most amenable to crosslinking were often difficult to access due to expense or lack of general availability. In our studies, we elected to use MB concentrations similar to those of the existing riboflavin crosslinking procedure.

6.1.3 Light Intensity Selection/Toxicity and MB Dark Toxicity

We used a light intensity exceeding the maximum permissible intensity safety threshold (for humans), reasoning that localized damage at a small beam spot would be a necessary tradeoff for protection of the greater visual acuity preserved through protection against glaucomatous damage. Ultimately, we did not see this protective effect in our glaucomatous rat studies, but we also did not see any evidence for retinal damage from light alone despite exceeding the intensity limits. We believe there is room for future treatment parameter optimization to lower the light intensity if harmful effects are discovered in the future.

Finally, we note that we did not study dark toxicity of MB in the retina or optic nerve explicitly. However, we believe MB alone was not toxic to the retina based on comparisons of histological sections in MB-injected eyes near the ONH and at more peripheral retinal regions. Peripheral regions did not show damage in contrast to the retina adjacent to the optic nerve where both MB and light were present. MB dark toxicity in the optic nerve is possible, especially since we found preferential accumulation of MB in the ON compared to sclera.

6.1.4 Significance of Establishing Experimental Photocrosslinking Protocol

Our experimental findings for targeted scleral photocrosslinking were significant not only for the demonstrated strain reduction effect, but also for the contribution of the targeted photocrosslinking methodology to the field. We constructed a microscope to simultaneously image the rat fundus and project an annular beam of prescribed dimensions around the ONH. This microscope utilized incoherent light at 660 nm near the peak absorbance of MB. It was mounted on a three-axis micropositioner stage for fine spatial targeting, and beam propagation through the cornea was facilitated by a commercially available refraction-negating contact lens. Future studies may be conducted using this methodology with various sensitizers by simply replacing the light source with one matching the sensitizer peak absorbance wavelength. Additionally, beam size may be adjusted to suit the needs of alternative localized crosslinking strategies or peripapillary crosslinking in species other than rats, for which the optics may be easily adapted.

6.2 Targeted Scleral Stiffening Effects on Glaucomatous Rats

Having tested the effects of targeted peripapillary scleral crosslinking in glaucomatous rats, we believe there is not a significant worsening of glaucomatous effects due to crosslinking as was found by Kimball et al.[5]. Included in our studies were morphological and functional investigations of glaucomatous effects including axon count/density, retinal thickness, eye size, resolved spatial frequency, resolved contrast sensitivity, pSTR amplitude, nSTR amplitude, b-wave amplitude, and oscillatory potential amplitude.

6.2.1 Potential Confounding Variable of Treatment Toxicity

Though we could not conclude that stiffening improved glaucomatous outcomes definitively, we have reasons to believe that future studies may be adapted to better test this hypothesis. For example, it is possible that protective effects of MB photocrosslinking were present but negated by the treatment toxicity. Therefore, reduction of treatment toxicity alone may yield positive results. Additionally, we recognized over the course of the study major limitations of the commonly used rat microbead model of glaucoma.

6.2.2 Microbead Rat Model Limitations

Our study, while thorough in scope of morphological and functional measurements, had some limitations worth noting that impact on conclusions and future directions. In our study, IOP increases one to three days after microbead injection saw pressure levels approaching that of ischemic conditions. These pressures then often dropped after three to five days, sometimes to values even below those indicating ocular hypertension. Signs of inflammation or ocular trauma were sometimes observed at 1-5 days post injection,

including redness of the cornea/limbus, cloudiness of the cornea/lens, and fluid discharge from the site of intracameral injection. We speculate from these observations that microbead-induced damage observed may have been in part caused by a temporarily activated inflammatory state of the eye. Such a state could have induced morphological and functional damage superseding that of ocular hypertension alone. If in fact the effects of such damage superseded those due to ocular hypertension alone, then our study would not have primarily measured the scleral stiffening treatment effects for the intended disease conditions. The implications of this possibility are 1) that stiffening may have protected against ocular hypertension-induced damage, but we may not have resolved the effects, and 2) that a more carefully controlled animal model is needed for future glaucoma research. Additional studies testing axon loss in rats treated with microbeads alone (where ocular hypertension does not result) may be used to adjust the axon count data reported in our studies. While this analysis technique does not allow for direct comparisons of axon loss in a contralateral control eye as in a paired design, it may reveal protective effects of crosslinking which were otherwise obscured by the microbead treatment.

6.2.3 Study Duration Limitations

Our study duration was limited to 14 days due to the frequent return of IOP to baseline by that time, indicating the microbead model was unable to sustain long-term ocular hypertension matching that of clinical glaucoma. It is possible that for rats having low but sustained IOP burdens tested for longer time scales, morphological and functional outcomes may have differed from the observations seen on the two-week time scale. Given that our MB photocrosslinking strain reduction effect was measured up to 6 weeks, the

stiffening treatment may be readily tested should an improved long-duration ocular hypertension animal model replace the microbead model.

6.2.4 Clinical and Research Impact of Microbead Study

From a clinical perspective, our microbead rat study does not support immediate investigation of photocrosslinking treatments for clinical translation. However, we are optimistic that stiffening treatments may find positive results in future studies with modified animal models where glaucomatous damage can be more precisely controlled. From a preclinical research perspective, this study provides a wealth of information against which future studies may be compared. For example, it contains control data for mechanical, ERG, OMR, OCT, eye size, and axon counts. It also contains baseline values in some cases for the effects of treatment parameters prior to crosslinking (as in the case of OMR).

6.3 Computational Model for Scleral Photocrosslinking

Having developed a computational model simulating corneal and scleral photocrosslinking, we discovered insights relevant to optimization of future MB crosslinking procedures. Additionally, we have demonstrated that a theoretical basis may be established to help explain existing photocrosslinking observations in riboflavin corneal photocrosslinking. This study expands an existing body of research traditionally focused on riboflavin crosslinking to the domains of scleral crosslinking using sensitizers other than riboflavin.

6.3.1 Photocrosslinking Dynamics Insights Relevant for Riboflavin Crosslinking

Though applied to a different sensitizer and tissue scenario than riboflavin crosslinking, the MB photocrosslinking simulation suggests that previous conclusions drawn for riboflavin crosslinking may require additional investigation. It has been suggested that oxygen-independent type I reactions must dominate in the low oxygen concentration environment observed in riboflavin crosslinking [236]. Our simulation, however, demonstrates that oxygen depletion may occur with continued oxygen-dependent crosslinking taking place despite low oxygen concentrations. We believe this phenomenon can be explained by the ever-present flux of oxygen over the steep concentration gradient in the anterior surface of the tissue undergoing crosslinking (choroid/sclera in the MB case). This finding has bearing on the ongoing discussion of whether type I or type II processes dominate riboflavin crosslinking.

6.3.2 Elucidation of MB Diffusion and Clearance Kinetics in Retrobulbar Tissue

Model development required accurate simulation of transport properties of MB in the retrobulbar tissue. Our experimental studies measuring the MB diffusion constant and concentration in the sclera 30 minutes post-injection not only enable the combined photocrosslinking model, but in themselves are useful for understanding retrobulbar transport of a small molecule. The complete photocrosslinking model is effectively comprised of three modules – the first encompassing light propagation/absorbance, the second encompassing chemical reactions, and the third encompassing transport phenomena (diffusion and clearance). The latter, describing retrobulbar transport phenomena, is itself

a useful tool even separate from the combined model for studying retrobulbar drug delivery.

6.3.3 MB Photocrosslinking Dynamics Affected by MB Concentration

After simulating our experimental MB photocrosslinking parameters with the computational model, we found a number of interesting results which have bearing on future treatment optimization. First, the finding that a local maximum in crosslinking efficiency exists as a function of sensitizer concentration is important for understanding photocrosslinking dynamics and practically for enhancing crosslink formation. We believe this maximum is likely caused by insufficient molecules for crosslinking at low concentrations and either dimerization, excessive light absorbance, or excessive oxygen consumption at high concentrations. Injection reservoir volume and MB concentration jointly determine total dose. Injection volume may be used to accommodate various sensitizer concentrations as the two appear to jointly influence crosslinking above 3 mM MB concentration.

6.3.4 MB Photocrosslinking Dynamics Affected by Oxygen Concentration

Oxygen concentration was found to have a substantial impact on crosslinking. Future studies should aim to supply oxygen to the sclera/choroid either through increased inspiration concentration or other means. For example, perhaps addition of oxygen generating species in the injection solution should be considered to enhance crosslinking. This strategy would require careful consideration as evolution of gasses within the tissue could have problematic consequences. Another possibility is injection of oxygen through a syringe to the retrobulbar space. In riboflavin crosslinking, the oxygen supply is naturally

higher than that of the interior tissues due to direct atmospheric exposure of the cornea. In the retrobulbar injection case, however, it is still possible to have a gaseous interface from which oxygen may be dissolved and diffused into tissue. We believe this approach would be safe, provided localized hyperoxia does not present toxicity issues.

6.3.5 MB Photocrosslinking Dynamics Affected by Light Intensity

Increased light intensities were found to improve crosslinking. Interestingly, for riboflavin crosslinking, this is not the case, and though MB photocrosslinking behaves differently, the effect of increasing intensity is still highly nonlinear, suggesting complex involvement of other processes such as oxygen diffusion. Longer wavelength excitation sources should improve crosslinking efficiency due to decreased absorbance by melanin and increased number of photons for a given fluence. The finding that MB photocrosslinking does not violate the Bunsen-Roscoe Law in the same way as does riboflavin crosslinking is an important finding which perhaps reflects the differences between type I and type II photosensitization processes.

6.3.6 MB Photocrosslinking Sensitivity Analysis

Finally, our sensitivity analysis revealed parameters of greatest importance for local parameter optimization in our MB photocrosslinking procedure. That tissue properties comprised eight out of the ten most sensitive parameters is an interesting finding which may have ramifications on studies conducted across various species. The two most sensitive parameters positively correlated with crosslinking were treatment duration and oxygen concentration in the choroid. We are optimistic that alternative strategies to improve crosslinking may be employed to enhance oxygen concentration at the site of

crosslinking. Perhaps unexpectedly, changes in sensitizer properties had relatively little impact on the magnitude of crosslinking. This may be encouraging as it perhaps opens the possibility to using less efficient sensitizers with more favorable toxicity profiles or other desirable properties. On the other hand, it indicates that improvement of crosslinking would need to come through other strategies. Naturally, the sensitivity analysis is relevant only to the specific parameters considered for our MB photocrosslinking treatment, and thus the results may vary under other combinations of default parameters.

6.3.7 Extrapolation to Larger Eyes Based on Sensitivity Analysis

The fact that choroid and scleral thicknesses were the two strongest negative correlates with crosslinking suggests that perhaps the transpupillary photocrosslinking approach will be less effective in larger eyes, though the sensitivity analysis should only be interpreted to the +1% parameter deviations analyzed. Should scaling to larger eyes prove to be difficult in future studies, transpupillary photocrosslinking may need to be enhanced with previously unexplored means. Perhaps crosslinking duration, for example, would need to be improved in a creative fashion harnessing natural light or other artificial sources over extended durations. Nonetheless, we reserve judgement on crosslinking efficiency in larger eyes until we have completed a future sensitivity analysis.

6.3.8 Model Limitations and Assumptions

Our model assumed a 1-dimensional spatial domain representative of a tissue cross-section in the peripapillary region where photocrosslinking would take place. The 1-dimensional assumption is inferior to a 2 or 3-dimensional assumption as a 1-dimensional model would not account for certain changes over more complex spatial domains. Parameters for which

inhomogeneous spatial distribution would be expected in such cases include light intensity and concentration of diffusing species. For example, light scattering was neglected in the model, but is likely to have resulted in decreased light intensities near the perimeter of the irradiated annular region. Photons entering the fundus near the perimeter may be scattered away from the peripapillary sclera, thus not inducing crosslinking. Additionally, oxygen concentration in the choroidal blood supply may become depleted differentially over the surface of the fundus. This may occur if MB present in the bloodstream becomes activated by incident light, thus consuming oxygen in photochemical processes within the blood vessels.

The model includes several assumptions used to bridge gaps in available literature information, decrease computational expense, and/or focus on experimental circumstances of interest. Specifically, we:

1. Neglected substrate-sensitizer binding interactions which could have increased quenching of sensitizer triplets
2. Neglected higher order aggregation of sensitizer molecules in favor of simpler monomer-dimer model
3. Assumed similar kinetics (but not equilibrium state) of sensitizer binding for riboflavin as for MB
4. Assumed constant oxygen concentration in the choroid and retrobulbar tissue source conditions
5. Assumed perfect clearance of sensitizer at the choroid and retrobulbar tissues
6. Assumed the distance to clearance boundary condition in the retrobulbar muscles was equal to the thickness of the choroid

7. Assumed homogeneous distributions of the amino acids and melanin
8. Assumed 100% of collagen was type I collagen
9. Approximated injection reservoir layer thickness using an estimate for muscle cone geometry
10. Neglected reaction of His, Trp, and Tyr residues with one another, instead assuming each reacted stoichiometrically with lysine which exists in excess concentration compared to these three
11. Neglected non-productive oxidation products of His, Trp, and Tyr residues after chemical reaction with singlet oxygen
12. Neglected kinetics and quenching of the singlet sensitizer, instead using triplet quantum yield to convert absorbed photons to triplet excited state species
13. Assumed irradiation began instantaneously after injection, not accounting for the experimental lag time between injection and application of light
14. The melanin concentration in the sclera was back calculated from melanin molar absorptivity and the approximate percentage of light known to penetrate the fundus

These assumptions, while numerous, were necessary to approximate the complex photosensitization processes *in vivo*. Future studies will be needed to eliminate some assumptions where information is lacking in the literature. Our model sensitivity analysis showed that the most sensitive parameters were not among those affected by these assumptions. However, that analysis assessed local sensitivities, and it does not therefore inform an investigator of changes in model outcomes with drastic changes in underlying assumptions.

CHAPTER 7. CONCLUSIONS

7.1 Targeted Scleral Photocrosslinking using MB

7.1.1 Targeted Peripapillary Stiffening Achieved in Rats

Our study is a proof of concept illustrating that MB photocrosslinking reduces scleral strain by as much as 56% at 6 weeks after treatment compared to untreated controls when excited with a transpupillary light source. Furthermore, stiffening was targeted to the peripapillary sclera, which we defined as the annular region having 2 mm outer diameter and 1 mm inner diameter centered on the optic nerve in the rat eye. To achieve targeted stiffening, we constructed a microscope capable of simultaneously projecting an annular beam onto the fundus while viewing the beam spot. Compared to the peripheral region of the treated eye, MB photocrosslinking reduced strain by as much as 47% in the peripapillary region compared to the peripheral region. Selective peripapillary crosslinking was therefore confirmed as successful using this approach.

7.1.2 Toxicity Characterization

Additionally, photocrosslinking procedure toxicity was characterized and found to have statistically significant effects on axon loss and retinal function. Axon count was decreased by 24% in rats receiving photocrosslinking treatment and ERG function was decreased with respect to pSTR amplitude, A-wave amplitude, B-wave amplitude, and PhNR amplitude. Damage was found to be localized to regions where both MB and light were present as indicated by histology. Light alone did not produce any visible damage in retinal histological sections.

7.2 Targeted Scleral Stiffening Effects on Glaucomatous Rats

7.2.1 Targeted Stiffening Confirmed in Glaucomatous Rats

Despite not having found significant protective effects of targeted peripapillary photocrosslinking with MB, we did confirm targeted stiffening (supporting our initial studies in healthy rats). For example, mean strain at a pressure of 22 mmHg was 2.41% strain in MB treated peripapillary sclerae compared to 6.07% strain in HBSS-treated controls. Peripheral strains did not differ significantly between MB and HBSS-treated groups, with mean strains of 4.51% strain for MB and 4.52% strain for HBSS.

7.2.2 Stiffening Did Not Worsen Glaucomatous Damage

Overall, targeted photocrosslinking did not significantly prevent or exacerbate glaucomatous damage in a rat microbead model compared to control HBSS (vehicle). However, we do not conclude definitively that targeted peripapillary photocrosslinking is inefficacious due to experimental limitations of the microbead animal model. Future studies will be needed with an improved animal model to determine conclusively the effects of scleral stiffening on ocular hypertension-induced glaucomatous damage.

7.2.3 Comparison with Stiffening Study of Kimball et al.

Targeted peripapillary scleral stiffening did not confer significant protective or damaging effects in a rat microbead model of glaucoma. Importantly, these data contrast with the study by Kimball et al. in which increased damage was found in mice with whole-sclera stiffening with glyceraldehyde in a microbead model of ocular hypertension[5]. The contrasting conclusions of these two studies is difficult to explain and could involve the 1)

difference in species, 2) difference in crosslinking agent, and 3) difference in crosslinking location. It is possible, for example, that the volume and concentration of injections in the Kimball et al. study resulted in additional toxicity that we did not observe in our study. In our studies, genipin served as an important positive control for whole-sclera stiffening. It was found that genipin, while stiffening the whole sclera, did not produce axon loss in excess of control eyes as was seen in the Kimball study, suggesting that either a difference existed in the stiffening extent/location or that treatment toxicity may explain the observed axon deficit seen in the Kimball study.

7.3 Computational Model for Scleral Photocrosslinking

We developed a theoretical predictive computational model simulating photocrosslinking dynamics in corneal and transpupillary scleral photocrosslinking scenarios that required no fitted parameters. The model used a finite difference scheme in 1-dimensional space to create and solve a system of ordinary differential equations in time for diffusion, light propagation, and chemical reaction phenomena. The model was validated against existing literature experimental data for riboflavin corneal crosslinking and subsequently used to model MB scleral photocrosslinking by substituting parameters available from the literature for the appropriate sensitizers and tissues involved.

7.3.1 Model Validation against Existing Riboflavin Crosslinking Experimental Studies

As an important validation step, our model was able to replicate oxygen concentration reported in literature by Kamaev et al. for *ex vivo* riboflavin crosslinking in porcine eyes [236]. Oxygen concentration was chosen for this important validation step because it depends in a complex way on all three model components – diffusion kinetics, light

propagation, and reaction dynamics. Furthermore, oxygen is central to crosslink chemistry and is the subject of much interest for understanding the relative involvement of type I and type II photochemical processes in crosslinking. This is the first time to our knowledge that a computational model was used to successfully replicate this experiment.

In addition, we demonstrated good agreement of the computational model's prediction for crosslinking magnitude by comparing with stiffening and enzymatic degradation studies investigating lack of concurrence of riboflavin crosslinking with the Bunsen-Roscoe Law. Our model shows good agreement with the data of Hammer et al. and Aldahlawi et al. who both showed that riboflavin crosslinking violates the Bunsen-Roscoe Law using mechanical tensile testing and enzymatic degradation, respectively. Both methods assess crosslink density implicitly by measuring corneal resistance to mechanical force and chemical degradation. Therefore, together, they provide two different points of reference supporting the experimental correspondence of crosslink formation with our model's prediction.

7.3.2 Measurement of Retrobulbar Clearance/Diffusion Kinetics

Having validated the computational model's underlying assumptions in the riboflavin crosslinking cases, we experimentally measured clearance and diffusion kinetics of MB in the retrobulbar space, determining the diffusion coefficient of MB to be 3.16×10^{-7} cm^2/s. Additionally, we measured the concentration of MB remaining in the sclera of Brown Norway rats at 30 minutes post-injection to be 14.4% of the initial injection concentration. Together, these experimentally derived values showed excellent agreement with our computational model's mass transport assumptions which predicted a scleral MB

concentration of 13.8% at 30 minutes post-injection, well within one standard deviation of our experimental measurement.

7.3.3 Effects of Experimentally Controlled Parameters on MB Scleral Photocrosslinking

We analyzed effects on crosslinking of parameters most easily controlled by experimental design in photocrosslinking studies including light intensity, injected sensitizer concentration, injection volume, and inspired oxygen concentration. Our model predicted that approximately 30% of all available crosslinking sites were utilized for the experimental conditions used in our proof of concept studies. We found that light intensity is generally positively correlated with crosslinking but depends on MB concentration. Crosslinking magnitude, for example, was similar for 30 mM MB injection concentration as for 3 mM injection concentration despite an order of magnitude difference (for 100% inspired oxygen case). Injection volume also importantly influenced crosslinking with larger injection volumes being more advantageous in all cases except for high MB concentrations (30 mM) where crosslinking goes through a local maximum at approximately 42 μl injection volume. An inspired oxygen concentration of 100% was found to be more advantageous for all MB concentrations studied (0.03, 0.3, 3, 30 mM), to be more advantageous with crosslinking magnitudes being approximately 6-fold higher for the conditions used in our MB photocrosslinking procedure. These results suggest that if our procedure were conducted with rats breathing atmospheric oxygen, the crosslinking magnitude would be significantly decreased compared to anesthesia with isoflurane and 100% oxygen. Finally, crosslinking as a function of MB concentration experiences a local maximum at around 8 mM resulting in 32% crosslinks utilized compared to 30% crosslinks

utilized at 3 mM. Below 3 mM and above approximately 15 mM, efficiency declines below 30% crosslinks utilized.

7.3.4 Evolution of Model Components over Time and Space

Additionally, we simulated the evolution of reactive species involved in MB photocrosslinking including light, MB, oxygen, amino acids, and melanin over time and space (choroid/sclera). Light intensity and MB concentration were found to quickly reach quasi-steady state profiles. Oxygen concentration was rapidly depleted through most of the sclera/choroid, resulting in a steep concentration gradient near the anterior choroid. The amino acids His, Met, Trp, and Tyr along with melanin were consumed by photochemical generation of singlet oxygen. Their initial depletion, which reduced both their chemical and physical quenching magnitudes locally at the anterior choroid surface, lead to their accelerating depletion over time. As a result of the observed changes in oxygen concentration and amino acids/melanin, we concluded that oxygen flux is important for supplying the oxygen-dependent crosslinking reactions and that oxygen flux is more important than oxygen concentration.

7.3.5 MB Scleral Photocrosslinking Parameter Sensitivity Analysis

Finally, we conducted a sensitivity analysis for the MB photocrosslinking model parameters using the conditions from our previous experimental proof of concept studies as a baseline against which deviations were compared. Crosslinking, represented as a percentage of available crosslinks utilized, was used as the model output for which effects of underlying parameter deviations were compared. We found that parameters related to tissue properties such as choroid and sclera thickness, melanin concentration in the choroid,

and diffusion constant of oxygen in the choroid/sclera, comprised eight of the top ten most sensitive parameters. Only irradiation duration and oxygen concentration in the blood were experimental parameters unrelated to tissue properties within the top ten most sensitive parameters. However, these were the two parameters having the largest positive impact on crosslinking.

7.4 Summary

In conclusion, we have 1) demonstrated the viability of MB photocrosslinking for inducing locally targeted scleral stiffening at the peripapillary sclera, 2) tested targeted MB scleral photocrosslinking effects on visual and morphological outcomes in glaucomatous rats, and 3) created a computational model demonstrating concurrence with existing riboflavin crosslinking experiments and predicting MB scleral photocrosslinking dynamics in space/time, providing insights for future treatment optimization. These studies represent the first use of a targeted transpupillary scleral photocrosslinking approach on the millimeter length scale, the first investigation of targeted peripapillary scleral crosslinking for treatment of glaucoma, and the first computational model simulating scleral photocrosslinking.

7.5 Publications Resulting from This Work

This work has resulted in the following publications, three of which are currently being drafted for publication. These include:

1. Gerberich BG, Hannon BG, Hejri A, Winger E, Schrader E, Nichols L, Gersch H, MacLeod N, Read T, Sridhar S, Ritch M, Toothman M, Gershon G, Schwaner S, Grossniklaus H, Pardue MT, Ethier CR, Prausnitz MR. Selective Stiffening of Peripapillary Sclera by Transpupillary Photocrosslinking.
2. Gerberich BG*, Hannon BG*, Read AT, Ritch MD, Schrader E, Nichols L, Pontis C, Sridhar S, Schwaner SA, Toothman M, Huang H, Gershon G, Feola AJ, Pardue MT, Prausnitz MR, Ethier, CR.
3. Gerberich BG, Radmand, Hejri A, Nichols L, Schrader E, Gersch H, Prausntiz MR. A Prediction of Scleral Photocrosslinking using a Computational Model.
4. Bailey G. Hannon, Stephen A. Schwaner, Elizabeth M. Boazak, Brandon G. Gerberich, Erin J. Winger, Mark R. Prausnitz and C. Ross Ethier 2019Sustained scleral stiffening in rats after a single genipin treatment. J. R. Soc. Interface.1620190427. http://doi.org/10.1098/rsif.2019.0427

CHAPTER 8. FUTURE DIRECTIONS

8.1 Targeted Scleral Photocrosslinking using Methylene Blue

Scleral photocrosslinking holds promise for the future of glaucoma and myopia treatment. In addition to these two clinical applications, there exist two technical challenges upon which future research may expand: 1) improved precision in crosslink spatial resolution, and 2) improved safety/efficacy profiles. We believe both areas may be addressed by ongoing research expanding the field of available sensitizers with enhanced properties suitable for these applications.

Improved spatial resolution of the crosslinked area will be an important future technical objective for treatment of both glaucoma and myopia for different reasons. In the case of glaucoma, peripapillary region requiring crosslinking has been shown to be linked to lamina cribrosa strain, but the exact diameter of the peripapillary space requiring crosslinking to reduce lamina cribrosa strain is yet uncertain. Increasing crosslinking spatial control will allow for localization to an even finer length scale having the dual effects of 1) reducing off-target stiffening, and 2) increasing the possible treatment strategies available. With finer spatial control, for example, targeting may eventually be localized to precise tissue depths rather than simply to two-dimensional regions defined by a light projected on the fundus. Addition of spatial control in the depth axis would potentially enable direct crosslinking of the lamina cribrosa in addition to, or in place of, peripapillary scleral crosslinking.

In the case of myopia, it may be advantageous to have greater spatial control of crosslinking in order to not only slow elongation of the eye, but perhaps even to reverse and nullify refractive errors through spatial modification of mechanical properties. For example, a patterned stiffening approach may cause collagen remodeling and redistribution of force at un-crosslinked regions. Clinically, non-uniform beam intensity profiles have been used to improve refractive error in riboflavin corneal crosslinking for treatment of keratoconus, suggesting the importance of spatial crosslink density for altering tissue shape[274,275].

Photocrosslinking safety should be a subject of importance in future studies and may be improved through increased spatial control and through advancement of new sensitizers with increased crosslinking efficiency. Improved spatial control will reduce the area affected by the crosslinking procedure, thus decreasing the total potential damage caused to the fundus and surrounding tissue. Improved crosslinker efficiency will allow for reduced light intensities to be used which would have the dual effects of decreasing the dose of photons to which the retina will be exposed as well as decreasing the potential for sensitization of non-targeted tissues by scattered photons.

Emergence of new photocrosslinkers will aid in reducing photocrosslinking procedure toxicity through a few different possible strategies. First, sensitizers enabling use of longer wavelengths would enhance photocrosslinking efficiency and safety. Second, the fundus is less absorptive at longer wavelengths, thus reducing the input energy dose required to achieve photocrosslinking. Third, longer wavelength photons are lower energy, meaning more photons are generated by the light source for an equivalent total energy dose compared to shorter wavelengths. Already, there exist sensitizers with absorbance at longer

wavelengths such as WST11 and indocyanine green holding promise for posterior targeted photocrosslinking[276,277].

Overall, scleral photocrosslinking is an area of ongoing active investigation, and this work contributes to the body of literature by demonstrating feasibility of a spatially targeted transpupillary crosslinking strategy. It is our desire that this work will inspire additional studies to improve photocrosslinking procedure toxicity using a transpupillary illumination source. Additionally, we hope applications for treatment of previously unconsidered ocular pathologies may be explored due to expanded access to posterior targeted scleral crosslinking described in this works.

8.2 Targeted Scleral Stiffening Effects on Glaucomatous Rats

While microbead-induced glaucomatous damage was not mitigated by targeted peripapillary scleral stiffening in this study, the effects of such scleral crosslinking on treatment of glaucoma are yet uncertain. Certain limitations of the study prevent us from making definitive conclusions. Specifically, the microbead rat model had significant limitations in its ability to replicate long-term hypertensive glaucomatous damage and therefore leaves room for future investigation. For example, in Chapter 4 it was explained that exclusion criteria were needed to remove rats from the study which had retinal electroretinography deficits uncharacteristic of glaucomatous damage. Additionally, it is unclear to what extent treatment toxicity may have played a role in lack of protective effects observed in this study.

Future studies should seek to develop improved glaucomatous animal models more closely replicating ocular hypertension-induced damage. Additionally, these models should be

well characterized over the extended time scales necessary to assess effects of biomechanical alterations on hypertension-induced damage. Protective effects of targeted peripapillary scleral stiffening may be efficacious in preventing glaucomatous damage on these longer time scales, although they were not observed over the short duration of our studies.

Photocrosslinking treatment toxicity alone was characterized in our studies to be moderate and is therefore a difficult effect to disentangle from the damaging effects of the microbead model. Future studies should seek to disentangle these effects, or better, to eliminate photocrosslinking procedure toxicity. We found that exceeding maximum permissible intensity limits for beam intensity by a factor of approximately 3-fold did not cause observable damage to the retina. This finding may be explained by the fact that maximum permissible ocular intensity limits have a 10-fold safety factor adjustment from the intensity at with 50% probability of minimum visible lesion is expected[123].

8.3 Computational Model for Scleral Photocrosslinking

In this study, a computational model was developed from experimental data in literature for riboflavin corneal crosslinking and substituted for parameters corresponding to methylene blue photocrosslinking in the posterior sclera. The model enables a host of future predictive studies which may be used to support future clinical procedure execution as well as experimental research towards advancement of photocrosslinking procedures in both the sclera and cornea.

Assuming scleral photocrosslinking finds future clinical use, our model may be used to tailor the treatment parameters to individual patients. For example, variations in individual

tissue thicknesses and melanin content may be accounted for to adjust light intensity, injection concentration, and treatment duration. Interestingly, the individual-specific parameters mentioned here are ones for which crosslinking was found to be most sensitive in our model's sensitivity analysis.

Our model can be adapted to predict photocrosslinking efficiency as a function of injection location not only in the retrobulbar space, but also for suprachoroidal injections, sub-Tenon injections, sub-conjunctival injections, and topical photosensitizer delivery. These may be achieved by simply modifying the spatial domain properties of the tissue layers considered while maintaining the photophysical and transport properties. However, in some cases, additional transport phenomena may need to be elucidated experimentally. For example, for a suprachoroidal injection, adjacency of the injection reservoir to the choroid opens the possibility of convective flux in addition to diffusive flux.

The model may additionally be used for various taxonomic species of interest. We have compiled literature data for humans, pigs, and rats pertaining to tissue thicknesses and amino acid concentrations. Therefore, sensitizer performance may be predicted in humans for clinical interest as well as for pre-clinical studies. Differences in photocrosslinking efficiencies in humans and animals would not be surprising, and the model can therefore provide important predictive capabilities to determine which species would be most appropriate for preclinical studies. Alternatively, in cases where human clinical translation is not of interest, but rather fundamental research is of interest, the model may be able to assist in species selection.

Finally, the model is useful for comparing efficacy of various sensitizers if sensitizer-specific input parameters are available. As fundamental research continues to expand the selection of available sensitizers, the need to predict which properties will be most suitable for crosslinking under circumstances of interest will increase. Additionally, our model may be used to inform future fundamental studies seeking to design sensitizers with optimal properties for specific crosslinking applications. Therefore, the model may be likened to existing computational models used to predict pharmacokinetics *in vivo* as it can be used both for predicting performance of existing sensitizers and may be used to predict optimal sensitizer properties which future research should aspire to emulate.

APPENDIX A. SUPPLEMENTAL INFORMATION FOR CHAPTER 3

8.4 OCT Images

OCT imaging was performed on the cohort of rats receiving light only (*n*=3). There is no apparent damage from light alone, further supporting retinal histology findings indicating that light alone does not damage the retina.

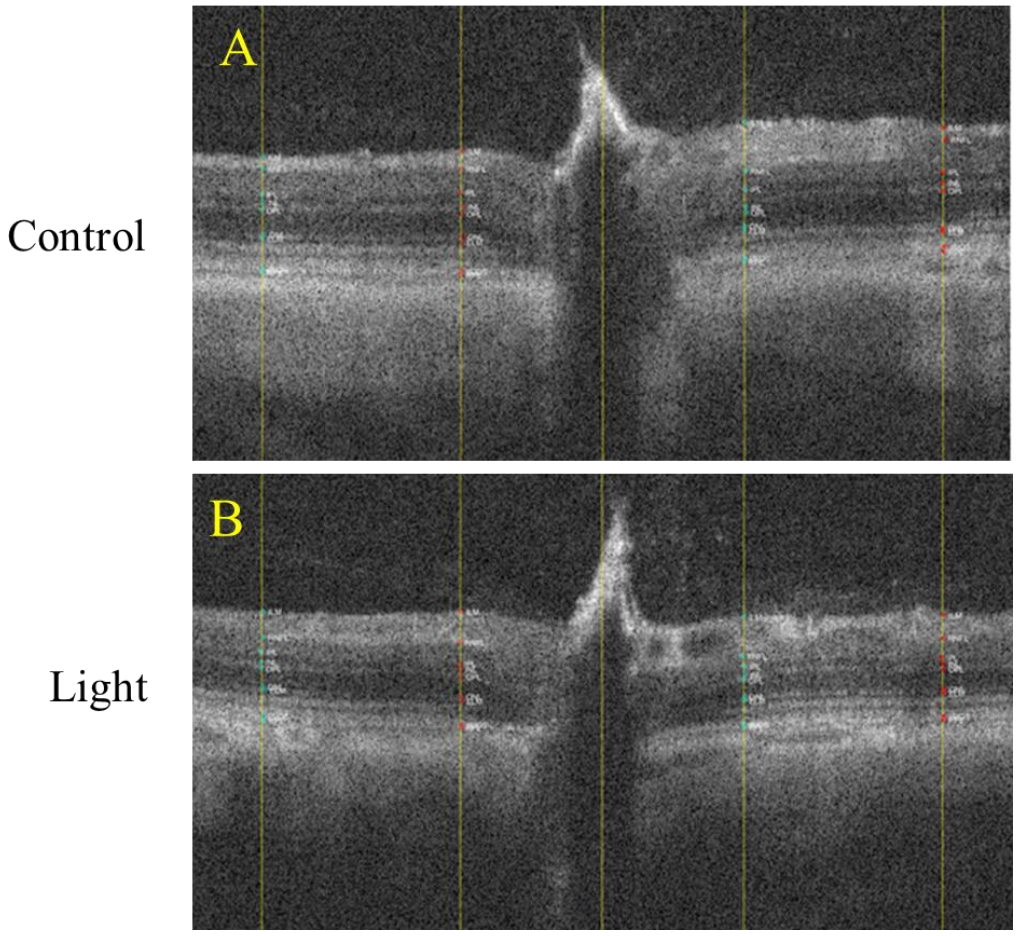

Figure 36: Representative OCT images from rat eyes treated with a targeted light beam without methylene blue. A) Control (untreated eye receiving no light exposure) and B) Contralateral eye exposed to 424 mW/cm^2 660 nm light treatment for 30 min without methylene blue using the same apparatus and protocol as used for selective photocrosslinking.

8.5 Surface area of sclera affected by targeted photocrosslinking

The photocrosslinked peripapillary sclera area represents a fraction of the total eye surface area, f_{surf}, equal to:

$$f_{surf} = \frac{\pi(r_2)^2 - \pi(r_1^2)}{4\pi(R)^2} \tag{38}$$

where r_1 and r_2 are the inner and outer radii of the annular light beam, and R is the radius of a rat eye. Thus, for the annulus size referenced (1 mm outer radius, 0.5 mm inner radius) and a rat eye diameter assumed to be 7 mm, the fraction of total eye surface area with reduced compliance would be 1.5%. Therefore, a large majority of the eye's compliance would be preserved with targeted scleral stiffening.

8.6 Calculation of percent strain reduction from Coudrillier et al [4]

Coudrillier et al. stiffened the peripapillary sclera of *ex vivo* porcine eyes and reported average strain versus pressure in Figure 7c of that manuscript. From this figure, we extracted the average peripapillary strain values at a pressure of 22 mmHg, which was used in our study. The extracted values were 21.5 mStrain for control and 13.3 mStrain for crosslinked eyes. From this we calculated the percent strain reduction according to:

$$\varepsilon_{\%} = \frac{\varepsilon_{ctrl} - \varepsilon_{exp}}{\varepsilon_{ctrl}}$$

where $\varepsilon_{\%}$ is the percent decrease in strain, ε_{ctrl} is the strain of the control eye, and ε_{exp} is the strain of the experimentally stiffened eye. The calculated percent decrease in strain at 22 mmHg in the Coudrillier et al. study was therefore 38% according to this calculation.

8.7 Calculation of maximum permissible intensity for 660nm red light

8.7.1 Maximum Permissible Radiant Power

We calculated the maximum permissible intensity for our photocrosslinking protocol based on guidance from the standards developed by the American National Standards Institute (ANSI) using the approach reported in Delori et al. [123]. From Table 3 in the Delori paper, maximum permissible radiant power, MP$\boldsymbol{\phi}$, (Watts) for an 1800s illumination exposure time is given by:

$$MP\Phi = 6.93 \times 10^{-4} C_T C_E P^{-1} t^{-0.25}$$

where C_T and C_E are functions of wavelength, P is a function of wavelength and the light source's angular subtense, and t is time in seconds. Using the derived values of these parameters shown below, we arrived at the value of $\mathbf{MP\phi = 4.96\ mW}$ spread over our beam area, A, calculated as:

$$A = \pi r_2^2 - \pi r_1^2$$

where r_2 and r_1 are the outer (0.1 cm) and inner (0.05 cm) beam annulus radii, respectively. We calculated A to be 0.0236 cm^2. Dividing MP$\boldsymbol{\phi}$ by A, we arrived at the final maximum permissible intensity of $\mathbf{211\ mW/cm^2}$.

Closer examination on the ANSI standard shows that the permissible illumination intensity has a factor of 10 margin of safety built into it below the intensity at which damage is expected with 50% probability. This suggests intensities exceeding the maximum permissible intensity may be tolerated with relatively low incidence of damage.

8.7.2 Angular Subtense, α

The beam's angular subtense, α, was calculated according to the equation on page 1252 of the Delori paper which is a small angle approximation:

$$\alpha = 2\tan^{-1}\frac{d_r}{2f_e} \approx \frac{d_r}{f_e}$$

where d_r is the diameter of retinal exposure and f_e is the eye's focal length, assumed to be 1.7cm. Assuming d_r to be 0.2 cm, we calculated **α = 117.6 mrad**.

8.7.3 Value of Parameter, C_T

C_T for a 660 nm light source is 1, according to Table 3 in the Delori paper.

8.7.4 Value of Parameter, C_E

C_E for an "extended" light source having an angular subtense greater than 100 mrad, according to Table 2 in the Delori paper, is:

$$C_E = 6.67 \times 10^{-3}\alpha^2$$

which, when substituting for α = 117.6 mrad gives **C_E = 92.2**.

8.7.5 Value of parameter, P

The pupil factor, P, for a 660 nm light source and illumination time greater than 0.7 seconds is:

$$P = 10^{0.0074(700-\lambda)}$$

where **λ** is the wavelength in the light source in nanometers. Since our source is 660 nm, we calculated **P = 1.977**.

APPENDIX B. SUPPLEMENTAL INFORMATION FOR CHAPTER 4

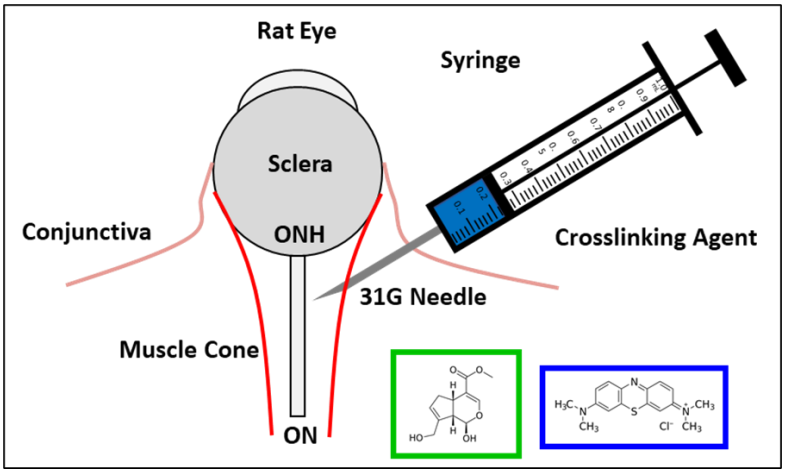

Figure 37: Chemical crosslinker genipin (left inset) or photocrosslinker methylene blue (right inset) were injected by retrobulbar injection to induce scleral crosslinking. Genipin induced non-targeted crosslinking. Methylene blue was activated with a transpupillary light beam to selectively crosslink peripapillary sclera.

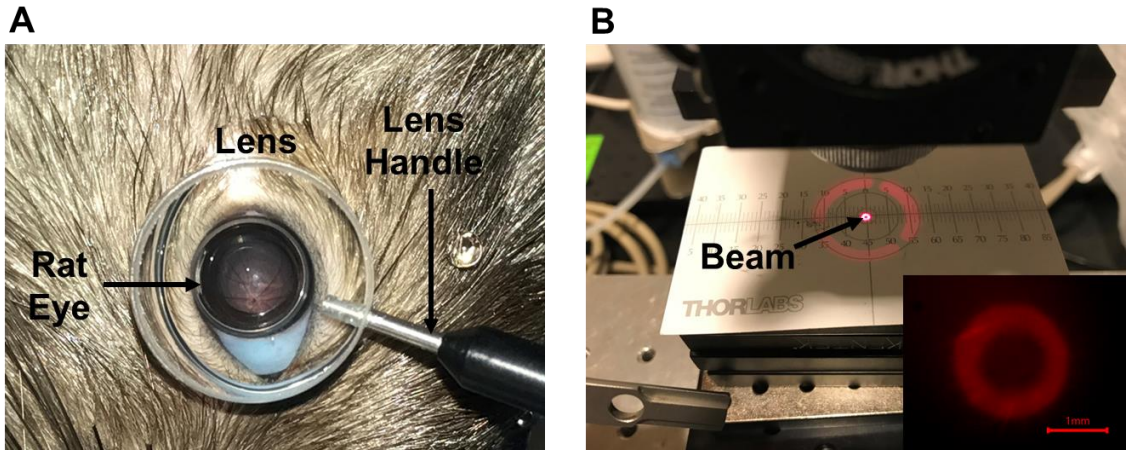

Figure 38: A) Image of BN rat fundus viewed through refraction-negating corneal contact lens showing optic nerve head and retinal vasculature. The lens created a clear optical path facilitating B) projection of an annular beam (measuring 2 mm outer diameter, 1 mm inner diameter) of 660 nm incoherent light from a custom-designed microscope to the peripapillary sclera following retrobulbar injection of MB. The inset shows an image of the beam projected onto a BN rat fundus as viewed using the microscope's camera (inset scale bar = 1 mm).

Table 13: Table of experimental variables investigated in this study compared with those of the Kimball et al. 2014 study which investigated effects of scleral crosslinking on visual/morphological outcomes in glaucomatous mice.

Variable	Kimball et al. (2014)	Genipin Crosslinking	Methylene Blue Crosslinking
Animal	Mouse	Rat	Rat
Model of Glaucoma	Microbead	Microbead	Microbead
Crosslinking Agent	Glyceraldehyde	Genipin	Methylene Blue
Photoactivation	No	No	Yes, 660 nm
Concentration	500 mM	15 mM	3 mM
Targeted scleral region	Sclera	Sclera	Peripapillary Sclera Only
Injection Method	Subconjunctival	Retrobulbar	Retrobulbar
Injection Volume	400 µl	150 µl	100 µl
Number of Injections	Three	One	One

Table 14: Two-way ANCOVA outcomes for measured parameters including main effects of crosslinking treatment (HBSS, GP, MB) and microbead treatment (normotensive, hypertensive) accounting for IOP burden as a covariate.

Outcome Parameter	Main Effects (p-value)			Interaction Terms (p-value)			Homogeneity of Variance (p-value)
	Crosslinking Treatment	Microbead Treatment	IOP Burden	Crosslinking X Microbead	Crosslinking X IOP Burden	Microbead X IOP Burden	Levene's Test
Peripapillary Strain	n.s.	n.s.	<0.01	<0.001	<0.05	n.s.	n.s.
Peripheral Strain	n.s.	n.s.	**<0.0001**	**<0.0001**	<0.05	<0.001	n.s.
Equatorial Diameter	n.s.	n.s.	**<0.0001**	n.s.	n.s.	**<0.0001**	<0.01
Axial Length	n.s.	<0.01	**<0.0001**	n.s.	n.s.	**<0.0001**	n.s.
Anterior Chamber Depth	n.s.	n.s.	n.s.	n.s.	<0.05	<0.05	n.s.
Nerve Cross-sectional Area	n.s.	n.s.	n.s.	n.s.	<0.05	n.s.	n.s.
Axon Count	n.s.	<0.05	<0.001	n.s.	n.s.	<0.01	<0.01
Axon Density	n.s.	<0.05	<0.001	n.s.	n.s.	<0.01	n.s.
Retinal Thickness at 0.5 mm	n.s.	n.s.	<0.05	<0.001	n.s.	<0.05	**<0.0001**
Retinal Thickness at 1.2 mm	n.s.	n.s.	n.s.	<0.01	<0.05	n.s.	<0.001
Contrast Sensitivity	n.s.	**<0.0001**	<0.05	n.s.	<0.05	**<0.0001**	n.s.
Spatial Frequency	n.s.	**<0.0001**	**<0.0001**	n.s.	n.s.	**<0.0001**	<0.01
pSTR Amplitude	n.s.	**<0.0001**	<0.05	<0.05	<0.05	<0.05	<0.05
nSTR Amplitude	n.s.	<0.05	n.s.	n.s.	n.s.	n.s.	<0.05
B-wave Amplitude	n.s.	**<0.0001**	n.s.	n.s.	n.s.	n.s.	n.s.
OP3 Amplitude	n.s.	n.s.	<0.05	n.s.	<0.05	<0.001	<0.05

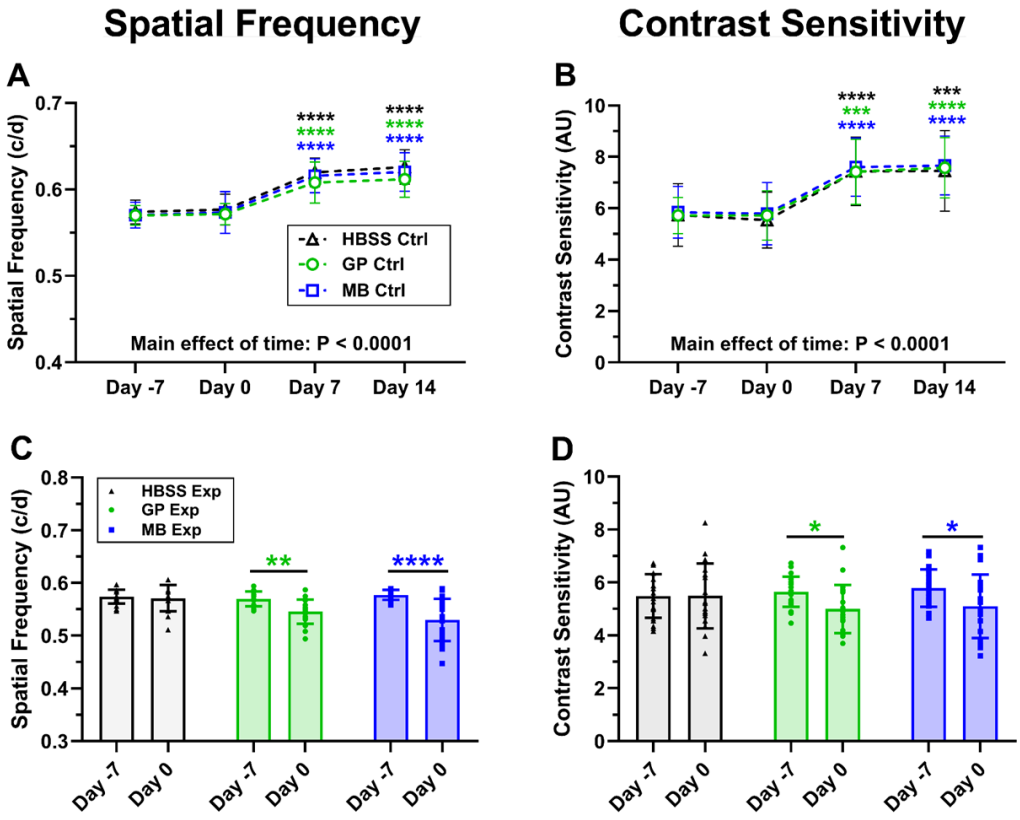

Figure 39: Resolved A) spatial frequency and B) contrast sensitivity of normotensive control eyes at Days -7, 0, 7, and 14 with respect to induction of hypertension at Day 0. Significant differences were found at Day 7 and Day 14 compared to Day -7 (baseline) for spatial frequency and for contrast sensitivity in all crosslinking treatment groups. These findings suggest the presence of a hyperacuity effect in the normotensive eye after induction of hypertension in the contralateral eye C) Spatial frequency differed between Day -7 (baseline) and Day 0 (after stiffening treatment) for GP ($p < 0.01$) and MB ($p < 0.0001$). D) Contrast Sensitivity differed between Day -7 (baseline) and Day 0 (after stiffening treatment) for GP ($p < 0.05$) and MB ($p < 0.05$).

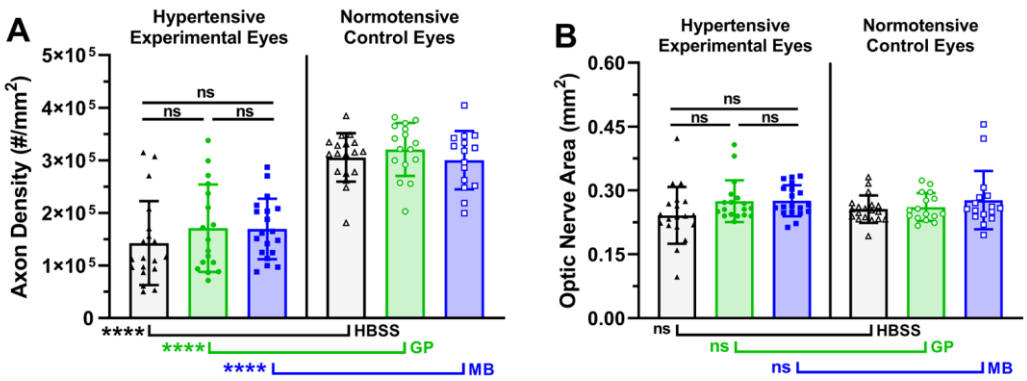

Figure 40: A) Axon density and B) optic nerve cross-sectional area were measured from sectioned optic nerves. Axon density was calculated as the measured axon count divided by measured area (B).

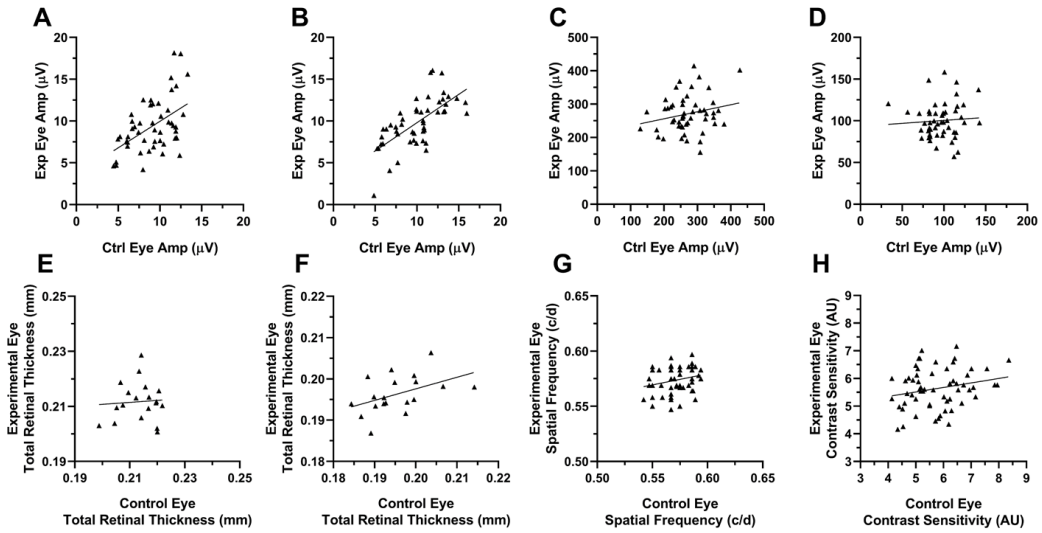

Figure 41: Correlations of baseline control and experimental eye values prior to treatments. “Control” indicates eyes designated to be normotensive. “Experimental” indicates eyes designated to be normotensive (microbead injection). A) pSTR amplitude, B) nSTR amplitude, C) b-wave amplitude, D) oscillatory potential 3 amplitude, E) retinal thickness at 0.5 mm from the ON, F) retinal thickness at 1.2 mm from the ON, G) spatial frequency, and H) contrast sensitivity, showed no significant correlation at baseline between eyes of the same rat.

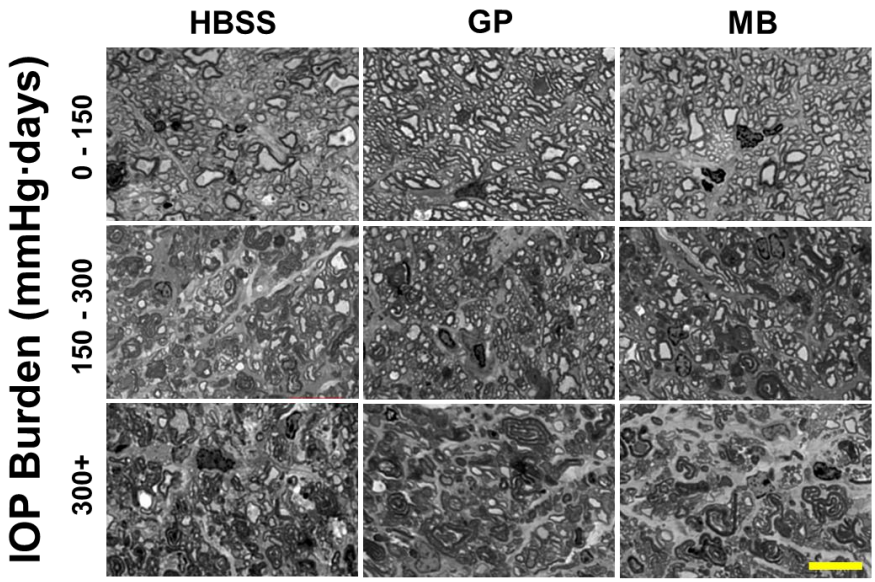

Figure 42: No qualitative differences were found in optic nerve cross-sections of hypertensive eyes between crosslinking treatment groups. Representative images from each treatment in specified range of IOP burden are shown. Images were taken from the central region of each nerve. Scale bar = 10 µm. Damage qualitatively increases with increasing IOP burden.

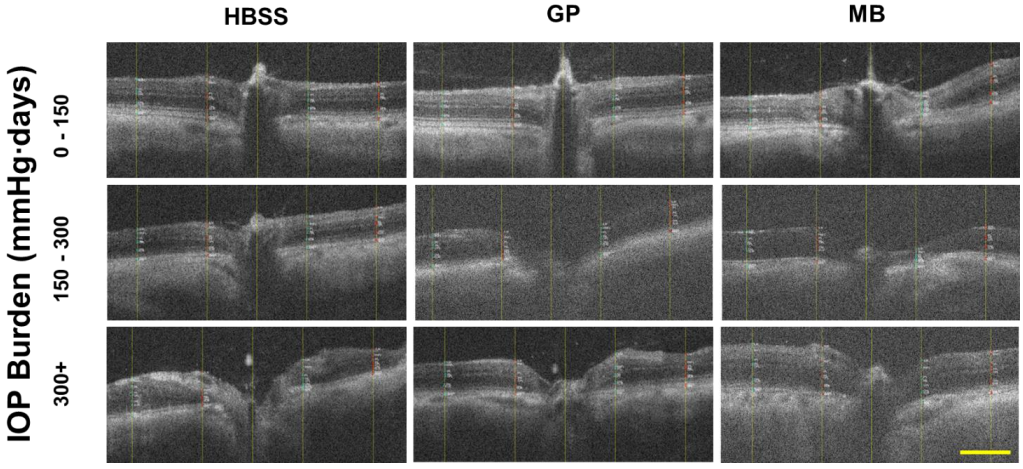

Figure 43: Representative experimental eye optic nerve/retina OCT images from each treatment in specified range of IOP burden. Damage qualitatively increases with increasing IOP burden. Vertical yellow lines on each image indicate (from left to right), -1.2 mm, -0.5 mm, 0 mm, 0.5 mm, 1.2 mm distances from center of optic nerve head at which retinal thickness measurements were taken. Scale bar = 0.5 mm. Specifically, cupping at the optic nerve head increases in all groups.

Table 15: Tabulated average IOP burden of rats included in each outcome parameter group with number of eyes in each group.

Outcome Parameter	Average IOP Burden (mmHg·days)	Normotensive Eye Sample Size				Hypertensive Eye Sample Size			
		HBSS	GP	MB	**Total**	HBSS	GP	MB	**Total**
Peripapillary Strain	218	15	11	15	41	16	10	13	39
Peripheral Strain	220	15	11	15	41	16	11	14	41
Equatorial Diameter	224	17	12	13	42	17	11	14	42
Axial Length	224	17	12	13	42	17	11	14	42
Anterior Chamber Depth	223	17	12	12	41	17	11	13	41
Nerve Cross-sectional Area	225	19	16	16	51	20	18	19	57
Axon Count	229	19	16	14	49	20	17	19	56
Axon Density	226	18	16	15	49	19	17	19	55
Retinal Thickness at 0.5 mm	222	19	18	16	53	20	18	18	56
Retinal Thickness at 1.2 mm	218	20	18	17	55	19	18	18	55
Contrast Sensitivity	226	21	20	19	60	20	18	18	56
Spatial Frequency	226	21	20	19	60	20	18	18	56
pSTR Amplitude	224	21	20	18	59	21	20	19	60
nSTR Amplitude	225	21	20	19	60	21	20	19	60
b-wave Amplitude	227	21	20	19	60	20	20	19	59
OP3 Amplitude	225	21	19	19	59	21	20	19	60

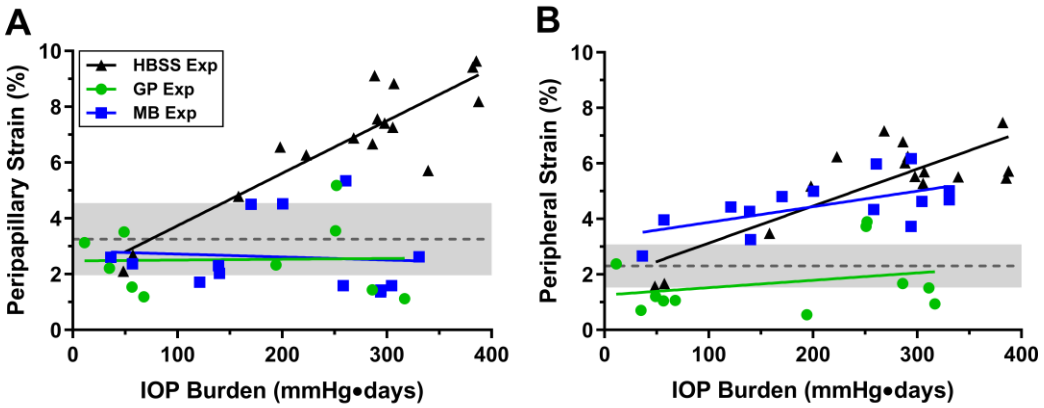

Figure 44: A) Peripapillary and B) peripheral strain as a function of IOP burden.

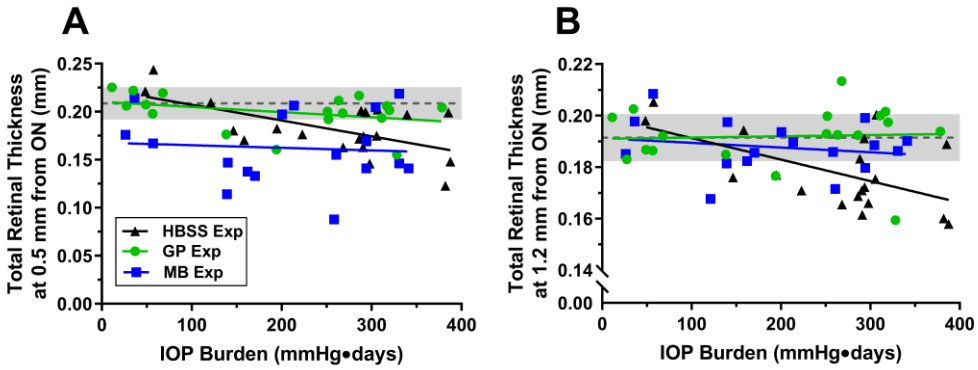

Figure 45: OCT retinal thickness measurements as a function of IOP burden at A) 0.5 mm from the ONH and B) 1.2 mm from the ONH.

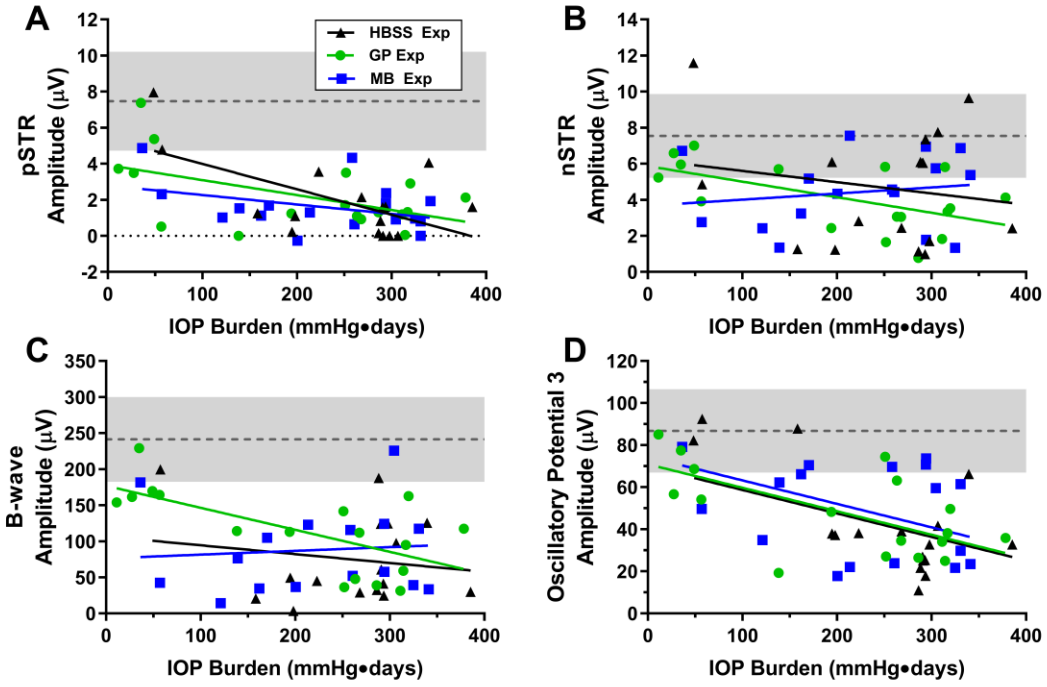

Figure 46: ERG outcomes vs IOP burden for A) pSTR amplitude, B) nSTR amplitude, C) b-wave amplitude, and D) oscillatory potential 3 amplitude.

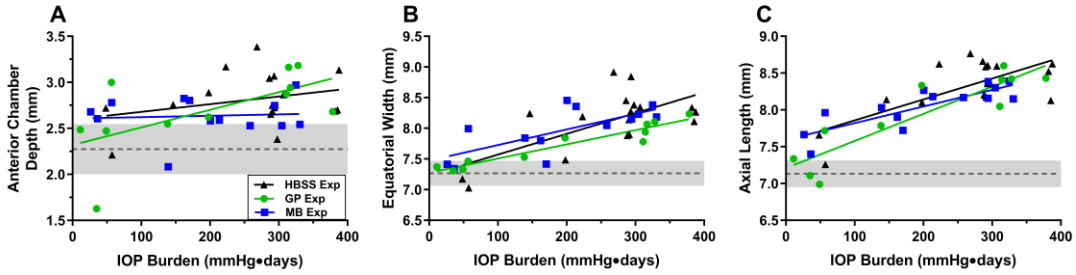

Figure 47: Eye size parameters vs IOP burden including A) anterior chamber depth, B) equatorial width, and C) axial length.

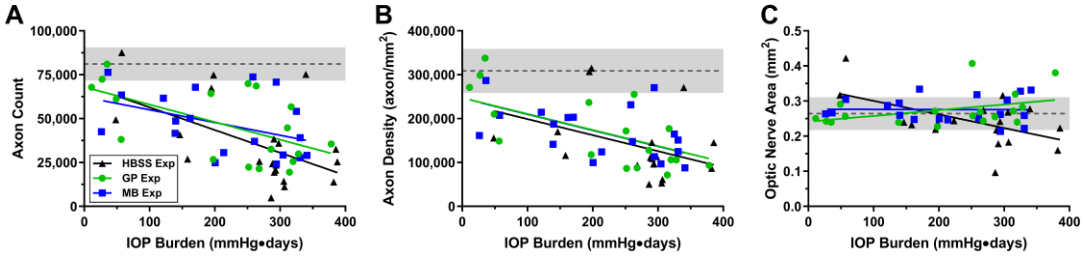

Figure 48: A) Axon count, B) axon density, and C) optic nerve cross-sectional area as functions of IOP burden.

APPENDIX C. SUPPLEMENTAL INFORMATION FOR CHAPTER 5

8.8 Calculation of Retrobulbar and Choroidal Dissolved Oxygen Concentrations

Yu et al. measured the oxygen tension in the rat retina/choroid as a function of tissue depth[244]. The peak oxygen tension was found in the choroid to be approximately 44 mmHg under 20% inspired oxygen, and 228 mmHg under 100% inspired oxygen. Assuming the oxygen gradient is similar on the anterior and posterior sides of the choroid, the oxygen concentration at a distance of 125 μm from the peak choroid oxygen tension was used as an estimate for the concentration in the posterior surface of the Tenon capsule. The tension at 125 μm distance from peak choroidal tension was 21 mmHg for 20% inspired oxygen and 98 mmHg for 100% inspired oxygen.

Oxygen concentration was derived using Henry's Law:

$$C = \alpha_H \times p \tag{39}$$

where C is the concentration of oxygen, α_H is the Henry solubility constant, and p is the partial pressure of oxygen in the tissue[278]. The value of α_H is 0.022 mL oxygen/1 mL solvent per 760 mmHg pressure (1 atmosphere) for blood plasma at 35 °C[279]. Using the ideal gas law, oxygen volume may be converted to molarity using:

$$f = \frac{1}{RT} \tag{40}$$

Where f is the factor for converting concentration from oxygen volume fraction to molarity, R is the gas constant (62.363 mmHg L mol^{-1} K^{-1}), and T is the absolute physiological temperature (assumed to be 308.15 K). The resulting Henry's Law with conversion factor, f, is:

$$C = \alpha_H \times p \times f \tag{41}$$

Table 16: Calculated dissolved oxygen concentrations

Inspired O_2 Concentration	**Tissue**	**O_2 Partial Pressure***	**Calculated Dissolved O_2 Concentration**
20%	Choroid	42 mmHg	4.81 x 10^{-5} M
20%	Retrobulbar	19 mmHg	2.18 x 10^{-5} M
100%	Choroid	228 mmHg	26.10 x 10^{-5} M
100%	Retrobulbar	93 mmHg	10.65 x 10^{-5} M

***** Based on Yu et al. [244]. Choroidal oxygen partial pressures were taken directly from the text. Retrobulbar oxygen partial pressures were derived from figure 2 taking pressure at a distance of 125 μm (scleral + Tenon thickness) from the center of the choroid.

8.9 Calculation of Amino Acid Concentrations in the Sclera

Concentrations of scleral amino acids were determined using the product of scleral collagen mass fraction and collagen amino acid mass fraction. Mass fraction of collagen in the sclera is approximately 22.5% and assumed to be composed of type I collagen [97].

The mass fraction (mg amino acid/mg collagen) of each amino acid was determined using the type I collagen alpha chain sequence[280]. The resulting values for rat, pig, and human are documented in Table 18 and Table 19. In the choroid, we assumed that the amino acid composition would be identical to that of the sclera, but the concentration was reduced by 40%, using the estimated volume fraction of the choroid occupied by vasculature estimated based on collagen content[249].

Table 17: Tissue dimensions by species

Tissue	Rat	Porcine	Human
Cornea	156 μm [281]	833 μm [282]	502 μm [146]
RPE	10 μm [283]	15 μm[284]	26 μm[285]
Choroid	45 μm [286] 57 μm [287]	140 μm [288]	150 μm [288] 162 μm (PP), 195 μm (Avg) [289]
Sclera	104 μm [287]	1100 μm (PPS), 560 μm (Eq)[290]	390 μm (PPS), 650 μm (Eq)[291]
Tenon	26 μm*	208 μm*	113 μm[292]

* Estimated to be 25% thickness of sclera

Table 18: Calculated corneal amino acid concentrations in rat, pig, and human cornea

Residue	Rat Cornea	Porcine Cornea	Human Cornea
Histidine	5.29×10^{-3} M	5.32×10^{-3} M	2.52×10^{-3} M
Methionine	8.81×10^{-3} M	7.68×10^{-3} M	6.71×10^{-3} M
Tryptophan	3.53×10^{-3} M	3.54×10^{-3} M	0.84×10^{-3} M
Tyrosine	8.23×10^{-3} M	8.86×10^{-3} M	2.52×10^{-3} M
Lysine	33.49×10^{-3} M	33.09×10^{-3} M	31.88×10^{-3} M

Table 19: Calculated scleral amino acid concentrations in rat, pig, and human sclerae

Residue	Rat Sclerae	Porcine Sclerae	Human Sclerae
Histidine	12.39×10^{-3} M	12.46×10^{-3} M	5.90×10^{-3} M
Methionine	20.66×10^{-3} M	18.00×10^{-3} M	15.73×10^{-3} M
Tryptophan	8.26×10^{-3} M	8.31×10^{-3} M	1.97×10^{-3} M
Tyrosine	19.28×10^{-3} M	20.77×10^{-3} M	5.90×10^{-3} M
Lysine	78.50×10^{-3} M	77.55×10^{-3} M	74.72×10^{-3} M

Table 20: Melanin Concentration by Tissue and Species*

Tissue	Rat	Porcine	Human
RPE	8.50×10^{-2} M† [293]	8.50×10^{-2} M [293]	7.35×10^{-2} M [293]
Choroid	30.50×10^{-2} M†[293]	30.50×10^{-2} M [293]	6.00×10^{-2} M [293]
Sclera	6.00×10^{-2} M [294]	3.96×10^{-2} M § [295]	7.48×10^{-2} M [295]

* Concentration was calculated assuming a molecular weight of 200 Da[267].
† Assumed similar to porcine sclera concentration
§ We selected the value for Yucatan minipig. Alternatively, concentration for Gottingen minipig is 1.41×10^{-2} M [295].

8.10 Estimate of Retrobulbar Injection Reservoir Depth

We assumed the distance from the posterior Tenon surface to extraocular muscles/blood could be approximated as a cylinder with radius equivalent to that of the eye. The reservoir depth, x, therefore as a function of eye radius, R, and injection volume, V, is:

$$x = \frac{V}{\pi R^2} \tag{42}$$

For example, for a rat eye of radius, R = 3.205 mm (see Hughes et al.) and injection volume of 100 μl, the equivalent reservoir depth would be 3.10 mm[296].

8.11 Estimate for Sub-Tenon Injection Reservoir Depth

We assumed the average distance from the posterior Tenon surface to extraocular muscles/blood vessels could be approximated as a spherical half shell covering the posterior half of the globe. Therefore, the thickness, x, of the half shell was calculated and used as the value for reservoir depth based on eye radius, r, and injection volume, V. The radius of the sphere defined as encompassing the eye and the injection reservoir was given radius, R. Reservoir thickness was calculated as:

$$V = \frac{1}{2}\left(\frac{4}{3}\pi R^3 - \frac{4}{3}\pi r^3\right) \tag{43}$$

$$R = \left(\frac{3V}{2\pi} + r^3\right)^{\frac{1}{3}} \tag{44}$$

$$x = R - r \tag{45}$$

$$x = \left(\frac{3V}{2\pi} + r^3\right)^{\frac{1}{3}} - r \tag{46}$$

For a rat eye of radius 3.205 mm and injection volume of 100 μl, the reservoir thickness would equate to 1.12 mm.

8.12 Calculation of Light Entering the Choroid:

The fundus reflects light with reflectivity of $\boldsymbol{\phi}_R$ defined as the fraction of incident light reflected. The fraction of light transmitted over the RPE can be calculated using the Beer-Lambert Law:

$$1 - f_{Abs} = 1 - 10^{-(\varepsilon_{Melanin} C_{Melanin} x)} \tag{47}$$

where f_{Abs} is the fraction of light transmitted, $\varepsilon_{Melanin}$ is the molar absorptivity of melanin, $C_{Melanin}$ is the concentration of melanin in the RPE, and x is the thickness of the RPE. The fraction of the source light reaching the choroid, $f_{Choroid}$ is the product of the light transmitted after accounting for reflection and absorbance in the RPE:

$$f_{Choroid} = 1 - (1 - \phi_R) \times (10^{-(\varepsilon_{Melanin} C_{Melanin} x)}) \tag{48}$$

Given the values for each parameter as previously stated, we calculated the fraction of incident light reaching the choroid for a transpupillary 660 nm light beam in a rat to be 20%. When also accounting for the absorbance of light in the choroid in a similar manner

to the RPE (though reflection was not considered at the choroid), the fraction of light energy reaching the sclera is approximately 18% of the incident energy on the RPE.

8.13 Optical Properties of Sclera

We found discrepancies in experimental estimates for scleral melanin concentration, molar absorptivity, and light absorbance in the literature. Experimental evidence suggests the absorbance of light in the human sclera is approximately 10% of incident energy at 660 nm[297]. If the linear absorption coefficient of approximately 1.75 cm^{-1} from Bashkatov et al. is used, the percentage absorbed light at 660 nm is approximately 23% (they reported 660 μm sclerae were used) [298]. This is in good agreement with Vogel's estimate since Vogel et al. accounted for an approximately 60% loss due to reflection of light entering the sclera[297]. However, if the scleral melanin concentration is 74.8 mM as in Durairaj et al., and if the molar absorptivity of melanin (monomeric) is 600 $M^{-1}cm^{-1}$, then the expected absorbance from melanin in a 650 μm thickness sclera would be >99%[295]. Literature values for melanin concentration in the sclera and choroid are similar, though qualitative visual evidence would suggest that scleral melanin concentrations are much lower than those of the choroid. Taking Bashkatov's finding of 1.75 cm^{-1} for the scleral linear absorption coefficient, the melanin concentration in human sclera would have to be 3 mM to produce the same degree of light absorption. For this reason, we used this value as an assumption for melanin concentration in the sclera.

8.14 Model Simulation 2D Heatmaps

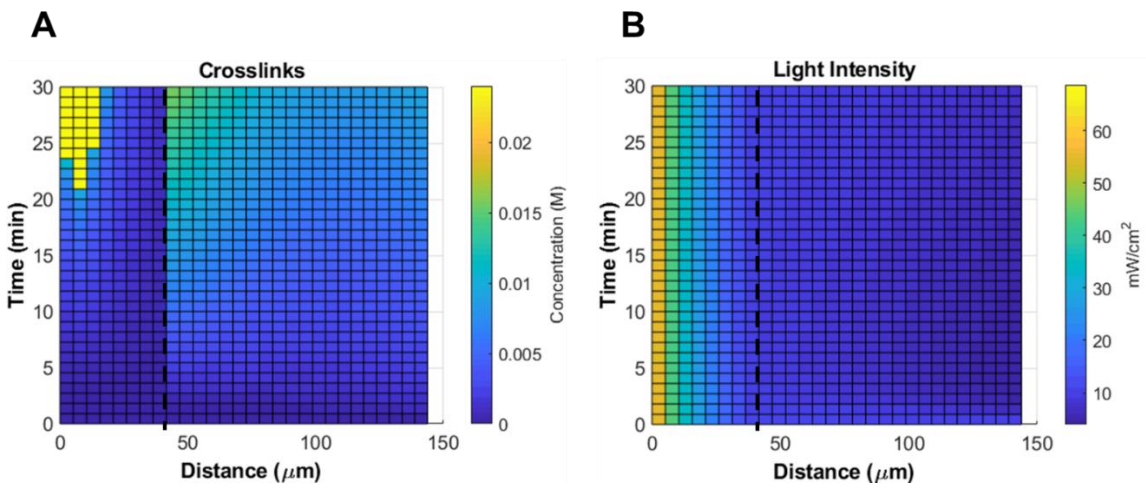

Figure 49: Spatiotemporal profiles of A) crosslink concentration, and B) light intensity model predictions over the choroid and sclera during 30-min MB photocrosslinking procedure. The dashed line demarcates the boundary of choroid (left) and sclera (right). A) The model predicts that crosslinking increases over time with the highest number of crosslinks in the choroid. In both the choroid and sclera, the anterior surfaces experience more crosslinking than the posterior surfaces. B) Light intensity maintains a relatively steady profile throughout the procedure due to relatively fast diffusion of MB which reaches a steady state profile within the first few minutes.

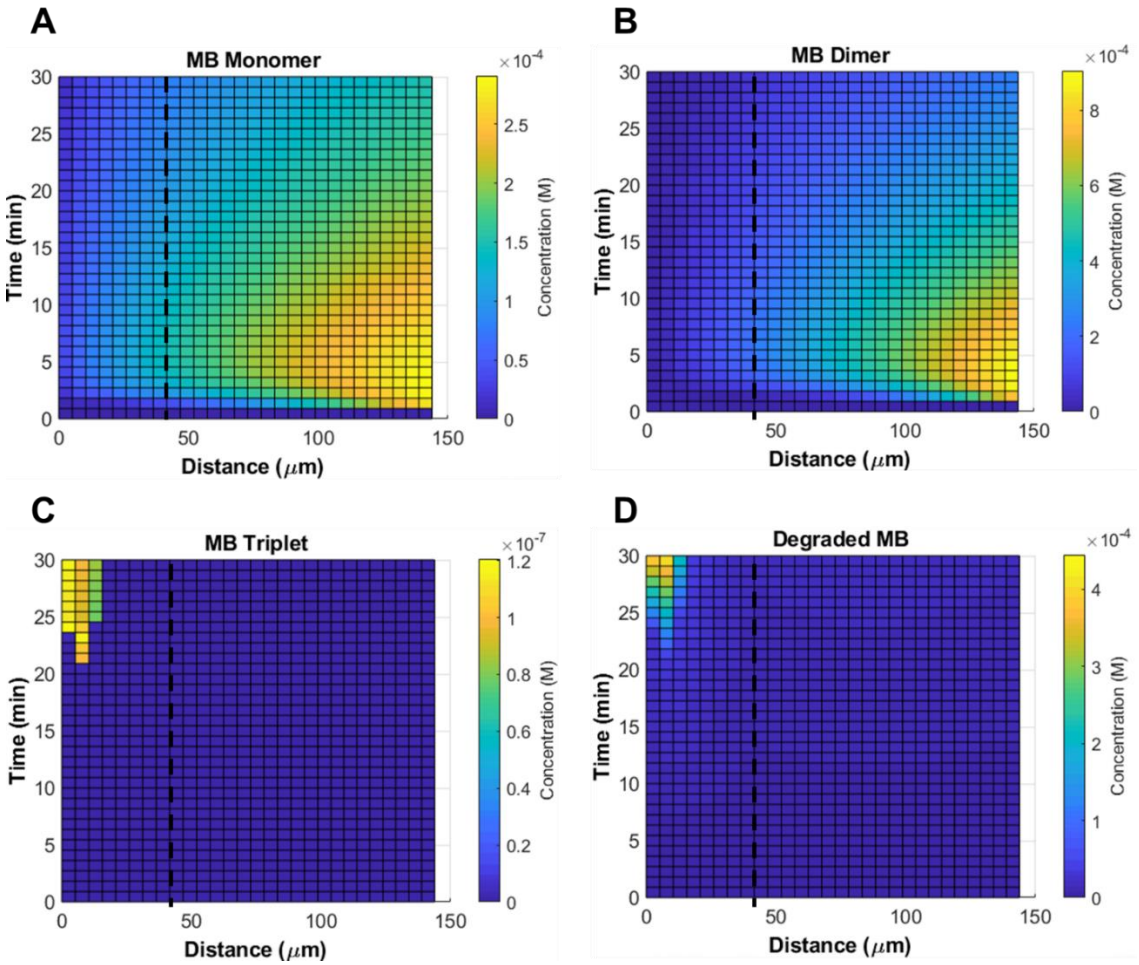

Figure 50: Spatiotemporal profiles of A) MB monomers, B) MB dimers, C) MB triplets, and D) degraded MB. The dashed line demarcates the boundary of choroid (left) and sclera (right). Note, degraded MB is a cumulative sum over time and does not account for diffusion dynamics in order to simply visualize the locations at which degradation was most prevalent. MB monomers, dimers, and triplets, on the other hand are represented as absolute values subject to all model diffusion and reaction dynamics.

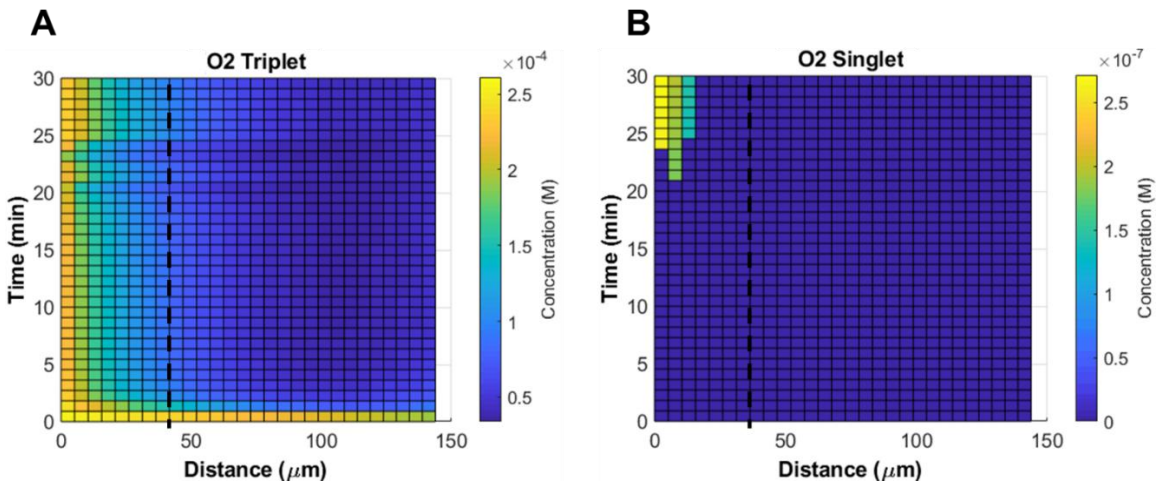

Figure 51: A) Triplet oxygen and B) singlet oxygen concentrations over space and time during MB photocrosslinking treatment in rat sclera/choroid. The dashed line demarcates the boundary of choroid (left) and sclera (right). A) Triplet oxygen is rapidly depleted in the sclera at early stages in the treatment, reaching a relatively steady state profile as diffusion equilibrates with photochemical consumption. B) Singlet oxygen generated throughout the course of the treatment reaches increased concentration late in the treatment duration due to the depletion of quenching species (amino acids and melanin).

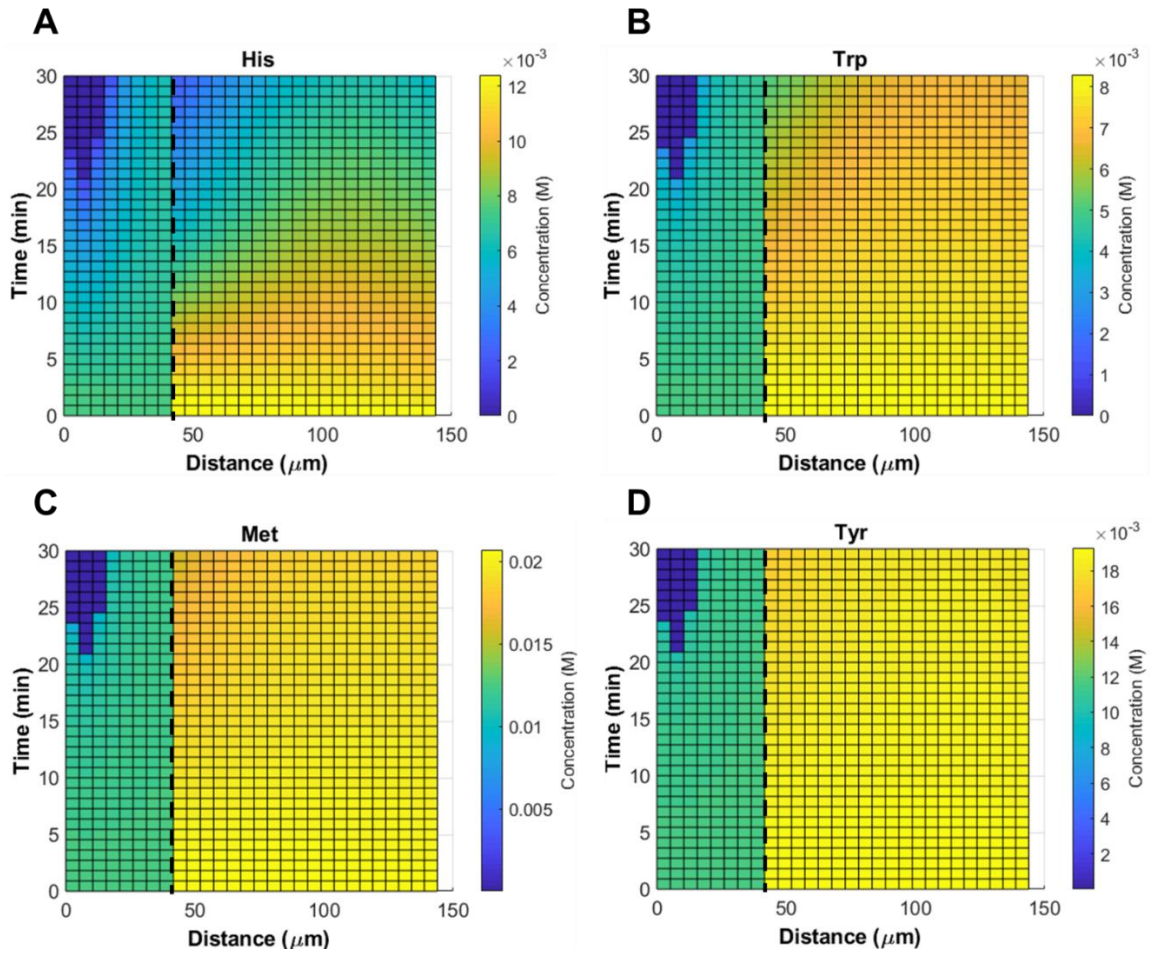

Figure 52: Spatiotemporal profiles of amino acid concentrations in the choroid and sclera during MB photocrosslinking. The dashed line demarcates the boundary of choroid (left) and sclera (right). A) Histidine, B) tryptophan, C) methionine, and D) tryptophan concentrations were modeled as they are believed to be the predominate species involved in crosslinking and quenching reactions.

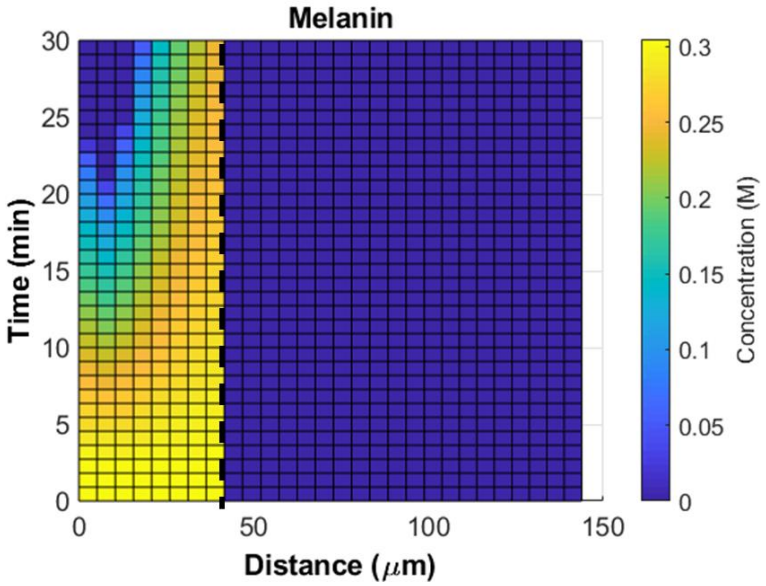

Figure 53: Spatiotemporal profiles of melanin concentration over space and time during MB photocrosslinking shows a gradual depletion in the choroid. The dashed line demarcates the boundary of choroid (left) and sclera (right). Initial concentration is higher in the choroid than in the sclera. Almost complete depletion of melanin occurs in the anterior choroid late in the procedure (>20 min).

APPENDIX D. COMPUTATIONAL MODEL CODE: RIBOFLAVIN CORNEAL CROSSLINKING

```
%Brandon Gerberich
%Last Updated 2020-04-21

clear all
pause(0.5)
clc
close all

tic
format compact
format long g

mastervector=ones(10,1);
ploton=1;
% Intensity=[3 6 9 20 34 45 50 60 67 90]/1000;
% Duration=[30 15 10 4.5 2.65 2 1.8 1.5 1.35 1]*60;
Intensity=3/1000;
Duration=1800;

for mastercounter=1:length(Intensity)
clearvars -except ploton Intensity Duration mastercounter mastervector

%Set Physical Parameters
I0=Intensity(mastercounter);
tmax=Duration(mastercounter);

BCMBres=0;                  %1 if reflection, otherwise Dirichlet
BCMBchor=1;                 %1 if reflection, otherwise Dirichlet
BCO2res=0;                  %1 if reflection, otherwise Dirichlet
BCO2chor=0;                 %1 if reflection, otherwise Dirichlet
BMBHres=0;                  %1 if reflection, otherwise

C0_MBres=0;                 %0.0027 for 0.1%, 0.00082 for 20 minute
presoak
C0_MBchor=0.00194*0;
O23res=1.94e-4*0;           %1.94e-4 Concentration of oxygen at tenon-
reservoir interface [M]
O23chor=1.94e-4;            %1.94e-4 Concentration of oxygen in choroid
[M]
```

```
 fexp=1;                    %Reduction of amino acid concentration
 fexp2=1;                   %Fraction of the triplet quenching rate of
amino acids
 fexp3=1;                   %Fraction of 3MB which is physically quenched
(returns 3MB to MBm, chemical quenching consumes 3MB
 fbleach=1;                 %Fraction of TRP, MET, and TYR which is
degraded after quenching 3MB, consumes TRP,MET,TYR only
 fanlink=1;                 %Fraction of TRP, MET, and TYR which form
xlinks after quenching 3MB and returns MBm
 fhisbleach=0;              %Fraction of HIS which is degraded after
quenching 3MB
 fxl=1;                     %Fraction of 3MB quenched by histidine which
form Xlinks
 fdiff=1;                   %Fraction of diffusion constant for MB
 oxdeg=1;                   %1 if oxygen is consumed in oxidation of MBH
and MBH2, 0 if not
 type2=1;                   %Fraction of type II reaction rates

 C0_HIS=0.0053/fexp;        %Concentration of histidine in the sclera
[M], Edwards & Prausnitz 1998
 C0_TRP=0.0035/fexp;        %Concentration of tryptophan in the sclera
[M], Edwards & Prausnitz 1998
 C0_MET=0.0088/fexp;        %Concentration of methionine in the sclera
[M], Edwards & Prausnitz 1998
 C0_TYR=0.0082/fexp;
 C0_MEL=0;                  %Concentration of melanin [M]

 lambda= 365*10^-9;         %Wavelenght of light, [m], 660 default
 Retchorabs=0;
 e_M=10800;
 e_D=6500;
 PhiT=0.61;
 PhiDeg=0.012;              %Photolysis, Default 0.012

 Scleralength=0.0833;       %[cm] 833 microns from Heichel 2016

 Resx=1;
 Tenx=1;
 Sclx=45;
 Chorx=10;

 Keq=125;                   %Equilibrium constant for dimerization
defined as K=[Dimer]/[Monomer]^2, [M]^-1, 2910 default. K=kf/kr=[D]/[M]^2
 kfm=10.93e8;               %Forward rate constant for dimerization, from
Spencer 1979
```

```
 krd=kfm/Keq;                %Reverse rate constant. Assuming the value
for kfm allows back calculation from K which is more widely available. The
value of kfm just needs to be large so reaction happens quickly if want to
assume instant dimerizastion
 k_singlet=1.62e9;            %Reaction rate for 3MB (triplet MB) and 3O2
(triplet oxygen), [M^-1 s^-1]
 k_mbdeg=9.66E8;             %Reaction rate for 1O2 (singlet oxygen) and
MB leading to degradation of MB, [M^-1 s^-1], 3E8 default (Schmidt 1980
referenced in Wilkinson 1995)
 k_mb2deg=k_mbdeg;           %Reaction rate for 1O2 with MB2 - 2*k_mbdeg
because the effective concentration of monomers is doubled for dimers
 k_triplet=2.56E5;            %Rate for 1O2 (singlet oxygen) relaxation to
3O2 (triplet oxygen), [M^-1 s^-1], 2.5E5 default.
 k_MB3relax=4.9E3;           %Relaxation rate of MB3 to MB calculated from
lifetime of 77us (Alacron 2012), [s^-1], 1.3E5 default
 kMBquench=1.2E8;            %Rate of ground state monomer quenching 3MB
 kMB3HIS=5.22E7*fexp2;       %Reaction rate for physical quenching of 3MB
by histidine, [M^-1 s^-1], 2E6 default
 kMB3TRP=1.75E9*fexp2;       %Reaction rate for physical quenching of 3MB
by tryptophan, [M^-1 s^-1], 6E8 default
 kMB3MET=6.36E7*fexp2;       %Reaction rate for physical quenching of 3MB
by methionine, [M^-1 s^-1], 1E8 default
 kMB3TYR=1.4e9*fexp2;        %Reaction rate for physical quenching of 3MB
by tyrosine, [M^-1 s^-1]
 kMB3ann=8.9e8*0;            %Rate of MB3 annihilation
 k3MBMB2=kMBquench;                  %Rate of MB3 quenching by dimer
 kHIS=1E8;                   %Reaction rate for 1O2 (singlet oxygen) and
histidine leading to crosslinks, [M^-1 s^-1], 5E7 default
 kTRP=3E7;                   %Reaction rate for chemical quenching of
singlet oxygen by tryptophan, [M^-1 s^-1], 4E6 default
 kMET=1.6E7;                 %Reaction rate for chemical quenching of
singlet oxygen by methionine, [M^-1 s^-1], 5E6 default
 kTYR=8e6;                   %Reaction rate for chemical quenching of
singlet oxygen by tyrosine, [M^-1 s^-1]
 k1O2HIS=0;                  %Reaction rate for physical quenching of 1O2
by histidine, [M^-1 s^-1], 4.2E7 default
 k1O2TRP=2.1E7;              %Reaction rate for physical quenching of 1O2
by tryptophan, [M^-1 s^-1], 4.6E7 default
 k1O2MET=0;                  %Reaction rate for physical quenching of 1O2
by methionine, [M^-1 s^-1], 2.5E7 default
 k1O2TYR=0;                  %Reaction rate for physical quenching of 1O2
by tyrosine, [M^-1 s^-1]
 kMEL=1.34E8;                %Reaction rate for melanin with singlet
oxygen, [M^-1 s^-1], 1.34E8 default
```

```
 kMBradq=7e5*type2*0;          %Reaction rate for 2 MB semiquinones with 1
triplet O2, returning 2MB ground state and 1 triplet O2?? (assumes peroxyl
and/or H2O2 quickly return 3O2)
 kMBH=4e6*type2*1;        %3e8 * 0.08 NOW RXN OF AA RADICALS WITH O2
 kMBH2MB=5.8e5*type2*0;      %Reaction rate for formation of 2 semiquinone
radicals from MB and MBH2
 kMBH2ox=1e2*type2;        %1e3 NOW SELF RELAXATION OF AA RADICALS

 avogadro=1/(6.022*10^23);   %Avogadro's number - converts number of
molecules to Moles, [Mole/units]
 planck=6.62607004*10^-34;   %Planck's constant, [J*s]
 ls=299792458;               %Speed of light, [m/s]
 Energy=planck*ls/lambda;    %Energy of a photon, [J]

 %Calculate #X Slices
 XS=Resx+Tenx+Sclx+Chorx;    %Number of x-steps
 xmax=Scleralength;          %*(1+Chorx/Sclx+Tenx/Sclx+Resx/Sclx);
 xspace=1:XS;
 plotlength=XS;

 %Create Tissue Indices
 Res=1:Resx;
 Ten=(Res(end)+1):(Res(end)+Tenx);
 Scl=(Ten(end)+1):(Ten(end)+Sclx);
 Chor=(Scl(end)+1):(Scl(end)+Chorx);

 %Diffusion Constants
 Dres=4.6e-7*fdiff;
 Dten=4.6e-7*fdiff;
 Dscl=4.6e-7*fdiff;
 Dchor=4.6e-7*fdiff;
 Dair=4.2e-6*fdiff;
 DO2=4e-6;                   %Diffusivity of oxygen in sclera, [cm^2/s],
1.7E-5 default. 4E-6 according to Kamaev 2012 (porcine sclera)
 DO2air=0.219;               %Diffusivity of oxygen in nitrogen

 %Mu Constants
 mures=17;
 muten=17;
 muscl=17;
 muchor=17;

 %Create Diffusion Vector
 DMB=ones(1,XS);
 DMB(Res)=Dres;
 DMB(Ten)=Dten;
```

```
DMB(Scl)=Dscl;
DMB(Chor)=Dchor;
DO2=DO2*ones(1,XS);

%Create mu Vector
mu=zeros(1,XS);
mu(Res)=mures;
mu(Ten)=muten;
mu(Scl)=muscl;
mu(Chor)=muchor;

%Calculate Space & Time Intervals
Dmax=max([Dres Dten Dscl Dchor DO2]);
dx=xmax/XS
dt=dx^2/Dmax;

%Calculate Constants
I0=(1-Retchorabs)*I0/Energy*avogadro/dx*1000;           %Converts
intensity units from [W/cm^2/s] to [M/s]
MBmres=(-1+sqrt(1+8*Keq*C0_MBres))/(4*Keq);
MBdres=0.5*(C0_MBres-(-1+sqrt(1+8*Keq*C0_MBres))/(4*Keq));
MBmchor=(-1+sqrt(1+8*Keq*C0_MBchor))/(4*Keq);
MBdchor=0.5*(C0_MBchor-(-1+sqrt(1+8*Keq*C0_MBchor))/(4*Keq));

%Set Initial Conditions
load('DiffusionICWernli57.mat','MBprofile');
% MBsemiinf=flip(0.5*C0_MBchor*erfc((1:N)/N*xmax/(2*sqrt(Dscl*1200))));
%semi infinite condition
MBm=(-1+sqrt(1+8*Keq*MBprofile))/(4*Keq);
MBd=0.5*(MBprofile-(-1+sqrt(1+8*Keq*MBprofile))/(4*Keq));
% MBm=linspace(MBmres,MBmchor,N);   %Steady state
% MBd=linspace(MBdres,MBdchor,N);   %Steady state

%For creating new initial profile (presoaking). Uncomment first two lines
% MBm=MBmchor*zeros(1,XS); %MBm(Chor)=0;
% MBd=MBdchor*zeros(1,XS); %MBd(Chor)=0;
% MBprofile=y(end,B)+2*y(end,C);
% save('DiffusionICWernli57.mat','MBprofile');

Light=10.^(-(e_M*MBm+e_D*MBd+mu)*dx);       %Pct transmitted in each step
MB3=zeros(1,XS);
MBdeg=zeros(1,XS);
% O23=O23res+(1:XS)/(XS+1)*(O23chor-O23res);
O23=O23chor*ones(1,XS);
O21=zeros(1,XS);
HIS=C0_HIS*ones(1,XS);
```

```
 TRP=C0_TRP*ones(1,XS);
 MET=C0_MET*ones(1,XS);
 MEL=C0_MEL*ones(1,XS);
 TYR=C0_TYR*ones(1,XS);
 Xlink=zeros(1,XS);
 MBH=zeros(1,XS);
 MBH2=zeros(1,XS);

 Xlinkspossible=mean(C0_HIS+C0_TRP+C0_TYR); %Max possible mean
concentration

 %Define Domains of DYDT
 A=1:XS; B=A+XS; C=B+XS; D=C+XS; E=D+XS; F=E+XS; G=F+XS; H=G+XS; I=H+XS;
J=I+XS; K=J+XS; L=K+XS; M=L+XS; N=M+XS; O=N+XS;
 %Define "Middle" Domains of DYDT
 a=2:(XS-1); b=a+XS; c=b+XS; d=c+XS; e=d+XS; f=e+XS; g=f+XS; h=g+XS;
i=h+XS; j=i+XS; k=j+XS; l=k+XS; m=l+XS; n=m+XS; o=n+XS;

 sizey=length([A B C D E F G H I J K L M N O]);
 tspan=0:dt:tmax;
 TS=length(tspan)

 if TS<10000
     TS=10000
     tspan=linspace(0,tmax,TS);
     disp('TS increased to 10000')
 else if TS>300000
         TS=300000
         tspan=linspace(0,tmax,TS);
         disp('TS reduced to 300000')
     end
 end

 %0 = zeros
 %1 = 0th diagonal     REACTIONS
 %2 = 0,1 diagonals
 %3 = -1,0,1 diagnoals DIFFUSION
 %4 = upper triangular
 %5 = upper triangular with diffusion
 jcell = {...
    %a b c d e f g h i j k l m n o
     4 3 3 1 1 1 0 1 1 1 0 0 1 1 1;        %a Light
     4 3 1 1 1 1 0 1 1 1 0 0 1 1 1;        %b MBm
     0 1 3 1 0 1 0 0 0 0 0 0 0 0 0;        %c MBd
     4 1 1 3 1 0 0 1 1 1 0 0 1 0 1;        %d 3MB
     0 0 0 1 3 1 0 1 1 1 1 0 1 1 1;        %e 3O2
```

```
    0 1 1 1 1 3 0 1 1 1 1 0 1 0 0;        %f 1O2
    4 1 1 0 1 1 0 0 0 0 0 0 0 0 1;        %g MBdeg
    0 0 0 1 0 1 0 1 0 0 1 0 0 0 0;        %h HIS
    0 0 0 1 0 1 0 0 1 0 0 0 0 1 0;        %i TRP
    0 0 0 1 0 1 0 0 0 1 0 0 0 0 0;        %j MET
    0 0 0 1 0 1 0 1 1 0 1 0 1 0 0;        %k MEL (HIS radical)
    0 0 0 0 1 1 0 1 1 0 1 0 1 1 1;        %l Xlink
    0 0 0 1 0 1 0 0 0 0 0 0 1 0 1;        %m TYR
    0 0 0 1 0 1 0 0 0 0 0 0 0 1 0;        %n MBH    (TRP radical)
    0 0 0 1 0 1 0 0 0 0 0 0 0 0 1 ...     %o MBH2 (TYR radical)
    };

 jcelllength=length(jcell);
 jspots=jcelllength^2;
 for counter=1:jspots
     if jcell{counter}==0
         jcell{counter}=zeros(XS);

     elseif jcell{counter}==1
         jcell{counter}=diag(ones(1,XS),0);

     elseif jcell{counter}==2
         jcell{counter}=diag(ones(1,XS-1),1)+diag(ones(1,XS),0);

     elseif jcell{counter}==3
         jcell{counter}=diag(ones(1,XS-1),1)+diag(ones(1,XS-1),-
1)+diag(ones(1,XS),0);

     elseif jcell{counter}==4
         jcell{counter}=triu(ones(XS));

     elseif jcell{counter}==5
         jcell{counter}=triu(ones(XS))+diag(ones(1,XS),0);
     end
 end

 Jsparse=cell2mat(jcell);

 options=odeset('InitialStep',0.000001,'MaxOrder',2,'RelTol',1E-
6,'AbsTol', 1E-8, 'JPattern',jsparse(Jsparse));  %Sets options for solver
 y0=[Light' MBm' MBd' MB3' O23' O21' MBdeg' HIS' TRP' MET' MEL' Xlink'
TYR' MBH' MBH2'];                      %Initial conditions
 [t, y]=ode15s(@(t,y)
odefcn(t,y,XS,sizey,a,b,c,d,e,f,g,h,i,j,k,l,m,n,o,B,C,I0,e_M,e_D,dx,DMB,DO
2,mu,PhiT,PhiDeg,MBmchor,MBdchor,MBmres,MBdres,O23chor,O23res,k_MB3relax,k
_singlet,k_mbdeg,k_mb2deg,k_triplet,kHIS,kTRP,kMET,kTYR,kMB3HIS,kMB3TRP,
```

```
kMB3MET,kMB3TYR,k1O2HIS,k1O2TRP,k1O2MET,k1O2TYR,kMB3ann,k3MBMB2,kMBquench,
kMEL,kfm,krd,BCMBres,BCMBchor,BCO2res,BCO2chor,fxl,fbleach,fanlink,fhisble
ach, kMBradq, kMBH, kMBH2MB, kMBH2ox,fexp3, oxdeg, Dair, DO2air,
BMBHres),tspan,y0,options);

 if ploton==1
 %Calculate Plot Grid Mesh
 xpoints=(1:XS)*dx;
 xpoints=xpoints';
 % [X T] = meshgrid(xpoints, tspan);
 r=round(linspace(1,size(y,1),plotlength));
 s=round(linspace(1,length(xpoints'),plotlength));
 t=round(linspace(1,length(tspan),plotlength));
 tlog=round(logspace(0,log10(length(tspan)),plotlength));
 mins=(1:TS)/TS*tmax/60;
 logswitch='linear';
%toggles linear or log scale plots

 if strcmp(logswitch,'log')==1
     t=round(logspace(0,log10(length(tspan)),plotlength));
     tspan=tspan/60;
 end

 %Calculating Photons Absorbed
 aflip=flip(a);

 Lightbeg=(1-y(:,1)).*y(:,XS).*prod(y(:,a),2)*I0;
 Lightmid=(1-y(:,a)).*cumprod(y(:,a+1),2,'reverse')*I0;
 Lightend=(1-y(:,XS))*I0;
 Abs=[Lightbeg Lightmid Lightend];

 LI1=fliplr(cumprod(fliplr(y(:,A)),2))*I0; %Light intensity from Pct
Transmitted

 %Another check for the Light Intensity
 LI2F=10.^(-(e_M*y(:,B)+e_D*y(:,C)+mu)*dx);     %Fraction light
transmitted at each step
 LI2=I0*fliplr(cumprod(fliplr(LI2F),2));   %Light intensity from
concentration

 %Plot Figures
 figure(1)
 surf(xpoints(s),tspan(t),y(t,A(s)))
 xlabel('Distance [cm]','FontSize',14,'FontWeight','bold','Color','k')
%Adds x-label
```

```
 ylabel('Time [s]','FontSize',14,'FontWeight','bold','Color','k')
%Adds y-label
 title('Fraction Light
Transmitted','FontSize',16,'FontWeight','bold','Color','k') %Adds title
 set(gca,'zscale',logswitch)
 set(gca,'yscale',logswitch)

 figure(2)
 surf(xpoints(s),tspan(t),y(t,B(s)))
 xlabel('Distance [cm]','FontSize',14,'FontWeight','bold','Color','k')
%Adds x-label
 ylabel('Time [s]','FontSize',14,'FontWeight','bold','Color','k')
%Adds y-label
 title('[Monomer]','FontSize',16,'FontWeight','bold','Color','k') %Adds
title
 set(gca,'zscale',logswitch)
 set(gca,'yscale',logswitch)

 figure(3)
 surf(xpoints(s),tspan(t),y(t,C(s)))
 xlabel('Distance [cm]','FontSize',14,'FontWeight','bold','Color','k')
%Adds x-label
 ylabel('Time [s]','FontSize',14,'FontWeight','bold','Color','k')
%Adds y-label
 title('[Dimer]','FontSize',16,'FontWeight','bold','Color','k') %Adds
title
 set(gca,'zscale',logswitch)
 set(gca,'yscale',logswitch)

 figure(4)
 surf(xpoints(s),tspan(t),y(t,D(s)))
 xlabel('Distance [cm]','FontSize',14,'FontWeight','bold','Color','k')
%Adds x-label
 ylabel('Time [s]','FontSize',14,'FontWeight','bold','Color','k')
%Adds y-label
 title('[3MB]','FontSize',16,'FontWeight','bold','Color','k') %Adds title
 set(gca,'zscale',logswitch)
 set(gca,'yscale',logswitch)

 figure(5)
 surf(xpoints(s),tspan(t),y(t,E(s)))
 xlabel('Distance [cm]','FontSize',14,'FontWeight','bold','Color','k')
%Adds x-label
 ylabel('Time [s]','FontSize',14,'FontWeight','bold','Color','k')
%Adds y-label
```

```
 title('[O2 Triplet]','FontSize',16,'FontWeight','bold','Color','k') %Adds
title
 set(gca,'zscale',logswitch)
 set(gca,'yscale',logswitch)

 figure(6)
 surf(xpoints(s),tspan(t),y(t,F(s)))
 xlabel('Distance [cm]','FontSize',14,'FontWeight','bold','Color','k')
%Adds x-label
 ylabel('Time [s]','FontSize',14,'FontWeight','bold','Color','k')
%Adds y-label
 title('[O2 Singlet]','FontSize',16,'FontWeight','bold','Color','k') %Adds
title
 set(gca,'zscale',logswitch)
 set(gca,'yscale',logswitch)

 figure(7)
 surf(xpoints(s),tspan(t),y(t,G(s)))
 xlabel('Distance [cm]','FontSize',14,'FontWeight','bold','Color','k')
%Adds x-label
 ylabel('Time [s]','FontSize',14,'FontWeight','bold','Color','k')
%Adds y-label
 title('Degraded MB','FontSize',16,'FontWeight','bold','Color','k') %Adds
title
 set(gca,'zscale',logswitch)
 set(gca,'yscale',logswitch)

 figure(8)
 surf(xpoints(s),tspan(t),y(t,L(s)))
 xlabel('Distance [cm]','FontSize',14,'FontWeight','bold','Color','k')
%Adds x-label
 ylabel('Time [s]','FontSize',14,'FontWeight','bold','Color','k')
%Adds y-label
 title('Xlinks','FontSize',16,'FontWeight','bold','Color','k') %Adds title
 set(gca,'zscale',logswitch)
 set(gca,'yscale',logswitch)

 figure(9)
 surf(xpoints(s),tspan(t),y(t,H(s)))
 xlabel('Distance [cm]','FontSize',14,'FontWeight','bold','Color','k')
%Adds x-label
 ylabel('Time [s]','FontSize',14,'FontWeight','bold','Color','k')
%Adds y-label
 title('HIS','FontSize',16,'FontWeight','bold','Color','k') %Adds title
 set(gca,'zscale',logswitch)
 set(gca,'yscale',logswitch)
```

```
 figure(10)
 surf(xpoints(s),tspan(t),y(t,I(s)))
 xlabel('Distance [cm]','FontSize',14,'FontWeight','bold','Color','k')
%Adds x-label
 ylabel('Time [s]','FontSize',14,'FontWeight','bold','Color','k')
%Adds y-label
 title('TRP','FontSize',16,'FontWeight','bold','Color','k') %Adds title
 set(gca,'zscale',logswitch)
 set(gca,'yscale',logswitch)

 figure(11)
 surf(xpoints(s),tspan(t),y(t,J(s)))
 xlabel('Distance [cm]','FontSize',14,'FontWeight','bold','Color','k')
%Adds x-label
 ylabel('Time [s]','FontSize',14,'FontWeight','bold','Color','k')
%Adds y-label
 title('MET','FontSize',16,'FontWeight','bold','Color','k') %Adds title
 set(gca,'zscale',logswitch)
 set(gca,'yscale',logswitch)

 figure(12)
 surf(xpoints(s),tspan(t),y(t,M(s)))
 xlabel('Distance [cm]','FontSize',14,'FontWeight','bold','Color','k')
%Adds x-label
 ylabel('Time [s]','FontSize',14,'FontWeight','bold','Color','k')
%Adds y-label
 title('TYR','FontSize',16,'FontWeight','bold','Color','k') %Adds title
 set(gca,'zscale',logswitch)
 set(gca,'yscale',logswitch)

 figure(13)
 surf(xpoints(s),tspan(t),y(t,N(s)))
 xlabel('Distance [cm]','FontSize',14,'FontWeight','bold','Color','k')
%Adds x-label
 ylabel('Time [s]','FontSize',14,'FontWeight','bold','Color','k')
%Adds y-label
 title('MBH','FontSize',16,'FontWeight','bold','Color','k') %Adds title
 set(gca,'zscale',logswitch)
 set(gca,'yscale',logswitch)

 figure(14)
 surf(xpoints(s),tspan(t),y(t,O(s)))
 xlabel('Distance [cm]','FontSize',14,'FontWeight','bold','Color','k')
%Adds x-label
```

```
 ylabel('Time [s]','FontSize',14,'FontWeight','bold','Color','k')
%Adds y-label
 title('MBH2','FontSize',16,'FontWeight','bold','Color','k') %Adds title
 set(gca,'zscale',logswitch)
 set(gca,'yscale',logswitch)

 figure(15)
 surf(xpoints(s),tspan(t),y(t,K(s)))
 xlabel('Distance [cm]','FontSize',14,'FontWeight','bold','Color','k')
%Adds x-label
 ylabel('Time [s]','FontSize',14,'FontWeight','bold','Color','k')
%Adds y-label
 title('AArads','FontSize',16,'FontWeight','bold','Color','k') %Adds title
 set(gca,'zscale',logswitch)
 set(gca,'yscale',logswitch)

 figure(30)
 surf(xpoints(s),tspan(t),Abs(t,s))
 xlabel('Distance [cm]','FontSize',14,'FontWeight','bold','Color','k')
%Adds x-label
 ylabel('Time [s]','FontSize',14,'FontWeight','bold','Color','k')
%Adds y-label
 title('Light Absorbed','FontSize',16,'FontWeight','bold','Color','k')
%Adds title
 set(gca,'zscale',logswitch)
 set(gca,'yscale',logswitch)

 figure(31)
 surf(xpoints(s),tspan(t),LI1(t,s))
 xlabel('Distance [cm]','FontSize',14,'FontWeight','bold','Color','k')
%Adds x-label
 ylabel('Time [s]','FontSize',14,'FontWeight','bold','Color','k')
%Adds y-label
 title('LI1','FontSize',16,'FontWeight','bold','Color','k') %Adds title
 set(gca,'zscale',logswitch)
 set(gca,'yscale',logswitch)

 figure(32)
 surf(xpoints(s),tspan(t),LI2(t,s))
 xlabel('Distance [cm]','FontSize',14,'FontWeight','bold','Color','k')
%Adds x-label
 ylabel('Time [s]','FontSize',14,'FontWeight','bold','Color','k')
%Adds y-label
 title('LI2','FontSize',16,'FontWeight','bold','Color','k') %Adds title
 set(gca,'zscale',logswitch)
 set(gca,'yscale',logswitch)
```

```
 %Find the oxygen profile at certain distance over certain time
 oxtime=9;
 oxdist=0.01;
 [~,oxtind]=min(abs(tspan-oxtime));
 [~,oxxind]=min(abs(xpoints-(xmax-oxdist)));

 figure(33)
 plot(xpoints,y(oxtind,E));
 oxconc=y(oxtind,E(oxxind))
 xlabel('Distance [cm]','FontSize',14,'FontWeight','bold','Color','k')
%Adds x-label
 ylabel('[3O2]','FontSize',14,'FontWeight','bold','Color','k')
%Adds y-label
 title('Triplet Oxygen
Concentration','FontSize',16,'FontWeight','bold','Color','k')

 % meanconc=mean(y(1:TS,B),2)/mean(y(1,B),2);
 meanconc=(mean(y(1:TS,B),2)+mean(y(1:TS,N),2)+mean(y(1:TS,O),2))/1000*514
*10^5;
 %
meanconc=(mean(y(1:TS,B),2)+mean(y(1:TS,G),2)+mean(y(1:TS,N),2))/1000*514*
10^5;
 % meanconc=(mean(y(1:TS,B),2)+mean(y(1:TS,G),2))/1000*514*10^5;
 % meanconc=mean(y(1:TS,B),2)/1000*514*10^5;

 figure(34)
 plot(mins,meanconc,'r');
 xlabel('Irradiation time
[min]','FontSize',11,'FontWeight','bold','Color','k')
%Adds x-label
 ylabel('Riboflavin Concentration [10^-5
gr/cm^3]','FontSize',11,'FontWeight','bold','Color','k')
%Adds y-label
 title(' ','FontSize',12,'FontWeight','bold','Color','k')
 xlim([0 30])
 ylim([2 18])
 set(gcf,'color','w');
 % save('Lombardo3mWprofile.mat','meanconc');

 %Find the oxygen profile at certain distance over certain time
 % oxdist2=0.013;
 % oxtime1=
 % [~,oxtind2]=min(abs(tspan-oxtime1));
 % [~,oxxind2]=min(abs(xpoints-(xmax-oxdist2)));
 %
```

```
 % figure(34)
 % plot(tspan(t),y(oxtind2,E());
 % xlabel('Time [min]','FontSize',14,'FontWeight','bold','Color','k')
%Adds x-label
 % ylabel('[3O2]','FontSize',14,'FontWeight','bold','Color','k')
%Adds y-label
 % title('Triplet Oxygen
Concentration','FontSize',16,'FontWeight','bold','Color','k')

 figure(35)
 loglog(mins,y(1:TS,D(oxxind)))
 xlabel('Time, min','FontSize',14,'FontWeight','bold','Color','k')
%Adds x-label
 ylabel('3MB Concentration','FontSize',14,'FontWeight','bold','Color','k')
%Adds y-label
 title('Brandon Model','FontSize',16,'FontWeight','bold','Color','k')
 xlim([0.01 100])
 ylim([1e-11 5e-10])
 ax=gca;
 ax.YGrid='on';
 ax.YMinorGrid='off';
 ax.GridAlpha=0.5;

 figure(36)
 loglog(mins,y(1:TS,F(oxxind)))
 xlabel('Time, min','FontSize',14,'FontWeight','bold','Color','k')
%Adds x-label
 ylabel('1O2 Concentration','FontSize',14,'FontWeight','bold','Color','k')
%Adds y-label
 title('Brandon Model','FontSize',16,'FontWeight','bold','Color','k')
 xlim([0.01 100])
 % ylim([1e-11 5e-10])
 ax=gca;
 ax.YGrid='on';
 ax.YMinorGrid='off';
 ax.GridAlpha=0.5;

 figure(37)
 loglog(mins,y(1:TS,B(oxxind)))
 xlabel('Time, min','FontSize',14,'FontWeight','bold','Color','k')
%Adds x-label
 ylabel('MBm Concentration','FontSize',14,'FontWeight','bold','Color','k')
%Adds y-label
 title('Brandon Model','FontSize',16,'FontWeight','bold','Color','k')
 xlim([0.01 100])
 % ylim([1e-11 5e-10])
```

```
 ax=gca;
 ax.YGrid='on';
 ax.YMinorGrid='off';
 ax.GridAlpha=0.5;

 figure(38)
 loglog(mins,y(1:TS,L(oxxind)))
 xlabel('Time, min','FontSize',14,'FontWeight','bold','Color','k')
%Adds x-label
 ylabel('Xlinks','FontSize',14,'FontWeight','bold','Color','k')
%Adds y-label
 title('Brandon Model','FontSize',16,'FontWeight','bold','Color','k')
 xlim([0.01 100])
 % ylim([1e-11 5e-10])
 ax=gca;
 ax.YGrid='on';
 ax.YMinorGrid='off';
 ax.GridAlpha=0.5;

 figure(39)
 plot(flip(xpoints)*10000,y(end,L(s)))
 xlabel('Depth (\mum)','FontSize',14,'FontWeight','bold','Color','k')
%Adds x-label
 ylabel('Xlinks','FontSize',14,'FontWeight','bold','Color','k')
%Adds y-label
 title('Brandon Model','FontSize',16,'FontWeight','bold','Color','k')

 figure(40)
 loglog(mins,32*1000*y(1:TS,E(oxxind)), 'k')
 xlabel('Time, min','FontSize',14,'FontWeight','bold','Color','k')
%Adds x-label
 ylabel('Oxygen Concentration,
mg/L','FontSize',14,'FontWeight','bold','Color','k')
%Adds y-label
 title(' ','FontSize',16,'FontWeight','bold','Color','k')
 xlim([0.01 100])
 ylim([0.01 10])
 ax=gca;
 ax.YGrid='on';
 ax.YMinorGrid='off';
 ax.GridAlpha=0.5;
 set(gcf,'color','w');

 Enorm=32*1000*y(1:TS,E(oxxind))/(32*1000*y(1,E(oxxind)));
 Dnorm=y(1:TS,D(oxxind))/(y(2,D(oxxind)));
 Inorm=y(1:TS,I(oxxind))/(y(2,I(oxxind)));
```

```
 Bnorm=y(1:TS,B(oxxind))/(y(2,B(oxxind)));
 Fnorm=y(1:TS,F(oxxind))/(y(2,F(oxxind)));
 LInorm=LI1(1:TS,oxxind)/(LI1(2,oxxind));
 Hnorm=y(1:TS,H(oxxind))/(y(2,H(oxxind)));
 Jnorm=y(1:TS,J(oxxind))/(y(2,J(oxxind)));
 Mnorm=y(1:TS,J(oxxind))/(y(2,M(oxxind)));
 Gnorm=y(1:TS,G(oxxind))/(y(end,G(oxxind)));
 Nnorm=y(1:TS,N(oxxind))/(y(end,N(oxxind)));
 Onorm=y(1:TS,O(oxxind))/(y(end,O(oxxind)));

 figure(41)
 plot(mins,Enorm,'c',mins,Dnorm,'m',mins,Hnorm,'g',mins,Bnorm,'b',mins,Fno
rm,'k',mins,LInorm,'r')
 hold on
 plot(mins,Inorm, 'Color', [0 190/256 0], 'LineStyle', '--')
 hold on
 plot(mins, Jnorm, 'Color', [0 100/256 0],'Linestyle', '-.')
 hold on
 plot(mins, Mnorm, 'Color', [0 200/256 0])
 hold on
 plot(mins, Gnorm, 'Color', [0 0 150/256])
 hold on
 plot(mins, Nnorm, 'Color', [138 43 226]/256)
 hold on
 plot(mins, Onorm, 'Color', [128 0 128]/256)
 set(gca,'xscale','log')
 set(gca,'yscale','log')
 legend('3O2',
'3MB','HIS','MBm','1O2','LI','TRP','MET','TYR','MBdeg','MBH','MBH2','Locat
ion','SouthWest')
 xlim([0.01 30])
 ylim([0.01 10])
 set(gcf,'color','w');

 %Check equivalence of light intensities
 L1=round(LI1(end,1)/I0,5);
 L2=round(LI2(end,1)/I0,5);
 PAbs=round(1-sum(Abs(end,A))/I0,5);

 if L1~=L2 || L1~=PAbs
     disp('Warning - light intensities not equal')
 end
 end
```

```
 Xlinkstot=mean(y(end,L([Res Ten Scl Chor]))) %Actually average
concentration. Just multiplying by dx/1000 converts from M to xlinks per
cm2
 fXlink=Xlinkstot/Xlinkspossible;
 mastervector(mastercounter,1)=Xlinkstot
 end
 toc

 function
dydt=odefcn(t,y,XS,sizey,a,b,c,d,e,f,g,h,i,j,k,l,m,n,o,B,C,I0,e_M,e_D,dx,D
MB,DO2,mu,PhiT,PhiDeg,MBmchor,MBdchor,MBmres,MBdres,O23chor,O23res,k_MB3re
lax,k_singlet,k_mbdeg,k_mb2deg,k_triplet,kHIS,kTRP,kMET,kTYR,kMB3HIS,kMB3T
RP,
kMB3MET,kMB3TYR,k1O2HIS,k1O2TRP,k1O2MET,k1O2TYR,kMB3ann,k3MBMB2,kMBquench,
kMEL,kfm,krd,BCMBres,BCMBchor,BCO2res,BCO2chor,fxl,fbleach,fanlink,fhisble
ach, kMBradq, kMBH, kMBH2MB, kMBH2ox,fexp3, oxdeg, Dair, DO2air,BMBHres)
 %Function containing differential equations

 % The first and last equations will be defined explicitly
 % The middle equations will have relative references
 % Equations are written with diffusion first, other, then reactions

 dydt=zeros(sizey,1);

 abeg=1; bbeg=abeg+XS; cbeg=bbeg+XS; dbeg=cbeg+XS; ebeg=dbeg+XS;
fbeg=ebeg+XS; gbeg=fbeg+XS; hbeg=gbeg+XS; ibeg=hbeg+XS; jbeg=ibeg+XS;
kbeg=jbeg+XS; lbeg=kbeg+XS; mbeg=lbeg+XS; nbeg=mbeg+XS; obeg=nbeg+XS;
 aend=XS; bend=aend+XS; cend=bend+XS; dend=cend+XS; eend=dend+XS;
fend=eend+XS; gend=fend+XS; hend=gend+XS; iend=hend+XS; jend=iend+XS;
kend=jend+XS; lend=kend+XS; mend=lend+XS; nend=mend+XS; oend=nend+XS;

 mid=2:(XS-1);
 DMB=DMB';
 DO2=DO2';
 mu=mu';


 DiffB=[(y(bbeg+1)-2*y(bbeg)+MBmres)/dx^2;    (y(b+1)-2*y(b)+y(b-1))/dx^2;
(MBmchor-2*y(bend)+y(bend-1))/dx^2];
 DiffC=[(y(cbeg+1)-2*y(cbeg)+ MBdres)/dx^2;   (y(c+1)-2*y(c)+y(c-1))/dx^2;
(MBdchor-2*y(cend)+y(cend-1))/dx^2];
 DiffD=[(y(dbeg+1)-2*y(dbeg)+0)/dx^2;         (y(d+1)-2*y(d)+y(d-1))/dx^2;
2*(-y(dend)+y(dend-1))/(dx)^2];
 DiffE=[(y(ebeg+1)-2*y(ebeg)+O23res)/dx^2;    (y(e+1)-2*y(e)+y(e-1))/dx^2;
(O23chor-2*y(eend)+y(eend-1))/dx^2];
```

```
 DiffF=[(y(fbeg+1)-2*y(fbeg)+0)/dx^2;          (y(f+1)-2*y(f)+y(f-1))/dx^2;
2*(-y(fend)+y(fend-1))/(dx)^2];
 DiffN=[(y(nbeg+1)-2*y(nbeg)+0)/dx^2;          (y(n+1)-2*y(n)+y(n-1))/dx^2;
2*(-y(nend)+y(nend-1))/(dx)^2];
 DiffO=[(y(obeg+1)-2*y(obeg)+0)/dx^2;          (y(o+1)-2*y(o)+y(o-1))/dx^2;
2*(-y(oend)+y(oend-1))/(dx)^2];

 if BCMBres==1
 %     DiffB(1)=DiffB(2);
 %     DiffC(1)=DiffC(2);
 DiffB(1)=2*(y(bbeg+1)-y(bbeg))/(dx)^2;
 DiffC(1)=2*(y(cbeg+1)-y(cbeg))/(dx)^2;
 end

 if BCMBchor==1
 %     DiffB(end)=DiffB(XS-1);
 %     DiffC(end)=DiffC(XS-1);
 DiffB(end)=2*(-y(bend)+y(bend-1))/(dx)^2;
 DiffC(end)=2*(-y(cend)+y(cend-1))/(dx)^2;
 end

 if BCO2res==1
 %     DiffE(1)=DiffE(2);
 DiffE(1)=2*(y(ebeg+1)-y(ebeg))/(dx)^2;
 end

 if BCO2chor==1
 %     DiffE(end)=DiffE(XS-1);
 DiffE(end)=2*(-y(eend)+y(eend-1))/(dx)^2;
 end

 if BMBHres==1
     DiffN(1)=2*(y(nbeg+1)-y(nbeg)+0)/dx^2;
     DiffO(1)=2*(y(obeg+1)-y(obeg)+0)/dx^2;
 end

 FLmon=e_M.*y(B)./(e_M*y(B)+e_D*y(C)+mu);

 DBDTbeg = DMB(1)*DiffB(1) -    PhiT*(1-
y(abeg))*y(aend)*prod(y(a),1)*I0.*FLmon(1)-    PhiDeg*(1-
y(abeg))*y(aend)*prod(y(a),1)*I0.*FLmon(1) -   2*kfm*y(bbeg).^2 -
kfm*y(bbeg).*y(dbeg) + 2*krd*y(cbeg) + k_MB3relax*y(dbeg) +
kMB3ann*y(dbeg).^2 + (kMB3HIS*y(dbeg).*y(hbeg) + kMB3TRP*y(dbeg).*y(ibeg)
+ kMB3MET*y(dbeg).*y(jbeg) + kMB3TYR*y(dbeg).*y(mbeg)) +
k3MBMB2*y(dbeg).*y(cbeg) + k_singlet*y(dbeg).*y(ebeg) +
```

```
k_mb2deg*y(cbeg).*y(fbeg) - k_mbdeg*y(bbeg).*y(fbeg)
+kMBquench*(y(bbeg)).*y(dbeg);
 DBDT =    DMB(mid).*DiffB(mid) -       PhiT*(1-
y(a)).*cumprod(y(a+1),1,'reverse')*I0.*FLmon(mid) - PhiDeg*(1-
y(a)).*cumprod(y(a+1),1,'reverse')*I0.*FLmon(mid) - 2*kfm*y(b).^2 -
kfm*y(b).*y(d)+    2*krd*y(c) +    k_MB3relax*y(d) +      kMB3ann*y(d).^2
+(kMB3HIS*y(d).*y(h) + kMB3TRP*y(d).*y(i) + kMB3MET*y(d).*y(j) +
kMB3TYR*y(d).*y(m)) + k3MBMB2*y(d).*y(c) +       k_singlet*y(d).*y(e) +
k_mb2deg*y(c).*y(f) -       k_mbdeg*y(b).*y(f) + kMBquench*(y(b)).*y(d);
 DBDTend = (2*DMB(end)*Dair)/(DMB(end)*Dair)*DiffB(end) - PhiT*(1-
y(aend))*I0.*FLmon(end) - PhiDeg*(1-y(aend))*I0.*FLmon(end) -
2*kfm*y(bend).^2 - kfm*y(bend).*y(dend) + 2*krd*y(cend) +
k_MB3relax*y(dend) + kMB3ann*y(dend).^2 + (kMB3HIS*y(dend).*y(hend) +
kMB3TRP*y(dend).*y(iend) + kMB3MET*y(dend).*y(jend) +
kMB3TYR*y(dend).*y(mend)) + k3MBMB2*y(dend).*y(cend) +
k_singlet*y(dend).*y(eend) + k_mb2deg*y(cend).*y(fend) -
k_mbdeg*y(bend).*y(fend) + kMBquench*(y(bend)).*y(dend);

 DCDTbeg = DMB(1).*DiffC(1) +   kfm*y(bbeg).^2 + kfm*y(bbeg).*y(dbeg)-
krd*y(cbeg) - k_mb2deg*y(cbeg).*y(fbeg);
 DCDT =    DMB(mid).*DiffC(mid) +        kfm*y(b).^2 + kfm*y(b).*y(d)-
krd*y(c) -    k_mb2deg*y(c).*y(f);
 DCDTend = (2*DMB(end)*Dair)/(DMB(end)*Dair).*DiffC(end) + kfm*y(bend).^2
+ kfm*y(bend).*y(dend)- krd*y(cend) - k_mb2deg*y(cend).*y(fend);

 %Left boundary
 dydt(abeg) = -dx*log(10)*(e_M*DBDTbeg+e_D*DCDTbeg).*10.^(-
(e_M*y(bbeg)+e_D*y(cbeg)+mu(1))*dx);
 dydt(bbeg) = DBDTbeg;
 dydt(cbeg) = DCDTbeg;
 dydt(dbeg) = DMB(1).*DiffD(1) + PhiT*(1-
y(abeg))*y(aend)*prod(y(a),1)*I0.*FLmon(1) - k_MB3relax*y(dbeg) -
kfm*y(bbeg).*y(dbeg) - kMB3HIS*y(dbeg).*y(hbeg) - kMB3TRP*y(dbeg).*y(ibeg)
- kMB3MET*y(dbeg).*y(jbeg) -kMB3TYR*y(dbeg).*y(mbeg)-
kMBquench*(y(bbeg)).*y(dbeg) - 2*kMB3ann*y(dbeg).^2 -
k3MBMB2*y(dbeg).*y(cbeg) - k_singlet*y(dbeg).*y(ebeg);
 dydt(ebeg) = DO2(1).*DiffE(1) - k_singlet*y(dbeg).*y(ebeg) +
k_triplet*y(fbeg) + k1O2HIS*y(fbeg).*y(hbeg) + k1O2TRP*y(fbeg).*y(ibeg) +
k1O2MET*y(fbeg).*y(jbeg) + k1O2TYR*y(fbeg).*y(mbeg) -
kMBH*(y(kbeg)+y(nbeg)+y(obeg)).*y(ebeg);
 dydt(fbeg) = DO2(1).*DiffF(1) + k_singlet*y(dbeg).*y(ebeg) -
k_triplet*y(fbeg) - k1O2HIS*y(fbeg).*y(hbeg) - k1O2TRP*y(fbeg).*y(ibeg) -
k1O2MET*y(fbeg).*y(jbeg) -k1O2TYR*y(fbeg).*y(mbeg) -
k_mb2deg*y(cbeg).*y(fbeg) - k_mbdeg*y(bbeg).*y(fbeg) -
kHIS*y(fbeg).*y(hbeg) - kTRP*y(fbeg).*y(ibeg) - kMET*y(fbeg).*y(jbeg) -
kTYR*y(fbeg).*y(mbeg);
```

```
 % dydt(gbeg) = PhiDeg*(1-y(abeg))*y(aend)*prod(y(a),1)*I0.*FLmon(1) +
k_mb2deg*y(cbeg).*y(fbeg) + k_mbdeg*y(bbeg).*y(fbeg) +
kMBH2ox*y(obeg).*y(ebeg);
 dydt(gbeg) = 0;
 dydt(hbeg) = -kHIS*y(fbeg).*y(hbeg)-(fbleach)*kMB3HIS*y(dbeg).*y(hbeg)+
kMBH2ox*y(kbeg);
 dydt(ibeg) = -kTRP*y(fbeg).*y(ibeg) - (fbleach)*kMB3TRP*y(dbeg).*y(ibeg)+
kMBH2ox*y(nbeg);
 dydt(jbeg) = -kMET*y(fbeg).*y(jbeg) - (fbleach)*kMB3MET*y(dbeg).*y(jbeg);
 dydt(kbeg) = fbleach*kMB3HIS*y(dbeg).*y(hbeg)-kMBH*y(kbeg).*y(ebeg)-
kMBH2ox*y(kbeg);
 dydt(lbeg) = kHIS*y(fbeg).*y(hbeg) +
kTRP*y(fbeg).*y(ibeg)+kTYR*y(fbeg).*y(mbeg)+
kMBH*(y(kbeg)+y(nbeg)+y(obeg)).*y(ebeg);
 dydt(mbeg) = -kTYR*y(fbeg).*y(mbeg) - (fbleach)*kMB3TYR*y(dbeg).*y(mbeg)+
kMBH2ox*y(obeg);
 dydt(nbeg) = fbleach*kMB3TRP*y(dbeg).*y(ibeg)-kMBH*y(nbeg).*y(ebeg)-
kMBH2ox*y(nbeg);
 dydt(obeg) = fbleach*kMB3TYR*y(dbeg).*y(mbeg)-kMBH*y(obeg).*y(ebeg)-
kMBH2ox*y(obeg);

 %Middle
 dydt(a) = -dx*log(10)*(e_M*DBDT+e_D*DCDT).*10.^(-
(e_M*y(b)+e_D*y(c)+mu(mid))*dx);
 dydt(b) = DBDT;
 dydt(c) = DCDT;
 dydt(d) = DMB(mid).*DiffD(mid) + PhiT*(1-
y(a)).*cumprod(y(a+1),1,'reverse')*I0.*FLmon(mid) - k_MB3relax*y(d) -
kfm*y(b).*y(d)- kMB3HIS*y(d).*y(h) - kMB3TRP*y(d).*y(i) -
kMB3MET*y(d).*y(j)-kMB3TYR*y(d).*y(m) - kMBquench*(y(b)+y(o)).*y(d) -
2*kMB3ann*y(d).^2 - k3MBMB2*y(d).*y(c) - k_singlet*y(d).*y(e);
 dydt(e) = DO2(mid).*DiffE(mid) - k_singlet*y(d).*y(e) + k_triplet*y(f) +
k1O2HIS*y(f).*y(h) + k1O2TRP*y(f).*y(i) + k1O2MET*y(f).*y(j) +
k1O2TYR*y(f).*y(m)  -kMBH*(y(k)+y(n)+y(o)).*y(e);
 dydt(f) = DO2(mid).*DiffF(mid) + k_singlet*y(d).*y(e) - k_triplet*y(f) -
k1O2HIS*y(f).*y(h) - k1O2TRP*y(f).*y(i) - k1O2MET*y(f).*y(j) -
k1O2TYR*y(f).*y(m) - k_mb2deg*y(c).*y(f) - k_mbdeg*y(b).*y(f)  -
kHIS*y(f).*y(h) - kTRP*y(f).*y(i) - kMET*y(f).*y(j)- kTYR*y(f).*y(m) ;
 % dydt(g) = PhiDeg*(1-y(a)).*cumprod(y(a+1),1,'reverse')*I0.*FLmon(mid) +
k_mb2deg*y(c).*y(f) + k_mbdeg*y(b).*y(f) + kMBH2ox*y(o).*y(e);
 dydt(g) = 0;
 dydt(h) = -kHIS*y(f).*y(h)-(fbleach)*kMB3HIS*y(d).*y(h) + kMBH2ox*y(k);
 dydt(i) = -kTRP*y(f).*y(i) - (fbleach)*kMB3TRP*y(d).*y(i)+ kMBH2ox*y(n);
 dydt(j) = -kMET*y(f).*y(j) - (fbleach)*kMB3MET*y(d).*y(j);
 dydt(k) = fbleach*kMB3HIS*y(d).*y(h)-kMBH*y(k).*y(e)-kMBH2ox*y(k);
```

```
 dydt(l) = kHIS*y(f).*y(h) + kTRP*y(f).*y(i)+kTYR*y(f).*y(m)+
kMBH*(y(k)+y(n)+y(o)).*y(e);
 dydt(m) = -kTYR*y(f).*y(m) - (fbleach)*kMB3TYR*y(d).*y(m)+ kMBH2ox*y(o);
 dydt(n) = fbleach*kMB3TRP*y(d).*y(i)-kMBH*y(n).*y(e)-kMBH2ox*y(n);
 dydt(o) = fbleach*kMB3TYR*y(d).*y(m)-kMBH*y(o).*y(e)-kMBH2ox*y(o);

 %Right boundary
 dydt(aend) = -dx*log(10)*(e_M*DBDTend+e_D*DCDTend).*10.^(-
(e_M*y(bend)+e_D*y(cend)+mu(end))*dx);   %Normal light propagation
 dydt(bend) = DBDTend;
 dydt(cend) = DCDTend;
 dydt(dend) = DMB(end).*DiffD(end) + PhiT*(1-y(aend))*I0.*FLmon(end) -
k_MB3relax*y(dend)- kfm*y(bend).*y(dend) - kMB3HIS*y(dend).*y(hend) -
kMB3TRP*y(dend).*y(iend) - kMB3MET*y(dend).*y(jend) -
kMB3TYR*y(dend).*y(mend)- kMBquench*(y(bend)).*y(dend) -
2*kMB3ann*y(dend).^2 - k3MBMB2*y(dend).*y(cend) -
k_singlet*y(dend).*y(eend);
 dydt(eend) = (2*DO2(end)*DO2air)/(DO2(end)+DO2air).*DiffE(end) -
k_singlet*y(dend).*y(eend) + k_triplet*y(fend) + k1O2HIS*y(fend).*y(hend)
+ k1O2TRP*y(fend).*y(iend) + k1O2MET*y(fend).*y(jend) +
k1O2TYR*y(fend).*y(mend)-kMBH*(y(kend)+y(nend)+ y(oend)).*y(eend);
 dydt(fend) = DO2(end).*DiffF(end) + k_singlet*y(dend).*y(eend) -
k_triplet*y(fend) - k1O2HIS*y(fend).*y(hend) - k1O2TRP*y(fend).*y(iend) -
k1O2MET*y(fend).*y(jend) - k1O2TYR*y(fend).*y(mend) -
k_mb2deg*y(cend).*y(fend) - k_mbdeg*y(bend).*y(fend)  -
kHIS*y(fend).*y(hend) - kTRP*y(fend).*y(iend) - kMET*y(fend).*y(jend)-
kTYR*y(fend).*y(mend);
 % dydt(gend) = PhiDeg*(1-y(aend))*I0.*FLmon(end) +
k_mb2deg*y(cend).*y(fend) + k_mbdeg*y(bend).*y(fend) +
kMBH2ox*y(oend).*y(eend);
 dydt(gend) = 0;
 dydt(hend) = -kHIS*y(fend).*y(hend)-
(fbleach)*kMB3HIS*y(dend).*y(hend)+kMBH2ox*y(kend);
 dydt(iend) = -kTRP*y(fend).*y(iend) -
(fbleach)*kMB3TRP*y(dend).*y(iend)+kMBH2ox*y(nend);
 dydt(jend) = -kMET*y(fend).*y(jend) - (fbleach)*kMB3MET*y(dend).*y(jend);
 dydt(kend) = fbleach*kMB3HIS*y(dend).*y(hend)-kMBH*y(kend).*y(eend)-
kMBH2ox*y(kend);
 dydt(lend) = kHIS*y(fend).*y(hend) +
kTRP*y(fend).*y(iend)+kTYR*y(fend).*y(mend)+
kMBH*(y(kend)+y(nend)+y(oend)).*y(eend);
 dydt(mend) = -kTYR*y(fend).*y(mend) -
(fbleach)*kMB3TYR*y(dend).*y(mend)+kMBH2ox*y(oend);
 dydt(nend) = fbleach*kMB3TRP*y(dend).*y(iend)-kMBH*y(nend).*y(eend)-
kMBH2ox*y(nend);
```

```
 dydt(oend) = fbleach*kMB3TYR*y(dend).*y(mend)-kMBH*y(oend).*y(eend)-
kMBH2ox*y(oend);

 % a = Light
 % b = MBm
 % c = MBd
 % d = MB3
 % e = O23
 % f = O21
 % g = MBdeg
 % h = HIS
 % i = TRP
 % j = MET
 % k = MEL
 % l = Xlink
 % m = TYR
 % N = MBH
 % O = MBH2
 end

 function J=jsparse(Jsparse)
     J=Jsparse;
 end

 function J=jacobian(XS)
 jcell = {...
    %a b c d e f g h i j k l
     4 3 3 1 1 1 0 1 1 1 0 0;        %a Light
     4 3 1 1 1 1 0 1 1 1 0 0;        %b MBm
     0 1 3 0 0 1 0 0 0 0 0 0;        %c MBd
     4 1 1 1 1 0 0 1 1 1 0 0;        %d 3MB
     0 0 0 1 3 1 0 1 1 1 0 0;        %e 3O2
     0 0 1 1 1 1 0 1 1 1 1 0;        %f 1O2
     4 1 1 0 0 1 0 0 0 0 0 0;        %g
     0 0 0 1 0 1 0 1 0 0 0 0;        %h
     0 0 0 1 0 1 0 0 1 0 0 0;        %i
     0 0 0 1 0 1 0 0 0 1 0 0;        %j
     0 0 0 0 0 1 0 0 0 0 1 0;        %k
     0 0 0 1 0 1 0 1 0 0 0 0 ...     %l
     };
 end
```

APPENDIX E. COMPUTATIONAL MODEL CODE: MB SCLERAL PHOTOCROSSLINKING

```
% Brandon Gerberich
% Last updated: 2020-04-13

clear all       %Clears all variables
pause(0.5)      %Pauses for 0.5 seconds to allow time for memory to clear
clc             %Clears command line text
close all       %Closes all MATLAB figure windows (graphs)

tic             %Starts timer to report code run time upon completion
(useful for estimating future run time)
format compact  %Changes command line text format to compact mode
format long g   %Changes command line number format to show decimals

ploton=0;               %Set to 1 if you want to plot the output data, 0
if not.
Agent='MB';             %Prints the sensitizer name in graphs (change if
using other sensitizer)
Lighttype='660nm';      %Prints the light name in graphs (change if using
other sensitizer)

Concentration=3/1000;   %Molar
counter2=0;             %Set loop counter to 0

for mastercounter=1:length(Concentration)
%Clears only the selected variables to reduce memory usage. These will
need to be adjusted based on what value you are changing each loop.
pause(1)
    clearvars -except counter2 ploton Agent Lighttype mastercounter
mastervector
pause(1)

counter2=counter2+1;    %Increase counter by 1;

%Set boundary conditions - this is a logical value used in the "odefcn"
where I defined the mathematical equations
BCMBres=0;                  %1 if reflection, otherwise Dirichlet. BC for
MB at retrobulbar tissue (posterior reservoir surface)
BCMBchor=0;                 %1 if reflection, otherwise Dirichlet. BC for
MB at choroid anterior surface
```

```
 BCO2res=0;                  %1 if reflection, otherwise Dirichlet. BC for
oxygen at retrobulbar tissue (posterior reservoir surface)
 BCO2chor=0;                 %1 if reflection, otherwise Dirichlet. BC for
oxygen at choroid anterior surface

 %Select boundary conditions. Comment/uncomment desired set for oxygen.
Note, these only apply if Dirichlet condition is selected above.
 % O23res=2.18e-5;             %20% O2 (normoxia), Concentration of oxygen
at tenon-reservoir interface [M]
 % O23chor=4.81e-5;            %20% O2 (normoxia), Concentration of oxygen
in choroid [M]
 O23res=10.65e-5;          %100% O2 (hyperoxia), Concentration of oxygen
at tenon-reservoir interface [M]
 O23chor=26.10e-5;         %100% O2, (hyperoxia),Concentration of oxygen
in choroid [M]

 C0_MBres=0;                 %Concentration of MB at muscle cone
 C0_MBchor=0;                %Concentration of MB at choroid

 %Set crosslinking treatment parameters
 Isource=0.424;              %Define light intensity (W/cm2)
 tmax=1800;                  %Procedure duration (Seconds)
 C0_MBinj=0.003;             %Initial condition for concentration of MB in
the injection reservoir
 O23inj=1.94e-4;             %Initial condition for concentration of
oxygen in injection solution [M] asssumed to be solubility limit at
atmospheric pressure

 %These parameters are not physical inputs. Rather, they are multipliers
that allow you to quickly include/exclude certain parameters for testing.
Ordinarily, users need not change these.
 fexp=1;                     %Reduction of amino acid concentration
 fexp2=1;                    %Reduction of the triplet quenching rate of
amino acids
 fdiff=1;                    %Fraction of diffusion constant for MB
 fbleach=0;                  %Fraction of TRP and MET which is degraded
after quenching 3MB, consumes MBm
 fanlink=0;                  %Fraction of TRP and MET which form xlinks
after quenching 3MB and returns MBm
 fhisbleach=0;               %Fraction of HIS which is degraded after
quenching 3MB
 fxl=0;                      %Fraction of 3MB quenched by histidine which
form Xlinks

 %Set initial concentrations of amino acids, melanin
```

```
 C0_HIS=0.0124*fexp;         %Concentration of histidine in the sclera
[M], Edwards & Prausnitz 1998
 C0_TRP=0.0083*fexp;         %Concentration of tryptophan in the sclera
[M], Edwards & Prausnitz 1998
 C0_MET=0.0207*fexp;         %Concentration of methionine in the sclera
[M], Edwards & Prausnitz 1998
 C0_TYR=0.0193*fexp;         %Concentration of tyrosine ""
 C0_MELscl=0.003;            %Concentration of melanin in sclera [M]
 C0_MELchor=0.305;           %Concentration of melanin in choroid [M]
 C0_MELrpe=0.085;            %Concentration of melanin in rpe [M]
 Chorlumen=0.4;              %Fraction of choroid which is blood vessels
(not collagen)

 %Set initial photophysical parameters
 lambda= 660*10^-9;          %Wavelenght of light, [m], 660 default
 Retchorabs=0.096;           %Fraction of light reflected by retina
 e_M=79800;                  %Molar absorptivity (epsilon) of sensitizer
monomer
 e_D=35300;                  %" " of sensitizer dimer
 e_MEL=646;                  %" " of melanin
 PhiT=0.52;                  %Triplet quantum yield of sensitizer
 PhiDeg=6.7e-6;              %Photodegradation quantum yield of sensitizer
 mures=0;                    %Linear attenuation coefficient of reservoir
 muten=1.75*0.001;           %" " of tenon. Set effectively to 0 for MB in
sclera
 muscl=1.75*0.001;           %" " of sclera. " "
 muchor=1.75*0.001;          %" " of choroid. " "

 %Set tissue dimension parameters
 Scleralength=0.0104;    %[cm] 833 microns from Heichel 2016
 Tenlength=0.0026;       %[cm] 26 microns
 Reslength=0.31;         %[cm] Calculated from injection volume 0.10885
 Chorlength=0.0045;      %Length of choroid [cm]
 RPElength=0.001;        %Length of RPE [cm]
 Cleardist=0.0045;       %Distance from reservoir to boundary condition in
the retrobulbar tissue

 Tenx=10;                %# Nodes in tenon layer
 Sclx=100;                %# Nodes in sclera
 Chorx=70;               %# Nodes in choroid
 Resfold=1.4;            %Used to compute uneven reservoir
nodes/thicknesses. Maximum ratio of adjacent node widths.

 %Kinetic rate constants
 Keq=10665;              %Equilibrium constant for dimerization defined as
K=[Dimer]/[Monomer]^2, [M]^-1, 2910 default. K=kf/kr=[D]/[M]^2
```

```
 kfm=10.93e8;            %Forward rate constant for dimerization, from
Spencer 1979
 krd=kfm/Keq;            %Reverse rate constant. Assuming the value for
kfm allows back calculation from K which is more widely available. The
value of kfm just needs to be large so reaction happens quickly if want to
assume instant dimerizastion
 k_singlet=2.6e9;        %Reaction rate for 3MB (triplet MB) and 3O2
(triplet oxygen), [M^-1 s^-1]
 k_mbdeg=3E8*0;          %Reaction rate for 1O2 (singlet oxygen) and MB
leading to degradation of MB, [M^-1 s^-1]
 k_mb2deg=2*k_mbdeg;     %Reaction rate for 1O2 with MB2 - 2*k_mbdeg
because the effective concentration of monomers is doubled for dimers
 k_triplet=2.56E5;       %Rate for 1O2 (singlet oxygen) relaxation to 3O2
(triplet oxygen), [s^-1], 2.5E5 default.
 k_MB3relax=1.3E4;       %Relaxation rate of MB3 to MB calculated from
lifetime of 77us (Alacron 2012), [s^-1], 1.3E5 default
 kMBquench=4.1E7;        %Rate of ground state monomer quenching 3MB Kamat
1981 "Photoinduced electron..."
 kMB3HIS=2E6*fexp2;      %Reaction rate for physical quenching of 3MB by
histidine, [M^-1 s^-1], 2E6 default
 kMB3TRP=6E8*fexp2;      %Reaction rate for physical quenching of 3MB by
tryptophan, [M^-1 s^-1], 6E8 default
 kMB3MET=1E8*fexp2;      %Reaction rate for physical quenching of 3MB by
methionine, [M^-1 s^-1], 1E8 default
 kMB3TYR=0*fexp2;        %Reaction rate for physical quenching of 3MB by
tyrosine, [M^-1 s^-1]
 kMB3ann=8.9e8*0;        %Rate of MB3 annihilation
 k3MBMB2=kMBquench;      %Rate of MB3 quenching by dimer
 kHIS=1E8;               %Reaction rate for 1O2 (singlet oxygen) and
collagen leading to crosslinks, [M^-1 s^-1], 5E7 default
 kTRP=3E7;               %Reaction rate for chemical quenching of singlet
oxygen by tryptophan, [M^-1 s^-1], 4E6 default
 kMET=1.6E7;             %Reaction rate for chemical quenching of singlet
oxygen by methionine, [M^-1 s^-1], 5E6 default
 kTYR=8e6;               %Reaction rate for chemical quenching of singlet
oxygen by tyrosine, [M^-1 s^-1]
 k1O2MB=3e8;             %Physical quenching of 1O2 by MB. 3E8 default
(Schmidt 1980 referenced in Wilkinson 1995)
 k1O2MB2=k1O2MB;         %Physical quenching of 1O2 by MB2. Estimated
based on monomer physical quenching of 1O2
 k1O2HIS=0;              %Reaction rate for physical quenching of 1O2 by
histidine, [M^-1 s^-1], 4.2E7 default
 k1O2TRP=2.1E7;          %Reaction rate for physical quenching of 1O2 by
tryptophan, [M^-1 s^-1], 4.6E7 default
 k1O2MET=0;              %Reaction rate for physical quenching of 1O2 by
methionine, [M^-1 s^-1], 2.5E7 default
```

```
 k1O2TYR=2.7e7;          %Reaction rate for physical quenching of 1O2 by
tyrosine, [M^-1 s^-1]
 kMEL=1.34E8;            %Reaction rate for melanin with singlet oxygen,
[M^-1 s^-1], 1.32E8 default

 %Diffusion Constants [cm2/s]
 Dres=4.6e-6*100;        %MB in reservoir. Multiplied by 100 to simulate
well-mixed condition
 Dten=3.16e-7*fdiff;     %MB in tenon
 Dscl=3.16e-7*fdiff;     %MB in sclera
 Dchor=3.16e-7*fdiff;    %MB in choroid
 DO2scl=4e-6;            %Oxygen in sclera
 DO2res=4.6e-6*100;      %Oxygen in water. Multiplied by 100 to simulate
well-mixed condition

 %Light conversion to energy
 avogadro=1/(6.022*10^23);   %Avogadro's number (inverse) - converts
number of molecules to Moles, [Mole/units]
 planck=6.62607004*10^-34;   %Planck's constant, [J*s]
 ls=299792458;               %Speed of light, [m/s]
 Energy=planck*ls/lambda;    %Energy of a photon, [J]

 % DEFINITION OF PARAMETERS ENDS HERE. BELOW BEGINS CONSTRUCTION OF
VECTORS
 % FOR MODEL INPUT

 %Define node thickness vectors. Indicates width of each node
 Scldx=Scleralength/Sclx;                %Sclera node thicknesses
 Tendx=Tenlength/Tenx;                   %Tenon node thicknesses
 Chordx=Chorlength/Chorx;                %Choroid node thicknesses

 %Below we calculate the undeven node spacing of reservoir. Selects
resfold to span the distance
 %defined by Reslength. Allows power spacing of reservoir slice
thicknesses
 %using a flexible value calcualted for the power, RESFOLD

 resl=0; %Counter for # nodes to span reservoir. Changes on each
iteration.
 resf=0; %Calcuated value of resfold from algorithm below. Changes on each
iteration

 while or(Resfold<resf,resf<1)
 resl=resl+1;
 syms RESFOLD; F1= 2*Tendx*RESFOLD.^([0 1:resl]); F2=sum(F1)==Reslength;
 resf=vpasolve(F2,RESFOLD,[0 Inf]);
```

```
 end

 Resx=2*resl+2;        %Need to double the reslength because the vector is
mirrored
 Resdx=[Tendx*resf.^([0 1:resl]) fliplr(Tendx*resf.^([0 1:resl]))];
%Mirroring the Resdx vector - symmetry makes

 %Create Tissue Indices
 Res=1:Resx;
 Ten=(Res(end)+1):(Res(end)+Tenx);
 Scl=(Ten(end)+1):(Ten(end)+Sclx);
 Chor=(Scl(end)+1):(Scl(end)+Chorx);
 TenScl=[Ten Scl];

 %Calculate #X Slices
 XS=Resx+Tenx+Sclx+Chorx;            %Number of nodes in model
 xmax=Scldx+Chordx;
 xspace=1:XS;
 plotlength=length([Ten Scl Chor]);

 %Create MB Diffusion Vector
 DMB=ones(1,XS);
 DMB(Res)=Dres;
 DMB(Ten)=Dten;
 DMB(Scl)=Dscl;
 DMB(Chor)=Dchor;

 DMBright=circshift([Dscl DMB Dchor],-1);
 DMBright=DMBright([2:(end-1)]);
 DMBleft=circshift([Dscl DMB Dchor],1);
 DMBleft=DMBleft([2:(end-1)]);

 %Create Oxygen Diffusion Vector
 DO2=DO2scl*ones(1,XS);
 DO2(Res)=DO2res;

 DO2right=circshift([DO2scl DO2 DO2scl],-1);
 DO2right=DO2right(2:(end-1));
 DO2left=circshift([DO2scl DO2 DO2scl],1);
 DO2left=DO2left(2:(end-1));

 %Create mu Vector
 mu=zeros(1,XS);
 mu(Res)=mures;
 mu(Ten)=muten;
 mu(Scl)=muscl;
```

```
 mu(Chor)=muchor;

 %Create Node Thickness Vector
 % dx=xmax/XS
 dxV=ones(1,XS);
 dxV(Ten)=Tendx;
 dxV(Scl)=Scldx;
 dxV(Chor)=Chordx;
 dxV(Res)=Resdx;

 dxVright=circshift([Scldx dxV Chordx],-1);    %Creates i+1 spatial
thickness vector for numerical diffusion equation
 dxVright=dxVright(2:(end-1));
 dxVleft=circshift([Cleardist dxV Chordx],1);      %Creates i-1 spatial
thickness vector for numerical diffusion equation
 dxVleft=dxVleft(2:(end-1));

 %Calculate Space & Time Intervals
 Dmax=max([Dres Dten Dscl Dchor DO2]);
 % dt=dx^2/Dmax;
 dt=min(min(dxV.^2./[DO2; DO2right; DO2left; DMB; DMBright; DMBleft]));

 %Calculate Constants
 I0fchor=(1-(1-Retchorabs)*10^-(e_MEL*C0_MELrpe*RPElength));
 I0=I0fchor*Isource/Energy*avogadro./dxV*1000;           %Converts
intensity units, [M/s]
 MBmres=(-1+sqrt(1+8*Keq*C0_MBinj))/(4*Keq);
 MBdres=0.5*(C0_MBinj-(-1+sqrt(1+8*Keq*C0_MBinj))/(4*Keq));
 MBmchor=(-1+sqrt(1+8*Keq*C0_MBchor))/(4*Keq);
 MBdchor=0.5*(C0_MBchor-(-1+sqrt(1+8*Keq*C0_MBchor))/(4*Keq));

 %Initialize variables
 cumdx=cumsum(dxV([Ten Scl Chor]));

 MBm=zeros(1,XS); MBm(Res)=MBmres;
 MBd=zeros(1,XS); MBd(Res)=MBdres;
 MB3=zeros(1,XS);
 MBdeg=zeros(1,XS);
 % O23=O23res+(1:XS)/(XS+1)*(O23chor-O23res);
 O23=zeros(1,XS);
 O23([Ten Scl Chor])=O23res+cumdx*(O23chor-O23res)/cumdx(end);
 O23(Res)=O23inj;
 % O23=O23chor*ones(1,XS);
 O21=zeros(1,XS);
 HIS=C0_HIS*ones(1,XS); HIS(Res)=0; HIS(Chor)=HIS(Chor)*(1-Chorlumen);
 TRP=C0_TRP*ones(1,XS); TRP(Res)=0; TRP(Chor)=TRP(Chor)*(1-Chorlumen);
```

```
 MET=C0_MET*ones(1,XS); MET(Res)=0; MET(Chor)=MET(Chor)*(1-Chorlumen);
 MEL=zeros(1,XS); MEL(Chor)=C0_MELchor; MEL(Scl)=C0_MELscl;
 TYR=C0_TYR*ones(1,XS); TYR(Res)=0; TYR(Chor)=TYR(Chor)*(1-Chorlumen);
 Xlink=zeros(1,XS);
 Light=10.^(-(e_M*MBm+e_D*MBd+e_MEL*MEL+mu).*dxV);       %Pct transmitted
in each step
 probe1=zeros(1,XS);
 probe2=zeros(1,XS);
 probe3=zeros(1,XS);

 Xlinkspossible=sum((HIS([Scl Chor])+TYR([Scl Chor])+TRP([Scl
Chor])).*dxV([Scl Chor]))/sum(dxV([Scl Chor]));

 %Define Domains of DYDT
 A=1:XS; B=A+XS; C=B+XS; D=C+XS; E=D+XS; F=E+XS; G=F+XS; H=G+XS; I=H+XS;
J=I+XS; K=J+XS; L=K+XS; M=L+XS; N=M+XS; O=N+XS; P=O+XS;
 %Define "Middle" Domains of DYDT
 a=2:(XS-1); b=a+XS; c=b+XS; d=c+XS; e=d+XS; f=e+XS; g=f+XS; h=g+XS;
i=h+XS; j=i+XS; k=j+XS; l=k+XS; m=l+XS; n=m+XS; o=n+XS; p=o+XS;

 sizey=length([A B C D E F G H I J K L M N O P]);
 tspan=0:1:18000; % tspan=0:dt:tmax;
 TS=length(tspan);

 if TS<10000
     TS=10000
     tspan=linspace(0,tmax,TS);
     disp('TS increased to 10000')
 else if TS>300000
         TS=300000
         tspan=linspace(0,tmax,TS);
         disp('TS reduced to 300000')
     end
 end

 %0 = zeros
 %1 = 0th diagonal     REACTIONS
 %2 = 0,1 diagonals
 %3 = -1,0,1 diagnoals DIFFUSION
 %4 = upper triangular
 %5 = upper triangular with diffusion
 jcell = {...
    %a b c d e f g h i j k l m n o p
     4 3 3 1 1 1 0 1 1 1 1 1 0 0 0 0;        %a Light
     4 3 1 1 1 1 0 1 1 1 1 1 0 0 0 0;        %b MBm
     0 1 3 1 0 1 0 0 0 0 0 0 0 0 0 0;        %c MBd
```

```
    4 1 1 3 1 0 0 1 1 1 1 1 0 0 0 0;        %d 3MB
    0 1 1 1 3 1 0 1 1 1 1 0 0 0 0 0;        %e 3O2 Unique from V33_RF
    0 0 1 1 1 3 0 1 1 1 1 1 0 0 0 0;        %f 1O2
    4 1 1 0 0 1 0 0 0 0 0 1 0 0 0 0;        %g MBdeg
    0 0 0 1 0 1 0 1 0 0 0 0 0 0 0 0;        %h HIS
    0 0 0 1 0 1 0 0 1 0 0 0 0 0 0 0;        %i TRP
    0 0 0 1 0 1 0 0 0 1 0 0 0 0 0 0;        %j MET
    0 0 0 1 0 1 0 0 0 0 1 0 0 0 0 0;        %k TYR
    0 0 0 0 0 1 0 0 0 0 0 1 0 0 0 0;        %l MEL
    0 0 0 1 0 1 0 1 1 0 1 0 0 0 0 0;        %m Xlink
    0 0 0 0 0 1 0 1 0 0 0 0 0 0 0 0;        %n probe1
    0 0 0 0 0 1 0 0 1 0 0 0 0 0 0 0;        %o probe2
    0 0 0 0 0 1 0 0 0 0 1 0 0 0 0 0 ...     %p probe3
    };

 jcelllength=length(jcell);
 jspots=jcelllength^2;
 for counter=1:jspots
     if jcell{counter}==0
         jcell{counter}=zeros(XS);

     elseif jcell{counter}==1
         jcell{counter}=diag(ones(1,XS),0);

     elseif jcell{counter}==2
         jcell{counter}=diag(ones(1,XS-1),1)+diag(ones(1,XS),0);

     elseif jcell{counter}==3
         jcell{counter}=diag(ones(1,XS-1),1)+diag(ones(1,XS-1),-
1)+diag(ones(1,XS),0);

     elseif jcell{counter}==4
         jcell{counter}=triu(ones(XS));

     elseif jcell{counter}==5
         jcell{counter}=triu(ones(XS))+diag(ones(1,XS),0);
     end
 end

 Jsparse=cell2mat(jcell);

 options=odeset('InitialStep',0.000001,'MaxOrder',5,'RelTol',1E-
12,'AbsTol', 1E-14, 'JPattern',jsparse(Jsparse));  %Sets options for
solver
```

```
 y0=[Light' MBm' MBd' MB3' O23' O21' MBdeg' HIS' TRP' MET' TYR' MEL'
Xlink' probe1', probe2', probe3'];                    %Initial
conditions
 [t, y]=ode15s(@(t,y)
odefcn(t,y,XS,sizey,a,b,c,d,e,f,g,h,i,j,k,l,m,n,o,p,B,C,L,I0,e_M,e_D,DMB,D
O2,mu,PhiT,PhiDeg,MBmchor,MBdchor,MBmres,MBdres,O23chor,O23res,k_MB3relax,
k_singlet,k_mbdeg,k_mb2deg,k_triplet,kHIS,kTRP,kMET,kTYR,kMB3HIS,kMB3TRP,
kMB3MET,kMB3TYR,k1O2HIS,k1O2TRP,k1O2MET,k1O2TYR,kMB3ann,k3MBMB2,kMBquench,
kMEL,kfm,krd,BCMBres,BCMBchor,BCO2res,BCO2chor,fxl,fbleach,fanlink,fhisble
ach,Reslength,k1O2MB,k1O2MB2,dxVright,dxVleft,DMBright,DMBleft,dxV,DO2righ
t,DO2left,C0_MBres,Chor, e_MEL),tspan,y0,options);

 %%

 if ploton==0
 %Calculate Plot Grid Mesh
 % xpoints=(1:XS)*dx;
 xpoints2=cumsum(dxV);
 xpoints=xpoints2-xpoints2(Ten(1));
%x distances in the actual tissue used for graphing
 xpoints=xpoints';

 r=round(linspace(1,size(y,1),plotlength));
 s=[Scl Chor];  %Index positions of the desired points for graphing
 % xpoints3=flip(xpoints(s)-min(xpoints(s)))*10000;
 xpoints3=flip(cumsum(dxV(flip(s)))*10000);
 % s=round(linspace(1,length(xpoints'),plotlength));
%Creates vector of XS length evenly spaced between 1 and length(xpoints)
 % tspan=tspan*60;
 t=round(linspace(1,length(tspan),plotlength));
 tlog=round(logspace(0,log10(length(tspan)),plotlength));
 mins=(1:TS)/TS*tmax/60;
 logswitch='linear';
%toggles linear or log scale plots

 tfam = round([0.001 5 10 15 20 25 30]/30*length(tspan));
 % tfam = round([0.001 0.1 0.3 1 3 10 30]/30*length(tspan));
 % tfam = round([20 21 22 23 24 25 26]/30*length(tspan));

 cmapset=hsv(9);
 cmapset=cmapset(1:7,:);
 legendstring=["0 min"; "5 min"; "10 min"; "15 min"; "20 min"; "25 min";
"30 min"];
 % legendstring=["0 min"; "0.1 min"; "0.3 min"; "1 min"; "3 min"; "10
min"; "30 min"];
```

```
 if strcmp(logswitch,'log')==1
     t=round(logspace(0,log10(length(tspan)),plotlength));
     tspan=tspan/60;
 end

 %Calculating Photons Absorbed
 aflip=flip(a);

 Lightbeg=(1-y(:,1)).*y(:,XS).*prod(y(:,a),2).*Isource;
 Lightmid=(1-y(:,a)).*cumprod(y(:,a+1),2,'reverse').*Isource;
 Lightend=(1-y(:,XS)).*Isource;
 Abs=[Lightbeg Lightmid Lightend];

 LI1=fliplr(cumprod(fliplr(y(:,A)),2))*Isource*I0fchor; %Light intensity
from Pct Transmitted

 %Another check for the Light Intensity
 LI2F=10.^(-(e_M*y(:,B)+e_D*y(:,C)+e_MEL*y(L)+mu).*dxV);     %Fraction
light transmitted at each step
 LI2=Isource*fliplr(cumprod(fliplr(LI2F),2));   %Light intensity from
concentration

 %Plot Figures
 figure(1)
 z=plot(xpoints3,y(tfam,A(s)),'LineWidth',2);
 set(z, {'color'}, num2cell(cmapset,2));
 set(gcf, 'Color', [1 1 1]); set(gca, 'color', 'w');
 xlabel('Distance (\mum)','FontSize',14,'FontWeight','bold','Color','k');
%Adds x-label
 ylabel('Fraction Light
Transmitted','FontSize',14,'FontWeight','bold','Color','k');
%Adds z-label
 title('Fraction Light
Transmitted','FontSize',16,'FontWeight','bold','Color','k'); %Adds title
 set(gca,'zscale',logswitch);
 set(gca,'yscale',logswitch);
 set(gcf,'color','w');
 set(gca,'FontSize',14);
 x1=xline(45,'--',{'Sclera'},'Linewidth',2);
 x1.LabelVerticalAlignment = 'bottom';
 x1.LabelHorizontalAlignment = 'right';
 x1.LabelOrientation = 'horizontal';
 x2=xline(45,'--',{'Choroid'},'Linewidth',2);
 x2.LabelVerticalAlignment = 'bottom';
 x2.LabelHorizontalAlignment = 'left';
 x2.LabelOrientation = 'horizontal';
```

```
 legend(legendstring);
 legend('location','eastoutside');
 set(gcf,'position',[0,0,620,400]);

 figure(2)
 z=plot(xpoints3,y(tfam,B(s)),'LineWidth',2);
 set(z, {'color'}, num2cell(cmapset,2))
 set(gcf, 'Color', [1 1 1]); set(gca, 'color', 'w');
 xlabel('Distance (\mum)','FontSize',14,'FontWeight','bold','Color','k')
%Adds x-label
 ylabel('Concentration (M)','FontSize',14,'FontWeight','bold','Color','k')
 title([Agent ' '
'Monomer'],'FontSize',16,'FontWeight','bold','Color','k') %Adds title
 set(gca,'zscale',logswitch)
 set(gca,'yscale',logswitch)
 set(gcf,'color','w');
 set(gca,'FontSize',14)
 x1=xline(45,'--',{'Sclera'},'Linewidth',2);
 x1.LabelVerticalAlignment = 'bottom';
 x1.LabelHorizontalAlignment = 'right';
 x1.LabelOrientation = 'horizontal';
 x2=xline(45,'--',{'Choroid'},'Linewidth',2);
 x2.LabelVerticalAlignment = 'bottom';
 x2.LabelHorizontalAlignment = 'left';
 x2.LabelOrientation = 'horizontal';
 legend(legendstring)
 legend('location','eastoutside')
 set(gcf,'position',[0,0,620,400]);
 set(gca,'YLim',[0 3e-4]);

 figure(3)
 z=plot(xpoints3,y(tfam,C(s)),'LineWidth',2);
 set(z, {'color'}, num2cell(cmapset,2))
 set(gcf, 'Color', [1 1 1]); set(gca, 'color', 'w');
 xlabel('Distance (\mum)','FontSize',14,'FontWeight','bold','Color','k')
%Adds x-label
 ylabel('Concentration (M)','FontSize',14,'FontWeight','bold','Color','k')
%Adds z-label
 title([Agent ' ' 'Dimer'],'FontSize',16,'FontWeight','bold','Color','k')
%Adds title
 set(gca,'zscale',logswitch)
 set(gca,'yscale',logswitch)
 set(gcf,'color','w');
 set(gca,'FontSize',14)
 x1=xline(45,'--',{'Sclera'},'Linewidth',2);
 x1.LabelVerticalAlignment = 'bottom';
```

```
 x1.LabelHorizontalAlignment = 'right';
 x1.LabelOrientation = 'horizontal';
 x2=xline(45,'--',{'Choroid'},'Linewidth',2);
 x2.LabelVerticalAlignment = 'bottom';
 x2.LabelHorizontalAlignment = 'left';
 x2.LabelOrientation = 'horizontal';
 legend(legendstring)
 legend('location','eastoutside')
 set(gcf,'position',[0,0,620,400]);

 figure(4)
 z=plot(xpoints3,y(tfam,D(s)),'LineWidth',2);
 set(z, {'color'}, num2cell(cmapset,2))
 set(gcf, 'Color', [1 1 1]); set(gca, 'color', 'w');

 xlabel('Distance (\mum)','FontSize',14,'FontWeight','bold','Color','k')
%Adds x-label
 ylabel('Concentration (M)','FontSize',14,'FontWeight','bold','Color','k')
%Adds z-label
 title([Agent ' '
'Triplet'],'FontSize',16,'FontWeight','bold','Color','k') %Adds title
 set(gca,'zscale',logswitch)
 set(gca,'yscale',logswitch)
 set(gcf,'color','w');
 set(gca,'FontSize',14)
 x1=xline(45,'--',{'Sclera'},'Linewidth',2);
 x1.LabelVerticalAlignment = 'bottom';
 x1.LabelHorizontalAlignment = 'right';
 x1.LabelOrientation = 'horizontal';
 x2=xline(45,'--',{'Choroid'},'Linewidth',2);
 x2.LabelVerticalAlignment = 'bottom';
 x2.LabelHorizontalAlignment = 'left';
 x2.LabelOrientation = 'horizontal';
 legend(legendstring)
 legend('location','eastoutside')
 set(gcf,'position',[0,0,620,400]);
 set(gca,'YLim',[0 2e-7]);

 figure(5)
 z=plot(xpoints3,y(tfam,E(s)),'LineWidth',2);
 set(z, {'color'}, num2cell(cmapset,2))
 set(gcf, 'Color', [1 1 1]); set(gca, 'color', 'w');
 xlabel('Distance (\mum)','FontSize',14,'FontWeight','bold','Color','k')
%Adds x-label
 ylabel('Concentration (M)','FontSize',14,'FontWeight','bold','Color','k')
```

```
 title('O_2 Triplet','FontSize',16,'FontWeight','bold','Color','k') %Adds
title
 x1=xline(45,'--',{'Sclera'},'Linewidth',2);
 x1.LabelVerticalAlignment = 'bottom';
 x1.LabelHorizontalAlignment = 'right';
 x1.LabelOrientation = 'horizontal';
 x2=xline(45,'--',{'Choroid'},'Linewidth',2);
 x2.LabelVerticalAlignment = 'bottom';
 x2.LabelHorizontalAlignment = 'left';
 x2.LabelOrientation = 'horizontal';
 set(gca,'zscale',logswitch)
 set(gca,'yscale',logswitch)
 set(gcf,'color','w');
 set(gca,'FontSize',14)
 legend(legendstring)
 legend('location','eastoutside')
 set(gcf,'position',[0,0,620,400]);

 figure(6)
 z=plot(xpoints3,y(tfam,F(s)),'LineWidth',2);
 set(z, {'color'}, num2cell(cmapset,2))
 set(gcf, 'Color', [1 1 1]); set(gca, 'color', 'w');
 xlabel('Distance (\mum)','FontSize',14,'FontWeight','bold','Color','k')
%Adds x-label
 ylabel('Concentration (M)','FontSize',14,'FontWeight','bold','Color','k')
%Adds z-label
 title('O_2 Singlet','FontSize',16,'FontWeight','bold','Color','k') %Adds
title
 set(gca,'zscale',logswitch)
 set(gca,'yscale',logswitch)
 set(gcf,'color','w');
 set(gca,'FontSize',14)
 x1=xline(45,'--',{'Sclera'},'Linewidth',2);
 x1.LabelVerticalAlignment = 'bottom';
 x1.LabelHorizontalAlignment = 'right';
 x1.LabelOrientation = 'horizontal';
 x2=xline(45,'--',{'Choroid'},'Linewidth',2);
 x2.LabelVerticalAlignment = 'bottom';
 x2.LabelHorizontalAlignment = 'left';
 x2.LabelOrientation = 'horizontal';
 legend(legendstring)
 legend('location','eastoutside')
 set(gcf,'position',[0,0,620,400]);
 set(gca,'YLim',[0 4e-7]);

 figure(7)
```

```
 z=plot(xpoints3,y(tfam,G(s)),'LineWidth',2);
 set(z, {'color'}, num2cell(cmapset,2))
 set(gcf, 'Color', [1 1 1]); set(gca, 'color', 'w');
 xlabel('Distance (\mum)','FontSize',14,'FontWeight','bold','Color','k')
%Adds x-label
 ylabel('Concentration (M)','FontSize',14,'FontWeight','bold','Color','k')
%Adds z-label
 title('Cumulative Degraded
MB','FontSize',16,'FontWeight','bold','Color','k') %Adds title
 set(gca,'zscale',logswitch)
 set(gca,'yscale',logswitch)
 set(gcf,'color','w');
 set(gca,'FontSize',14)
 x1=xline(45,'--',{'Sclera'},'Linewidth',2);
 x1.LabelVerticalAlignment = 'bottom';
 x1.LabelHorizontalAlignment = 'right';
 x1.LabelOrientation = 'horizontal';
 x2=xline(45,'--',{'Choroid'},'Linewidth',2);
 x2.LabelVerticalAlignment = 'bottom';
 x2.LabelHorizontalAlignment = 'left';
 x2.LabelOrientation = 'horizontal';
 legend(legendstring)
 legend('location','eastoutside')
 set(gcf,'position',[0,0,620,400]);
 set(gca,'YLim',[0 7e-4]);

 figure(8)
 z=plot(xpoints3,y(tfam,M(s)),'LineWidth',2);
 set(z, {'color'}, num2cell(cmapset,2))
 set(gcf, 'Color', [1 1 1]); set(gca, 'color', 'w');
 xlabel('Distance (\mum)','FontSize',14,'FontWeight','bold','Color','k')
%Adds x-label
 ylabel('Concentration (M)','FontSize',14,'FontWeight','bold','Color','k')
 title('Crosslinks','FontSize',16,'FontWeight','bold','Color','k') %Adds
title
 set(gca,'zscale',logswitch)
 set(gca,'yscale',logswitch)
 set(gcf,'color','w');
 set(gca,'FontSize',14)
 x1=xline(45,'--',{'Sclera'},'Linewidth',2);
 x1.LabelVerticalAlignment = 'bottom';
 x1.LabelHorizontalAlignment = 'right';
 x1.LabelOrientation = 'horizontal';
 x2=xline(45,'--',{'Choroid'},'Linewidth',2);
 x2.LabelVerticalAlignment = 'bottom';
 x2.LabelHorizontalAlignment = 'left';
```

```
 x2.LabelOrientation = 'horizontal';
 legend(legendstring)
 legend('location','eastoutside')
 set(gcf,'position',[0,0,620,400]);
 set(gca,'YLim',[0 0.025]);

 figure(9)
 z=plot(xpoints3,y(tfam,H(s)),'LineWidth',2);
 set(z, {'color'}, num2cell(cmapset,2))
 set(gcf, 'Color', [1 1 1]); set(gca, 'color', 'w');
 xlabel('Distance (\mum)','FontSize',14,'FontWeight','bold','Color','k')
%Adds x-label
 ylabel('Concentration (M)','FontSize',14,'FontWeight','bold','Color','k')
 title('His','FontSize',16,'FontWeight','bold','Color','k') %Adds title
 set(gca,'zscale',logswitch)
 set(gca,'yscale',logswitch)
 set(gcf,'color','w');
 set(gca,'FontSize',14)
 x1=xline(45,'--',{'Sclera'},'Linewidth',2);
 x1.LabelVerticalAlignment = 'bottom';
 x1.LabelHorizontalAlignment = 'right';
 x1.LabelOrientation = 'horizontal';
 x2=xline(45,'--',{'Choroid'},'Linewidth',2);
 x2.LabelVerticalAlignment = 'bottom';
 x2.LabelHorizontalAlignment = 'left';
 x2.LabelOrientation = 'horizontal';
 legend(legendstring)
 legend('location','eastoutside')
 set(gcf,'position',[0,0,620,400]);

 figure(10)
 z=plot(xpoints3,y(tfam,I(s)),'LineWidth',2);
 set(z, {'color'}, num2cell(cmapset,2))
 set(gcf, 'Color', [1 1 1]); set(gca, 'color', 'w');
 xlabel('Distance (\mum)','FontSize',14,'FontWeight','bold','Color','k')
%Adds x-label
 ylabel('Concentration (M)','FontSize',14,'FontWeight','bold','Color','k')
%Adds z-label
 title('Trp','FontSize',16,'FontWeight','bold','Color','k') %Adds title
 set(gca,'zscale',logswitch)
 set(gca,'yscale',logswitch)
 set(gcf,'color','w');
 set(gca,'FontSize',14)
 x1=xline(45,'--',{'Sclera'},'Linewidth',2);
 x1.LabelVerticalAlignment = 'bottom';
 x1.LabelHorizontalAlignment = 'right';
```

```
 x1.LabelOrientation = 'horizontal';
 x2=xline(45,'--',{'Choroid'},'Linewidth',2);
 x2.LabelVerticalAlignment = 'bottom';
 x2.LabelHorizontalAlignment = 'left';
 x2.LabelOrientation = 'horizontal';
 legend(legendstring)
 legend('location','eastoutside')
 set(gcf,'position',[0,0,620,400]);

 figure(11)
 z=plot(xpoints3,y(tfam,J(s)),'LineWidth',2);
 set(z, {'color'}, num2cell(cmapset,2))
 set(gcf, 'Color', [1 1 1]); set(gca, 'color', 'w');
 xlabel('Distance (\mum)','FontSize',14,'FontWeight','bold','Color','k')
%Adds x-label
 ylabel('Concentration (M)','FontSize',14,'FontWeight','bold','Color','k')
%Adds z-label
 title('Met','FontSize',16,'FontWeight','bold','Color','k') %Adds title
 set(gca,'zscale',logswitch)
 set(gca,'yscale',logswitch)
 set(gcf,'color','w');
 set(gca,'FontSize',14)
 x1=xline(45,'--',{'Sclera'},'Linewidth',2);
 x1.LabelVerticalAlignment = 'bottom';
 x1.LabelHorizontalAlignment = 'right';
 x1.LabelOrientation = 'horizontal';
 x2=xline(45,'--',{'Choroid'},'Linewidth',2);
 x2.LabelVerticalAlignment = 'bottom';
 x2.LabelHorizontalAlignment = 'left';
 x2.LabelOrientation = 'horizontal';
 legend(legendstring)
 legend('location','southeast')
 set(gcf,'position',[0,0,620,400]);
 set(gca,'YLim',[0 0.025]);

 figure(12)
 z=plot(xpoints3,y(tfam,K(s)),'LineWidth',2);
 set(z, {'color'}, num2cell(cmapset,2))
 set(gcf, 'Color', [1 1 1]); set(gca, 'color', 'w');
 xlabel('Distance (\mum)','FontSize',14,'FontWeight','bold','Color','k')
%Adds x-label
 ylabel('Concentration (M)','FontSize',14,'FontWeight','bold','Color','k')
%Adds z-label
 title('Tyr','FontSize',16,'FontWeight','bold','Color','k') %Adds title
 set(gca,'zscale',logswitch)
 set(gca,'yscale',logswitch)
```

```
 set(gcf,'color','w');
 set(gca,'FontSize',14)
 x1=xline(45,'--',{'Sclera'},'Linewidth',2);
 x1.LabelVerticalAlignment = 'bottom';
 x1.LabelHorizontalAlignment = 'right';
 x1.LabelOrientation = 'horizontal';
 x2=xline(45,'--',{'Choroid'},'Linewidth',2);
 x2.LabelVerticalAlignment = 'bottom';
 x2.LabelHorizontalAlignment = 'left';
 x2.LabelOrientation = 'horizontal';
 legend(legendstring)
 legend('location','eastoutside')
 set(gcf,'position',[0,0,620,400]);

 figure(13)
 z=plot(xpoints3,y(tfam,L(s)),'LineWidth',2);
 set(z, {'color'}, num2cell(cmapset,2))
 set(gcf, 'Color', [1 1 1]); set(gca, 'color', 'w');
 xlabel('Distance (\mum)','FontSize',14,'FontWeight','bold','Color','k')
%Adds x-label
 ylabel('Concentration (M)','FontSize',14,'FontWeight','bold','Color','k')
%Adds z-label
 title('Melanin','FontSize',16,'FontWeight','bold','Color','k') %Adds
title
 set(gca,'zscale',logswitch)
 set(gca,'yscale',logswitch)
 set(gcf,'color','w');
 set(gca,'FontSize',14)
 x1=xline(45,'--',{'Sclera'},'Linewidth',2);
 x1.LabelVerticalAlignment = 'bottom';
 x1.LabelHorizontalAlignment = 'right';
 x1.LabelOrientation = 'horizontal';
 x2=xline(45,'--',{'Choroid'},'Linewidth',2);
 x2.LabelVerticalAlignment = 'bottom';
 x2.LabelHorizontalAlignment = 'left';
 x2.LabelOrientation = 'horizontal';
 legend(legendstring)
 legend('location','eastoutside')
 set(gcf,'position',[0,0,620,400]);

 figure(29)
 hold on
 plot(mins,sum(y(1:TS,M([Scl Chor])).*dxV([Scl Chor]),2)/(sum(dxV([Scl
Chor]))),'k','LineWidth',2);
 plot(mins,sum(y(1:TS,N([Scl Chor])).*dxV([Scl Chor]),2)/(sum(dxV([Scl
Chor]))),'r','LineWidth',2);
```

```
 plot(mins,sum(y(1:TS,P([Scl Chor])).*dxV([Scl Chor]),2)/(sum(dxV([Scl
Chor]))),'b','LineWidth',2);
 plot(mins,sum(y(1:TS,O([Scl Chor])).*dxV([Scl Chor]),2)/(sum(dxV([Scl
Chor]))),'g','LineWidth',2);
 xlabel('Time (min)','FontSize',14,'FontWeight','bold','Color','k')
%Adds x-label
 ylabel('Concentration (M)','FontSize',14,'FontWeight','bold','Color','k')
%Adds z-label
 title('Cumulative
Crosslinks','FontSize',16,'FontWeight','bold','Color','k') %Adds title
 set(gcf, 'Color', [1 1 1]); set(gca, 'color', 'w');
 set(gca,'zscale',logswitch)
 set(gca,'yscale',logswitch)
 set(gcf,'color','w');
 set(gca,'FontSize',14)
 set(gcf,'position',[0,0,620,400]);
 set(gca,'YLim',[0 0.012]);
 legend('Total','His-XL','Trp-XL','Tyr-XL')
 legend('location','northwest')
 set(gcf,'position',[0,0,620,400]);

 figure(31)
 z=plot(xpoints3,LI1(tfam,s)*1000,'LineWidth',2);
 set(z, {'color'}, num2cell(cmapset,2))
 set(gcf, 'Color', [1 1 1]); set(gca, 'color', 'w');
 xlabel('Distance (\mum)','FontSize',14,'FontWeight','bold','Color','k')
%Adds x-label
 ylabel('Intensity
(mW/cm^2)','FontSize',14,'FontWeight','bold','Color','k')
 title('Light Intensity','FontSize',16,'FontWeight','bold','Color','k')
%Adds title
 set(gca,'zscale',logswitch)
 set(gca,'yscale',logswitch)
 set(gcf,'color','w');
 set(gca,'FontSize',14)
 x1=xline(45,'--',{'Sclera'},'Linewidth',2);
 x1.LabelVerticalAlignment = 'bottom';
 x1.LabelHorizontalAlignment = 'right';
 x1.LabelOrientation = 'horizontal';
 x2=xline(45,'--',{'Choroid'},'Linewidth',2);
 x2.LabelVerticalAlignment = 'bottom';
 x2.LabelHorizontalAlignment = 'left';
 x2.LabelOrientation = 'horizontal';
 legend(legendstring)
 legend('location','eastoutside')
 set(gcf,'position',[0,0,620,400]);
```

```
 %Check equivalence of light intensities
 L1=round(LI1(end,1)/Isource,5);
 L2=round(LI2(end,1)/Isource,5);
 PAbs=round(1-sum(Abs(end,A))/Isource,5);

 if L1~=L2 || L1~=PAbs
     disp('Warning - light intensities not equal')
 end
 end

 MBconcfract=mean(y(end,B(Scl))+ 2*y(end,C(Scl)))/C0_MBinj
 Xlinkstot=sum(y(end,M([Scl Chor])).*dxV([Scl Chor]))/(sum(dxV([Scl
Chor])))
 fXlink=Xlinkstot/sum(Xlinkspossible)
 mastervector(mastercounter,1)=Xlinkstot
 end
 toc
 beep

 %%

 function
dydt=odefcn(t,y,XS,sizey,a,b,c,d,e,f,g,h,i,j,k,l,m,n,o,p,B,C,L,I0,e_M,e_D,
DMB,DO2,mu,PhiT,PhiDeg,MBmchor,MBdchor,MBmres,MBdres,O23chor,O23res,k_MB3r
elax,k_singlet,k_mbdeg,k_mb2deg,k_triplet,kHIS,kTRP,kMET,kTYR,
kMB3HIS,kMB3TRP,
kMB3MET,kMB3TYR,k1O2HIS,k1O2TRP,k1O2MET,k1O2TYR,kMB3ann,k3MBMB2,kMBquench,
kMEL,kfm,krd,BCMBres,BCMBchor,BCO2res,BCO2chor,fxl,fbleach,fanlink,fhisble
ach,Reslength,k1O2MB,k1O2MB2,dxVright,dxVleft,DMBright,DMBleft,dxV,DO2righ
t,DO2left,C0_MBres,Chor, e_MEL)
 %Function containing differential equations

 % The first and last equations will be defined explicitly
 % The middle equations will have relative references
 % Equations are written with diffusion first, other, then reactions

 dydt=zeros(sizey,1);

 abeg=1; bbeg=abeg+XS; cbeg=bbeg+XS; dbeg=cbeg+XS; ebeg=dbeg+XS;
fbeg=ebeg+XS; gbeg=fbeg+XS; hbeg=gbeg+XS; ibeg=hbeg+XS; jbeg=ibeg+XS;
kbeg=jbeg+XS; lbeg=kbeg+XS; mbeg=lbeg+XS; nbeg=mbeg+XS; obeg=nbeg+XS;
pbeg=obeg+XS;
 aend=XS; bend=aend+XS; cend=bend+XS; dend=cend+XS; eend=dend+XS;
fend=eend+XS; gend=fend+XS; hend=gend+XS; iend=hend+XS; jend=iend+XS;
```

```
kend=jend+XS; lend=kend+XS; mend=lend+XS; nend=mend+XS; oend=nend+XS;
pend=oend+XS;

 mid=2:(XS-1);
 DMB=DMB';
 DMBleft=DMBleft';
 DMBright=DMBright';
 dxV=dxV';
 dxVleft=dxVleft';
 dxVright=dxVright';
 DO2=DO2';
 DO2right=DO2right';
 DO2left=DO2left';
 mu=mu';
 I0=I0';

 DO2(Chor)=O23chor;

 % Diffusion Conditions
 DiffB=
[16*DMB(1)./(dxVleft(1)+2*dxV(1)+dxVright(1)).*(DMBright(1)./(DMBright(1)+
DMB(1)).*(y(bbeg+1)-y(bbeg))./(dxVright(1)+dxV(1))-
DMBleft(1)./(DMBleft(1)+DMB(1)).*(y(bbeg)-C0_MBres)./(dxVleft(1)+dxV(1)));
16*DMB(mid)./(dxVleft(mid)+2*dxV(mid)+dxVright(mid)).*(DMBright(mid)./(DMB
right(mid)+DMB(mid)).*(y(b+1)-y(b))./(dxVright(mid)+dxV(mid))-
DMBleft(mid)./(DMBleft(mid)+DMB(mid)).*(y(b)-y(b-
1))./(dxVleft(mid)+dxV(mid)));
16*DMB(end)./(dxVleft(end)+2*dxV(end)+dxVright(end)).*(DMBright(end)./(DMB
right(end)+DMB(end)).*(MBmchor-y(bend-1))./(dxVright(end)+dxV(end))-
DMBleft(end)./(DMBleft(end)+DMB(end)).*(y(bend)-y(bend-
1))./(dxVleft(end)+dxV(end)))];
 DiffC=
[16*DMB(1)./(dxVleft(1)+2*dxV(1)+dxVright(1)).*(DMBright(1)./(DMBright(1)+
DMB(1)).*(y(cbeg+1)-y(cbeg))./(dxVright(1)+dxV(1))-
DMBleft(1)./(DMBleft(1)+DMB(1)).*(y(cbeg)-C0_MBres)./(dxVleft(1)+dxV(1)));
16*DMB(mid)./(dxVleft(mid)+2*dxV(mid)+dxVright(mid)).*(DMBright(mid)./(DMB
right(mid)+DMB(mid)).*(y(c+1)-y(c))./(dxVright(mid)+dxV(mid))-
DMBleft(mid)./(DMBleft(mid)+DMB(mid)).*(y(c)-y(c-
1))./(dxVleft(mid)+dxV(mid)));
16*DMB(end)./(dxVleft(end)+2*dxV(end)+dxVright(end)).*(DMBright(end)./(DMB
right(end)+DMB(end)).*(MBdchor-y(cend-1))./(dxVright(end)+dxV(end))-
DMBleft(end)./(DMBleft(end)+DMB(end)).*(y(cend)-y(cend-
1))./(dxVleft(end)+dxV(end)))];
 DiffD=
[16*DMB(1)./(dxVleft(1)+2*dxV(1)+dxVright(1)).*(DMBright(1)./(DMBright(1)+
DMB(1)).*(y(dbeg+1)-y(dbeg))./(dxVright(1)+dxV(1))-
```

```
DMBleft(1)./(DMBleft(1)+DMB(1)).*(y(dbeg)-0)./(dxVleft(1)+dxV(1)));
16*DMB(mid)./(dxVleft(mid)+2*dxV(mid)+dxVright(mid)).*(DMBright(mid)./(DMB
right(mid)+DMB(mid)).*(y(d+1)-y(d))./(dxVright(mid)+dxV(mid))-
DMBleft(mid)./(DMBleft(mid)+DMB(mid)).*(y(d)-y(d-
1))./(dxVleft(mid)+dxV(mid)));
16*DMB(end)./(dxVleft(end)+2*dxV(end)+dxVright(end)).*(DMBright(end)./(DMB
right(end)+DMB(end)).*(0-y(dend-1))./(dxVright(end)+dxV(end))-
DMBleft(end)./(DMBleft(end)+DMB(end)).*(y(dend)-y(dend-
1))./(dxVleft(end)+dxV(end)))];
 DiffE=
[16*DO2(1)./(dxVleft(1)+2*dxV(1)+dxVright(1)).*(DO2right(1)./(DO2right(1)+
DO2(1)).*(y(ebeg+1)-y(ebeg))./(dxVright(1)+dxV(1))-
DO2left(1)./(DO2left(1)+DO2(1)).*(y(ebeg)-O23res)./(dxVleft(1)+dxV(1)));
16*DO2(mid)./(dxVleft(mid)+2*dxV(mid)+dxVright(mid)).*(DO2right(mid)./(DO2
right(mid)+DO2(mid)).*(y(e+1)-y(e))./(dxVright(mid)+dxV(mid))-
DO2left(mid)./(DO2left(mid)+DO2(mid)).*(y(e)-y(e-
1))./(dxVleft(mid)+dxV(mid)));
16*DO2(end)./(dxVleft(end)+2*dxV(end)+dxVright(end)).*(DO2right(end)./(DO2
right(end)+DO2(end)).*(O23chor-y(eend-1))./(dxVright(end)+dxV(end))-
DO2left(end)./(DO2left(end)+DO2(end)).*(y(eend)-y(eend-
1))./(dxVleft(end)+dxV(end)))];
 DiffF=
[16*DO2(1)./(dxVleft(1)+2*dxV(1)+dxVright(1)).*(DO2right(1)./(DO2right(1)+
DO2(1)).*(y(fbeg+1)-y(fbeg))./(dxVright(1)+dxV(1))-
DO2left(1)./(DO2left(1)+DO2(1)).*(y(fbeg)-0)./(dxVleft(1)+dxV(1)));
16*DO2(mid)./(dxVleft(mid)+2*dxV(mid)+dxVright(mid)).*(DO2right(mid)./(DO2
right(mid)+DO2(mid)).*(y(f+1)-y(f))./(dxVright(mid)+dxV(mid))-
DO2left(mid)./(DO2left(mid)+DO2(mid)).*(y(f)-y(f-
1))./(dxVleft(mid)+dxV(mid)));
16*DO2(end)./(dxVleft(end)+2*dxV(end)+dxVright(end)).*(DO2right(end)./(DO2
right(end)+DO2(end)).*(0-y(fend-1))./(dxVright(end)+dxV(end))-
DO2left(end)./(DO2left(end)+DO2(end)).*(y(fend)-y(fend-
1))./(dxVleft(end)+dxV(end)))];

 % DiffB=[(y(bbeg+1)-2*y(bbeg)+0)/Reslength^2;    (y(b+1)-2*y(b)+y(b-
1))/dx^2;             (MBmchor-2*y(bend)+y(bend-1))/dx^2];
 % DiffC=[(y(cbeg+1)-2*y(cbeg)+0)/Reslength^2;   (y(c+1)-2*y(c)+y(c-
1))/dx^2;             (MBdchor-2*y(cend)+y(cend-1))/dx^2];
 % DiffE=[(y(ebeg+1)-2*y(ebeg)+0)/Reslength^2;    (y(e+1)-2*y(e)+y(e-
1))/dx^2;             (O23chor-2*y(eend)+y(eend-1))/dx^2];

 if BCMBres==1
 %     DiffB(1)=DiffB(2);
 %     DiffC(1)=DiffC(2);
 DiffB(1)=2*(y(bbeg+1)-y(bbeg))/(dx)^2;
 DiffC(1)=2*(y(cbeg+1)-y(cbeg))/(dx)^2;
```

```
end

if BCMBchor==1
%     DiffB(end)=DiffB(XS-1);
%     DiffC(end)=DiffC(XS-1);
DiffB(end)=2*(-y(bend)+y(bend-1))/(dx)^2;
DiffC(end)=2*(-y(cend)+y(cend-1))/(dx)^2;
end

if BCO2res==1
%     DiffE(1)=DiffE(2);
DiffE(1)=2*(y(ebeg+1)-y(ebeg))/(dx)^2;
end

if BCO2chor==1
%     DiffE(end)=DiffE(XS-1);
DiffE(end)=2*(-y(eend)+y(eend-1))/(dx)^2;
end

FLmon=e_M.*y(B)./(e_M*y(B)+e_D*y(C)+e_MEL*y(L)+mu);

DBDTbeg = DiffB(1) -    PhiT*(1-
y(abeg))*y(aend)*prod(y(a),1).*I0(1).*FLmon(1)-    PhiDeg*(1-
y(abeg))*y(aend)*prod(y(a),1).*I0(1).*FLmon(1) -   2*kfm*y(bbeg).^2 -
kfm*y(bbeg).*y(dbeg) + 2*krd*y(cbeg) + k_MB3relax*y(dbeg) + (1-fxl-
fhisbleach)*kMB3HIS*y(dbeg).*y(hbeg) + (1-
fbleach)*kMB3TRP*y(dbeg).*y(ibeg) + (1-fbleach)*kMB3MET*y(dbeg).*y(jbeg)+
(1-fbleach)*kMB3TYR*y(dbeg).*y(kbeg) + kMBquench*y(bbeg).*y(dbeg) +
2*kMB3ann*y(dbeg).^2 + k3MBMB2*y(dbeg).*y(cbeg) +
k_singlet*y(dbeg).*y(ebeg) + k_mb2deg*y(cbeg).*y(fbeg) -
k_mbdeg*y(bbeg).*y(fbeg);
DBDT =    DiffB(mid) -       PhiT*(1-
y(a)).*cumprod(y(a+1),1,'reverse').*I0(mid).*FLmon(mid) - PhiDeg*(1-
y(a)).*cumprod(y(a+1),1,'reverse').*I0(mid).*FLmon(mid) - 2*kfm*y(b).^2 -
kfm*y(b).*y(d) +    2*krd*y(c) +    k_MB3relax*y(d) +    (1-fxl-
fhisbleach)*kMB3HIS*y(d).*y(h) +       (1-fbleach)*kMB3TRP*y(d).*y(i) +
(1-fbleach)*kMB3MET*y(d).*y(j)+   (1-fbleach)*kMB3TYR*y(d).*y(k)+
kMBquench*y(b).*y(d) +       2*kMB3ann*y(d).^2 +    k3MBMB2*y(d).*y(c) +
k_singlet*y(d).*y(e) +       k_mb2deg*y(c).*y(f) -
k_mbdeg*y(b).*y(f);
DBDTend = DiffB(end) - PhiT*(1-y(aend)).*I0(end).*FLmon(end) - PhiDeg*(1-
y(aend)).*I0(end).*FLmon(end) - 2*kfm*y(bend).^2 - kfm*y(bend).*y(dend) +
2*krd*y(cend) + k_MB3relax*y(dend) + (1-fxl-
fhisbleach)*kMB3HIS*y(dend).*y(hend) + (1-
fbleach)*kMB3TRP*y(dend).*y(iend) + (1-fbleach)*kMB3MET*y(dend).*y(jend)+
(1-fbleach)*kMB3TYR*y(dend).*y(kend) + kMBquench*y(bend).*y(dend) +
```

```
2*kMB3ann*y(dend).^2 + k3MBMB2*y(dend).*y(cend) +
k_singlet*y(dend).*y(eend) + k_mb2deg*y(cend).*y(fend) -
k_mbdeg*y(bend).*y(fend);

 DCDTbeg = DiffC(1) +   kfm*y(bbeg).^2 + kfm*y(bbeg).*y(dbeg)- krd*y(cbeg)
- k_mb2deg*y(cbeg).*y(fbeg);
 DCDT =    DiffC(mid) +        kfm*y(b).^2 + kfm*y(b).*y(d)-    krd*y(c) -
k_mb2deg*y(c).*y(f);
 DCDTend = DiffC(end) + kfm*y(bend).^2 + kfm*y(bend).*y(dend) -
krd*y(cend) - k_mb2deg*y(cend).*y(fend);

 %Left boundary
 dydt(abeg) = -dxV(1)*log(10)*(e_M*DBDTbeg+e_D*DCDTbeg).*10.^(-
(e_M*y(bbeg)+e_D*y(cbeg)+e_MEL*y(lbeg)+mu(1))*dxV(1));
 dydt(bbeg) = DBDTbeg;
 dydt(cbeg) = DCDTbeg;
 dydt(dbeg) = DiffD(1) + PhiT*(1-
y(abeg))*y(aend)*prod(y(a),1).*I0(1).*FLmon(1) - k_MB3relax*y(dbeg) -
kfm*y(bbeg).*y(dbeg) - kMB3HIS*y(dbeg).*y(hbeg) - kMB3TRP*y(dbeg).*y(ibeg)
- kMB3MET*y(dbeg).*y(jbeg)- kMB3TYR*y(dbeg).*y(kbeg) -
kMBquench*y(bbeg).*y(dbeg) - 2*kMB3ann*y(dbeg).^2 -
k3MBMB2*y(dbeg).*y(cbeg) - k_singlet*y(dbeg).*y(ebeg);
 dydt(ebeg) = DiffE(1) - k_singlet*y(dbeg).*y(ebeg) + k_triplet*y(fbeg) +
k1O2HIS*y(fbeg).*y(hbeg) + k1O2TRP*y(fbeg).*y(ibeg) +
k1O2MET*y(fbeg).*y(jbeg)+k1O2TYR*y(fbeg).*y(kbeg) +
k1O2MB*y(fbeg).*y(bbeg) + k1O2MB2*y(fbeg).*y(cbeg);
 dydt(fbeg) = DiffF(1) + k_singlet*y(dbeg).*y(ebeg) - k_triplet*y(fbeg) -
k1O2HIS*y(fbeg).*y(hbeg) - k1O2TRP*y(fbeg).*y(ibeg) -
k1O2MET*y(fbeg).*y(jbeg)- k1O2TYR*y(fbeg).*y(kbeg) -
k_mb2deg*y(cbeg).*y(fbeg) - k_mbdeg*y(bbeg).*y(fbeg) -
kMEL*y(lbeg).*y(fbeg) - kHIS*y(fbeg).*y(hbeg) - kTRP*y(fbeg).*y(ibeg) -
kTYR*y(fbeg).*y(kbeg) -kMET*y(fbeg).*y(jbeg) -k1O2MB*y(fbeg).*y(bbeg)-
k1O2MB2*y(fbeg).*y(cbeg);
 dydt(gbeg) = PhiDeg*(1-y(abeg))*y(aend)*prod(y(a),1).*I0(1).*FLmon(1) +
k_mb2deg*y(cbeg).*y(fbeg) + k_mbdeg*y(bbeg).*y(fbeg);
 dydt(hbeg) = -kHIS*y(fbeg).*y(hbeg)-
(fhisbleach+fxl)*kMB3HIS*y(dbeg).*y(hbeg);
 dydt(ibeg) = -kTRP*y(fbeg).*y(ibeg) -
(fbleach+fanlink)*kMB3TRP*y(dbeg).*y(ibeg);
 dydt(jbeg) = -kMET*y(fbeg).*y(jbeg) -
(fbleach+fanlink)*kMB3MET*y(dbeg).*y(jbeg);
 dydt(kbeg) = -kTYR*y(fbeg).*y(kbeg) -
(fbleach+fanlink)*kMB3TYR*y(dbeg).*y(kbeg);
 dydt(lbeg) = -kMEL*y(lbeg).*y(fbeg);
 dydt(mbeg) = kHIS*y(fbeg).*y(hbeg)+ kTYR*y(fbeg).*y(kbeg) +
kTRP*y(fbeg).*y(ibeg)+ fxl*kMB3HIS*y(dbeg).*y(hbeg)+
```

```
fanlink*kMB3TRP*y(dbeg).*y(ibeg) + fanlink*kMB3MET*y(dbeg).*y(jbeg)+
fanlink*kMB3TYR*y(dbeg).*y(kbeg);
 dydt(nbeg) = kHIS*y(fbeg).*y(hbeg);
 dydt(obeg) = kTRP*y(fbeg).*y(ibeg);
 dydt(pbeg) = kTYR*y(fbeg).*y(kbeg);
 %Middle
 dydt(a) = -dxV(mid).*log(10).*(e_M*DBDT+e_D*DCDT).*10.^(-
(e_M*y(b)+e_D*y(c)+e_MEL*y(l)+mu(mid)).*dxV(mid));
 dydt(b) = DBDT;
 dydt(c) = DCDT;
 dydt(d) = DiffD(mid) + PhiT*(1-
y(a)).*cumprod(y(a+1),1,'reverse').*I0(mid).*FLmon(mid) - k_MB3relax*y(d)
- kfm*y(b).*y(d) - kMB3HIS*y(d).*y(h) - kMB3TRP*y(d).*y(i) -
kMB3MET*y(d).*y(j)- kMB3TYR*y(d).*y(k) - kMBquench*y(b).*y(d) -
2*kMB3ann*y(d).^2 - k3MBMB2*y(d).*y(c) - k_singlet*y(d).*y(e);
 dydt(e) = DiffE(mid) - k_singlet*y(d).*y(e) + k_triplet*y(f) +
k1O2HIS*y(f).*y(h) + k1O2TRP*y(f).*y(i) + k1O2MET*y(f).*y(j)+
k1O2TYR*y(f).*y(k) + k1O2MB*y(f).*y(b)+ k1O2MB2*y(f).*y(c);
 dydt(f) = DiffF(mid) + k_singlet*y(d).*y(e) - k_triplet*y(f) -
k1O2HIS*y(f).*y(h) - k1O2TRP*y(f).*y(i) - k1O2MET*y(f).*y(j)-
k1O2TYR*y(f).*y(k) - k_mb2deg*y(c).*y(f) - k_mbdeg*y(b).*y(f) -
kMEL*y(l).*y(f) - kHIS*y(f).*y(h) - kTRP*y(f).*y(i) - kMET*y(f).*y(j)-
kTYR*y(f).*y(j) -k1O2MB*y(f).*y(b)-k1O2MB2*y(f).*y(c);
 dydt(g) = PhiDeg*(1-
y(a)).*cumprod(y(a+1),1,'reverse').*I0(mid).*FLmon(mid) +
k_mb2deg*y(c).*y(f) + k_mbdeg*y(b).*y(f);
 dydt(h) = -kHIS*y(f).*y(h)-(fhisbleach+fxl)*kMB3HIS*y(d).*y(h);
 dydt(i) = -kTRP*y(f).*y(i) - (fbleach+fanlink)*kMB3TRP*y(d).*y(i);
 dydt(j) = -kMET*y(f).*y(j) - (fbleach+fanlink)*kMB3MET*y(d).*y(j);
 dydt(k) = -kTYR*y(f).*y(k) - (fbleach+fanlink)*kMB3TYR*y(d).*y(k);
 dydt(l) = -kMEL*y(l).*y(f);
 dydt(m) = kHIS*y(f).*y(h)+kTYR*y(f).*y(k) + kTRP*y(f).*y(i)+
fxl*kMB3HIS*y(d).*y(h) + fanlink*kMB3TRP*y(d).*y(i) +
fanlink*kMB3MET*y(d).*y(j) + fanlink*kMB3MET*y(d).*y(k);
 dydt(n) = kHIS*y(f).*y(h);
 dydt(o) = kTRP*y(f).*y(i);
 dydt(p) = kTYR*y(f).*y(k);

 %Right boundary
 dydt(aend) = -dxV(end)*log(10)*(e_M*DBDTend+e_D*DCDTend).*10.^(-
(e_M*y(bend)+e_D*y(cend)+e_MEL*y(lend)+mu(end))*dxV(end));   %Normal light
propagation
 dydt(bend) = DBDTend;
 dydt(cend) = DCDTend;
 dydt(dend) = DiffD(end) + PhiT*(1-y(aend)).*I0(end).*FLmon(end) -
k_MB3relax*y(dend) - kfm*y(bend).*y(dend)- kMB3HIS*y(dend).*y(hend) -
```

```
kMB3TRP*y(dend).*y(iend) - kMB3MET*y(dend).*y(jend) -
kMB3TYR*y(dend).*y(kend) - kMBquench*y(bend).*y(dend) -
2*kMB3ann*y(dend).^2 - k3MBMB2*y(dend).*y(cend) -
k_singlet*y(dend).*y(eend);
 dydt(eend) = DiffE(end) - k_singlet*y(dend).*y(eend) + k_triplet*y(fend)
+ k1O2HIS*y(fend).*y(hend) + k1O2TRP*y(fend).*y(iend) +
k1O2MET*y(fend).*y(jend) +k1O2TYR*y(fend).*y(kend) +
k1O2MB*y(fend).*y(bend)+ k1O2MB2*y(fend).*y(cend);
 dydt(fend) = DiffF(end) + k_singlet*y(dend).*y(eend) - k_triplet*y(fend)
- k1O2HIS*y(fend).*y(hend) - k1O2TRP*y(fend).*y(iend) -
k1O2MET*y(fend).*y(jend)- k1O2TYR*y(fend).*y(kend) -
k_mb2deg*y(cend).*y(fend) - k_mbdeg*y(bend).*y(fend) -
kMEL*y(lend).*y(fend) - kHIS*y(fend).*y(hend) - kTRP*y(fend).*y(iend) -
kMET*y(fend).*y(jend)- kTYR*y(fend).*y(kend) -k1O2MB*y(fend).*y(bend)-
k1O2MB2*y(fend).*y(cend);
 dydt(gend) = PhiDeg*(1-y(aend)).*I0(end).*FLmon(end) +
k_mb2deg*y(cend).*y(fend) + k_mbdeg*y(bend).*y(fend);
 dydt(hend) = -kHIS*y(fend).*y(hend)-
(fhisbleach+fxl)*kMB3HIS*y(dend).*y(hend);
 dydt(iend) = -kTRP*y(fend).*y(iend) -
(fbleach+fanlink)*kMB3TRP*y(dend).*y(iend);
 dydt(jend) = -kMET*y(fend).*y(jend) -
(fbleach+fanlink)*kMB3MET*y(dend).*y(jend);
 dydt(kend) = -kTYR*y(fend).*y(kend) -
(fbleach+fanlink)*kMB3TYR*y(dend).*y(kend);
 dydt(lend) = -kMEL*y(lend).*y(fend);
 dydt(mend) = kHIS*y(fend).*y(hend)+kTYR*y(fend).*y(kend)
+kTRP*y(fend).*y(iend) + fxl*kMB3HIS*y(dend).*y(hend) +
fanlink*kMB3TRP*y(dend).*y(iend) + fanlink*kMB3MET*y(dend).*y(jend)+
fanlink*kMB3TYR*y(dend).*y(kend);
 dydt(nend) = kHIS*y(fend).*y(end);
 dydt(oend) = kTRP*y(fend).*y(iend);
 dydt(pend) = kTYR*y(fend).*y(kend);
 % a = Light
 % b = MBm
 % c = MBd
 % d = MB3
 % e = O23
 % f = O21
 % g = MBdeg
 % h = HIS
 % i = TRP
 % j = MET
 % k = TYR
 % l = MEL
 % m = Xlink
```

```
% n = probe 1
% o = probe 2
% p = probe 3
end

function J=jsparse(Jsparse)
    J=Jsparse;
end
```

REFERENCES

[1] H. a Quigley, a T. Broman, The number of people with glaucoma worldwide in 2010 and 2020., Br. J. Ophthalmol. 90 (2006) 262–267. https://doi.org/10.1136/bjo.2005.081224.

[2] C. Stowell, C.F. Burgoyne, E.R. Tamm, C.R. Ethier, J.E. Dowling, C. Downs, M.H. Ellisman, S. Fisher, B. Fortune, M. Fruttiger, T. Jakobs, G. Lewis, R.H. Masland, C.H. Mitchell, J. Morrison, S.C. Sharma, I. Sigal, M. Sofroniew, L. Wang, J. Wiggs, S. Wu, Biomechanical aspects of axonal damage in glaucoma: A brief review, Exp. Eye Res. 157 (2017) 13–19. https://doi.org/10.1016/j.exer.2017.02.005.

[3] M.S. Dikopf, T.S. Vajaranant, D.P. Edward, Topical treatment of glaucoma: established and emerging pharmacology, Expert Opin. Pharmacother. 18 (2017) 885–898. https://doi.org/10.1080/14656566.2017.1328498.

[4] B. Coudrillier, I.C. Campbell, A.T. Read, D.M. Geraldes, N.T. Vo, A. Feola, J. Mulvihill, J. Albon, R.L. Abel, C.R. Ethier, Effects of peripapillary scleral stiffening on the deformation of the lamina cribrosa, Investig. Ophthalmol. Vis. Sci. 57 (2016) 2666–2677. https://doi.org/10.1167/iovs.15-18193.

[5] E.C. Kimball, C. Nguyen, M.R. Steinhart, T.D. Nguyen, M.E. Pease, E.N. Oglesby, B.C. Oveson, H.A. Quigley, Experimental scleral cross-linking increases glaucoma damage in a mouse model, Exp. Eye Res. 128 (2014) 129–140. https://doi.org/https://doi.org/10.1016/j.exer.2014.08.016.

[6] R. Russo, G. Pasquale, A. Adornetto, C. Nucci, M. Tiziana, G. Bagetta, L. Antonio, Retinal ganglion cell death in glaucoma : Exploring the role of neuroin fl ammation, 787 (2016) 134–142. https://doi.org/10.1016/j.ejphar.2016.03.064.

[7] T.E. Yap, P. Donna, M.T. Almonte, M.F. Cordeiro, Real-Time Imaging of Retinal Ganglion Cell Apoptosis., Cells. 7 (2018). https://doi.org/10.3390/cells7060060.

[8] C.F. Burgoyne, A biomechanical paradigm for axonal insult within the optic nerve head in aging and glaucoma., Exp. Eye Res. 93 (2011) 120–132. https://doi.org/10.1016/j.exer.2010.09.005.

[9] S.D. Wadhwa, E.J. Higginbotham, Ethnic differences in glaucoma: prevalence, management, and outcome, Curr. Opin. Ophthalmol. 16 (2005). https://journals.lww.com/co-ophthalmology/Fulltext/2005/04000/Ethnic_differences_in_glaucoma__prevalence,.6.aspx.

[10] J.M. Tielsch, A. Sommer, J. Katz, R.M. Royall, H.A. Quigley, J. Javitt, Racial variations in the prevalence of primary open-angle glaucoma. The Baltimore Eye Survey., JAMA. 266 (1991) 369–374.

[11] H.A. Quigley, Glaucoma, (2011) 1367–1377. https://doi.org/10.1016/S0140-6736(10)61423-7.

[12] A. Cheema, R.T. Chang, A. Shrivastava, K. Singh, Update on the Medical Treatment of Primary Open-Angle Glaucoma, 5 (2016) 51–58. https://doi.org/10.1097/APO.0000000000000181.

[13] H.E. Killer, A. Pircher, Normal tension glaucoma : review of current understanding and mechanisms of the pathogenesis, Eye. (2018) 924–930. https://doi.org/10.1038/s41433-018-0042-2.

[14] D.W. Abu-Hassan, T.S. Acott, M.J. Kelley, The Trabecular Meshwork: A Basic Review of Form and Function, J. Ocul. Biol. 2 (2014) http://fulltextarticles.avensonline.org/JOCB-2334-. https://doi.org/10.13188/2334-2838.1000017.

[15] S. Sampathkumar, C.B. Toris, 9. Uveoscleral outflow, Glaucoma Res. Clin. Adv. 2016 to 2018. 1 (2016) 139.

[16] K. Wang, G. Li, A.T. Read, I. Navarro, A.K. Mitra, W.D. Stamer, T. Sulchek, C.R. Ethier, The relationship between outflow resistance and trabecular meshwork stiffness in mice, Sci. Rep. 8 (2018) 5848. https://doi.org/10.1038/s41598-018-24165-w.

[17] C. Luna, G. Li, P.B. Liton, D.L. Epstein, P. Gonzalez, Alterations in gene expression induced by cyclic mechanical stress in trabecular meshwork cells, Mol. Vis. 15 (2009) 534–544. https://pubmed.ncbi.nlm.nih.gov/19279691.

[18] D.W. Abu-Hassan, X. Li, E.I. Ryan, T.S. Acott, M.J. Kelley, Induced pluripotent stem cells restore function in a human cell loss model of open-angle glaucoma., Stem Cells. 33 (2015) 751–761. https://doi.org/10.1002/stem.1885.

[19] H. Levkovitch-Verbin, Chapter 2 - Retinal ganglion cell apoptotic pathway in glaucoma: Initiating and downstream mechanisms, in: G. Bagetta, C.B.T.-P. in B.R. Nucci (Eds.), New Trends Basic Clin. Res. Glaucoma A Neurodegener. Dis. Vis. Syst. Part A, Elsevier, 2015: pp. 37–57. https://doi.org/https://doi.org/10.1016/bs.pbr.2015.05.005.

[20] M. Almasieh, A.M. Wilson, B. Morquette, J.L. Cueva Vargas, A. Di Polo, The molecular basis of retinal ganglion cell death in glaucoma., Prog. Retin. Eye Res. 31 (2012) 152–181. https://doi.org/10.1016/j.preteyeres.2011.11.002.

[21] M.H. Kang, D.-Y. Yu, Distribution pattern of axonal cytoskeleton proteins in the human optic nerve head, Neural Regen. Res. 10 (2015) 1198–1200. https://doi.org/10.4103/1673-5374.162691.

[22] D.C. Musch, B.W. Gillespie, L.M. Niziol, P.R. Lichter, Intraocular Pressure Control and Long-term Visual Field Loss in the Collaborative Initial Glaucoma Treatment

Study, OPHTHA. 118 (2011) 1766–1773. https://doi.org/10.1016/j.ophtha.2011.01.047.

[23] L.A. Levin, M.E. Crowe, H.A. Quigley, T. Lasker, I. Initiative, G.N. Participants, F. Cordeiro, L. Donoso, J. Liao, R. Libby, R. Masland, R. Nickells, P. Sieving, A. Sommer, Neuroprotection for glaucoma : Requirements for clinical translation *, 157 (2017) 2011–2014. https://doi.org/10.1016/j.exer.2016.12.005.

[24] K. Tian, S. Shibata-Germanos, M. Pahlitzsch, M.F. Cordeiro, Current perspective of neuroprotection and glaucoma, Clin. Ophthalmol. 9 (2015) 2109–2118. https://doi.org/10.2147/OPTH.S80445.

[25] S. Bhartiya, P. Ichhpujani, M. Gandhi, The Glaucoma Treatment Paradigm: An Overview, in: M. Gandhi, S. Bhartiya (Eds.), Glaucoma Drain. Devices A Pract. Illus. Guid., Springer Singapore, Singapore, 2019: pp. 1–6. https://doi.org/10.1007/978-981-13-5773-2_1.

[26] E.M. Schehlein, G.D. Novack, A.L. Robin, New classes of glaucoma medications, Curr. Opin. Ophthalmol. 28 (2017). https://journals.lww.com/co-ophthalmology/Fulltext/2017/03000/New_classes_of_glaucoma_medications.9.aspx.

[27] A. Narayanaswamy, C.K. Leung, D. V Istiantoro, S.A. Perera, C.-L. Ho, M.E. Nongpiur, M. Baskaran, H.M. Htoon, T.T. Wong, D. Goh, D.H. Su, M. Belkin, T. Aung, Efficacy of Selective Laser Trabeculoplasty in Primary Angle-Closure Glaucoma: A Randomized Clinical Trial, JAMA Ophthalmol. 133 (2015) 206–212. https://doi.org/10.1001/jamaophthalmol.2014.4893.

[28] K.S. Arora, A.L. Robin, K.J. Corcoran, S.L. Corcoran, P.Y. Ramulu, Use of Various Glaucoma Surgeries and Procedures in Medicare Beneficiaries from 1994 to 2012, Ophthalmology. 122 (2015) 1615–1624. https://doi.org/https://doi.org/10.1016/j.ophtha.2015.04.015.

[29] R.N. Weinreb, J.M. Liebmann, G.A. Cioffi, I. Goldberg, J.D. Brandt, C.A. Johnson, L.M. Zangwill, S. Schneider, H. Badger, M. Bejanian, Oral Memantine for the Treatment of Glaucoma: Design and Results of 2 Randomized, Placebo-Controlled, Phase 3 Studies, Ophthalmology. 125 (2018) 1874–1885. https://doi.org/https://doi.org/10.1016/j.ophtha.2018.06.017.

[30] C. Nucci, A. Martucci, C. Giannini, L.A. Morrone, G. Bagetta, R. Mancino, Neuroprotective agents in the management of glaucoma, Eye. 32 (2018) 938–945. https://doi.org/10.1038/s41433-018-0050-2.

[31] D.B. Yan, F.M. Coloma, A. Metheetrairut, G.E. Trope, J.G. Heathcote, C.R. Ethier, Deformation of the lamina cribrosa by elevated intraocular pressure., Br. J. Ophthalmol. 78 (1994) 643–648. https://doi.org/10.1136/bjo.78.8.643.

[32] H.A. Quigley, E.M. Addicks, W.R. Green, A.E. Maumenee, Optic Nerve Damage

in Human Glaucoma: II. The Site of Injury and Susceptibility to Damage, JAMA Ophthalmol. 99 (1981) 635–649. https://doi.org/10.1001/archopht.1981.03930010635009.

[33] R.L. Radius, M. Gonzales, Anatomy of the Lamina Cribrosa in Human Eyes, JAMA Ophthalmol. 99 (1981) 2159–2162. https://doi.org/10.1001/archopht.1981.03930021035010.

[34] J.C. Downs, M.D. Roberts, C.F. Burgoyne, Mechanical environment of the optic nerve head in glaucoma., Optom. Vis. Sci. Off. Publ. Am. Acad. Optom. 85 (2008) 425–435. https://doi.org/10.1097/OPX.0b013e31817841cb.

[35] S.C. Park, J. Brumm, R.L. Furlanetto, C. Netto, Y. Liu, C. Tello, J.M. Liebmann, R. Ritch, Lamina Cribrosa Depth in Different Stages of Glaucoma, Invest. Ophthalmol. Vis. Sci. 56 (2015) 2059–2064. https://doi.org/10.1167/iovs.14-15540.

[36] G. Wollstein, L.A. Paunescu, T.H. Ko, J.G. Fujimoto, A. Kowalevicz, I. Hartl, S. Beaton, H. Ishikawa, C. Mattox, O. Singh, J. Duker, W. Drexler, J.S. Schuman, Ultrahigh-resolution optical coherence tomography in glaucoma, Ophthalmology. 112 (2005) 229–237. https://doi.org/10.1016/j.ophtha.2004.08.021.

[37] P.G. Watson, R.D. Young, Scleral structure, organisation and disease. A review, Exp. Eye Res. 78 (2004) 609–623. https://doi.org/https://doi.org/10.1016/S0014-4835(03)00212-4.

[38] M.J.A. Girard, J.C. Downs, C.F. Burgoyne, J.-K.F. Suh, Peripapillary and Posterior Scleral Mechanics—Part I: Development of an Anisotropic Hyperelastic Constitutive Model, J. Biomech. Eng. 131 (2009). https://doi.org/10.1115/1.3113682.

[39] P.G. Watson, R.D. Young, Scleral structure, organisation and disease. A review, Exp. Eye Res. 78 (2004) 609–623. https://doi.org/10.1016/S0014-4835(03)00212-4.

[40] F.W. Keeley, J.D. Morin, S. Vesely, Characterization of collagen from normal human sclera., Exp. Eye Res. 39 (1984) 533–542. https://doi.org/10.1016/0014-4835(84)90053-8.

[41] M.D. Shoulders, R.T. Raines, Collagen Structure and Stability, (2009). https://doi.org/10.1146/annurev.biochem.77.032207.120833.

[42] K. Takahara, Y. Sato, K. Okazawa, N. Okamoto, A. Noda, Y. Yaoi, I. Kato, Complete primary structure of human collagen alpha 1 (V) chain., J. Biol. Chem. 266 (1991) 13124–13129.

[43] N.C. Avery, A.J. Bailey, Restraining Cross-Links Responsible for the Mechanical Properties of Collagen Fibers: Natural and Artificial BT - Collagen: Structure and Mechanics, in: P. Fratzl (Ed.), Springer US, Boston, MA, 2008: pp. 81–110.

https://doi.org/10.1007/978-0-387-73906-9_4.

[44] H.A. Quigley, A. Brown, M.E. Dorman-Pease, Alterations in elastin of the optic nerve head in human and experimental glaucoma., Br. J. Ophthalmol. 75 (1991) 552 LP – 557. https://doi.org/10.1136/bjo.75.9.552.

[45] I.A. Sigal, J.G. Flanagan, I. Tertinegg, C.R. Ethier, Finite Element Modeling of Optic Nerve Head Biomechanics, Invest. Ophthalmol. Vis. Sci. 45 (2004) 4378–4387. https://doi.org/10.1167/iovs.04-0133.

[46] I.A. Sigal, J.G. Flanagan, C.R. Ethier, Factors Influencing Optic Nerve Head Biomechanics, Invest. Ophthalmol. Vis. Sci. 46 (2005) 4189–4199. https://doi.org/10.1167/iovs.05-0541.

[47] S.I. Fox, Human physiology, 12. ed., McGraw-Hill, New York, 2011.

[48] L. Cheng, Y. Ding, X. Duan, Z. Wu, Ocular pulse amplitude in different types of glaucoma using dynamic contour tonometry: Diagnosis and follow-up of glaucoma, Exp. Ther. Med. 14 (2017) 4148–4152. https://doi.org/10.3892/etm.2017.5074.

[49] I. Stalmans, A. Harris, V. Vanbellinghen, T. Zeyen, B. Siesky, Ocular Pulse Amplitude in Normal Tension and Primary Open Angle Glaucoma, J. Glaucoma. 17 (2008). https://journals.lww.com/glaucomajournal/Fulltext/2008/08000/Ocular_Pulse_Amplitude_in_Normal_Tension_and.13.aspx.

[50] B. Ballantyne, R.C. Myers, The acute toxicity and primary irritancy of glutaraldehyde solutions, Vet. Hum. Toxicol. 43 (2001) 193–202. http://europepmc.org/abstract/MED/11474730.

[51] I.C. Campbell, B.G. Hannon, A.T. Read, M. Sherwood, S.A. Schwaner, C.R. Ethier, Quantification of the efficacy of collagen cross-linking agents to induce stiffening of rat sclera, (2017).

[52] B.G. Hannon, S.A. Schwaner, E.M. Boazak, B.G. Gerberich, E.J. Winger, M.R. Prausnitz, C.R. Ethier, Sustained scleral stiffening in rats after a single genipin treatment, J. R. Soc. Interface. 16 (2019) 20190427. https://doi.org/10.1098/rsif.2019.0427.

[53] L.H.H. Olde Damink, P.J. Dijkstra, M.J.A. Van Luyn, P.B. Van Wachem, P. Nieuwenhuis, J. Feijen, Glutaraldehyde as a crosslinking agent for collagen-based biomaterials, J. Mater. Sci. Mater. Med. 6 (1995) 460–472. https://doi.org/10.1007/BF00123371.

[54] N.A. Danilov, N.Y. Ignatieva, E.N. Iomdina, S.A. Semenova, G.N. Rudenskaya, T.E. Grokhovskaya, V. V Lunin, Stabilization of scleral collagen by glycerol aldehyde cross-linking, Biochim. Biophys. Acta - Gen. Subj. 1780 (2008) 764–772. https://doi.org/https://doi.org/10.1016/j.bbagen.2008.01.014.

[55] M. Butler, M.F. Butler, Y. Ng, P.D.A. Pudney, Mechanism and kinetics of crosslinking reaction between biopolymers containing primary amine groups and genipin Mechanism and Kinetics of the Crosslinking Reaction between Biopolymers Containing Primary Amine Groups and Genipin, (2016) 3941–3953. https://doi.org/10.1002/pola.10960.

[56] S.B. Brown, E.A. Brown, I. Walker, Present-Future-Role-Pdt-Cancer, (2004).

[57] D. Van Straten, V. Mashayekhi, H.S. De Bruijn, S. Oliveira, D.J. Robinson, Oncologic Photodynamic Therapy : Basic Principles , Current Clinical Status and Future Directions, (2017) 1–54. https://doi.org/10.3390/cancers9020019.

[58] M.A. Moore, I.K. Bohachevsky, D.T. Cheung, B.D. Boyan, W. -M Chen, R.R. Bickers, B.K. McIlroy, Stabilization of pericardial tissue by dye-mediated photooxidation, J. Biomed. Mater. Res. 28 (1994) 611–618. https://doi.org/10.1002/jbm.820280511.

[59] B.P. Chan, C. Amann, A.N. Yaroslavsky, C. Title, D. Smink, B. Zarins, I.E. Kochevar, R.W. Redmond, Photochemical repair of Achilles tendon rupture in a rat model, J. Surg. Res. 124 (2005) 274–279. https://doi.org/10.1016/j.jss.2004.09.019.

[60] A.S. Fawzy, L.I. Nitisusanta, K. Iqbal, U. Daood, J. Neo, Riboflavin as a dentin crosslinking agent: Ultraviolet A versus blue light, Dent. Mater. 28 (2012) 1284–1291. https://doi.org/10.1016/j.dental.2012.09.009.

[61] D.E.J.G.J. Dolmans, D. Fukumura, R.K. Jain, Photodynamic therapy for cancer, Nat. Rev. Cancer. 3 (2003) 380–387. https://doi.org/10.1038/nrc1071.

[62] A.B. Ormond, H.S. Freeman, Dye sensitizers for photodynamic therapy, Materials (Basel). 6 (2013) 817–840. https://doi.org/10.3390/ma6030817.

[63] W.M. Sharman, C.M. Allen, J.E. Van Lier, Photodynamic therapeutics: Basic principles and clinical applications, Drug Discov. Today. 4 (1999) 507–517. https://doi.org/10.1016/S1359-6446(99)01412-9.

[64] L.B. Rocha, F. Schaberle, J.M. Dąbrowski, S. Simões, L.G. Arnaut, Intravenous single-dose toxicity of redaporfin-based photodynamic therapy in rodents, Int. J. Mol. Sci. 16 (2015) 29236–29249. https://doi.org/10.3390/ijms161226162.

[65] M. Kim, Y.H. Jung, J.H. Park, Topical PDT in the Treatment of Benign Skin Diseases: Principles and New Applications, Int. J. Mol. Sci. . 16 (2015). https://doi.org/10.3390/ijms161023259.

[66] H. Abrahamse, M.R. Hamblin, New photosensitizers for photodynamic therapy, Biochem. J. 473 (2016) 347–364. https://doi.org/10.1042/bj20150942.

[67] J.M. Dąbrowski, L.G. Arnaut, Photodynamic therapy (PDT) of cancer: From local to systemic treatment, Photochem. Photobiol. Sci. 14 (2015) 1765–1780.

https://doi.org/10.1039/c5pp00132c.

[68] A.F. Uchoa, K.T. de Oliveira, M.S. Baptista, A.J. Bortoluzzi, Y. Iamamoto, O.A. Serra, Chlorin photosensitizers sterically designed to prevent self-aggregation, J. Org. Chem. 76 (2011) 8824–8832.

[69] O. Mazor, A. Brandis, V. Plaks, E. Neumark, V. Rosenbach-Belkin, Y. Salomon, A. Scherz, WST11, A Novel Water-soluble Bacteriochlorophyll Derivative; Cellular Uptake, Pharmacokinetics, Biodistribution and Vascular-targeted Photodynamic Activity Using Melanoma Tumors as a Model¶, Photochem. Photobiol. 81 (2005) 342. https://doi.org/10.1562/2004-06-14-ra-199.1.

[70] K. Plaetzer, B. Krammer, J. Berlanda, F. Berr, T. Kiesslich, Photophysics and photochemistry of photodynamic therapy: Fundamental aspects, Lasers Med. Sci. 24 (2009) 259–268. https://doi.org/10.1007/s10103-008-0539-1.

[71] S. Salzmann, C.M. Marian, V. Martinez-Junza, B. Zorn, S.E. Braslavsky, M. Mansurova, W. Gärtner, Photophysical properties of structurally and electronically modified flavin derivatives determined by spectroscopy and theoretical calculations, J. Phys. Chem. A. 113 (2009) 9365–9375. https://doi.org/10.1021/jp905724b.

[72] E.I. Alarcon, M. González-Béjar, P. Montes-Navajas, H. Garcia, E.A. Lissi, J.C. Scaiano, Unexpected solvent isotope effect on the triplet lifetime of methylene blue associated to cucurbit[7]uril, Photochem. Photobiol. Sci. 11 (2012) 269–273. https://doi.org/10.1039/c1pp05227f.

[73] R.J. Crutchley, M.C. DeRosa, Photosensitized Singlet Oxygen and its Applications, Coord. Chem. Rev. 233–234 (2002) 351–371.

[74] J.D. Spikes, J.C. Bommer, PHOTOBLEACHING OF MONO-l-ASPARTYL CHLORIN e6 (NPe6): A CANDIDATE SENSITIZER FOR THE PHOTODYNAMIC THERAPY OF TUMORS, Photochem. Photobiol. 58 (1993) 346–350. https://doi.org/10.1111/j.1751-1097.1993.tb09572.x.

[75] R.A. Lustig, T.J. Vogl, D. Fromm, R. Cuenca, R.A. Hsi, A.K. D'Cruz, Z. Krajina, M. Turić, A. Singhal, J.C. Chen, A multicenter phase I safety study of intratumoral photoactivation of talaporfin sodium in patients with refractory solid tumors, Cancer. 98 (2003) 1767–1771. https://doi.org/10.1002/cncr.11708.

[76] A. Fernández-Pérez, T. Valdés-Solís, G. Marbán, Visible light spectroscopic analysis of Methylene Blue in water; the resonance virtual equilibrium hypothesis, Dye. Pigment. 161 (2019) 448–456. https://doi.org/10.1016/j.dyepig.2018.09.083.

[77] J.M. Fernandez, M.D. Bilgin, L.I. Grossweiner, Singlet oxygen generation by photodynamic agents, J. Photochem. Photobiol. B Biol. 37 (1997) 131–140. https://doi.org/10.1016/S1011-1344(96)07349-6.

[78] W.S.G. Medina, N.A.G. dos Santos, C. Curti, A.C. Tedesco, A.C. dos Santos,

Effects of zinc phthalocyanine tetrasulfonate-based photodynamic therapy on rat brain isolated mitochondria, Chem. Biol. Interact. 179 (2009) 402–406. https://doi.org/10.1016/j.cbi.2009.01.007.

[79] A. Ogunsipe, J. Chen, T. Nyokong, Photophysical and photochemical studies of zinc(, New J. Chem. 28 (2004) 822–827. https://doi.org/10.1002/hlca.200390279.

[80] N.A. Kuznetsova, N.S. Gretsova, V.M. Derkacheva, O.L. Kaliya, E.A. Lukyanets, Sulfonated phthalocyanines: aggregation and singlet oxygen quantum yield in aqueous solutions, J. Porphyr. Phthalocyanines. 07 (2003) 147–154. https://doi.org/10.1142/s1088424603000203.

[81] D. Kessel, Photodynamic therapy and neoplastic disease., Oncol. Res. 4 (1992) 219–225.

[82] R. Bonnett, Photosensitizers of the porphyrin and phthalocyanine series for photodynamic therapy, Chem. Soc. Rev. 24 (1995) 19–33.

[83] B. Aveline, T. Hasan, R.W. Redmond, PHOTOPHYSICAL AND PHOTOSENSITIZING PROPERTIES OF BENZOPORPHYRIN DERIVATIVE MONOACID RING A (BPD-MA)*, Photochem. Photobiol. 59 (1994) 328–335. https://doi.org/10.1111/j.1751-1097.1994.tb05042.x.

[84] L.I. Grossweiner, M.D. Bilgin, P. Berdusis, T.D. Mody, Singlet Oxygen Generation by Metallotexaphyrins, Photochem. Photobiol. 70 (1999) 138–145. https://doi.org/10.1111/j.1751-1097.1999.tb07981.x.

[85] I. Ashur, R. Goldschmidt, I. Pinkas, Y. Salomon, G. Szewczyk, T. Sarna, A. Scherz, Photocatalytic generation of oxygen radicals by the water-soluble bacteriochlorophyll derivative WST1l, noncovalently bound to serum albumin, J. Phys. Chem. A. 113 (2009) 8027–8037. https://doi.org/10.1021/jp900580e.

[86] K. Licha, B. Riefke, V. Ntziachristos, A. Becker, B. Chance, W. Semmler, Hydrophilic cyanine dyes as contrast agents for near-infrared tumor imaging: synthesis, photophysical properties and spectroscopic in vivo characterization., Photochem Photobiol. 72 (2000) 392–398. https://doi.org/10.1562/0031-8655(2000)0720392HCDACA2.0.CO2.

[87] J. a Cardillo, R. Jorge, R. a Costa, S.M.T. Nunes, D. Lavinsky, B.D. Kuppermann, a C. Tedesco, M.E. Farah, Experimental selective choriocapillaris photothrombosis using a modified indocyanine green formulation., Br. J. Ophthalmol. 92 (2008) 276–80. https://doi.org/10.1136/bjo.2007.129395.

[88] A. Del, C. Santos, D. Oliveira, D. Santesso, H. Couto, D. Batista, D. Severino, M.S. Baptista, Methylene blue in photodynamic therapy : From basic mechanisms to clinical applications Rozane de F ´, 1000 (2005). https://doi.org/10.1016/S1572-1000(05)00097-9.

[89] J.P. Kamat, T.P.A. Devasagayam, Methylene blue plus light-induced lipid peroxidation in rat liver microsomes: inhibition by nicotinamide (vitamin B3) and other antioxidants, Chem. Biol. Interact. 99 (1996) 1–16. https://doi.org/https://doi.org/10.1016/0009-2797(95)03653-9.

[90] W.B. WENDEL, METHYLENE BLUE, METHEMOGLOBIN, AND CYANIDE POISONING, J. Pharmacol. Exp. Ther. 54 (1935) 283 LP – 298. http://jpet.aspetjournals.org/content/54/3/283.abstract.

[91] R.H. Schirmer, H. Adler, M. Pickhardt, E. Mandelkow, "Lest we forget you — methylene blue …," Neurobiol. Aging. 32 (2011) 2325.e7-2325.e16. https://doi.org/https://doi.org/10.1016/j.neurobiolaging.2010.12.012.

[92] M. FIEDOROWICZ, F. SCHUETTAUF, C. HARITOGLOU, C.A. MAY, A. MESSIAS, A. KAMPIK, T.J. CHORAGIEWICZ, A. SCHATZ, S. THALER, E. ZRENNER, in Vivo Toxicity Testing of Methyl Blue and Aniline Blue As Vital Dyes for Intraocular Surgery, Retina. 29 (2009) 1257–1265. https://doi.org/10.1097/iae.0b013e3181b8615b.

[93] M. Oz, D.E. Lorke, G.A. Petroianu, Methylene blue and Alzheimer's disease, Biochem. Pharmacol. 78 (2009) 927–932. https://doi.org/https://doi.org/10.1016/j.bcp.2009.04.034.

[94] Z. Zhao, E.R. Malinowski, Window factor analysis of methylene blue in water, J. Chemom. 13 (1999) 83–94. https://doi.org/10.1002/(SICI)1099-128X(199903/04)13:2<83::AID-CEM529>3.0.CO;2-2.

[95] M.R. Prausnitz, J.S. Noonan, Permeability of cornea, sclera, and conjunctiva: a literature analysis for drug delivery to the eye., J. Pharm. Sci. 87 (1998) 1479–88. http://www.ncbi.nlm.nih.gov/pubmed/10189253.

[96] L. Rice, M. Wainwright, D.A. Phoenix, M. Wainwright, D.A.P.P. Photosensitizers, Phenothiazine Photosensitizers . III . Activity of Methylene Blue Derivatives against Pigmented Melanoma Cell Lines Activity of Methylene Blue Derivatives against, 9478 (2013).

[97] A. Edwards, M.R. Prausnitz, Fiber matrix model of sclera and corneal stroma for drug delivery to the eye, AIChE J. 44 (1998) 214–225. https://doi.org/10.1002/aic.690440123.

[98] V. Au, S.A. Madison, Effects of singlet oxygen on the extracellular matrix protein collagen: Oxidation of the collagen crosslink histidinohydroxylysinonorleucine and histidine, Arch. Biochem. Biophys. 384 (2000) 133–142. https://doi.org/10.1006/abbi.2000.2070.

[99] H.R. Shen, J.D. Spikes, P. Kopečeková, J. Kopeček, Photodynamic crosslinking of proteins. I. Model studies using histidine- and lysine-containing N-(2-hydroxypropyl) methacrylamide copolymers, J. Photochem. Photobiol. B Biol. 34

(1996) 203–210. https://doi.org/10.1016/1011-1344(96)07286-7.

[100] V. V. Agon, W.A. Bubb, A. Wright, C.L. Hawkins, M.J. Davies, Sensitizer-mediated photooxidation of histidine residues: Evidence for the formation of reactive side-chain peroxides, Free Radic. Biol. Med. 40 (2006) 698–710. https://doi.org/10.1016/j.freeradbiomed.2005.09.039.

[101] M.J. Davies, Singlet oxygen-mediated damage to proteins and its consequences, Biochem. Biophys. Res. Commun. 305 (2003) 761–770. https://doi.org/10.1016/S0006-291X(03)00817-9.

[102] J.A.M. Ramshaw, L.J. Stephens, P.A. Tulloch, Biochi~ic~a et Biophysica A~ta, 1206 (1994) 225–230.

[103] K.J. Mellish, S.B. Brown, Verteporfin: a milestone in opthalmology and photodynamic therapy, Expert Opin. Pharmacother. 2 (2001) 351–361. https://doi.org/10.1517/14656566.2.2.351.

[104] G. Wollensak, E. Spoerl, T. Seiler, Stress-strain measurements of human and porcine corneas after riboflavin-ultraviolet-A-induced cross-linking, J. Cataract Refract. Surg. 29 (2003) 1780–1785. https://doi.org/10.1016/S0886-3350(03)00407-3.

[105] F. Raiskup, A. Theuring, L.E. Pillunat, Corneal collagen crosslinking with riboflavin and ultraviolet-A light in progressive keratoconus : Ten-year results, J. Cart. Refract. Surg. 41 (2015) 41–46. https://doi.org/10.1016/j.jcrs.2014.09.033.

[106] G. Wollensak, E. Spoerl, Collagen crosslinking of human and porcine sclera, (2004). https://doi.org/10.1016/j.jcrs.2003.11.032.

[107] Y. Zhang, Z. Li, L. Liu, X. Han, X. Zhao, G. Mu, Comparison of riboflavin/ultraviolet-A cross-linking in porcine, rabbit, and human sclera, Biomed Res. Int. 2014 (2014). https://doi.org/10.1155/2014/194204.

[108] A. Urtti, Challenges and obstacles of ocular pharmacokinetics and drug delivery, Adv. Drug Deliv. Rev. 58 (2006) 1131–1135. https://doi.org/https://doi.org/10.1016/j.addr.2006.07.027.

[109] S.R. Patel, A.S.P. Lin, H.F. Edelhauser, M.R. Prausnitz, Suprachoroidal drug delivery to the back of the eye using hollow microneedles, Pharm. Res. 28 (2011) 166–176. https://doi.org/10.1007/s11095-010-0271-y.

[110] D.H. Geroski, H.F. Edelhauser, Drug Delivery for Posterior Segment Eye Disease, Invest. Ophthalmol. Vis. Sci. 41 (2000) 961–964.

[111] J.H. Jung, P. Desit, M.R. Prausnitz, Targeted Drug Delivery in the Suprachoroidal Space by Swollen Hydrogel Pushing, (2018).

[112] B. Chiang, K. Wang, C. Ross Ethier, M.R. Prausnitz, Clearance kinetics and clearance routes of molecules from the suprachoroidal space after microneedle injection, Investig. Ophthalmol. Vis. Sci. 58 (2017) 545–554. https://doi.org/10.1167/iovs.16-20679.

[113] B. Chiang, N. Venugopal, H.E. Grossniklaus, J.H. Jung, H.F. Edelhauser, M.R. Prausnitz, Thickness and closure kinetics of the suprachoroidal space following microneedle injection of liquid formulations, Investig. Ophthalmol. Vis. Sci. 58 (2017) 555–564. https://doi.org/10.1167/iovs.16-20377.

[114] Q. Li, X. Wang, P. Wang, K. Zhang, H. Wang, X. Feng, Q. Liu, Efficacy of Chlorin e6-Mediated Sono-Photodynamic Therapy on 4T1 Cells, Cancer Biother. Radiopharm. 29 (2013) 42–52. https://doi.org/10.1089/cbr.2013.1526.

[115] A.M. Bugaj, Vascular targeted photochemotherapy using padoporfin and padeliporfin as a method of the focal treatment of localised prostate cancer - clinician's insight, World J. Methodol. 6 (2016) 65. https://doi.org/10.5662/wjm.v6.i1.65.

[116] E.A. Boettner, J.R. Wolter, Transmission of the Ocular Media, Invest. Ophthalmol. Vis. Sci. 1 (1962) 776–783. https://doi.org/10.1017/S0025315406014421.

[117] V.-P. Gabel, R. Birngruber, F. Hillenkamp, Visible and near infrared light absorption in pigment epithelium and choroid, XXIII Concil. Ophthaimologicum. (1978) 658–662.

[118] W.J. Geeraets, R.C. Williams, G. Chan, W.T. Ham, D. Guerry, F.H. Schmidt, The loss of light energy in retina and choroid, Arch. Ophthalmol. 64 (1960) 606–615. https://doi.org/10.1001/archopht.1960.01840010608020.

[119] M. Hammer, a Roggan, D. Schweitzer, G. Müller, G. Muller, Optical properties of ocular fundus tissues--an in vitro study using the double-integrating-sphere technique and inverse Monte Carlo simulation., Phys. Med. Biol. 40 (1995) 963–78. https://doi.org/10.1088/0031-9155/40/6/001.

[120] B. Nemati, H.G. Rylander Iii, a J. Welch, Optical properties of conjunctiva, sclera, and the ciliary body and their consequences for transscleral cyclophotocoagulation., Appl. Opt. 35 (1996) 3321–3327. https://doi.org/10.1364/AO.35.003321.

[121] Vogel 1991 Optical_Properties_of_Human_Sclera.pdf, (n.d.).

[122] ICNRIP, Guideilnes - On Limits of Exposure to Broadband Incoherent Optical Radiation 0.38 to 3um, Health Phys. (1997) 539–554.

[123] F.C. Delori, R.H. Webb, D.H. Sliney, Maximum permissible exposures for ocular safety (ANSI 2000), with emphasis on ophthalmic devices, J. Opt. Soc. Am. A. 24 (2007) 1250. https://doi.org/10.1364/josaa.24.001250.

[124] G. Wollensak, E. Iomdina, D.-D. Dittert, O. Salamatina, G. Stoltenburg, Cross-linking of scleral collagen in the rabbit using riboflavin and UVA, Acta Ophthalmol. Scand. 83 (2005) 477–482. https://doi.org/10.1111/j.1600-0420.2005.00447.x.

[125] T.-C. Huang, C.-J. Chen, S.-J. Ding, C.-C. Chen, Antimicrobial efficacy of methylene blue-mediated photodynamic therapy on titanium alloy surfaces in vitro, Photodiagnosis Photodyn. Ther. 25 (2019) 7–16. https://doi.org/https://doi.org/10.1016/j.pdpdt.2018.11.008.

[126] K. Orth, G. Beck, F. Genze, A. Rück, Methylene blue mediated photodynamic therapy in experimental colorectal tumors in mice, J. Photochem. Photobiol. B Biol. 57 (2000) 186–192. https://doi.org/https://doi.org/10.1016/S1011-1344(00)00105-6.

[127] A. Semchishen, M. Mrochen, V. Semchishen, Model for Optimization of the UV-A/Riboflavin Strengthening (cross-linking) of the Cornea: Percolation Threshold, Photochem. Photobiol. 91 (2015) 1403–1411. https://doi.org/10.1111/php.12498.

[128] S. Schumacher, M. Mrochen, J. Wernli, M. Bueeler, T. Seiler, Optimization model for UV-riboflavin corneal cross-linking, Investig. Ophthalmol. Vis. Sci. 53 (2012) 762–769. https://doi.org/10.1167/iovs.11-8059.

[129] P. Kamaev, M.D. Friedman, E. Sherr, D. Muller, Photochemical kinetics of corneal cross-linking with riboflavin, Investig. Ophthalmol. Vis. Sci. 53 (2012) 2360–2367. https://doi.org/10.1167/iovs.11-9385.

[130] S. Kling, F. Hafezi, An Algorithm to Predict the Biomechanical Stiffening Effect in Corneal Cross-linking, J. Refract. Surg. 33 (2017) 128–136. https://doi.org/10.3928/1081597x-20161206-01.

[131] J.T. Lin, H.W. Liu, D.C. Cheng, On the dynamic of UV-Light initiated corneal cross linking, J. Med. Biol. Eng. 34 (2014) 247–250. https://doi.org/10.5405/jmbe.1532.

[132] T.H. Foster, R.S. Murant, R.G. Bryant, R.S. Knox, L. Gibson, R. Hilf, T.H. Foster, R.S. Murant, R.G. Bryant, R.S. Knox, S.L. Gibson, R. Hilft, Oxygen Consumption and Diffusion Effects in Photodynamic Therapy Linked references are available on JSTOR for this article : Oxygen Consumption and Diffusion Effects in Photodynamic Therapy, 126 (2017) 296–303.

[133] J.P. Henning, R.L. Fournier, J.A. Hampton, A Transient Mathematical Model of Oxygen Depletion during Photodynamic Therapy, Radiat. Res. 142 (2006) 221. https://doi.org/10.2307/3579032.

[134] J.M. Parnis, K.B. Oldham, Beyond the beer-lambert law: The dependence of absorbance on time in photochemistry, J. Photochem. Photobiol. A Chem. 267 (2013) 6–10. https://doi.org/10.1016/j.jphotochem.2013.06.006.

[135] C. Tanielian, C. Schweitzer, R. Mechin, C. Wolff, Quantum yield of singlet oxygen

production by monomeric and aggregated forms of hematoporphyrin derivative, Free Radic. Biol. Med. 30 (2001) 208–212. https://doi.org/https://doi.org/10.1016/S0891-5849(00)00460-3.

[136] R. Bonnett, G. Martinez, ChemInform Abstract: Photobleaching of Sensitisers Used in Photodynamic Therapy, ChemInform. 33 (2010) no-no. https://doi.org/10.1002/chin.200211234.

[137] W.M. Moore, C. Baylor, The Photochemistry of Riboflavin. IV. The Photobleaching of Some Nitrogen-9 Substituted Isoalloxazines and Flavins, J. Am. Chem. Soc. 91 (1969) 7170–7179. https://doi.org/10.1021/ja01053a048.

[138] Knowles 1972 A study of the methylene blue-sensitized oxidation of amino acids.pdf, (n.d.).

[139] S.F. Baranovskii, P.A. Bolotin, Association of riboflavin, caffeine, and sodium salicylate in aqueous solution, J. Appl. Spectrosc. 74 (2007) 211–218. https://doi.org/10.1007/s10812-007-0033-8.

[140] E. Braswell, Evidence for trimerization in aqueous solutions of methylene blue, J. Phys. Chem. 72 (1968) 2477–2483. https://doi.org/10.1021/j100853a035.

[141] D. Heger, J. Jirkovský, P. Klán, Aggregation of methylene blue in frozen aqueous solutions studied by absorption spectroscopy, J. Phys. Chem. A. 109 (2005) 6702–6709. https://doi.org/10.1021/jp050439j.

[142] R. NILSSON, P.B. MERKEL, D.R. KEARNS, UNAMBIGUOUS EVIDENCE FOR THE PARTICIPATION OF SINGLET OXYGEN (1δ) IN PHOTODYNAMIC OXIDATION OF AMINO ACIDS, Photochem. Photobiol. 16 (1972) 117–124. https://doi.org/10.1111/j.1751-1097.1972.tb07343.x.

[143] I.B.C. Matheson, J. Lee, Chemical Reaction Rates of Amino Acids With Singlet Oxygen, Photochem. Photobiol. 29 (1979) 879–881. https://doi.org/10.1111/j.1751-1097.1979.tb07786.x.

[144] Y.P. Tsentalovich, J.J. Lopez, P.J. Hore, R.Z. Sagdeev, Mechanisms of reactions of flavin mononucleotide triplet with aromatic amino acids, Spectrochim. Acta - Part A Mol. Biomol. Spectrosc. 58 (2002) 2043–2050. https://doi.org/10.1016/S1386-1425(01)00652-7.

[145] J. Wernli, S. Schumacher, E. Spoerl, M. Mrochen, The efficacy of corneal cross-linking shows a sudden decrease with very high intensity UV light and short treatment time, Investig. Ophthalmol. Vis. Sci. 54 (2013) 1176–1180. https://doi.org/10.1167/iovs.12-11409.

[146] M. Lombardo, G. Lombardo, Noninvasive real-time assessment of riboflavin consumption in standard and accelerated corneal crosslinking, J. Cataract Refract. Surg. 45 (2019) 80–86. https://doi.org/10.1016/j.jcrs.2018.07.062.

[147] D. Chai, R.N. Gaster, R. Roizenblatt, T. Juhasz, D.J. Brown, J. V. Jester, Quantitative assessment of UVA-riboflavin corneal cross-linking using nonlinear optical microscopy, Investig. Ophthalmol. Vis. Sci. 52 (2011) 4231–4238. https://doi.org/10.1167/iovs.10-7105.

[148] J.-T. Lin, Efficacy S-formula and Kinetics of Non-oxygen-mediated (Type-I) and Oxygen-mediated (Type-II) Corneal Cross-linking, Ophthalmol. Res. An Int. J. 8 (2018) 1–11. https://doi.org/10.9734/or/2018/39089.

[149] S. Lin, L. Gu, Influence of crosslink density and stiffness on mechanical properties of type I collagen gel, Materials (Basel). 8 (2015) 551–560. https://doi.org/10.3390/ma8020551.

[150] B. Depalle, Z. Qin, S.J. Shefelbine, M.J. Buehler, Influence of cross-link structure, density and mechanical properties in the mesoscale deformation mechanisms of collagen fibrils, J. Mech. Behav. Biomed. Mater. 52 (2015) 1–13. https://doi.org/10.1016/j.jmbbm.2014.07.008.

[151] M. Wang, F. Zhang, X. Qian, X. Zhao, Regional Biomechanical Properties of Human Sclera After Cross-linking by Riboflavin/Ultraviolet A, J. Refract. Surg. 28 (2012) 723–728. https://doi.org/10.3928/1081597X-20120921-08.

[152] G. Wollensak, E. Iomdina, Long-term biomechanical properties of rabbit sclera after collagen crosslinking using riboflavin and ultraviolet A (UVA), Acta Ophthalmol. 87 (2009) 193–198. https://doi.org/10.1111/j.1755-3768.2008.01229.x.

[153] Y.-C. Tham, X. Li, T.Y. Wong, H.A. Quigley, T. Aung, C.-Y. Cheng, Global Prevalence of Glaucoma and Projections of Glaucoma Burden through 2040: A Systematic Review and Meta-Analysis, Ophthalmology. 121 (2014) 2081–2090. https://doi.org/10.1016/j.ophtha.2014.05.013.

[154] S. Kingman, Glaucoma is second leading cause of blindness globally., Bull. World Health Organ. 82 (2004) 887–888. https://www.scopus.com/inward/record.uri?eid=2-s2.0-14544301551&partnerID=40&md5=12220dded577e176dd21ceef8f42b900.

[155] N.G. Strouthidis, M.J.A. Girard, Altering the way the optic nerve head responds to intraocular pressure—a potential approach to glaucoma therapy, Curr. Opin. Pharmacol. 13 (2013) 83–89. https://doi.org/https://doi.org/10.1016/j.coph.2012.09.001.

[156] K. Clayson, X. Pan, E. Pavlatos, R. Short, H. Morris, R.T. Hart, J. Liu, Corneoscleral stiffening increases IOP spike magnitudes during rapid microvolumetric change in the eye, Exp. Eye Res. 165 (2017) 29–34. https://doi.org/https://doi.org/10.1016/j.exer.2017.08.015.

[157] G. Wollensak, E. Spoerl, T. Seiler, Riboflavin/ultraviolet-a–induced collagen crosslinking for the treatment of keratoconus, Am. J. Ophthalmol. 135 (2003) 620–

627. https://doi.org/https://doi.org/10.1016/S0002-9394(02)02220-1.

[158] S.J.J. Kwok, S. Forward, C.M. Wertheimer, A.C. Liapis, H.H. Lin, M. Kim, T.G. Seiler, R. Birngruber, I.E. Kochevar, T. Seiler, S.-H. Yun, Selective Equatorial Sclera Crosslinking in the Orbit Using a Metal-Coated Polymer Waveguide, Invest. Ophthalmol. Vis. Sci. 60 (2019) 2563–2570. https://doi.org/10.1167/iovs.19-26709.

[159] M.Y. Avila, V.A. Gerena, J.L. Navia, Corneal crosslinking with genipin, comparison with UV-riboflavin in ex-vivo model, Mol. Vis. 18 (2012) 1068–1073. https://www.ncbi.nlm.nih.gov/pubmed/22605919.

[160] T.X. Liu, Z. Wang, Collagen crosslinking of porcine sclera using genipin, Acta Ophthalmol. 91 (2013) 253–257. https://doi.org/10.1111/aos.12172.

[161] M. Kim, A. Takaoka, Q. V. Hoang, S.L. Trokel, D.C. Paik, Pharmacologic alternatives to riboflavin photochemical corneal cross-linking: A comparison study of cell toxicity thresholds, Investig. Ophthalmol. Vis. Sci. 55 (2014) 3247–3257. https://doi.org/10.1167/iovs.13-13703.

[162] P. Ken Gillman, Review: CNS toxicity involving methylene blue: The exemplar for understanding and predicting drug interactions that precipitate serotonin toxicity, J. Psychopharmacol. 25 (2011) 429–436. https://doi.org/10.1177/0269881109359098.

[163] E. Alarcón, A.M. Edwards, A. Aspee, F.E. Moran, C.D. Borsarelli, E.A. Lissi, D. Gonzalez-Nilo, H. Poblete, J.C. Scaiano, Photophysics and photochemistry of dyes bound to human serum albumin are determined by the dye localization, Photochem. Photobiol. Sci. 9 (2010) 93–102. https://doi.org/10.1039/b9pp00091g.

[164] A. Sionkowska, The influence of methylene blue on the photochemical stability of collagen, Polym. Degrad. Stab. 67 (2000) 79–83. https://doi.org/https://doi.org/10.1016/S0141-3910(99)00084-1.

[165] E.M. Kozma, G. Wisowski, A. Jura-Poltorak, P. Olczyk, K. Olczyk, Z. Nawrat, The influence of physical and chemical agents on photooxidation of porcine pericardial collagen., Biomed. Mater. Eng. 15 (2005) 137–144.

[166] I.C. Campbell, B.G. Hannon, A.T. Read, J.M. Sherwood, S.A. Schwaner, C.R. Ethier, Quantification of the efficacy of collagen cross-linking agents to induce stiffening of rat sclera, J R Soc Interface. 14 (2017). https://doi.org/10.1098/rsif.2017.0014.

[167] J.M. Chisholm, D.S.J. Pang, Assessment of Carbon Dioxide, Carbon Dioxide/Oxygen, Isoflurane and Pentobarbital Killing Methods in Adult Female Sprague-Dawley Rats., PLoS One. 11 (2016) e0162639. https://doi.org/10.1371/journal.pone.0162639.

[168] H. Valentine, W.O. Williams, K.J. Maurer, Sedation or inhalant anesthesia before euthanasia with CO2 does not reduce behavioral or physiologic signs of pain and

stress in mice., J. Am. Assoc. Lab. Anim. Sci. 51 (2012) 50–57.

[169] L.A. Mihai, L. Chin, P.A. Janmey, A. Goriely, A comparison of hyperelastic constitutive models applicable to brain and fat tissues, J. R. Soc. Interface. 12 (2015) 486. https://doi.org/10.1098/rsif.2015.0486.

[170] M.D. Ritch, B.G. Hannon, A.T. Read, A.J. Feola, G.A. Cull, J. Reynaud, J.C. Morrison, C.F. Burgoyne, M.T. Pardue, C.R. Ethier, AxoNet: an AI-based tool to count retinal ganglion cell axons, ArXiv E-Prints. (2019). https://ui.adsabs.harvard.edu/abs/2019arXiv190802919R.

[171] S. Banfi, E. Caruso, S. Caprioli, L. Mazzagatti, G. Canti, R. Ravizza, M. Gariboldi, E. Monti, Photodynamic effects of porphyrin and chlorin photosensitizers in human colon adenocarcinoma cells, Bioorg. Med. Chem. 12 (2004) 4853–4860. https://doi.org/https://doi.org/10.1016/j.bmc.2004.07.011.

[172] W. Bäumler, C. Abels, S. Karrer, T. Weiß, H. Messmann, M. Landthaler, R.-M. Szeimies, Photo-oxidative killing of human colonic cancer cells using indocyanine green and infrared light, Br. J. Cancer. 80 (1999) 360–363. https://doi.org/10.1038/sj.bjc.6690363.

[173] L. Xiao, L. Gu, S.B. Howell, M.J. Sailor, Porous Silicon Nanoparticle Photosensitizers for Singlet Oxygen and Their Phototoxicity against Cancer Cells, ACS Nano. 5 (2011) 3651–3659. https://doi.org/10.1021/nn1035262.

[174] D.G. Green, Scotopic and photopic components of the rat electroetinogram, J. Physiol. 228 (1973) 781–797. https://doi.org/10.1113/jphysiol.1973.sp010112.

[175] T.D. Lamb, Photoreceptor spectral sensitivities: Common shape in the long-wavelength region, Vision Res. 35 (1995) 3083–3091. https://doi.org/https://doi.org/10.1016/0042-6989(95)00114-F.

[176] J. Wernli, S. Schumacher, E. Spoerl, M. Mrochen, The efficacy of corneal cross-linking shows a sudden decrease with very high intensity UV light and short treatment time, Investig. Ophthalmol. Vis. Sci. 54 (2013) 1176–1180. https://doi.org/10.1167/iovs.12-11409.

[177] A. Hammer, O. Richoz, S.A. Mosquera, D. Tabibian, F. Hoogewoud, F. Hafezi, Corneal biomechanical properties at different corneal cross-linking (CXL) irradiances, Investig. Ophthalmol. Vis. Sci. 55 (2014) 2881–2884. https://doi.org/10.1167/iovs.13-13748.

[178] A. Brandis, O. Mazor, E. Neumark, V. Rosenbach-Belkin, Y. Salomon, A. Scherz, Novel Water-soluble Bacteriochlorophyll Derivatives for Vascular-targeted Photodynamic Therapy: Synthesis, Solubility, Phototoxicity and the Effect of Serum Proteins¶, Photochem. Photobiol. 81 (2005) 983. https://doi.org/10.1562/2004-12-01-ra-389r1.1.

[179] B.A. Gawargious, A. Le, M. Lesgart, S. Ugardar, J.L. Demer, Differential Regional Stiffening of Sclera by Collagen Cross-linking, Curr. Eye Res. (2019) 1–8.

[180] Y. Li, C. Liu, M. Sun, X. Lv, M. Wang, X. Jiao, L. Zhang, N. Wang, F. Zhang, Ocular safety evaluation of blue light scleral cross-linking in vivo in rhesus macaques, Graefe's Arch. Clin. Exp. Ophthalmol. 257 (2019) 1435–1442.

[181] R.N. Weinreb, P.T. Khaw, Primary open-angle glaucoma, Lancet. 363 (2004) 1711–1720. https://doi.org/10.1016/S0140-6736(04)16257-0.

[182] B.E. Klein, R. Klein, W.E. Sponsel, T. Franke, L.B. Cantor, J. Martone, M.J. Menage, Prevalence of glaucoma. The Beaver Dam Eye Study, Ophthalmology. 99 (1992) 1499–1504. https://www.ncbi.nlm.nih.gov/pubmed/1454314.

[183] A. Heijl, M.C. Leske, B. Bengtsson, L. Hyman, B. Bengtsson, M. Hussein, G. Early Manifest Glaucoma Trial, Reduction of intraocular pressure and glaucoma progression: results from the Early Manifest Glaucoma Trial, Arch Ophthalmol. 120 (2002) 1268–1279. https://www.ncbi.nlm.nih.gov/pubmed/12365904.

[184] J.H. Gurwitz, S.M. Yeomans, R.J. Glynn, B.E. Lewis, R. Levin, J. Avorn, Patient noncompliance in the managed care setting. The case of medical therapy for glaucoma, Med Care. 36 (1998) 357–369. https://doi.org/10.1097/00005650-199803000-00012.

[185] I.C. Campbell, B. Coudrillier, C. Ross Ethier, Biomechanics of the posterior eye: a critical role in health and disease, J Biomech Eng. 136 (2014) 21005. https://doi.org/10.1115/1.4026286.

[186] S. Asrani, R. Zeimer, J. Wilensky, D. Gieser, S. Vitale, K. Lindenmuth, Large diurnal fluctuations in intraocular pressure are an independent risk factor in patients with glaucoma., J. Glaucoma. 9 (2000) 134–142. https://doi.org/10.1097/00061198-200004000-00002.

[187] L.L. Huang, H.W. Sung, C.C. Tsai, D.M. Huang, Biocompatibility study of a biological tissue fixed with a naturally occurring crosslinking reagent, J Biomed Mater Res. 42 (1998) 568–576. https://www.ncbi.nlm.nih.gov/pubmed/9827681.

[188] M.Y. Avila, J.L. Navia, Effect of genipin collagen crosslinking on porcine corneas, J Cataract Refract Surg. 36 (2010) 659–664. https://doi.org/10.1016/j.jcrs.2009.11.003.

[189] T.X. Liu, Z. Wang, Biomechanics of sclera crosslinked using genipin in rabbit, Int J Ophthalmol. 10 (2017) 355–360. https://doi.org/10.18240/ijo.2017.03.05.

[190] W. Song, Y. Tang, J. Qiao, H. Li, B. Rong, S. Yang, Y. Wu, X. Yan, The comparative safety of genipin versus UVA-riboflavin crosslinking of rabbit corneas, Mol Vis. 23 (2017) 504–513. https://www.ncbi.nlm.nih.gov/pubmed/28761323.

[191] E.C. Johnson, L.M.H. Deppmeier, S.K.F. Wentzien, I. Hsu, J.C. Morrison, Chronology of optic nerve head and retinal responses to elevated intraocular pressure, Invest. Ophthalmol. Vis. Sci. 41 (2000) 431–442.

[192] L. Guo, S.E. Moss, R.A. Alexander, R.R. Ali, F.W. Fitzke, M.F. Cordeiro, Retinal ganglion cell apoptosis in glaucoma is related to intraocular pressure and IOP-induced effects on extracellular matrix, Invest. Ophthalmol. Vis. Sci. 46 (2005) 175–182.

[193] J.C. Morrison, W.O.C.Y. Guo, E.C. Johnson, Pathophysiology of human glaucomatous optic nerve damage: insights from rodent models of glaucoma, Exp. Eye Res. 93 (2011) 156–164.

[194] S. Remtulla, P.E. Hallett, A schematic eye for the mouse, and comparisons with the rat., Vision Res. 25 (1985) 21–31. https://doi.org/10.1016/0042-6989(85)90076-8.

[195] L. Jia, W.O. Cepurna, E.C. Johnson, J.C. Morrison, Effect of General Anesthetics on IOP in Rats with Experimental Aqueous Outflow Obstruction, Invest. Ophthalmol. Vis. Sci. 41 (2000) 3415–3419.

[196] R.M. Douglas, N.M. Alam, B.D. Silver, T.J. McGill, W.W. Tschetter, G.T. Prusky, Independent visual threshold measurements in the two eyes of freely moving rats and mice using a virtual-reality optokinetic system, Vis Neurosci. 22 (2005) 677–684. https://doi.org/10.1017/S0952523805225166.

[197] J.C. Morrison, E.C. Johnson, W. Cepurna, L. Jia, Understanding mechanisms of pressure-induced optic nerve damage., Prog. Retin. Eye Res. 24 (2005) 217–240. https://doi.org/10.1016/j.preteyeres.2004.08.003.

[198] B.J. Frankfort, A.K. Khan, D.Y. Tse, I. Chung, J.J. Pang, Z. Yang, R.L. Gross, S.M. Wu, Elevated intraocular pressure causes inner retinal dysfunction before cell loss in a mouse model of experimental glaucoma, Invest Ophthalmol Vis Sci. 54 (2013) 762–770. https://doi.org/10.1167/iovs.12-10581.

[199] R.M. Sappington, B.J. Carlson, S.D. Crish, D.J. Calkins, The microbead occlusion model: a paradigm for induced ocular hypertension in rats and mice., Invest. Ophthalmol. Vis. Sci. 51 (2010) 207–216. https://doi.org/10.1167/iovs.09-3947.

[200] F. Mabuchi, M. Aihara, M.R. Mackey, J.D. Lindsey, R.N. Weinreb, Optic nerve damage in experimental mouse ocular hypertension., Invest. Ophthalmol. Vis. Sci. 44 (2003) 4321–4330. https://doi.org/10.1167/iovs.03-0138.

[201] P. V Turner, M.A. Albassam, Susceptibility of rats to corneal lesions after injectable anesthesia, Comp. Med. 55 (2005) 175–182.

[202] H. Chen, Y. Zhao, M. Liu, L. Feng, Z. Puyang, J. Yi, P. Liang, H.F. Zhang, J. Cang, J.B. Troy, X. Liu, Progressive degeneration of retinal and superior collicular functions in mice with sustained ocular hypertension, Invest Ophthalmol Vis Sci. 56

(2015) 1971–1984. https://doi.org/10.1167/iovs.14-15691.

[203] B. V Bui, B. Edmunds, G.A. Cioffi, B. Fortune, The gradient of retinal functional changes during acute intraocular pressure elevation, Invest Ophthalmol Vis Sci. 46 (2005) 202–213. https://doi.org/10.1167/iovs.04-0421.

[204] B. V Bui, B. Fortune, Ganglion cell contributions to the rat full-field electroretinogram, J Physiol. 555 (2004) 153–173. https://doi.org/10.1113/jphysiol.2003.052738.

[205] B. V Bui, Z. He, A.J. Vingrys, C.T. Nguyen, V.H. Wong, B. Fortune, Using the electroretinogram to understand how intraocular pressure elevation affects the rat retina, J Ophthalmol. 2013 (2013) 262467. https://doi.org/10.1155/2013/262467.

[206] C.S. Matsumoto, K. Shinoda, K. Nakatsuka, High correlation of scotopic and photopic electroretinogram components with severity of central retinal artery occlusion, Clin. Ophthalmol. (Auckland, NZ). 5 (2011) 115.

[207] Y. Zhao, B. Yu, Y.H. Xiang, X.J. Han, Y. Xu, K.F. So, A.D. Xu, Y.W. Ruan, Changes in retinal morphology, electroretinogram and visual behavior after transient global ischemia in adult rats, PLoS One. 8 (2013) e65555. https://doi.org/10.1371/journal.pone.0065555.

[208] G.T. Prusky, N.M. Alam, S. Beekman, R.M. Douglas, Rapid quantification of adult and developing mouse spatial vision using a virtual optomotor system, Invest Ophthalmol Vis Sci. 45 (2004) 4611–4616. https://doi.org/10.1167/iovs.04-0541.

[209] D.J. Calkins, Critical pathogenic events underlying progression of neurodegeneration in glaucoma, Prog. Retin. Eye Res. 31 (2012) 702–719.

[210] M.A. Fazio, M.J.A. Girard, W. Lee, J.S. Morris, C.F. Burgoyne, J.C. Downs, The Relationship Between Scleral Strain Change and Differential Cumulative Intraocular Pressure Exposure in the Nonhuman Primate Chronic Ocular Hypertension Model, Invest Ophthalmol Vis Sci. 60 (2019) 4141–4150. https://doi.org/10.1167/iovs.19-27060.

[211] T.T. Andreassen, A. Hjorth Simonsen, H. Oxlund, Biomechanical properties of keratoconus and normal corneas, Exp. Eye Res. 31 (1980) 435–441. https://doi.org/https://doi.org/10.1016/S0014-4835(80)80027-3.

[212] N.A. McBrien, A.I. Jobling, A. Gentle, Biomechanics of the sclera in myopia: extracellular and cellular factors, Optom. Vis. Sci. 86 (2009) E23–E30.

[213] N.S. Gokhale, Epidemiology of keratoconus, Indian J. Ophthalmol. 61 (2013) 382–383. https://doi.org/10.4103/0301-4738.116054.

[214] E.N. Gorskova, E.N. Sevost'ianov, [Epidemiology of keratoconus in the Urals]., Vestn. Oftalmol. 114 (1998) 38–40.

[215] J.B. Jonas, V. Nangia, A. Matin, M. Kulkarni, K. Bhojwani, Prevalence and associations of keratoconus in rural maharashtra in central India: the central India eye and medical study., Am. J. Ophthalmol. 148 (2009) 760–765. https://doi.org/10.1016/j.ajo.2009.06.024.

[216] B.A. Holden, T.R. Fricke, D.A. Wilson, M. Jong, K.S. Naidoo, P. Sankaridurg, T.Y. Wong, T.J. Naduvilath, S. Resnikoff, Global Prevalence of Myopia and High Myopia and Temporal Trends from 2000 through 2050, Ophthalmology. 123 (2016) 1036–1042. https://doi.org/https://doi.org/10.1016/j.ophtha.2016.01.006.

[217] Y. Ikuno, OVERVIEW OF THE COMPLICATIONS OF HIGH MYOPIA, RETINA. 37 (2017). https://journals.lww.com/retinajournal/Fulltext/2017/12000/OVERVIEW_OF_THE_COMPLICATIONS_OF_HIGH_MYOPIA.18.aspx.

[218] S.-M. Saw, G. Gazzard, E.C. Shih-Yen, W.-H. Chua, Myopia and associated pathological complications, Ophthalmic Physiol. Opt. 25 (2005) 381–391. https://doi.org/10.1111/j.1475-1313.2005.00298.x.

[219] L. Chen, X. Li, Z. Li, The risk factors of rhegmatogenous retinal detachment: A case control study, 21 (2003) 203–205.

[220] S.Y. Cohen, A. Laroche, Y. Leguen, G. Soubrane, G.J. Coscas, Etiology of choroidal neovascularization in young patients., Ophthalmology. 103 (1996) 1241–1244. https://doi.org/10.1016/s0161-6420(96)30515-0.

[221] L. Xu, Y. Wang, S. Wang, Y. Wang, J.B. Jonas, High myopia and glaucoma susceptibility the Beijing Eye Study., Ophthalmology. 114 (2007) 216–220. https://doi.org/10.1016/j.ophtha.2006.06.050.

[222] C. Stowell, C.F. Burgoyne, E.R. Tamm, C.R. Ethier, J.E. Dowling, C. Downs, M.H. Ellisman, S. Fisher, B. Fortune, M. Fruttiger, T. Jakobs, G. Lewis, R.H. Masland, C.H. Mitchell, J. Morrison, S.C. Sharma, I. Sigal, M. Sofroniew, L. Wang, J. Wiggs, S. Wu, Biomechanical aspects of axonal damage in glaucoma: A brief review, Exp. Eye Res. 157 (2017) 13–19. https://doi.org/https://doi.org/10.1016/j.exer.2017.02.005.

[223] G. Wollensak, E. Spoerl, T. Seiler, Riboflavin/ultraviolet-A-induced collagen crosslinking for the treatment of keratoconus, Am. J. Ophthalmol. 135 (2003) 620–627. https://doi.org/10.1016/S0002-9394(02)02220-1.

[224] G. Wollensak, E. Spoerl, Collagen crosslinking of human and porcine sclera, J. Cataract Refract. Surg. 30 (2004) 689–695. https://doi.org/10.1016/j.jcrs.2003.11.032.

[225] M.W. Belin, L. Lim, R.K. Rajpal, F. Hafezi, J.A.P. Gomes, B. Cochener, Corneal Cross-Linking: Current USA Status: Report From the Cornea Society., Cornea. 37 (2018) 1218–1225. https://doi.org/10.1097/ICO.0000000000001707.

[226] P. Kamaev, M. Smirnov, M. Friedman, E. Sherr, D. Muller, Aggregation and photoreduction in anaerobic solutions of flavin mononucleotide, J. Photochem. Photobiol. A Chem. 310 (2015) 60–65. https://doi.org/10.1016/j.jphotochem.2015.04.025.

[227] A. Scott McCall, S. Kraft, H.F. Edelhauser, G.W. Kidder, R.R. Lundquist, H.E. Bradshaw, Z. Dedeic, M.J.C. Dionne, E.M. Clement, G.W. Conrad, Mechanisms of corneal tissue cross-linking in response to treatment with topical riboflavin and Long-Wavelength Ultraviolet Radiation (UVA), Investig. Ophthalmol. Vis. Sci. 51 (2010) 129–138. https://doi.org/10.1167/iovs.09-3738.

[228] A. AU - Dotan, I. AU - Kremer, O. AU - Gal-Or, T. AU - Livnat, A. AU - Zigler, D. AU - Bourla, D. AU - Weinberger, Scleral Cross-linking Using Riboflavin and Ultraviolet-A Radiation for Prevention of Axial Myopia in a Rabbit Model, JoVE. (2016) e53201. https://doi.org/doi:10.3791/53201.

[229] E. Lanchares, M.A. del Buey, J.A. Cristóbal, L. Lavilla, B. Calvo, Biomechanical property analysis after corneal collagen cross-linking in relation to ultraviolet A irradiation time, Graefe's Arch. Clin. Exp. Ophthalmol. 249 (2011) 1223–1227. https://doi.org/10.1007/s00417-011-1674-0.

[230] N.A.L. O'Brart, D.P.S. O'Brart, N.H. Aldahlawi, S. Hayes, K.M. Meek, An Investigation of the Effects of Riboflavin Concentration on the Efficacy of Corneal Cross-Linking Using an Enzymatic Resistance Model in Porcine Corneas, Invest. Ophthalmol. Vis. Sci. 59 (2018) 1058–1065. https://doi.org/10.1167/iovs.17-22994.

[231] A.B. Cummings, R. McQuaid, S. Naughton, E. Brennan, M. Mrochen, Optimizing Corneal Cross-Linking in the Treatment of Keratoconus: A Comparison of Outcomes After Standard- and High-Intensity Protocols, Cornea. 35 (2016). https://journals.lww.com/corneajrnl/Fulltext/2016/06000/Optimizing_Corneal_Cross_Linking_in_the_Treatment.17.aspx.

[232] S. Schumacher, M. Mrochen, J. Wernli, M. Bueeler, T. Seiler, Optimization model for UV-riboflavin corneal cross-linking, Investig. Ophthalmol. Vis. Sci. 53 (2012) 762–769. https://doi.org/10.1167/iovs.11-8059.

[233] B. Chiang, J.H. Jung, M.R. Prausnitz, The suprachoroidal space as a route of administration to the posterior segment of the eye, Adv. Drug Deliv. Rev. 126 (2018) 58–66. https://doi.org/10.1016/j.addr.2018.03.001.

[234] J.H. Jung, P. Desit, M.R. Prausnitz, Targeted Drug Delivery in the Suprachoroidal Space by Swollen Hydrogel Pushing, Invest. Ophthalmol. Vis. Sci. 59 (2018) 2069–2079. https://doi.org/10.1167/iovs.17-23758.

[235] S. Liu, S. Li, B. Wang, X. Lin, Y. Wu, H. Liu, X. Qu, J. Dai, X. Zhou, H. Zhou, Scleral Cross-Linking Using Riboflavin UVA Irradiation for the Prevention of Myopia Progression in a Guinea Pig Model: Blocked Axial Extension and Altered Scleral Microstructure, PLoS One. 11 (2016) e0165792–e0165792.

https://doi.org/10.1371/journal.pone.0165792.

[236] P. Kamaev, M.D. Friedman, E. Sherr, D. Muller, Photochemical kinetics of corneal cross-linking with riboflavin, Investig. Ophthalmol. Vis. Sci. 53 (2012) 2360–2367. https://doi.org/10.1167/iovs.11-9385.

[237] N.H. Aldahlawi, S. Hayes, D.P.S. O'Brart, K.M. Meek, Standard versus accelerated riboflavin-ultraviolet corneal collagen crosslinking: Resistance against enzymatic digestion, J. Cataract Refract. Surg. 41 (2015) 1989–1996. https://doi.org/10.1016/j.jcrs.2015.10.004.

[238] M.M. Rahaman, M. Sikdar, M.B. Hossain, M. Rahaman, Mj. Hossain, A. Professor, Numerical Solution of Diffusion Equation by Finite Difference Method, IOSR J. Math. 11 (2015) 2278–5728. https://doi.org/10.9790/5728-11641925.

[239] R.J. LeVeque, Finite difference methods for ordinary and partial differential equations: steady-state and time-dependent problems, Siam, 2007.

[240] O.P. Iliev, A finite-difference scheme of second-order accuracy for elliptic equations with discontinuous coefficients, Differ. Equations. 36 (2000) 928–930. https://doi.org/10.1007/BF02754419.

[241] W. Spencer, J.R. Sutter, Kinetic study of the monomer-dimer equilibrium of methylene blue in aqueous solution, J. Phys. Chem. 83 (1979) 1573–1576. https://doi.org/10.1021/j100475a004.

[242] D. Xu, D.C. Neckers, Aggregation of rose bengal molecules in solution, J. Photochem. Photobiol. A Chem. 40 (1987) 361–370. https://doi.org/https://doi.org/10.1016/1010-6030(87)85013-X.

[243] F. Bettanin, T.A. de Carvalho Fontinelles, C.D. Maciel, L.G. Dias, M.D. Coutinho-Neto, P. Homem-de-Mello, Aggregation of photosensitizers: the role of dispersion and solvation on dimer formation energetics, Theor. Chem. Acc. 134 (2015) 152. https://doi.org/10.1007/s00214-015-1732-5.

[244] D.Y. Yu, S.J. Cringle, V. Alder, E.N. Su, Intraretinal oxygen distribution in the rat with graded systemic hyperoxia and hypercapnia, Investig. Ophthalmol. Vis. Sci. 40 (1999) 2082–2087.

[245] G. Bracchitta, A. Catalfo, G. De Guidi, UVA photoinduced yeast protein modifications by methylene blue and naproxen, Photochem. Photobiol. Sci. 12 (2013) 967–973. https://doi.org/10.1039/c3pp25359g.

[246] H.-R. Shen, J.D. Spikes, C.J. Smith, J. Kopeček, Photodynamic cross-linking of proteins: IV. Nature of the His–His bond(s) formed in the rose bengal-photosensitized cross-linking of N-benzoyl-L-histidine, J. Photochem. Photobiol. A Chem. 130 (2000) 1–6. https://doi.org/https://doi.org/10.1016/S1010-6030(99)00200-2.

[247] M. Mariotti, F. Leinisch, D.J. Leeming, B. Svensson, M.J. Davies, Mass-Spectrometry-Based Identi fi cation of Cross-Links in Proteins Exposed to Photo-Oxidation and Peroxyl Radicals Using 18 O Labeling and Optimized Tandem Mass Spectrometry Fragmentation, (2018). https://doi.org/10.1021/acs.jproteome.7b00881.

[248] E.F. Marques, M.H.G. Medeiros, P. Di Mascio, Singlet oxygen - induced protein aggregation : Lysozyme crosslink formation and nLC - MS / MS characterization, (2019) 894–905. https://doi.org/10.1002/jms.4448.

[249] O. Schmut, The organization of tissues of the eye by different collagen types, Albr. von Graefes Arch. Für Klin. Und Exp. Ophthalmol. 207 (1978) 189–199.

[250] D.E. Liu, T.J. Dursch, N.O. Taylor, S.Y. Chan, D.T. Bregante, C.J. Radke, Diffusion of water-soluble sorptive drugs in HEMA/MAA hydrogels, J. Control. Release. 239 (2016) 242–248. https://doi.org/10.1016/j.jconrel.2016.08.025.

[251] N. Miložič, M. Lubej, U. Novak, P. Žnidaršič-Plazl, I. Plazl, Evaluation of Diffusion Coefficient Determination using a Microfluidic Device, Chem. Biochem. Eng. Q. J. 28 (2014) 215–223. https://doi.org/10.15255/cabeq.2014.1938.

[252] M.D. Friedman, R. Pertaub, D. Usher, E. Sherr, P. Kamaev, D. Muller, Advanced corneal cross-linking system with fluorescence dosimetry, J. Ophthalmol. 2012 (2012). https://doi.org/10.1155/2012/303459.

[253] M. Liska, L. Bartos, J. Valasek, Dimerization of methylene blue in aqueous solutions of inorganic electrolytes, Chem. Pap. 43 (1989) 303–313.

[254] M. Hammer, D. Schweitzer, Quantitative reflection spectroscopy at the human ocular fundus, Phys. Med. Biol. 47 (2002) 179–191. https://doi.org/10.1088/0031-9155/47/2/301.

[255] T. Sarna, H.A. Swartz, The Physical Properties of Melanins, Pigment. Syst. (2006) 311–341. https://doi.org/doi:10.1002/9780470987100.ch16.

[256] J.N. Chacon, J. McLearie, R.S. Sinclair, SINGLET OXYGEN YIELDS AND RADICAL CONTRIBUTIONS IN THE DYE-SENSITISED PHOTO-OXIDATION IN METHANOL OF ESTERS OF POLYUNSATURATED FATTY ACIDS (OLEIC, LINOLEIC, LINOLENIC AND ARACHIDONIC), Photochem. Photobiol. 47 (1988) 647–656. https://doi.org/10.1111/j.1751-1097.1988.tb02760.x.

[257] D.R. Cardoso, D.W. Franco, K. Olsen, M.L. Andersen, L.H. Skibsted, Reactivity of bovine whey proteins, peptides, and amino acids toward triplet riboflavin as studied by laser flash photolysis, J. Agric. Food Chem. 52 (2004) 6602–6606. https://doi.org/10.1021/jf0401165.

[258] L.P. Candeias, P. Wardman, R.P. Mason, The reaction of oxygen with radicals from

oxidation of tryptophan and indole-3-acetic acid., Biophys. Chem. 67 (1997) 229–237. https://doi.org/10.1016/s0301-4622(97)00052-5.

[259] M. Goldsmith, P. Rogers, N.M. Cabral, K.P. Ghiggino, F. Roddick, Riboflavin triplet quenchers inhibit lightstruck flavor formation in beer, J. Am. Soc. Brew. Chem. 63 (2005) 177–184. https://doi.org/10.1094/ASBCJ-63-0177.

[260] M. González-Béjar, P. Montes-Navajas, H. García, J.C. Scaiano, Methylene blue encapsulation in cucurbit[7]uril: laser flash photolysis and near-IR luminescence studies of the interaction with oxygen, Langmuir. 25 (2009) 10490–10494. https://doi.org/10.1021/la9011923.

[261] B.J. Fritz, K. Matsui, S. Kasai, A. Yoshimura, TRIPLET LIFETIMES OF SOME FLAVINS, Photochem. Photobiol. 45 (1987) 539–541. https://doi.org/10.1111/j.1751-1097.1987.tb05415.x.

[262] P. V. Kamat, N.N. Lichtin, Photoinduced electron ejection from methylene blue in water and acetonitrile, J. Phys. Chem. 85 (1981) 3864–3868. https://doi.org/10.1021/j150625a031.

[263] M.A.J. Rodgers, P.T. Snowden, Lifetime of O2(1Δg) in Liquid Water As Determined by Time-Resolved Infrared Luminescence Measurements, J. Am. Chem. Soc. 104 (1982) 5541–5543. https://doi.org/10.1021/ja00384a070.

[264] S.G. Bertolotti, N.A. García, G.A. Argüello, Effect of the peptide bond on the singlet-molecular-oxygen-mediated sensitized photo-oxidation of tyrosine and tryptophan dipeptides. A kinetic study, J. Photochem. Photobiol. B Biol. 10 (1991) 57–70. https://doi.org/https://doi.org/10.1016/1011-1344(91)80212-Z.

[265] N.A. García, G. Rossbroich, S.E. Braslavsky, H. Dürr, C. Dorweiler, Photoacoustic measurements and mindo/3 calculations of energy storage by short-lived species: the spiro[1,8-a]dihydroindolizine-betaine system, J. Photochem. 31 (1985) 297–305. https://doi.org/https://doi.org/10.1016/0047-2670(85)85098-X.

[266] H. Schmidt, A. Al-Ibrahim, U. Dietzel, L. Bieker, ON THE ACRIDINE AND THIAZINE DYE SENSITIZED PHOTODYNAMIC INACTIVATION OF LYSOZYME—SINGLET OXYGEN SELF-QUENCHING BY THE SENSITIZERS, Photochem. Photobiol. 33 (1981) 127–130. https://doi.org/10.1111/j.1751-1097.1981.tb04310.x.

[267] S. Ito, M. Kikuta, S. Koike, G. Szewczyk, M. Sarna, A. Zadlo, T. Sarna, K. Wakamatsu, Roles of reactive oxygen species in UVA-induced oxidation of 5,6-dihydroxyindole-2-carboxylic acid-melanin as studied by differential spectrophotometric method, Pigment Cell Melanoma Res. 29 (2016) 340–351. https://doi.org/10.1111/pcmr.12469.

[268] R.W. Bunsen, H.E. Roscoe, Photochemical Researches.--Part V. On the Measurement of the Chemical Action of Direct and Diffuse Sunlight. [Abstract],

Proc. R. Soc. London. 12 (1862) 306–312. http://www.jstor.org/stable/112258.

[269] A. Wright, W.A. Bubb, C.L. Hawkins, M.J. Davies, Singlet oxygen-mediated protein oxidation: evidence for the formation of reactive side chain peroxides on tyrosine residues., Photochem. Photobiol. 76 (2002) 35–46. https://doi.org/10.1562/0031-8655(2002)076<0035:sompoe>2.0.co;2.

[270] O. Richoz, A. Hammer, D. Tabibian, Z. Gatzioufas, The Biomechanical Effect of Corneal Collagen Cross-Linking (CXL) With Riboflavin and UV-A is Oxygen Dependent, 2 (2013) 1–5. https://doi.org/10.1167/tvst.2.7.6.

[271] S. Pescina, P. Santi, G. Ferrari, C. Padula, P. Cavallini, P. Govoni, S. Nicoli, Ex vivo models to evaluate the role of ocular melanin in trans-scleral drug delivery., Eur. J. Pharm. Sci. 46 (2012) 475–483. https://doi.org/10.1016/j.ejps.2012.03.013.

[272] E.I. Alarcon, H. Poblete, H. Roh, I.E. Kochevar, Rose Bengal Binding to Collagen and Tissue Photobonding, (2017). https://doi.org/10.1021/acsomega.7b00675.

[273] M.M. Kim, A.A. Ghogare, A. Greer, T.C. Zhu, On the in vivo photochemical rate parameters for PDT reactive oxygen species modeling, Phys. Med. Biol. 62 (2017) R1–R48. https://doi.org/10.1088/1361-6560/62/5/R1.

[274] R. Herber, K.S. Kunert, V. Veliká, E. Spoerl, L.E. Pillunat, F. Raiskup, Influence of the beam profile crosslinking setting on changes in corneal topography and tomography in progressive keratoconus: Preliminary results, J. Cataract Refract. Surg. 44 (2018) 718–724.

[275] R. Shetty, N. Pahuja, T. Roshan, R. Deshmukh, M. Francis, A. Ghosh, A.S. Roy, Customized corneal cross-linking using different UVA beam profiles, J. Refract. Surg. 33 (2017) 676–682.

[276] J. Brekelmans, A. Goz, M.M. Dickman, A. Brandis, X. Sui, H.D. Wagner, R.M.M.A. Nuijts, A. Scherz, A.L. Marcovich, Long-Term Biomechanical and Histologic Results of WST-D/NIR Corneal Stiffening in Rabbits, Up to 8 Months Follow-up, Invest. Ophthalmol. Vis. Sci. 58 (2017) 4089–4095. https://doi.org/10.1167/iovs.17-22108.

[277] G. Wollensak, E. Spoerl, C. Wirbelauer, D.T. Pham, Influence of indocyanine green staining on the biomechanical strength of porcine internal limiting membrane, Ophthalmologica. 218 (2004) 278–282. https://doi.org/10.1159/000078621.

[278] K.M. Christmas, J.B. Bassingthwaighte, Equations for O(2) and CO(2) solubilities in saline and plasma: combining temperature and density dependences, J. Appl. Physiol. 122 (2017) 1313–1320. https://doi.org/10.1152/japplphysiol.01124.2016.

[279] J. Sendroy, R.T. Dillon, D.D. Van Slyke, W. the technical assistance of D. Kertesz, STUDIES OF GAS AND ELECTROLYTE EQUILIBRIA IN BLOOD: XIX. THE SOLUBILITY AND PHYSICAL STATE OF UNCOMBINED OXYGEN IN

BLOOD , J. Biol. Chem. . 105 (1934) 597–632. http://www.jbc.org/content/105/3/597.short.

[280] T.U. Consortium, UniProt: a worldwide hub of protein knowledge, Nucleic Acids Res. 47 (2018) D506–D515. https://doi.org/10.1093/nar/gky1049.

[281] G. Bawa, T. V Tkatchenko, I. Avrutsky, A. V Tkatchenko, Variational analysis of the mouse and rat eye optical parameters, Biomed. Opt. Express. 4 (2013) 2585–2595. https://doi.org/10.1364/BOE.4.002585.

[282] J. Heichel, F. Wilhelm, K.S. Kunert, T. Hammer, Topographic Findings of the Porcine Cornea., Med. Hypothesis, Discov. Innov. Ophthalmol. J. 5 (2016) 125–131.

[283] R.C. Ryals, M.D. Andrews, S. Datta, A.S. Coyner, C.M. Fischer, Y. Wen, M.E. Pennesi, T.J. McGill, Long-term Characterization of Retinal Degeneration in Royal College of Surgeons Rats Using Spectral-Domain Optical Coherence Tomography, Invest. Ophthalmol. Vis. Sci. 58 (2017) 1378–1386. https://doi.org/10.1167/iovs.16-20363.

[284] W. Xie, M. Zhao, S.-H. Tsai, W.L. Burkes, L.B. Potts, W. Xu, H.R. Payne, T.W. Hein, L. Kuo, R.H. Rosa, Correlation of spectral domain optical coherence tomography with histology and electron microscopy in the porcine retina, Exp. Eye Res. 177 (2018) 181–190. https://doi.org/https://doi.org/10.1016/j.exer.2018.08.003.

[285] F. Ko, P.J. Foster, N.G. Strouthidis, Y. Shweikh, Q. Yang, C.A. Reisman, Z.A. Muthy, U. Chakravarthy, A.J. Lotery, P.A. Keane, A. Tufail, C.M. Grossi, P.J. Patel, Associations with Retinal Pigment Epithelium Thickness Measures in a Large Cohort: Results from the UK Biobank, Ophthalmology. 124 (2017) 105–117. https://doi.org/https://doi.org/10.1016/j.ophtha.2016.07.033.

[286] S. Hariri, A.A. Moayed, V. Choh, K. Bizheva, In Vivo Assessment of Thickness and Reflectivity in a Rat Outer Retinal Degeneration Model with Ultrahigh Resolution Optical Coherence Tomography, Invest. Ophthalmol. Vis. Sci. 53 (2012) 1982–1989. https://doi.org/10.1167/iovs.11-8395.

[287] M. Pazos, H. Yang, S.K. Gardiner, W.O. Cepurna, E.C. Johnson, J.C. Morrison, C.F. Burgoyne, Expansions of the neurovascular scleral canal and contained optic nerve occur early in the hypertonic saline rat experimental glaucoma model, Exp. Eye Res. 145 (2016) 173–186. https://doi.org/10.1016/j.exer.2015.10.014.

[288] I.P. Herring, R.B. Duncan, J.P. Pickett, C.R. Bass, The Porcine Eye as a Surrogate Model for the Human Eye: Anatomical and Mechanical Relationships, (n.d.).

[289] E.A. Maul, D.S. Friedman, D.S. Chang, M. V Boland, P.Y. Ramulu, H.D. Jampel, H.A. Quigley, Choroidal thickness measured by spectral domain optical coherence tomography: factors affecting thickness in glaucoma patients., Ophthalmology. 118

(2011) 1571–1579. https://doi.org/10.1016/j.ophtha.2011.01.016.

[290] T.W. Olsen, S. Sanderson, X. Feng, W.C. Hubbard, Porcine sclera: thickness and surface area., Invest. Ophthalmol. Vis. Sci. 43 (2002) 2529–2532.

[291] T.W. Olsen, S.Y. Aaberg, D.H. Geroski, H.F. Edelhauser, Human sclera: thickness and surface area., Am. J. Ophthalmol. 125 (1998) 237–241. https://doi.org/10.1016/s0002-9394(99)80096-8.

[292] T. Chiba, H. Takahashi, N. Chiba, H. Iijima, In Vivo Thickness Measurements of Conjunctiva and Tenon's capsule with Optical Coherence Tomography in Healthy Subjects, Invest. Ophthalmol. Vis. Sci. 55 (2014) 4873.

[293] X. Shu, H. Li, B. Dong, C. Sun, H.F. Zhang, Quantifying melanin concentration in retinal pigment epithelium using broadband photoacoustic microscopy., Biomed. Opt. Express. 8 (2017) 2851–2865. https://doi.org/10.1364/BOE.8.002851.

[294] N.P.S. Cheruvu, A.C. Amrite, U.B. Kompella, Effect of eye pigmentation on transscleral drug delivery, Investig. Ophthalmol. Vis. Sci. 49 (2008) 333–341. https://doi.org/10.1167/iovs.07-0214.

[295] C. Durairaj, J.E. Chastain, U.B. Kompella, Intraocular distribution of melanin in human, monkey, rabbit, minipig and dog eyes, Exp. Eye Res. 98 (2012) 23–27. https://doi.org/https://doi.org/10.1016/j.exer.2012.03.004.

[296] A. Hughes, A schematic eye for the rat, Vision Res. 19 (1979) 569–588. https://doi.org/https://doi.org/10.1016/0042-6989(79)90143-3.

[297] A. Vogel, C. Dlugos, R. Nuffer, R. Birngruber, Optical properties of human sclera, and their consequences for transscleral laser applications., Lasers Surg. Med. 11 (1991) 331–340. https://doi.org/10.1002/lsm.1900110404.

[298] a N. Bashkatov, E. a Genina, V.I. Kochubey, V.V.C. 19/7/12 Tuchin, Estimation of wavelength dependence of refractive index of collagen fibers of scleral tissue, Control. Tissue Opt. Prop. Appl. Clin. Study. 1 (2000) 33–265. https://doi.org/10.1117/12.405952.